
Characterization of two novel kinesin-14 subfamilies from *Arabidopsis thaliana*

Dissertation with the aim of achieving a doctoral degree
at the Faculty of Mathematics, Informatics, and Natural Sciences

Department of Biology

University of Hamburg

submitted by

Isabel Machens

from Kiel

Hamburg, 2018

This thesis was performed from April 2014 till April 2018 in the department of Molecular Plant Physiology at the University of Hamburg (Biozentrum Klein Flottbek).

Supervisor: Jun.-Prof. Wim Walter, PhD

First reviewer: Jun.-Prof. Wim Walter, PhD

Second reviewer: Prof. Dr. Sigrun Reumann

Date of oral defense: 29.06.2018

Head of the examination committee: Prof. Dr. Julia Kehr

Table of Contents

List of abbreviations

1 Zusammenfassung	1
2 Abstract	2
3 General introduction	3
4 F-BAR kinesins in <i>Arabidopsis thaliana</i>	10
4.1 Introduction.....	10
4.2 Results of the <i>in silico</i> and <i>in vitro</i> experiments.....	14
4.2.1 <i>bark1</i> and <i>bark2</i> have a high resemblance of gene organization	14
4.2.2 Expression and purification of <i>AtBARK</i> constructs for <i>in vitro</i> analyses.....	15
4.2.3 <i>AtBARK</i> proteins bind microtubules stiffly or diffusively in gliding assays	17
4.2.4 Single <i>AtBARK</i> molecules or <i>AtBARK</i> complexes show diffusive movement on microtubules	18
4.2.5 Integrity tests with FRAP microscopy prove a successful generation of supported lipid bilayers.....	19
4.2.6 <i>AtBARK</i> proteins diffusively link microtubules to supported lipid bilayers.....	20
4.2.7 <i>AtBARK</i> proteins specifically bind to unilamellar vesicles.....	21
4.2.8 <i>AtBARK</i> proteins are a minus end-directed motor proteins that transport vesicles along microtubules	22
4.3 Results of the <i>in vivo</i> experiments	28
4.3.1 <i>bark1</i> and <i>bark2</i> are expressed in pollen.....	28
4.3.2 Homozygous <i>bark1-1</i> plants show aborted pollen grains and modifications in pollen tube development	29
4.3.3 Oryzalin impairs pollen tube development in a similar way as the <i>bark1-1</i> line.	32
4.3.4 Multiple punctuated, motile <i>AtBARK</i> signals were detected in growing pollen tubes.....	32
4.3.5 Homozygous <i>bark1-1</i> plants show an increased number of smaller siliques and a reduced seed number per silique	33

4.3.6	The pollen, silique, and seed phenotypes of homozygous <i>bark1-1</i> plants are temperature-independent.....	34
4.3.7	The pollen, silique, and seed phenotypes of homozygous <i>bark1-1</i> plants are humidity-independent.....	37
4.4	Discussion.....	39
4.4.1	The influence of motor functionality on gliding and stepping assays with <i>AtBARK</i> proteins.....	39
4.4.2	The influence of membrane fluidity, motor density, and motor functionality on membrane gliding assays with <i>AtBARK</i> proteins.....	41
4.4.3	The influence of roadblocks on minus end-directed vesicle transport by <i>AtBARK</i> proteins.....	42
4.4.4	The potential role of <i>AtBARK</i> proteins and microtubules during pollen development.....	45
4.4.5	Proposed model for <i>AtBARK</i> involvement during endocytosis in angiosperm pollen tube development.....	50
4.4.6	Conclusion.....	51
5	A novel microtubule segregating kinesin in <i>Arabidopsis thaliana</i>.....	52
5.1	Introduction.....	52
5.2	Results of the <i>in silico</i> and <i>in vitro</i> experiments.....	54
5.2.1	<i>misk1</i> and <i>misk2</i> show a similarity in gene organization.....	54
5.2.2	Expression and purification of <i>AtMISK1</i> for <i>in vitro</i> analyses.....	55
5.2.3	The minus end-directed <i>AtMISK1</i> transports microtubules with a distinct velocity.....	56
5.2.4	<i>AtMISK1</i> shows diffusive and non-processive interactions with microtubules... ..	57
5.2.5	<i>AtMISK1</i> crosslinks or slides microtubules along each other dependent on microtubule polarity.....	59
5.3	Results of the <i>in vivo</i> experiments.....	61
5.3.1	<i>misk1</i> is strongly expressed in the vascular tissue of growing roots.....	61
5.3.2	Homozygous T-DNA insertion lines of <i>misk1</i> do not show a root or annular xylem phenotype.....	62

5.4	Discussion	63
5.4.1	The N-terminal motor domain of <i>AtMISK1</i> probably contains a neck linker for minus end-directed movement	63
5.4.2	<i>AtMISK1</i> probably forms a tetrameric or a flexible, dimeric structure in <i>in vitro</i> assays.....	63
5.4.3	The potential role of <i>AtMISK1</i> during secondary cell wall development in xylem tissue.....	67
5.4.4	Conclusion.....	70
6	General discussion.....	71
7	Material and methods	73
7.1	Organisms	73
7.1.1	Bacterial strains	73
7.1.2	Plant lines of <i>Arabidopsis thaliana</i>	73
7.1.3	Vectors.....	74
7.2	Material	75
7.2.1	Chemicals	75
7.2.2	Kits	78
7.2.3	Antibodies	78
7.2.4	Enzymes	78
7.2.5	Equipment	78
7.3	Molecular biological methods.....	81
7.3.1	RNA-synthesis	81
7.3.2	cDNA-synthesis	81
7.3.3	Verification of <i>Arabidopsis thaliana</i> knockout plant lines with PCR	81
7.3.4	Genomic DNA isolation of <i>Arabidopsis thaliana</i> plants	82
7.3.5	Genotyping of <i>Arabidopsis thaliana</i> plants with PCR.....	82
7.3.6	Agarose gel electrophoresis.....	83
7.3.7	Overlap extension cloning.....	83

7.3.8	Gateway cloning.....	83
7.3.9	Site-directed mutagenesis.....	84
7.3.10	Preparation of chemically competent cells.....	84
7.3.11	Preparation of electrocompetent agrobacteria.....	84
7.3.12	Transformation of chemically competent cells.....	85
7.3.13	Electroporation of electrocompetent agrobacteria.....	85
7.3.14	Colony PCR.....	85
7.3.15	Sequencing.....	86
7.3.16	Molecular cloning of expression constructs for <i>in vitro</i> analyses.....	86
7.3.17	Molecular cloning of constructs for <i>in vivo</i> analyses.....	89
7.4	Protein biochemical methods.....	91
7.4.1	Protein expression test.....	91
7.4.2	SDS-PAGE.....	92
7.4.3	Protein expression.....	93
7.4.4	Protein purification.....	93
7.4.5	Tubulin purification from porcine brain.....	94
7.4.6	Tubulin labeling.....	95
7.4.7	Preparation of microtubules.....	96
7.5	Methods for characterization of kinesin motor proteins.....	97
7.5.1	Generation of unilamellar vesicles from an inversed emulsion.....	97
7.5.2	Vesicle-binding assay.....	97
7.5.3	Preparation of flow cell chambers for <i>in vitro</i> assays.....	98
7.5.4	Gliding assay.....	99
7.5.5	Sliding assay.....	100
7.5.6	Stepping assay.....	101
7.5.7	Vesicle transport assay.....	102
7.5.8	Components used for the solutions of the motility assays.....	103
7.5.9	Total internal reflection fluorescence microscopy.....	103

7.5.10	Generation of supported lipid bilayers.....	104
7.5.11	Fluorescence recovery after photobleaching microscopy.....	105
7.5.12	Membrane gliding assay	105
7.6	Methods for cultivation and analysis of <i>Arabidopsis thaliana</i> plants.....	106
7.6.1	Cultivation of <i>Arabidopsis thaliana</i> plants	106
7.6.2	Phenotype analyses of <i>bark</i> T-DNA insertion lines.....	107
7.6.3	Phenotype analyses of <i>misk1</i> T-DNA insertion lines.....	109
7.6.4	Floral painting and selection of transgenic plants	110
7.6.5	Generation of promotor-GUS lines and 35S- <i>bark1</i> -GFP lines	110
7.6.6	β -glucuronidase staining	111
7.7	Software and databases	112
8	References	113
9	Appendix	124
	Paper 1	
	Paper 2	
	List of publications	
	Acknowledgements	
	English certificate	
	Affidavit	

List of abbreviations

°C	degree Celsius
%	percent
μl	microliter
μM	micromolar
μm	micrometer
aa	amino acid
AP2	adaptor protein 2
<i>A. tumefaciens</i>	<i>Agrobacterium tumefaciens</i>
ANTH	AP180 N-terminal homology
<i>A. thaliana (At)</i>	<i>Arabidopsis thaliana</i>
ATK1	<i>Arabidopsis thaliana</i> kinesin1
ATK5	<i>Arabidopsis thaliana</i> kinesin5
BAR	Bin Amphiphysin Rvs
BARK	Bin Amphiphysin Rvs kinesin
BAR-PH	Bin Amphiphysin Rvs-Pleckstrin homology
bp	base pair
CC	coiled-coil
cDNA	complementary deoxyribonucleic acid
CENP-E	centrosome-associated protein E
CIP4/ Toca-3	Cdc42-interacting protein 4
CME	clathrin-mediated endocytosis
CO ₂	carbon dioxide
Col-0	Columbia wild-type
D	diffusion coefficient
DLK	dual localization kinesin
<i>E.coli</i>	<i>Escherichia coli</i>
e.g.	exempli gratia (= for example)
EGFP	enhanced green fluorescent protein
et al.	et alii (= and others)
FBP17/ Toca-2	formin-binding protein 17
FCH/EFC	Fes/Cip4 homology/extended FCH
FCHo	Fer/Cip4 homology
FIESTA	fluorescent image evaluation software for tracking & analysis
FRAP	fluorescence recovery after photobleaching
x g	times gravity

gDNA	genomic deoxyribonucleic acid
GFP	green fluorescent protein
GST	glutathione S-transferase
GTP	guanosine triphosphate
GUS	β -glucuronidase
His	histidine
Hz	hertz
I-BAR	inverse-Bin Amphiphysin Rvs
kb	kilobase
KCBP	kinesin-like calmodulin binding protein
KCH	kinesins with a calponin homology domain
kDA	kilodalton
Kif17	kinesin family17
Kin-14D	kinesin-14D
M	molar
MAP	microtubule-associated protein
MATLAB	matrix laboratory
MCAK	mitotic centromere-associated kinesin
MIDD1	microtubule depletion domain1
MISK	microtubule segregating kinesin
min	minute
ml	milliliter
mM	millimolar
MSD	mean square displacement
N	number
N-BAR	N-terminal amphipathic helix-Bin Amphiphysin Rvs
Ncd	non-claret disjunctional
ng	nanogram
nm	nanometer
nt	nucleotide
OD ₆₀₀	optical density ₆₀₀
<i>Os</i>	<i>Oryza sativa</i>
PC	phosphatidylcholine
PCR	polymerase chain reaction
pH	potential of hydrogen
PS	phosphatidylserine
qPCR	quantitative polymerase chain reaction
ROP	Rac/Rho small GTPase

RNA	ribonucleic acid
RT	room temperature
RT-PCR	reverse transcriptase-polymerase chain reaction
s	second
s.d.	standard deviation
SDS-PAGE	sodium dodecyl sulfate-polyacrylamide gel electrophoresis
seg. WT	segregating wild-type
SH3	SRC homology 3
SLB	supported lipid bilayer
suz1	suppressor of zwichell
TAIR	The Arabidopsis Information Resource
TASH3	TPLATE-associated SRC homology 3
T-DNA	transfer-deoxyribonucleic acid
TIRF	total internal reflection fluorescence microscopy
UTR	untranslated region
V	volt
WT	wild-type
X-Gluc	5-bromo-4-chloro-3-indolyl glucuronide

The abbreviations for the chemicals are listed in Table 8 (see **7.2.1**).

1 Zusammenfassung

Die minusendgerichtete Kinesin-14 Familie ist mit 21 Mitgliedern, die verschiedene, teilweise pflanzenspezifische Funktionen ausführen, die größte Kinesin Unterfamilie in *Arabidopsis thaliana* (*At*, *A. thaliana*). In dieser Arbeit werden verschiedene *At*Kinesin-14 Mitglieder bezüglich ihrer Strukturen, Eigenschaften, Funktionen und Lokalisation untersucht, um eine Vorstellung von möglichen physiologischen Rollen zu erhalten.

Eine Untergruppe der *At*Kinesin-14 Motoren (*At*BARK) zeichnet sich strukturell durch eine interne Motordomäne flankiert von ‘Coiled-coil‘ Domänen und einer N-terminalen F-BAR Domäne aus. In dieser Arbeit wurde gezeigt, dass *At*BARK1 und *At*BARK2 minusendgerichtete, nicht prozessive Motoren sind, die Membranen und Mikrotubuli erkennen und binden. Zudem transportieren sie Vesikel entlang von Mikrotubuli. Weitere Analysen ergaben eine hohe Sequenzähnlichkeit beider Proteine und eine Expression in Pollen. Eine *bark1* T-DNA Insertionslinie zeigte einen Phänotyp bezüglich Pollen-, Schoten- und Samenentwicklung. Diese Ergebnisse könnten auf eine Rolle von *At*BARK Proteinen während der Endozytose im wachsenden Pollenschlauch hinweisen.

Die zweite Untergruppe (*At*MISK) umfasst pflanzenspezifische *At*Kinesin-14 Motoren mit einer N-terminalen Motordomäne. Eigene *in vitro* Analysen haben gezeigt, dass *At*MISK1 ohne seinen ‘Tail‘ ein minusendgerichteter, nicht prozessiver, diffusiver Motor ist. *At*MISK1 kann Mikrotubuli, abhängig von ihrer Polarität, stabil quervernetzen oder aneinander entlang verschieben. Weitere Analysen zeigten eine Expression im Wurzelxylem. Diese Ergebnisse könnten auf eine Rolle in der Zytoskelettorganisation während der Zellwandentwicklung im Wurzelxylem hinweisen.

Wie anhand der zwei untersuchten Gruppen zu sehen, umfasst die *At*Kinesin-14 Familie Motoren, die unterschiedliche Domänenstrukturen und -organisation, Expressionsorte, Eigenschaften und Funktionen aufweisen. Aufgrund dieser Unterschiede könnte diese große Gruppe in folgende Untergruppen unterteilt werden:

- (1) archetypische Kinesin-14 Motoren mit C-terminaler Motordomäne und möglicher Funktion in der Zellteilung (*At*KatA-C, *At*Kin-14D);
- (2) pflanzenspezifische Kinesin-14 Motoren mit N-terminaler (*At*MISK1-2, *At*Kin-14S) oder interner Motordomäne (*At*DGBLK, *At*DGBK) flankiert von einer ‘Coiled-coil‘ Domäne;
- (3) Kinesin-14 Motoren mit einer internen Motordomäne flankiert von zwei ‘Coiled-coil‘ Domänen (*At*KCH1-7, *At*BARK1-2).

2 Abstract

The minus end-directed kinesin-14 family is the largest kinesin subfamily in *Arabidopsis thaliana* (*At*, *A. thaliana*). Twenty-one members enable different, partially plant-specific functions. This thesis deals with different *At*kinesin-14 members that were analyzed concerning their structures, properties, functions, and localization to gain an insight into possible physiological roles.

One subgroup of *At*kinesin-14 motors (*At*BARK) has an internal motor domain flanked by coiled-coil domains and an N-terminal F-BAR domain. The results of this thesis showed that *At*BARK1 and *At*BARK2 are minus end-directed, non-processive motors with membrane- and microtubule-sensing and binding properties. Moreover, they are able to transport vesicles along microtubules with a distinct velocity. Further experiments showed a high sequence similarity of the two proteins and an expression in pollen. Analyses of one *bark1* T-DNA insertion line offered pollen, silique, and seed phenotypes. Taken together, these results indicate an involvement of *At*BARK proteins in endocytosis during pollen tube growth.

The motors of the second subgroup - containing an N-terminal motor domain - were named *At*MISK. *In vitro* analyses showed that *At*MISK1 - without its tail domain - is a minus end-directed, non-processive and diffusive motor. *At*MISK1 stably crosslinks or slides microtubules depending on their polarity. Further analyses showed an expression in the xylem tissue of roots. Taken together, these results indicate a role in the rearrangement of the cytoskeleton for cell wall development in differentiating xylem tissue of the root.

These analyses of the subgroups *At*BARK and *At*MISK demonstrate the diversity of the *At*kinesin-14 family due to different domain structures and organization, expression areas, properties, and functions. These differences suggest that this large group could be further subdivided. The following classification might be possible:

- (1) archetypic kinesin-14 motors with a C-terminal motor domain and putative functions in cell division (*At*KatA-C, *At*Kin-14D);
- (2) plant-specific kinesin-14 motors with an N-terminal (*At*MISK1-2, *At*Kin-14S) or an internal motor domain (*At*DGBLK, *At*DGBK) flanked by one coiled-coil domain;
- (3) kinesins with an internal motor domain flanked by two coiled-coil domains (*At*KCH1-7, *At*BARK1-2).

3 General introduction

The cytoskeletal network (microtubules, actin, and intermediate filaments) and interacting motor proteins play an important role in fundamental development processes in eukaryotes such as cell growth, cell differentiation, or cell division [1-3]. There are three main classes of motor proteins in eukaryotes: myosins, dyneins, and kinesins [1, 4]. All three proteins are mechanochemical enzymes, which obtain energy from ATP hydrolysis for conformational changes. These conformational changes are necessary for unidirectional transport processes along specific cytoskeletal structures [1, 4, 5]. In this thesis, different minus end-directed *At*kinesin-14 motor proteins were investigated.

Kinesins exist in each eukaryotic organism [1-3, 6]. The first kinesin was identified in 1985 involved in vesicle transport processes in squid giant axons [1, 7]. From that time onwards, research in the field of kinesin motor proteins has continuously increased.

The generally admitted structure of kinesins comprises two motor heads/ domains, a neck linker, a stalk, and a tail domain (Figure 1A) [1, 5, 8]. The motor heads form a highly conserved catalytic core with nucleotide- and microtubule-binding sites (Figure 1B) [1, 5]. The neck linker, which determines the directionality [5, 9], connects both heads with the filamentous stalk. This stalk comprises an α -helical coiled-coil domain, which is necessary for protein dimerization [1, 5, 6, 8]. The weakly conserved tail enables different motor-specific interactions with cargo molecules [1, 5, 6, 8].

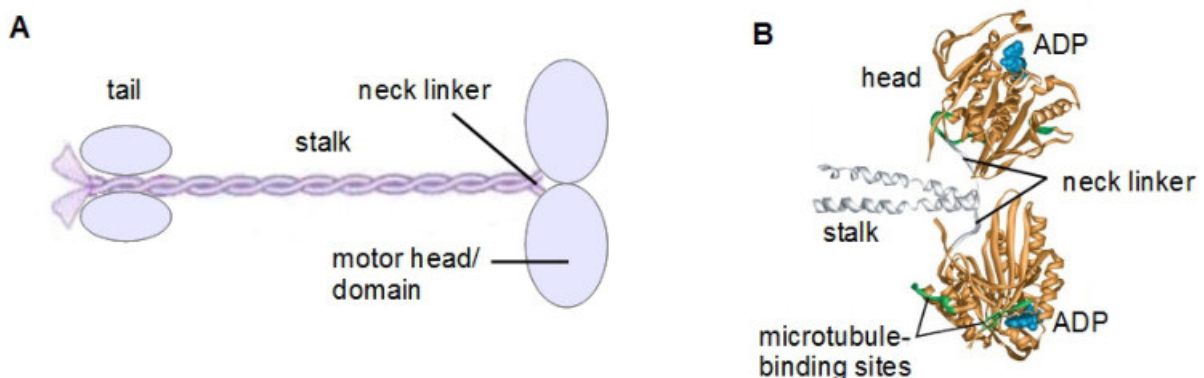


Figure 1: General structure of kinesin motor proteins.

(A) The schematic model shows the structure of a kinesin motor protein with two motor heads/ domains attached to a filamentous coiled-coil stalk with a neck linker, and a tail domain. Modified from [10].

(B) Three-dimensional structure analysis of two kinesin heads with x-ray crystallography. Both heads have nucleotide- and microtubule-binding sites. Modified from [10].

The microtubule-binding sites enable contact between the kinesin and its track for movement. Microtubules comprise α - and β -tubulin heterodimers, which are longitudinally organized to linear protofilaments and connected through covalent bonds. *In vivo*, thirteen protofilaments again are longitudinally organized into cylindrical, tubular microtubules with a diameter of 25 nm and a length of several micrometers (Figure 2A) [10].

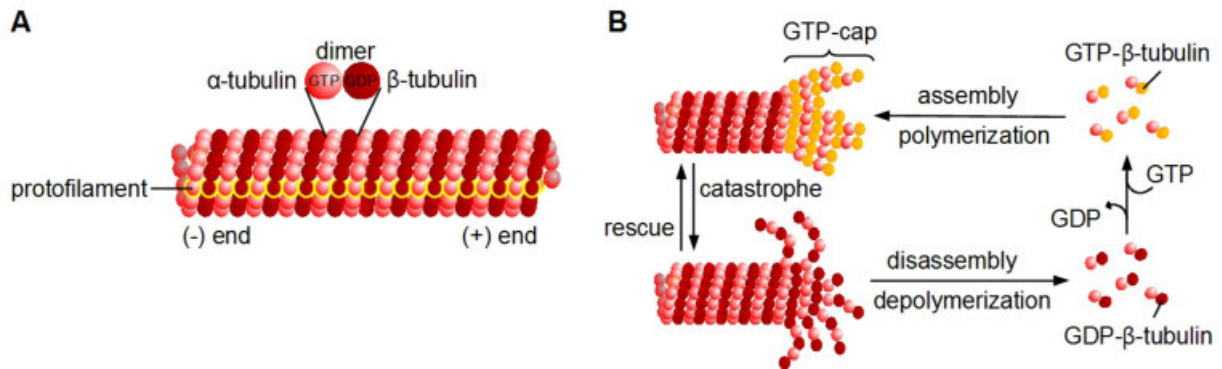


Figure 2: Structure, components, and dynamics of microtubules.

(A) Microtubule subunits are heterodimers comprising α - and β - tubulin. The dimers are longitudinally organized into linear protofilaments. *In vivo*, thirteen longitudinally organized protofilaments form a cylindrical, tubular microtubule. Modified from [10].

(B) Dynamic instability of microtubules occurs through polymerization (assembly) and depolymerization (disassembly) processes in stochastically recurring cycles depending on GTP hydrolysis. Microtubules with a GTP-cap strongly favor growing due to the straight, stabilizing orientation of adjacent protofilaments. By contrast, GDP- β -tubulin bound to the protofilament ends prevents lateral contact, which leads to a curved structure favoring shrinkage (disassembly). Modified from [10].

Microtubules are highly dynamic, polar structures (plus end and minus end). Comparing the kinetics of both ends, growth and shrinkage occur faster at the plus end. The dynamic instability arises from polymerization (growth/ assembly) and depolymerization (shrinkage/ disassembly) processes in stochastically recurring cycles depending on GTP hydrolysis. Growing microtubules have a GTP-cap, which enables a straight organization and a stabilizing contact between the protofilaments (Figure 2B). Shrinking microtubules have GTP- β -tubulin bound to the end, which prevents the stabilizing lateral contact between the protofilaments (Figure 2B). Both processes depend on the concentration of GTP-bound tubulin dimers and other parameters like temperature or microtubule-associating proteins [10].

As already mentioned, kinesins interact with microtubules and enable transport processes through ATP hydrolysis [1, 4, 5]. The respective specific functions of each kinesin are connected to distinct protein properties [1, 11]. These properties include the processivity and direction of movement on the microtubule regulated by the motor domain and the neck linker (Figure 3A, B) [11].

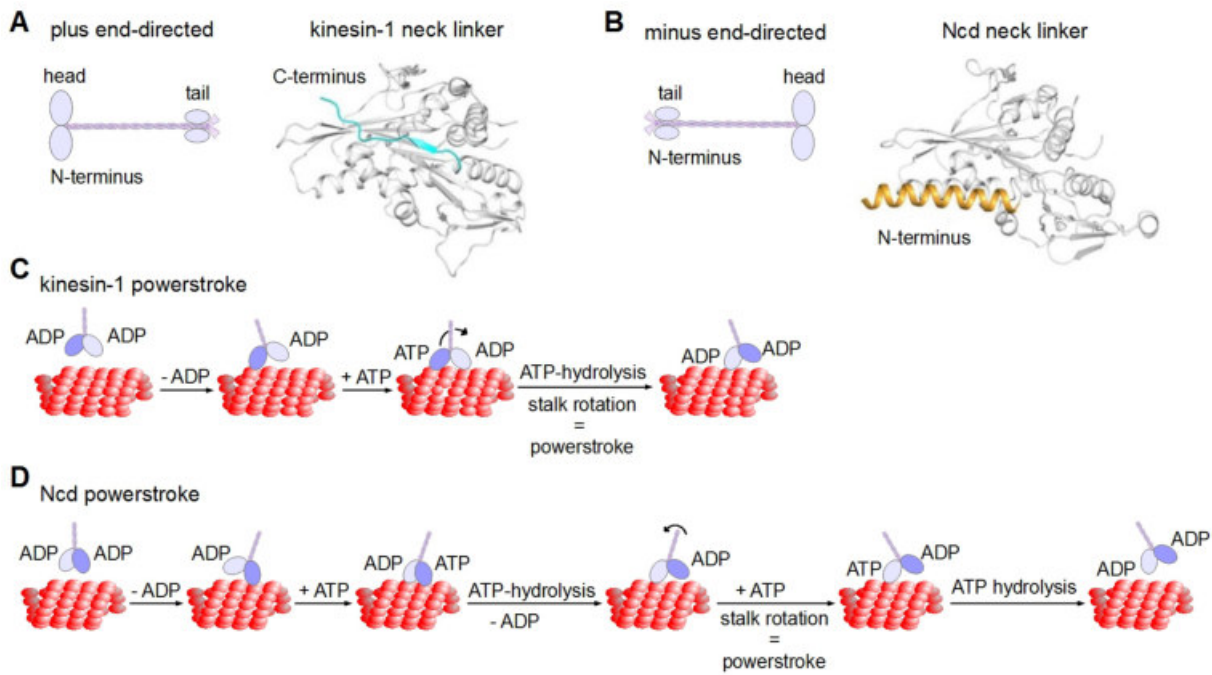


Figure 3: Schematic models of the topological organization of plus and minus end-directed kinesins and their powerstroke mechanisms.

(A) Plus end-directed kinesin with an N-terminal motor domain (left) and the crystal structures of the neck linker sequence of kinesin-1 (right). The neck linker of the plus end-directed kinesin-1 is C-terminally located to the motor domain with a random coil and a β -strand secondary structure. Modified from [12].

(B) Minus end-directed kinesin with a C-terminal motor domain (left) and the crystal structure of the neck linker sequence of Ncd (right). The neck linker of the minus end-directed Ncd is N-terminally located to the motor domain. It exists as an α -helix, which forms a coiled-coil with the second head of the dimer. Modified from [12].

(C) Processive long-range transport of plus end-directed kinesins by the hand-over-hand mechanism. One head domain (dark purple) binds to the microtubule, releases ADP, and binds ATP. ATP hydrolysis causes a conformational change (stalk rotation), which leads to a change in the leading and trailing head position. This chemomechanical reaction sequence occurs in cycles, which consume one ATP molecule for one turnover. At least one head domain is bound to the microtubule at all time. Modified from [13].

(D) Non-processive movement of minus end-directed kinesins by the hold-and-release mechanism. One head domain (dark purple) binds to the microtubule and releases ADP. The binding of ATP promotes the association of the second head (light purple) to the adjacent microtubule protofilament. ATP hydrolysis at the first head is connected to ADP release at the second head. Through ATP hydrolysis head one detaches from the microtubule. A further binding of ATP at the second head leads to a stalk rotation and a powerstroke. ATP hydrolysis at the second head causes the complete motor detachment from the microtubule. Modified from [14].

There are processive and non-processive motor proteins, which can be plus and minus end-directed. The neck linker is responsible for determining the directionality of movement [9]. The neck linker sequence and accruing structural elements differ between plus and minus end-directed motor proteins [9, 15]. For instance, the neck linker of the plus end-directed kinesin-1 is C-terminally located to the motor domain and forms a random coil and a β -strand secondary structure [12]. By contrast, the neck linker of the minus end-directed Ncd is N-terminally located to the motor domain. It exists as an α -helix, which forms a coiled-coil with the second head of the dimer [12]. Based on aforementioned structural elements the angle between the two linked motor heads also differs between plus and minus end-directed proteins [9, 15]. These structural differences can be visualized by crystal structure analyses, where the heads are differently orientated in relation to the stalk (Figure 3A, B). In turn, they

are the reason for different directions of movement [9, 12]. Usually, plus end-directed kinesins are processive for long-range transport. They move several steps along the microtubule by the hand-over-hand mechanism, which consumes one ATP molecule for one turnover (Figure 3C) [11, 13, 16, 17]. By contrast, minus end-directed, non-processive kinesins like Ncd only take one step on the microtubule before they detach. This hold-and-release mechanism needs two ATP hydrolyses for one turnover (Figure 3D) [11, 14, 16, 18, 19].

Besides motor domain and neck linker, the non-motor region (tail) also enables specific protein functions. They are based on posttranslational modifications, interactions with own structures (oligomerization, self-interaction) or different structures like receptors, microtubules, kinesin-associated proteins, vesicles, organelles, and DNA (Figure 4A-H) [11].

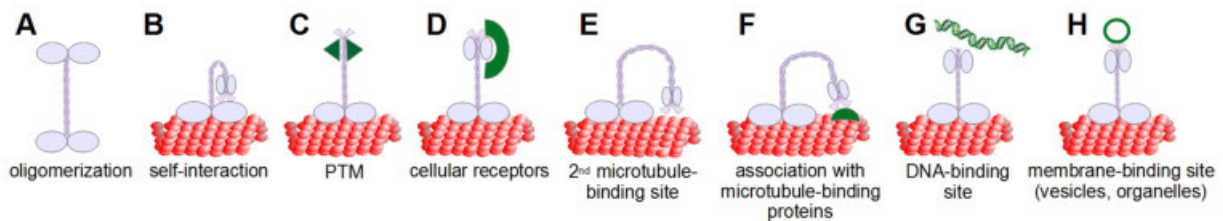


Figure 4: Schematic models of tail domain interactions that are responsible for specific protein functions. The models display interactions of the kinesin tail domain with own structures (oligomerization (A) and self-interaction (B)) or other structures like receptors (D), microtubules (E), kinesin-associated proteins (F), DNA (G), vesicles or organelles (H), and posttranslational modifications (C). Modified from [11].

The oligomerization of motor proteins can enable a change or an increase in motor processivity (Figure 4A) [11]. One example is artificial clustering of kinesin-14 proteins, which are non-processive as dimers and processive as tetramers [20]. It is also described in the literature that the C-terminus of kinesin-5 proteins increases motor processivity [21].

Furthermore, self-interactions can regulate the activity/ functionality of motor proteins (Figure 4B) [11]. An example of this regulation mechanism is provided by kinesin-1. It is known that kinesin-1 remains in an auto-inhibited state (tail region bound to/ inhibiting the two ATPase motor domains) without ATP consume, until a cargo molecule binds to the motor [11, 22-24]. A similar mechanism is also known for kinesin-2 (Kif17) [11, 25].

Posttranslational modifications can also regulate the activity/ functionality of motor proteins. In addition, they have an influence on localization, affinity and targeting properties of motor proteins (Figure 4C) [11]. A common posttranslational modification, which changes electrostatic kinesin surface properties, is phosphorylation [11]. Phosphorylation nearby or in the positively charged neck region can negatively impair the activity of kinesins as shown for kinesin-7 (CENP-E). A phosphorylation nearby the neck linker of CENP-E causes a decreasing affinity to microtubules and a decreasing processivity [11, 26, 27]. By contrast,

phosphorylation of non-motor regions can increase the affinity to microtubules as shown for kinesin-5 (Eg5) [11, 28]. Another example shows the disruption of protein-protein interaction and localization through electrostatic repulsion and steric hindrance caused by phosphorylation [11]. MCAK belongs to the kinesin-1 family, which destabilizes microtubules. Phosphorylation of the EB-binding motif of MCAK disrupts MCAK-EB interactions. This disruption prevents the localization of MCAK on the microtubule plus end and leads to a spatially limited, decreasing MCAK activity [11, 29-31].

Further factors that have an influence on protein functions are tail domain interactions with various external structures (Figure 4D-H) [11]. Receptors allow specific targeting of kinesins to defined sub-cellular locations [11]. Additional microtubule- or actin-binding domains in the tail region enable sliding of microtubules or actin filaments along microtubules by different members of the kinesin-5 [11, 21, 32] and kinesin-14 family [32-34]. Other motor proteins have to interact with further proteins for a correct function. One of these kinesin-associated proteins is Tpx2, which interacts - among others - with kinesin-5 (Eg5) to enable a correct localization for promoting spindle bipolarity [35, 36]. The binding affinity to membranes through additional domains in the tail can enable vesicle or organelle transport [37-39], membrane deformation processes [37, 40], and the connection of cytoskeletal structures and membranes [38].

With the help of aforementioned properties, kinesins can organize and regulate microtubule arrays due to crosslinking, translocation, polymerization, and depolymerization. These are important processes during cell division or cell shape formation [1, 5, 6, 16, 21, 32, 33, 41]. On the other hand, they can enable microtubule-based activities as directed transport processes of cellular components or linking of cellular structures. These properties are important for processes like cell growth, cell shape formation, or endocytosis [1, 5, 6, 34, 41, 42].

The sequence of the highly conserved kinesin motor domain was used for phylogenetic analyses in various organisms [1, 5, 6, 43, 44]. Concerning a study by Lawrence et al. [43], kinesins were classified into fourteen groups. Members of the groups 1 to 12 are plus end-directed kinesins with an N-terminal motor domain. The members of group 13 are depolymerizing kinesins with an internal motor domain and the members of group 14 are minus end-directed kinesins with a C-terminal motor domain [43]. Ten of these fourteen kinesin families were also found in *Giardia lamblia*, which represents the deepest known branch of eukaryotic lineage. This indicates that many kinesins already exist in an early stage of development [1].

A high number of kinesins also exists in flowering plants [1, 2, 5]. *A. thaliana* represents a popular model organism for flowering plants according to the following advantages: it has a comparatively short and completely sequenced genome, acceptable cultivation conditions, and a short generation time. Additionally, it is self-fertilizing and comparable to other higher plants and further eukaryotic systems [45].

In *A. thaliana* 61 kinesin genes were identified [1, 4, 6]. According to a multiple sequence alignment (Clustal Omega, EMBL-EBI [46-48]) based on their complete amino acid sequences, they can be allocated to the groups 4, 5, 7, 8, 10, 12, 13, 14 and orphan kinesins (Figure 5).

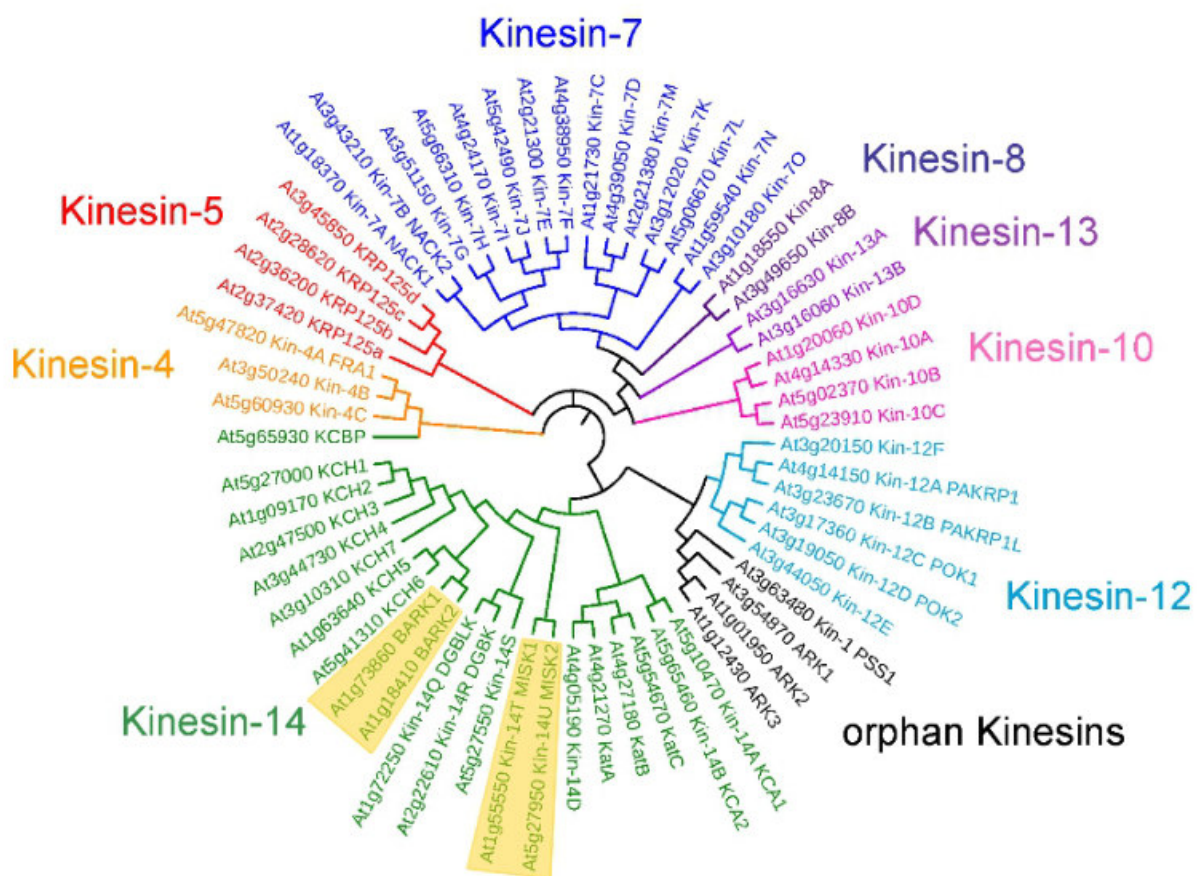


Figure 5: Phylogenetic tree of kinesins in *A. thaliana*.

A multiple sequence alignment was performed based on the complete amino acid sequences of 61 *At*kinesin genes with Clustal Omega (EMBL-EBI) [46-48]. The phylogenetic tree was designed with iTOL [49]. According to these analyses, the kinesins of *A. thaliana* were assigned to 9 of the 14 existing groups of kinesin motor proteins. Kinesin genes analyzed in this study are marked in yellow.

The kinesin-14 family is the largest group in *A. thaliana* with 21 members (Figure 5) [1, 4, 6]. Some of these kinesins have no analogs in other organisms thus far. This indicates a functional specification for unique processes in plants [1, 5, 6]. It is conspicuous that several members of the *At*kinesin-14 family differ in their domain organization and their specific tails.

Atkinesin-14 members like KatA-C and Kin-14D have a C-terminal motor domain, which was defined in the classical description of the kinesin-14 group by Lawrence et al. [43]. However, there are also plant-specific *Atkinesin-14* genes, which code for proteins with an N-terminal motor domain flanked by one coiled-coil domain (MISK1-2, Kin-14S) or an internal motor domain (DGBK, DGBLK) [1, 5, 6]. Furthermore, there is a certain similarity between *Atkinesin-14* genes, which code for KCH and BARK proteins. They share an internal motor domain flanked by two coiled-coil domains. The tail domain differs between the two groups, with an actin-binding domain for the KCHs and a membrane-binding domain for the BARKs [1, 5, 6].

Two *Atkinesin-14* members with a C-terminal motor domain enable functions in cell division [50-52]. Based on these data, it is interesting to analyze further members of the large *Atkinesin-14* family to expand the knowledge of their biophysical characteristics and their physiological functions.

The following thesis is separated into two chapters dealing with different *Atkinesin-14* motor proteins. In **Chapter 4** two F-BAR kinesins of *A. thaliana* were investigated, while **Chapter 5** deals with a novel microtubule segregating kinesin in *A. thaliana*.

4 F-BAR kinesins in *Arabidopsis thaliana*

4.1 Introduction

Membranes are flexible barriers that surround cells and their compartments. They are composed of a lipid bilayer containing mainly different phospholipids but also some glycolipids, various peripheral, integral, or transmembrane proteins, and a variable amount of carbohydrates and cholesterol [40, 53]. Membranes enable - among others - a continuous influx of nutrients and secretion of waste as well as sensing and communication of signals between cells and with the environment. Therefore, it is important to deliberately control the membrane shape with a high spatial and temporal accuracy [40, 53]. Membrane curvature and remodeling are connected to diverse processes [40, 53]. Therefore, research on mechanisms and participating proteins has become increasingly important over recent years. Some exemplary mechanisms for membrane deformation are depicted in Figure 6.

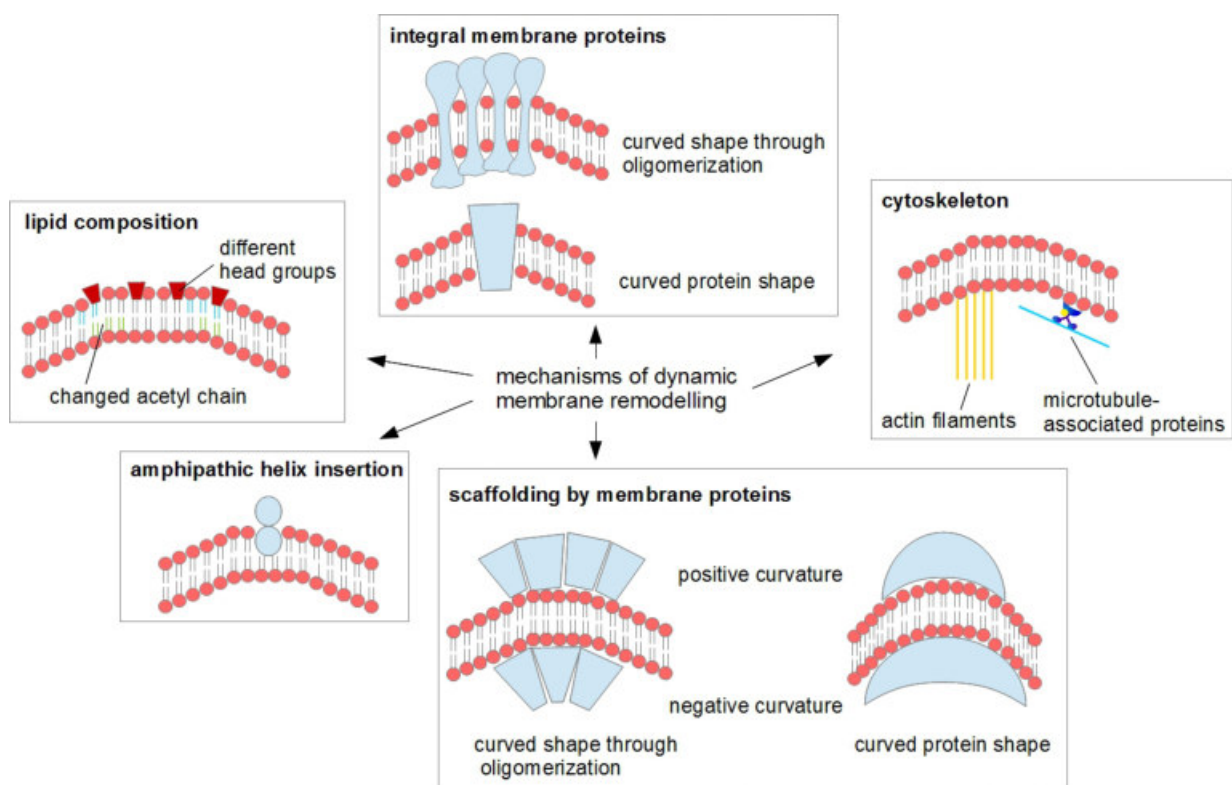


Figure 6: Mechanisms of dynamic membrane remodeling.

It is possible to deliberately control the membrane shape with a high spatial and temporal accuracy through:

- (i) changes in the lipid composition (phospholipid head groups or chains);
- (ii) the influence of integral membrane proteins;
- (iii) changes of the cytoskeletal structures partially connected to motor proteins;
- (iv) the scaffolding mechanism;
- (v) amphipathic helix insertions into one leaflet of the bilayer.

Modified from [54].

Several lipid acyl chains or head groups with different chemical properties favor different membrane curvatures and recruit different proteins [54, 55]. Additionally, some integral membrane proteins can influence membrane curvature. They either have a conical shape or form a conical shape through oligomerization or conformational changes to deform the membrane [54, 55]. Further tools for the formation of membrane curvature are cytoskeletal structures. For instance, actin filaments or microtubules can maintain and change membrane tension through structural rearrangement in interplay with motor proteins [54, 56]. Amphipathic helix insertions and protein scaffolding are two further mechanisms discussed in the literature [53]. Proteins, which remodel membranes through amphipathic helix insertion, need this special structure for deforming processes [53-56]. By contrast, the scaffolding mechanism makes demands on peripheral membrane proteins. Important properties of these proteins are - among others - an intrinsic shape, an intrinsic rigidity, and a specific affinity to certain lipid head groups. With these requirements, they are able to bind membranes and deform them according to their own shapes [53-57].

Bin/Amphiphysin/Rvs (BAR) domain-containing proteins are an example of these membrane-shaping molecules. They can sense specific membrane compositions and structures, interact with membranes, and remodel membranes [37, 40, 53, 55, 57, 58].

The BAR domain is an evolutionarily conserved module that was originally identified in the yeast proteins Rvs161 and Rvs167 and in metazoans amphiphysin (splicing variation BIN) [40, 53, 58]. It is formed by dimerization of two monomers, which consist of three anti-parallel α -helices (Figure 7). The monomers are arranged at a specific angle in the opposite orientation to generate the curved structure of the six-helix bundle homo- or heterodimer [40, 53, 59]. Dimerization by coiled-coil domains is crucial for the functionality of the BAR domain. It generates the positively charged surface, which is necessary for the interaction with negatively charged phospholipids of the membrane [37, 40, 53, 57-61].

Crystal structure analyses of the BAR domain superfamily showed different subsets of unique families: (i) classical BARs;

(ii) FCH/ EFC (F)-BARs;

(iii) inverse (I)-BARs.

All subfamilies share distinct elements of the BAR domain, but there are differences concerning further supplemental domains and distinct membrane curvatures [37, 40, 53, 55, 58, 61-64] (Figure 7).

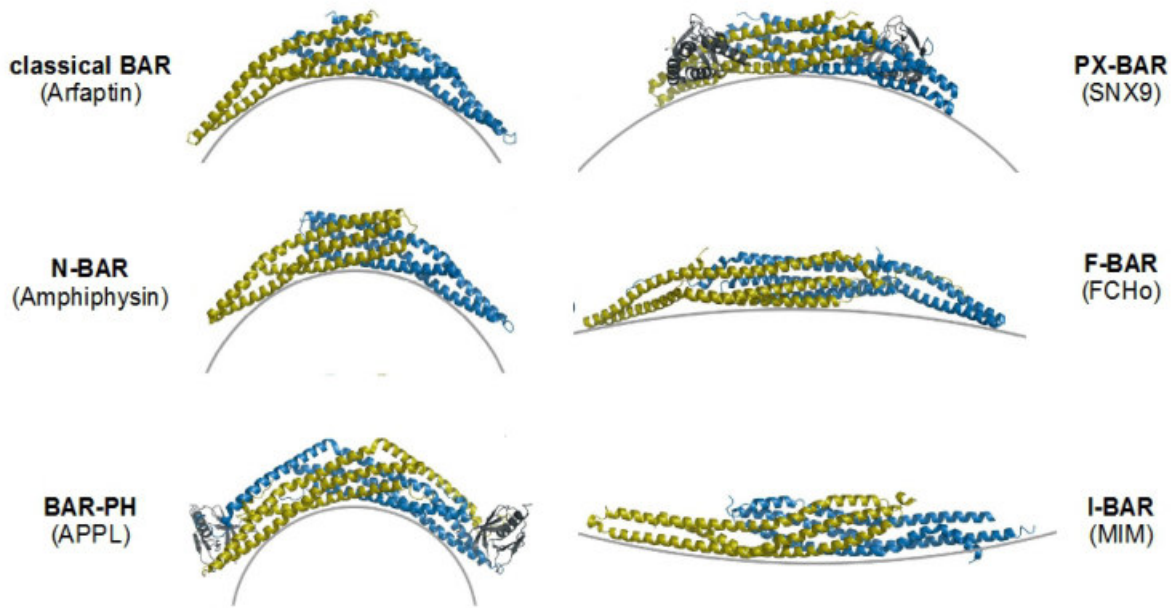


Figure 7: Crystal structures of membrane-shaping BAR domains.

Crystal structures of BAR domains show that they are formed by dimerization of two monomers (one monomer in yellow, the other in blue). The monomers comprise three parallel α -helices, which are arranged in a specific angle in the opposite orientation to generate the curved structure of the six-helix bundle homo- or heterodimer. Further domains are marked in gray. BAR domains of different subfamilies have different membrane curvatures. Modified from [55].

Classical BAR domains have the highest intrinsic curvature forming a ‘banana shape’ structure, which supports and promotes positive membrane bending. Their attachment is observed at strongly curved membrane elements. Their membrane tubulation activity creates flexible tubes with a small diameter. According to additional membrane-binding domains, they are further sub-divided into N-terminal amphipathic helix (N)-BAR domains, BAR-Pleckstrin homology (PH) domains, and PXo-BAR domains [40, 53, 55, 59, 64].

I-BAR domains show another shape. Although they also form dimers with an elongated structure and a positively charged surface, their shape is straight (‘zeppelin-like’). They additionally support and promote negative curvature to generate extrusions [37, 40, 53, 58, 65, 66].

F-BAR domains represent the most diverse subfamily of the BAR domain superfamily. The range of intrinsic F-BAR domain curvatures goes from high (e.g. syndapin) [37, 40, 60] to almost planar shapes (e.g. FCHo) [40, 60]. They promote positive curvature through interactions with negatively charged phospholipids [61]. Similar to classical BAR domains, F-BAR domains show membrane tubulation activity. However, they form less flexible tubes with a large diameter in comparison to classical BAR domains [37, 40, 53, 60, 61].

Depending on their structure, most BAR/ F-BAR-membrane interactions occur through the scaffolding mechanism. However, there are also some BAR proteins that have domains for membrane integration (e.g. N-BAR domains) [40, 54, 56].

The structural diversity of BAR domains and their combination with further domains (e.g. SH3 domains, phosphoinositide-binding domains, GTPase regulator domains) enable different features and different functions in various processes [40, 53, 58, 62, 63]. Most of these processes are linked to membrane traffic [53, 65], cell division [37, 40, 58], cell migration [37, 40, 58], signaling [53], and endocytosis [53, 59, 61, 65]. Thereby, they act as multifunctional receptors, membrane stabilizers, or have membrane-remodeling functions [53, 59, 67].

The structural and functional characterization of BAR, I-BAR, and F-BAR domains is mainly based on *in vivo* and *in vitro* experiments with human [57, 64, 68, 69], animal [53, 59, 61, 69-71], or yeast [72] proteins to date. Excitingly, two *A. thaliana* genes (*At1g73860*, *At1g18410*) encode for members of the kinesin-14 subfamily, which also contain an F-BAR domain. Due to this characterizing F-BAR domain, the two genes were called *bark1* and *bark2* and the proteins *AtBARK1* and *AtBARK2* in this study. The aim of this study was to reveal the biophysical properties and the physiological role of these unique proteins in *A. thaliana*.

4.2 Results of the *in silico* and *in vitro* experiments

4.2.1 *bark1* and *bark2* have a high resemblance of gene organization

The gene organizations of *bark1* (*At1g73860*) and *bark2* (*At1g18410*) were generated on gene information obtained from The Arabidopsis Information Resource (TAIR, The Ohio State University [73]) (Figure 8A, B).

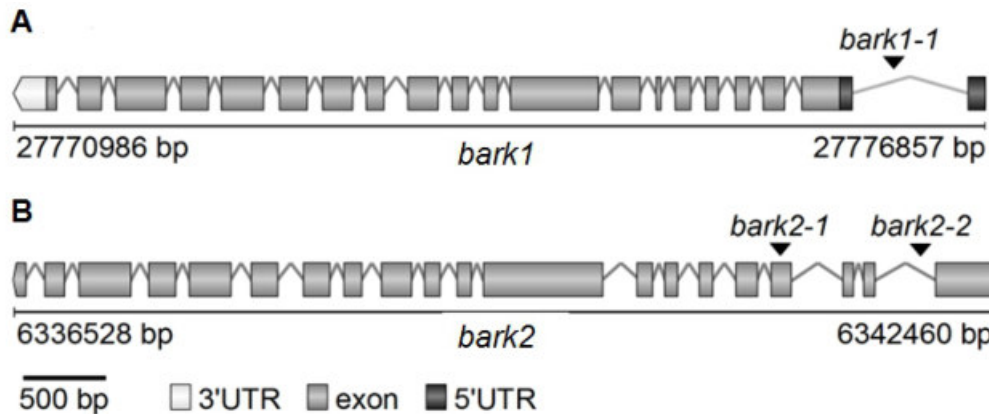


Figure 8: Gene organizations of *bark1* and *bark2*.

The gene organizations of *bark1* (*At1g73860*) (A) and *bark2* (*At1g18410*) (B) were generated on gene information obtained from TAIR (The Ohio State University [73]) and marked with experimentally relevant T-DNA insertion lines (*bark1-1*, *bark2-1*, *bark2-2*).

Comparing the two gene structures, the strong resemblance of gene organization was remarkable, indicating a common ancestry through gene duplication (Figure 8A, B). An alignment of the amino acid sequences of *AtBARK1* and *AtBARK2* over 1002 amino acids with the EMBOSS Matcher (EMBL-EBI) [74] was performed, revealing an amino acid sequence identity of 66 % and an even higher amino acid sequence similarity of 79 %. Furthermore, different algorithms were used to identify specific domains of *AtBARK* proteins based on their amino acid sequence (Figure 9).

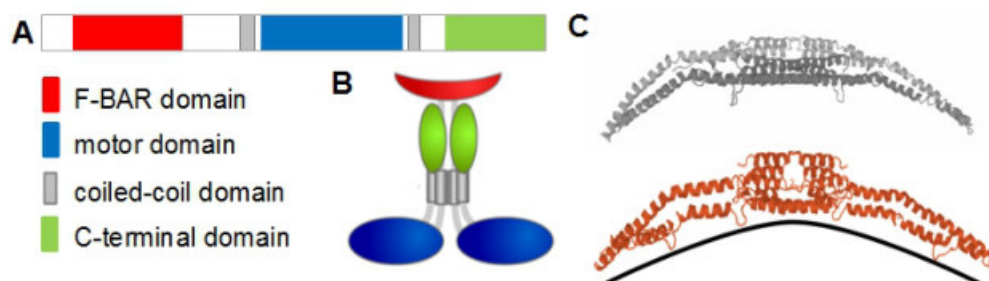


Figure 9: Structural features of *AtBARK* proteins.

(A) General domain structure of *AtBARK* proteins based on their amino acid sequences.

(B) Proposed model for the dimeric structure of *AtBARK* proteins.

(C) Side view of the F-BAR domain of PACSIN 2 (3HAJ.pdb, gray) and the putative F-BAR domain of *AtBARK1* (red), modeled into the PACSIN 2 structure with SWISS-MODEL [75].

AtBARK1 and *AtBARK2* share a domain arrangement, which contains an internal motor domain flanked by two coiled-coil domains. Additionally, both proteins have an N-terminal cargo-binding domain, identified as F-BAR domain, and a C-terminal domain of unknown structure and function (Figure 9A). The F-BAR domain and the kinesin-14 motor domain were identified using the DELTA-BLAST algorithm (National Library of Medicine, USA [76]). Putative coiled-coils were identified using the ExPASy COILS algorithm [77]. According to the location of the coiled-coil domains and the domain structure similarity with other kinesin-14 plant motors, it seemed fair to assume that *AtBARK* proteins form a homodimer (Figure 9B). In order to gain an insight into the three-dimensional F-BAR domain structure, the predicted F-BAR domain of *AtBARK1* was modeled into the structure of the human F-BAR protein PACSIN 2 (3HAJ.pdb) using SWISS-MODEL (Figure 9C) [75]. The model showed an F-BAR domain dimer, composed of six helices, which generate a curved surface with protruding residues.

4.2.2 Expression and purification of *AtBARK* constructs for *in vitro* analyses

In order to generate *AtBARK* constructs, the sequences of *bark1* and *bark2* were amplified and cloned into the expression vector pET28a by overlap extension cloning. A C-terminal 6xhistidin (His)-tag was fused to both constructs for purification. A C-terminal EGFP-tag was additionally fused to the *AtBARK2* construct for protein detection in single molecule assays (Figure 10).

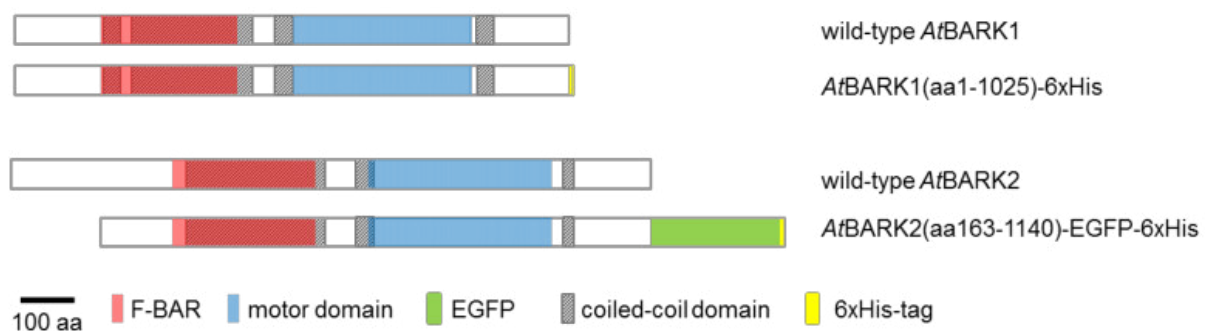


Figure 10: Schematic representation of the domain organization of wild-type *AtBARK1/2* and of the recombinant expression constructs used for *in vitro* characterization.

The *AtBARK1* wild-type protein has a sequence of 1025 amino acids with a kinesin-14 motor domain flanked by two coiled-coil domains and an N-terminal F-BAR domain, which also contains two coiled-coil domains. The expression construct of *AtBARK1* contains the whole wild-type sequence and a C-terminal 6xHis-tag for purification.

The *AtBARK2* wild-type protein has a sequence of 1140 amino acids with a kinesin-14 motor domain flanked by two coiled-coil domains and an N-terminal F-BAR domain, which also contains one coiled-coil domain. The *AtBARK2* expression construct contains the main part of the wild-type sequence with all important functional domains and additionally a C-terminal EGFP-6xHis-tag for purification and detection.

These expression constructs (Figure 10) were transformed into different *E. coli* strains for an expression test. This test showed the best results for all constructs in *E. coli* BL21(DE3) RIPL cells under different expression conditions listed in Table 16. Both constructs were expressed, and purified by affinity chromatography. In order to prove the protein expression and purification, SDS-PAGEs of the purification fractions were performed. The gels were stained with colloidal Coomassie (Figure 11).

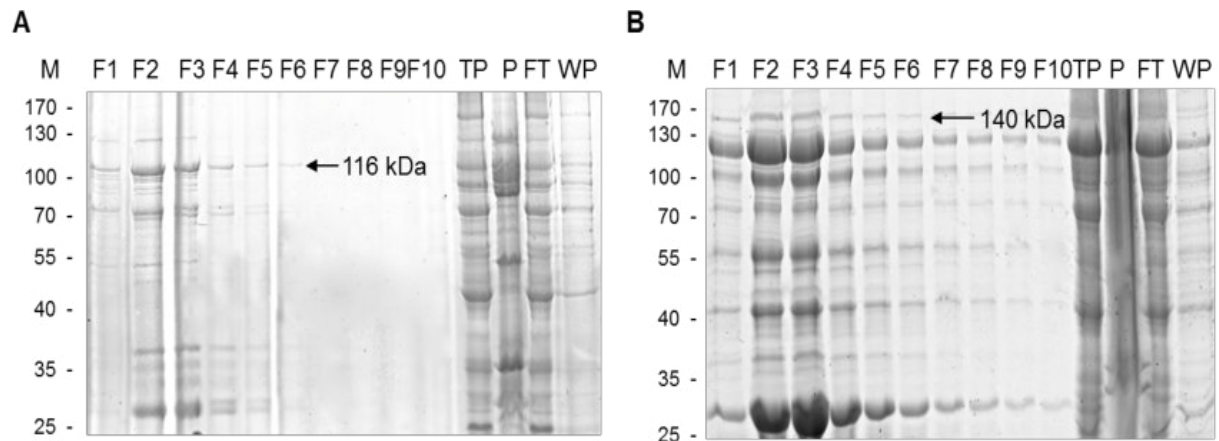


Figure 11: SDS-PAGEs of the *AtBARK* purification fractions after affinity chromatography.

Both proteins were expressed and purified, proved by a protein band on the right marker level (black arrow): *AtBARK1*(aa1-1025)-6xHis (**A**, 116 kDa), *AtBARK2*(aa163-1140)-EGFP-6xHis (**B**, 140 kDa).

Despite affinity chromatography, other protein bands and/ or protein fragment bands were detected in the gels, especially for the *AtBARK2* construct.

Legend: M = marker, F1-F10 = fraction 1-10, TP = total protein amount, which was applied to the affinity column, P = pellet after cell lysis, FT = flow through, which was collected after the column run, WP = washing buffer, which was collected after the column run

The stained gels of both constructs showed that the proteins *AtBARK1*(aa1-1025)-6xHis (116 kDa, Figure 11A) and *AtBARK2*(aa163-1140)-EGFP-6xHis (140 kDa, Figure 11B) were expressed and purified. Despite affinity chromatography, there were still impurities in the fractions, especially for the *AtBARK2*(aa163-1140)-EGFP-6xHis construct (Figure 11B). Nevertheless, one purification fraction was used for further *in vitro* analyses.

4.2.3 *AtBARK* proteins bind microtubules stiffly or diffusively in gliding assays

Gliding assays were performed to determine the velocity of the motors that transport microtubules along the surface [78-80]. Experiments were performed in flow cells constructed from hydrophobic glass coverslips separated by stripes of parafilm. The interactions of fluorescence-labeled microtubules with immobilized *AtBARK1*(aa1-1025)-6xHis were detected by epifluorescence microscopy (Figure 12A).

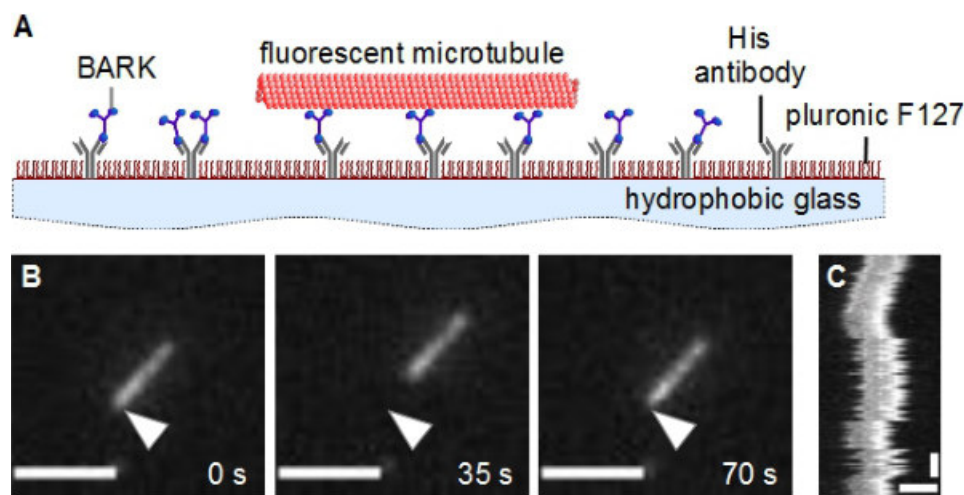


Figure 12: Gliding assay of *AtBARK1*.

(A) Schematic representation of a gliding assay with *AtBARK*. The interactions of fluorescence-labeled microtubules with immobilized motor proteins were detected by epifluorescence microscopy.

(B) Time-lapse imaging of a fluorescence-labeled microtubule (gray), which was diffusively bound by *AtBARK1*(aa1-1025)-6xHis in a gliding assay. The starting position of the microtubule was marked by white arrowheads (scale bar = 3 μ m).

(C) Kymograph of a fluorescence-labeled microtubule, which was diffusively bound by *AtBARK1*(aa1-1025)-6xHis (horizontal scale bar = 2 μ m, vertical scale bar = 60 s).

Time-lapse imaging of gliding assays and kymograph analyses showed that microtubules were stiffly bound by *AtBARK1* in most cases. Sometimes also diffusive interactions were detected (Figure 12B, C). As a short explanation, a kymograph is a one-dimensional display, which shows the kind of microtubule movement over time. The same assays, performed without motor protein, did not show any microtubule interactions. Therefore, they were not depicted.

These results proved *AtBARK1*-microtubule interactions in the absence of cargo molecules, which could be bound by the F-BAR tail domain. However, no directed movement was observed.

4.2.4 Single *AtBARK* molecules or *AtBARK* complexes show diffusive movement on microtubules

Stepping assays were performed to determine the velocity, direction, and processivity of single motor molecules that move on microtubules [78, 80]. Experiments were performed in flow cells constructed as described before (see 4.2.3). The interactions of fluorescence-labeled *AtBARK2*(aa163-1140)-EGFP-6xHis with immobilized, fluorescence-labeled microtubules were detected by total internal reflection fluorescence (TIRF) microscopy (Figure 13A).

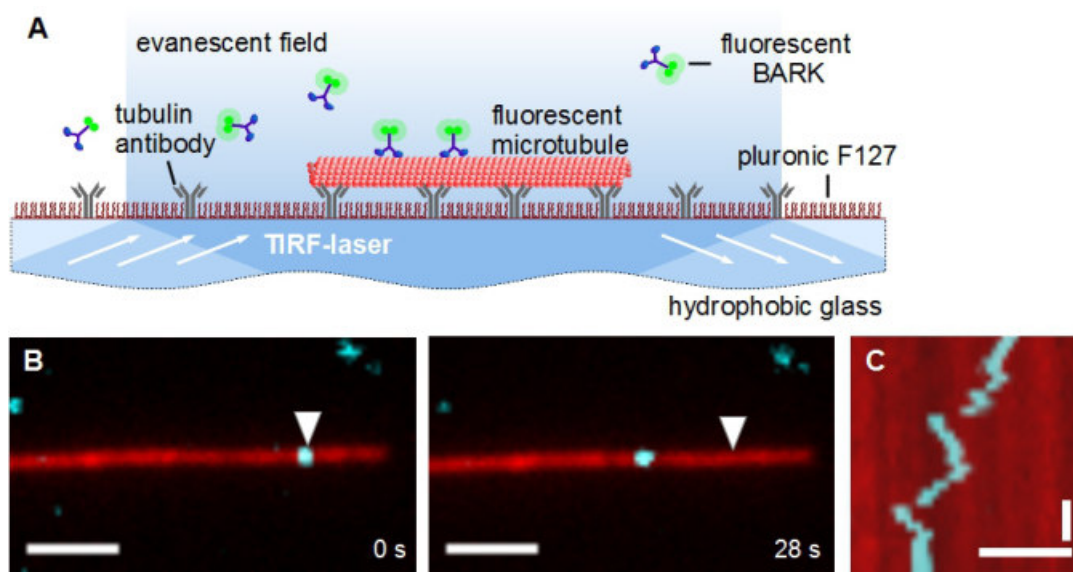


Figure 13: Stepping assay of *AtBARK2*.

(A) Schematic representation of a stepping assay with *AtBARK*. The interactions of fluorescence-labeled motors with immobilized, fluorescence-labeled microtubules were detected by TIRF microscopy.

(B) Time-lapse imaging of a stepping assay with *AtBARK2*(aa163-1140)-EGFP-6xHis. A brightly shining *AtBARK2* signal (cyan) covered a distance on a microtubule (red) over time. The starting position was marked by white arrowheads (scale bar = 2 μm).

(C) Kymograph of the *AtBARK2* signal shown in (B). Analyses indicated diffusive movement, apparently with short switches to directed motion (horizontal scale bar = 2 μm , vertical scale bar = 5 s).

Stepping assays and kymograph analyses showed that bright, fluorescence-labeled *AtBARK2* signals covered a distance on immobilized, fluorescence-labeled microtubules over time (Figure 13B). A closer look at their kymographs showed diffusive movement, apparently with short switches to directed motion (Figure 13C). As these diffusing *AtBARK2* signals seemed very bright, it was assumed that *AtBARK2* molecules formed complexes.

Similar to gliding assays, stepping assays showed *AtBARK*-microtubule interactions without cargo interaction of the F-BAR domain.

4.2.5 Integrity tests with FRAP microscopy prove a successful generation of supported lipid bilayers

SLB assays were used to characterize protein-membrane-microtubule interactions on a single molecule level [81]. For the generation of the SLBs cleaned coverslips and multilamellar vesicles from a stock organic solution of phospholipids were used (Figure 14A).

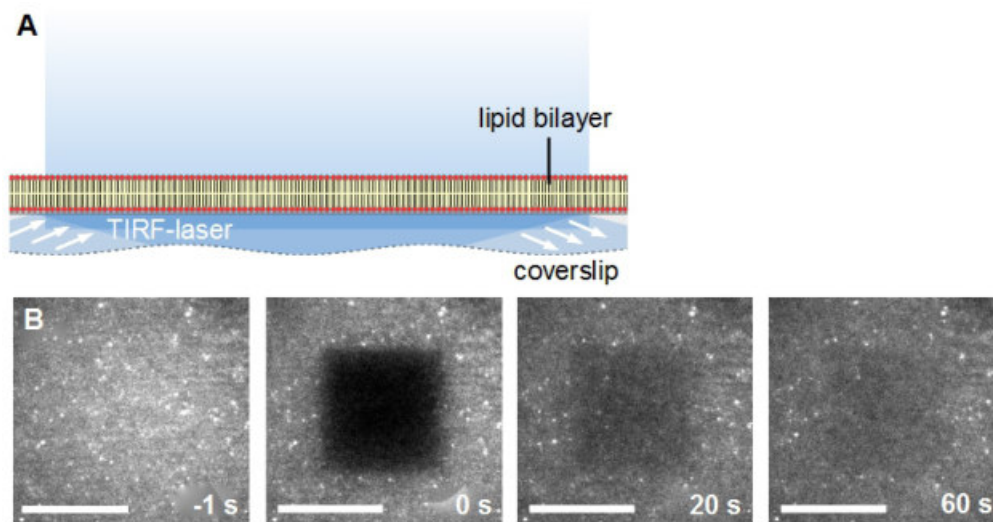


Figure 14: Preparation and testing of a supported lipid bilayer.

(A) Schematic representation of an SLB.

(B) Integrity test of an SLB by FRAP microscopy with TIRF-laser. For the FRAP test, the lipophilic dye DiD was added to the SLB as fluorescence marking. The different stages of the photobleaching process were analyzed by a time-lapse series (pre-bleaching phase = -1 s, phase after UV-photobleaching of a rectangular membrane area = 0 s / 20 s / 60 s, scale bar = 15 μ m).

The integrity of prepared SLBs was tested by fluorescence recovery after photobleaching (FRAP) microscopy. For the FRAP test, the lipophilic dye DiD was added to the SLB as fluorescence marking. In the beginning, the TIRF-laser illuminated the membrane (Figure 14C, -1 s). For photobleaching, a rectangular area was bleached with a high-intensity UV-laser (Figure 14B, 0 s). Thereafter, the bleaching area was observed again with the TIRF-laser (Figure 14B, 20 s, 60 s).

The experiments showed a functional, fluid membrane, in which incorporated membrane dye could freely diffuse in the bleached membrane area (Figure 14B, 20 s, 60 s). Therefore, it was possible to use this method for the preparation of SLBs for membrane assays.

4.2.6 *AtBARK* proteins diffusively link microtubules to supported lipid bilayers

Gliding and stepping assays were performed without cargo molecules for the F-BAR domain of *AtBARK*. Therefore, membrane gliding assays were performed to investigate whether *AtBARK* proteins could interact with membranes and microtubules simultaneously. Additionally, it should be analyzed if cargo interactions caused transport processes. The SLBs were prepared as described before (see 4.2.5). The interactions between *AtBARK1*(aa1-1025)-6xHis, fluorescence-labeled microtubules, and the membrane were observed by epifluorescence microscopy (Figure 15A).

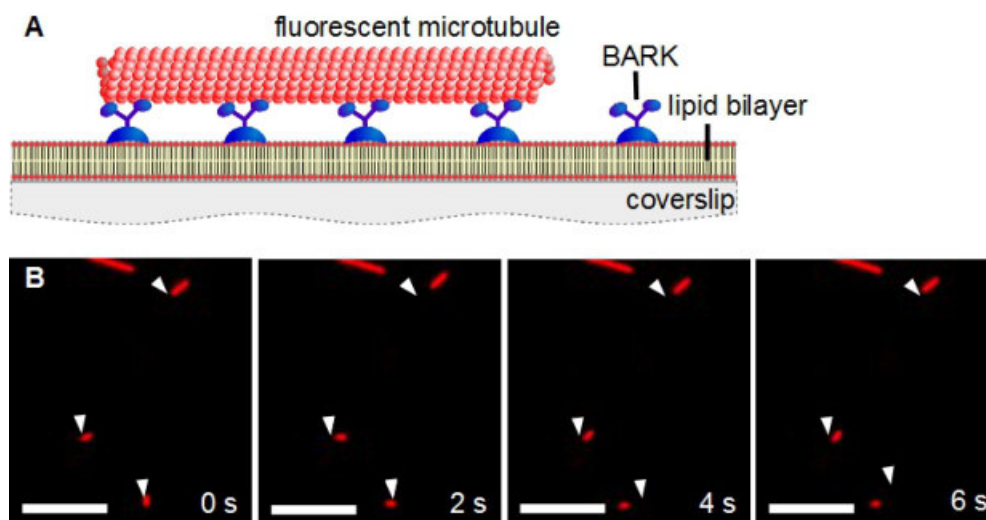


Figure 15: Membrane gliding assay of *AtBARK1*.

(A) Schematic representation of a membrane gliding assay with *AtBARK*. The interactions between motors, fluorescence-labeled microtubules, and the membrane were observed by epifluorescence microscopy.

(B) Time-lapse imaging of a membrane gliding assay with *AtBARK1*(aa1-1025)-6xHis. Fluorescence-labeled microtubules (red) were diffusively linked to the membrane by *AtBARK1*. The starting positions of the microtubules were marked by white arrowheads (scale bar = 5 μm). The SLB was composed of a phospholipid composition with 20 % phosphatidylserine.

In membrane gliding assays most microtubules were diffusively linked to the membrane by *AtBARK1* (Figure 15B). A constant, directed movement was not detected. The membrane gliding assays were performed on membranes with different phospholipid compositions (PC with a content of 0 %, 20 %, 50 % PS) as well as different cholesterol amounts (0 %, 20 %, 60 %). The changing lipid composition should have an influence on the binding affinity of F-BAR domains to the membrane [61]. The changing cholesterol content should have an influence on the membrane stiffness, which influences the transport efficiency [81]. However, no differences were observed between these conditions. The same assays, performed without motor protein, did not show any membrane-microtubule interactions. Therefore, they were not depicted.

The membrane gliding assays showed that *AtBARK1* diffusively linked microtubules to planar membranes.

4.2.7 *AtBARK* proteins specifically bind to unilamellar vesicles

As different F-BAR domains have various curvature rates [40, 54, 57, 63, 64], the interaction between *AtBARK* proteins and vesicles (size distribution: 0.1 - 5 μm) was tested. These unilamellar vesicles were created by sedimentation of an emulsion, composed of buffer and phospholipid suspension, through a phospholipid-covered oil-water interface (Figure 16A, B).

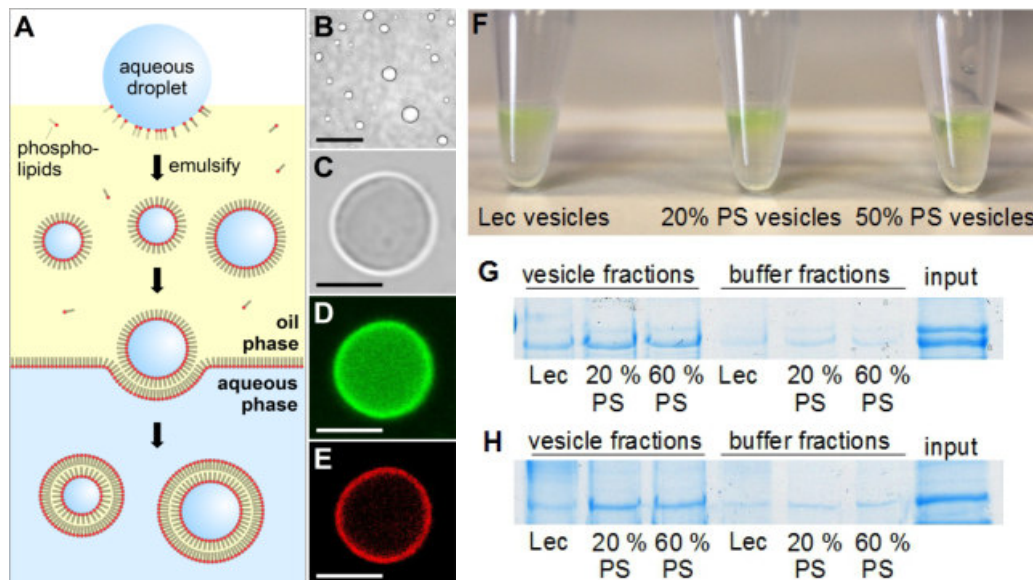


Figure 16: Vesicle assay with *AtBARK* proteins.

(A) Schematic representation of unilamellar vesicle preparation.

(B) Bright field image of unilamellar vesicles (size distribution: 0.1 - 5 μm , scale bar = 20 μm).

(C-E) Unilamellar vesicle enclosing a solution of buffer containing DyLight594-labeled tubulin and incubated with lipophilic dye (DiD) (C: bright-field, D/E: epifluorescence, scale bar = 5 μm).

(F) Vesicle assay with *AtBARK2*(aa163-1140)-EGFP-6xHis. The protein was incubated with vesicles, composed of different phospholipid compositions (Lecithin, compositions with 20 % and 50 % phosphatidylserine). Vesicles and most fluorescence-labeled protein (green) accumulated at the top of the solution.

(G, H) Coomassie gels of vesicle assay with *AtBARK1*(aa1-1025)-6xHis (G) and *AtBARK2*(aa163-1140)-EGFP-6xHis (H). The proteins were incubated with vesicles as described in (F). In the next step, the upper and lower phases were separated. Fractions were applied to an SDS gel, which was stained with colloidal Coomassie after the run. A strong protein band in all vesicle fractions showed that both proteins bound at all three kinds of vesicles in an equal manner. A minor part of the motor remained in the buffer. The respective motor protein, incubated without vesicles, was also applied to the gel as a control.

In order to test a successful preparation of vesicles, they were prepared with buffer containing DyLight594-labeled tubulin and incubated with lipophilic dye (DiD). It was possible to detect illuminated vesicles with fluorescence microscopy (Figure 16D). This indicates that fluorescence-labeled tubulin was enclosed by a stable vesicle. Imaging also showed fluorescent vesicle membranes as a proof for unilamellarity (Figure 16E). These tests were successfully performed with different buffers and different phospholipid compositions. The phospholipid composition should have an effect on the binding efficiency of F-BAR domains to membranes [61]. *AtBARK1* and *AtBARK2* were incubated with vesicles composed of lecithin (97 % PC) and vesicles comprising a phospholipid mixture with 20 % PS or 50 % PS.

During incubation, fluorescence-labeled *AtBARK2* accumulated at the top of the solution together with the vesicles (Figure 16F). After incubation, the upper and lower phases were separated and the fractions were applied to SDS gels. Gels were stained with colloidal Coomassie (Figure 16G, H). The Coomassie gels showed a strong protein band for all vesicle fractions indicating that both proteins bound at all three kinds of vesicles (Lecithin, 20 % PS, and 50 % PS vesicles) in an equal manner. The approach with 20 % PS was used for further vesicle transport assays.

4.2.8 *AtBARK* proteins are a minus end-directed motor proteins that transport vesicles along microtubules

Vesicle transport assays were performed to analyze the interactions of *AtBARK* proteins and cargo molecules for a further determination of transport velocity and direction. Flow cells were constructed as described before (see 4.2.3). The interactions between *AtBARK1*(aa1-1025)-6xHis or *AtBARK2*(aa163-1140)-EGFP-6xHis, immobilized, fluorescence-labeled microtubules, and fluorescence-labeled vesicles were observed by TIRF microscopy (Figure 17A).

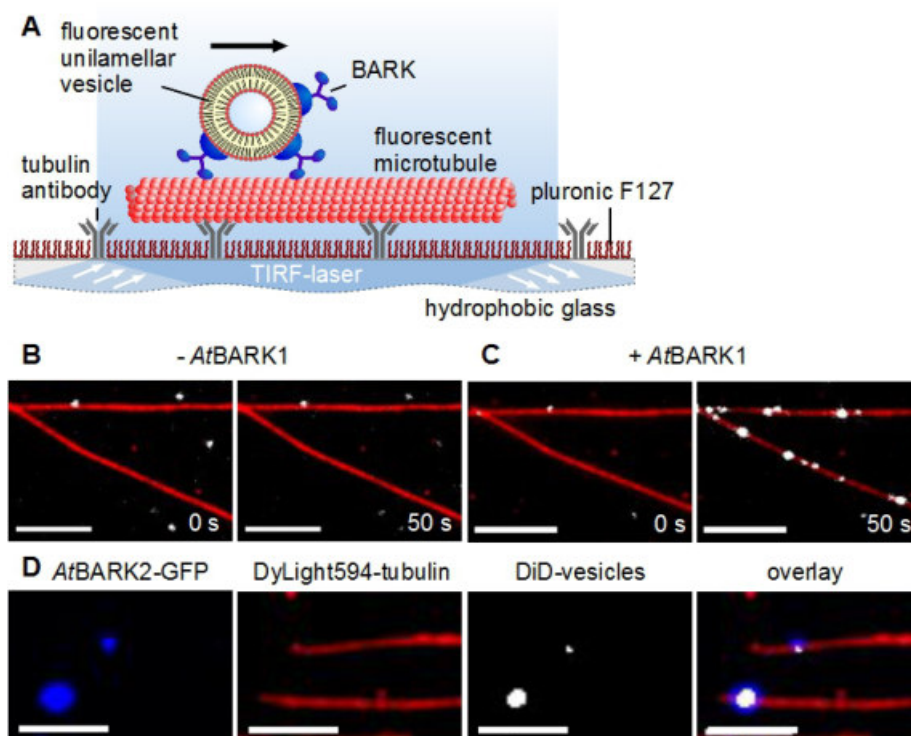


Figure 17: Vesicle transport assay with *AtBARK* proteins.

(A) Schematic representation of a vesicle transport assay with *AtBARK*. The interactions between motors, immobilized, fluorescence-labeled microtubules, and fluorescence-labeled vesicles were observed by TIRF microscopy.

(B) Time-lapse imaging of a vesicle transport assay without *AtBARK1*(aa1-1025)-6xHis. A colocalization of vesicles (gray) and microtubules (red) was not detected over time (scale bar = 5 μ m).

(C) Time-lapse imaging of a vesicle transport assay with *AtBARK1*(aa1-1025)-6xHis. The injection of *AtBARK1* to the assay performed in (B), caused a vesicle-microtubule colocalization (scale bar = 5 μ m).

(D) Time-lapse imaging of a vesicle transport assay with *AtBARK2*(aa163-1140)-EGFP-6xHis. The injection of *AtBARK2* (blue) in vesicle transport assays, performed as described in (C), showed a colocalization of motor proteins and vesicles (scale bar = 3 μ m).

In a first step, the direct interaction between microtubules and vesicles was tested. Therefore, fluorescence-labeled microtubules were immobilized to the surface and fluorescence-labeled vesicles were added to the assay in the absence of motor (Figure 17B). During observation by TIRF microscopy, no colocalization was detected. In the next step, *At*BARK1(aa1-1025)-6xHis was added to the same flow channel (Figure 17C) leading to a colocalization of microtubules and vesicles.

This fact proved that vesicles and microtubules only colocalized in the presence of *At*BARK proteins.

In a second attempt, *At*BARK2(aa163-1140)-EGFP-6xHis was used in the previously described assay. These experiments additionally showed a colocalization of motors and vesicles (Figure 17D).

Next, the mean vesicle transport velocities of *At*BARK proteins were analyzed (Figure 18).

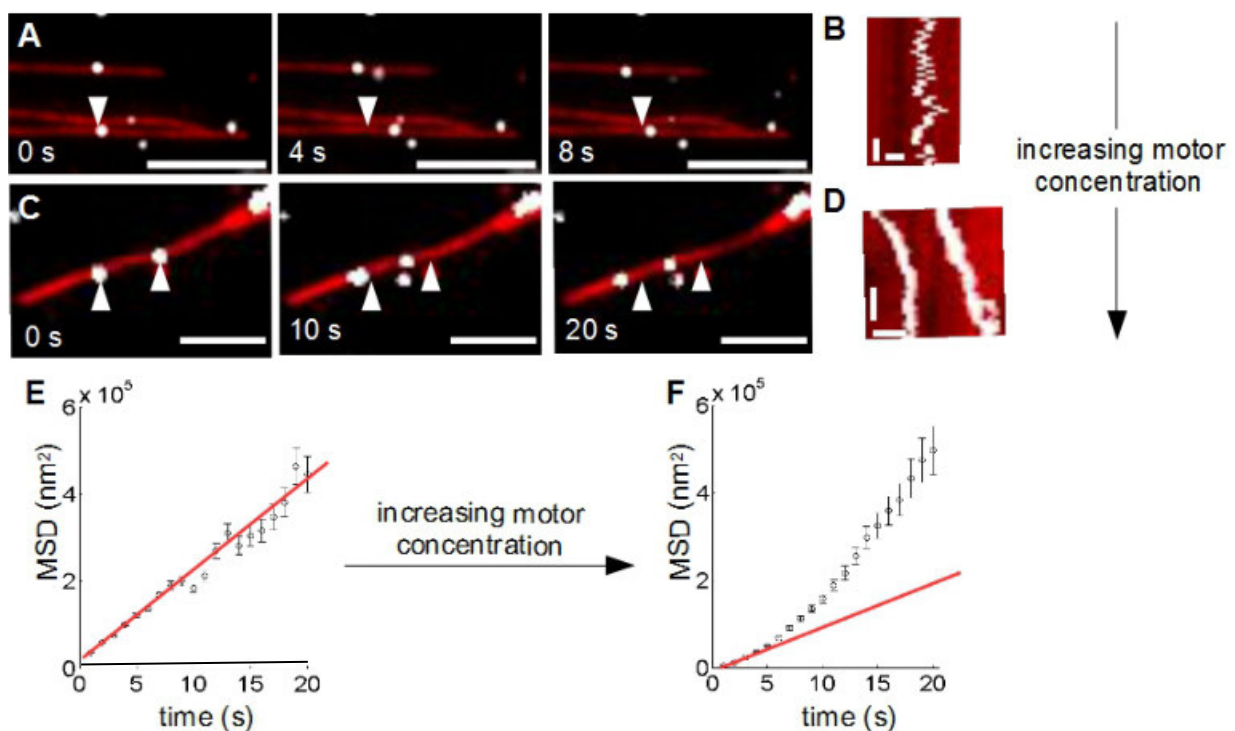


Figure 18: Vesicle transport assay of *At*BARK proteins.

(A) Time-lapse imaging of a vesicle transport assay with a low *At*BARK1(aa1-1025)-6xHis motor concentration showed diffusive movement of the vesicles (white) on the microtubules (red, scale bar = 5 μ m).

(B) Kymograph of the vesicle that was marked in (A). Analyses indicated diffusive movement (horizontal scale bar = 1 μ m, vertical scale bar = 10 s).

(C) Time-lapse imaging of a vesicle transport assay with an increased *At*BARK1(aa1-1025)-6xHis motor concentration showed directed transport of vesicles along microtubules (scale bar = 2.5 μ m).

(D) Kymograph of the vesicles that were marked in (C). Analyses indicated directed movement (horizontal scale bar = 1 μ m, vertical scale bar = 10 s).

(E, F) Mean square displacement (MSD) analyses of vesicle movement under different *At*BARK1(aa1-1025)-6xHis motor concentrations in vesicle transport assays. The MSD data at low motor concentration could be linearly fitted, which pled for diffusive vesicle movement (E). By contrast, the MSD data at a higher motor concentration could not be linearly fitted. The plot showed a parabolic course, which pled for directed vesicle movement (F). The red line indicates a linear fit through the first four data points.

The vesicle transport assays, performed with *AtBARK1* and *AtBARK2*, showed similar results. The motor concentration had an influence on the mode of vesicle movement. At lower motor concentration a diffusive movement of vesicles on microtubules was detected (Figure 18A, B). With an increasing motor concentration, the undirected diffusion changed to directed movement (Figure 18C, D). This change of movement was also proven by mean square displacement (MSD) analyses. The MSD plot of vesicle assays at low motor concentration could be linearly fitted, indicating diffusively moving vesicles (Figure 18E). By contrast, vesicles at a higher motor concentration showed directed movement as proven by a parabolic MSD plot (Figure 18F).

By using polarity-marked microtubules, it was also possible to define the transport direction. 86 out of 91 vesicles moving in a clear direction were transported towards the microtubule minus-end. Therefore, *AtBARK* proteins were identified as minus end-directed motor proteins (Figure 19).

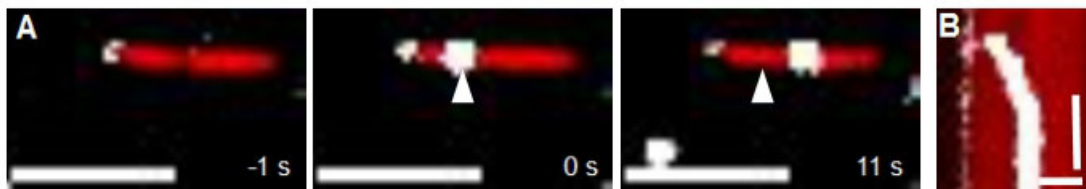


Figure 19: Vesicle transport assay of *AtBARK1* with polarity-marked microtubules.

(A) Time-lapse imaging of the vesicle transport assays with *AtBARK1*(aa1-1025)-6xHis on polarity-marked microtubules. The vesicles (gray) were transported along the microtubules (red) in direction of the unlabeled minus-ends. The microtubule plus-end was marked in gray. The starting position of the vesicle was marked with white arrowheads. Experiments indicated that *AtBARK* is a minus end-directed motor protein.

(B) Kymograph of the vesicle shown in **(A)**. Analyses indicated directed movement (horizontal scale bar = 10 s, vertical scale bar = 1 μ m).

In the next step, vesicles were tracked with the Fluorescent Image Evaluation Software for Tracking and Analysis (FIESTA) [82]. The mean velocity and run length of vesicles, transported by *AtBARK* proteins, were evaluated with MATLAB (Figure 20A-D).

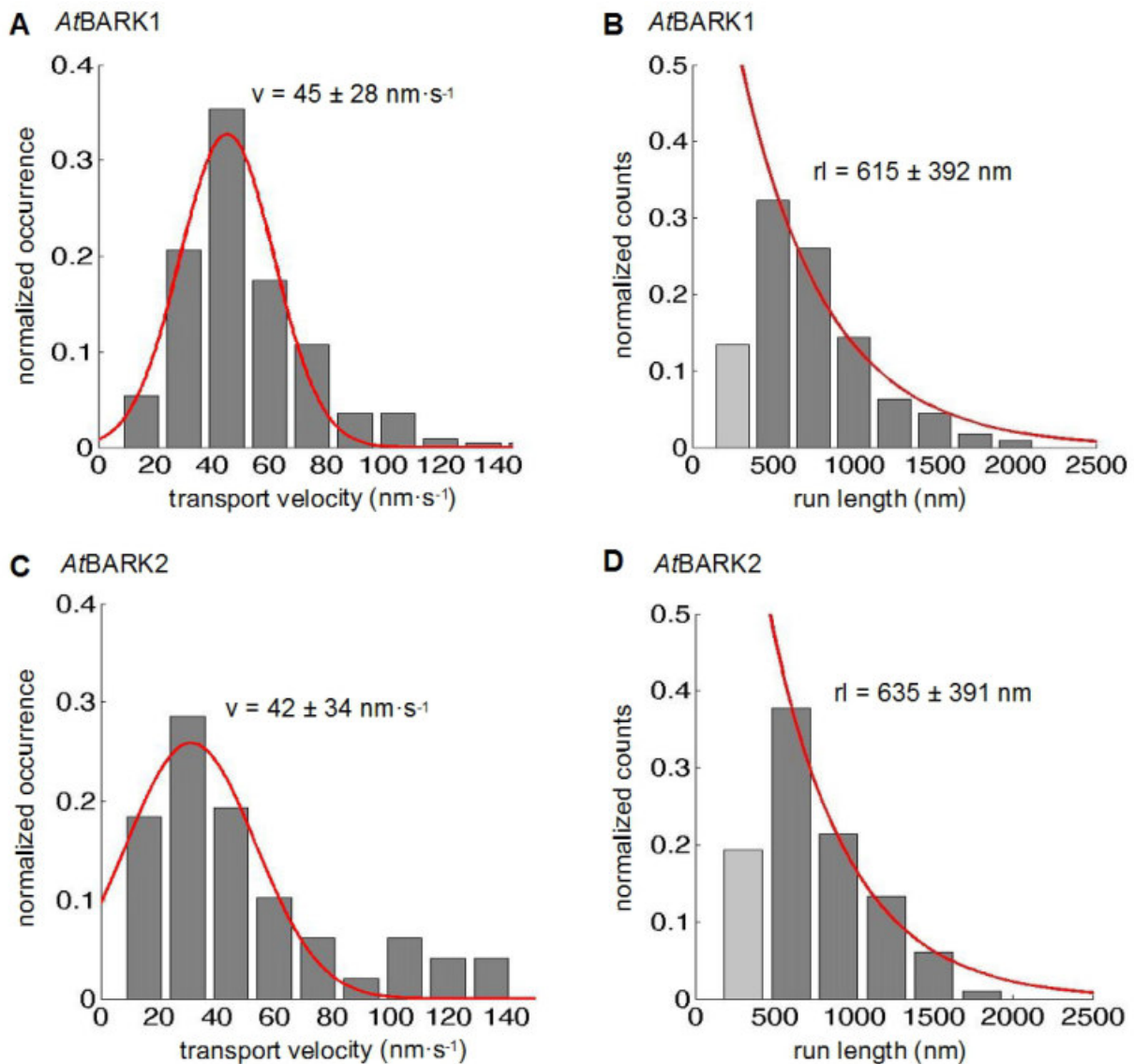


Figure 20: Velocity and run length analyses of *AtBARK1* and *AtBARK2* in vesicle transport assays.

(A, B) Histogram of the mean transport velocity and run length for 223 vesicles transported by *AtBARK1*(aa1-1025)-6xHis. A mean transport velocity of $45 \pm 28 \text{ nm}\cdot\text{s}^{-1}$ with a mean run length of $615 \pm 392 \text{ nm}$ (mean \pm s.d) was measured.

(C, D) Histogram of the mean transport velocity and run length for 96 vesicles transported by *AtBARK2*(aa163-1140)-EGFP-6xHis. A mean transport velocity of $42 \pm 34 \text{ nm}\cdot\text{s}^{-1}$ with a mean run length of $635 \pm 391 \text{ nm}$ (mean \pm s.d.) was measured.

The data of the light gray bar were excluded for the run length fit because short interactions were underrepresented due to the recorded time interval of 1 s.

Vesicles, transported by *AtBARK1*, had a mean velocity of $45 \pm 28 \text{ nm}\cdot\text{s}^{-1}$ (mean \pm s.d., $N = 223$) with a mean run length of $615 \pm 392 \text{ nm}$ (Figure 20A, B). Vesicles, transported by *AtBARK2*, had a mean velocity of $42 \pm 34 \text{ nm}\cdot\text{s}^{-1}$ (mean \pm s.d., $N = 96$) with a mean run length of $635 \pm 391 \text{ nm}$ (Figure 20C, D).

It was conspicuous that directed vesicle movement stopped after 500 - 700 nm in each assay. Therefore, variations of different parameters were tested to increase the mean run length of the vesicles (Figure 21A-F).

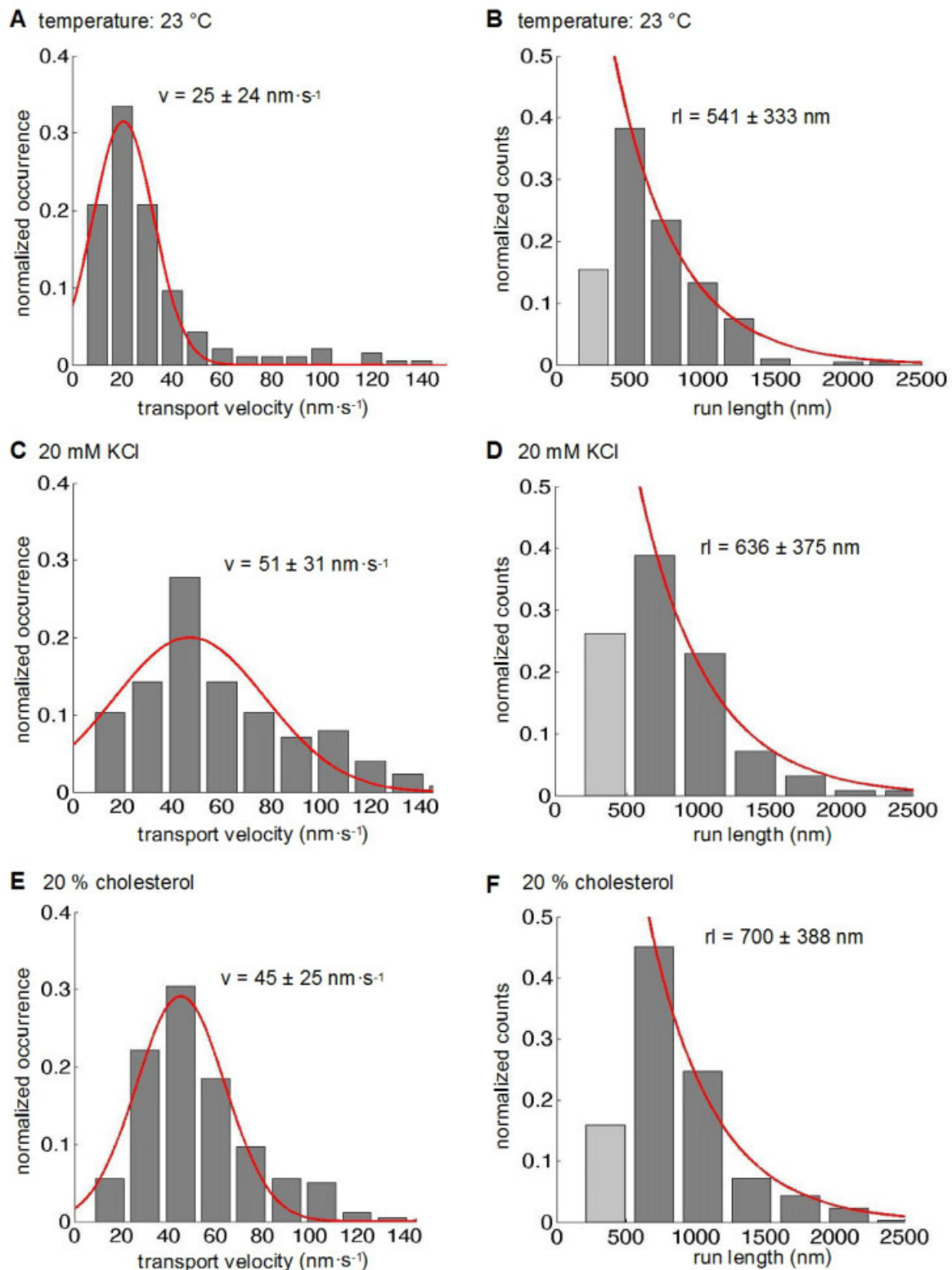


Figure 21: Velocity and run length analyses of *AtBARK1* in vesicle transport assays with varying parameters.

(A, B) The variation of the temperature enabled a mean velocity of $25 \pm 24 \text{ nm}\cdot\text{s}^{-1}$ with a mean run length of $541 \pm 333 \text{ nm}$ for 188 vesicles transported by *AtBARK1(aa1-1025)-6xHis* at $23 \text{ }^\circ\text{C}$ (histogram, mean \pm s.d.).

(C, D) An addition of 20 mM KCl led to a mean velocity of $51 \pm 31 \text{ nm}\cdot\text{s}^{-1}$ with a mean run length of $636 \pm 375 \text{ nm}$ for 96 vesicles transported by *AtBARK1(aa1-1025)-6xHis* (histogram, mean \pm s.d.).

(E, F) A phospholipid composition with 20 % cholesterol led to a mean velocity of $45 \pm 25 \text{ nm}\cdot\text{s}^{-1}$ with a mean run length of $700 \pm 388 \text{ nm}$ for 433 vesicles transported by *AtBARK1(aa1-1025)-6xHis* (histogram, mean \pm s.d.).

The data of the light gray bar were excluded for the run length fit because short interactions were underrepresented due to the recorded time interval of 1 s.

Vesicle transport assays with *AtBARK1*, performed at a lower temperature (23 °C), showed a lower mean vesicle transport velocity of $25 \pm 24 \text{ nm}\cdot\text{s}^{-1}$ and a slightly lower mean vesicle run length of $541 \pm 333 \text{ nm}$ (Figure 21A, B). An increasing salt concentration (20 mM potassium chloride (KCl)) led to a slightly faster mean vesicle transport velocity of $51 \pm 31 \text{ nm}\cdot\text{s}^{-1}$. However, the transport still stopped after $636 \pm 375 \text{ nm}$ (Figure 21C, D). An additional content of 20 % cholesterol in the vesicle membrane did not show a significant change of vesicle transport velocity ($45 \pm 25 \text{ nm}\cdot\text{s}^{-1}$, Figure 21E) and only a little increase in the mean vesicle run length ($700 \pm 388 \text{ nm}$, Figure 21F).

Even if some modifications showed a minor change in the mean vesicle run length, the transport stopped after approximately 600 - 700 nm in each case. Interestingly, stepping assays performed with a high motor concentration showed that microtubules were totally covered by fluorescence-labeled molecules over time. Several of these molecules seemed to be immobile (Figure 22).

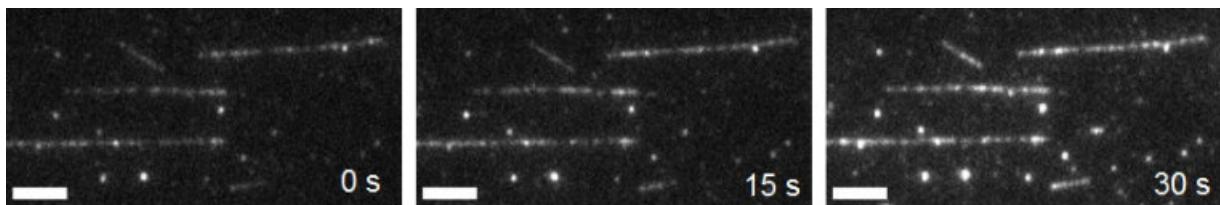


Figure 22: Stepping assay with *AtBARK2*.

Time-lapse imaging of a stepping assay with a high concentration of *AtBARK2*(aa163-1140)-EGFP-6xHis. *AtBARK2* molecules (gray) covered the whole microtubule over time (scale bar = 5 μm).

4.3 Results of the *in vivo* experiments

4.3.1 *bark1* and *bark2* are expressed in pollen

In order to gain an overview of existing gene expression data for *bark1* and *bark2* in different tissues, *GeneVestigator* [83, 84] was used. This software comprises data of published microarray and RNA sequencing experiments (Figure 23).

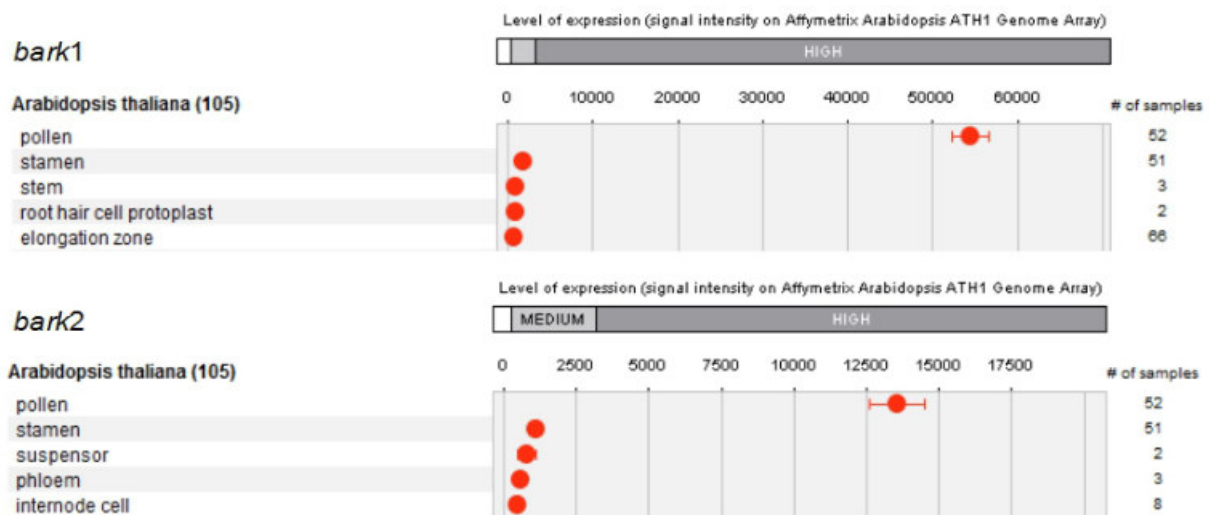


Figure 23: Expression levels of the *bark* genes in different *A. thaliana* tissues.

GeneVestigator data [83, 84] displayed the expression levels of *bark1* and *bark2* in different tissues based on published microarray and RNA sequencing data. The evaluation was described as a scatterplot-list with a linear display. *bark1* and *bark2* showed a high expression in pollen.

bark1: 54366.68 ± 15445.86 (mean \pm s.d., $N = 52$), AT-00178, AT-00317, AT-00323 (ArrayExpress) and AT-00465 and AT-00466 (GEO), *bark2*: (13581.58 ± 6859.13) (mean \pm s.d., $N = 52$), AT-00178, AT-00317, AT-00323 (ArrayExpress) and AT-00465 and AT-00466 (GEO).

The evaluation showed a high expression level of *bark1* and *bark2* in pollen, besides further medium and low expression levels in other tissues (Figure 23) [83, 84].

Furthermore, β -glucuronidase reporter gene assays were performed to analyze the promotor activity of *bark1* and *bark2*. For this purpose, the promotor of *bark1* or *bark2* was cloned into a vector in front of the GUS gene, respectively (appendix: Figure 66). The resulting vectors were each transformed into Columbia wild-type (Col-0) plants through *A. tumefaciens*. A successful transformation was proven by PCR analyses (appendix: Figure 67). In the tissue, where the promotor is active, the enzyme β -glucuronidase is expressed and hydrolyzes 5-bromo-4-chloro-3-indolyl glucuronide (X-Gluc) to glucuronic acid and 5-bromo-4-chloro-indoxyl. Furthermore, 5-bromo-4-chloro-indoxyl is oxidized to the non-soluble, blue dye 5,5'-dibrom-4,4'-dichloro-indigo [85]. Therefore, *bark* promotor activity could be detected by a blue tissue staining (Figure 24).

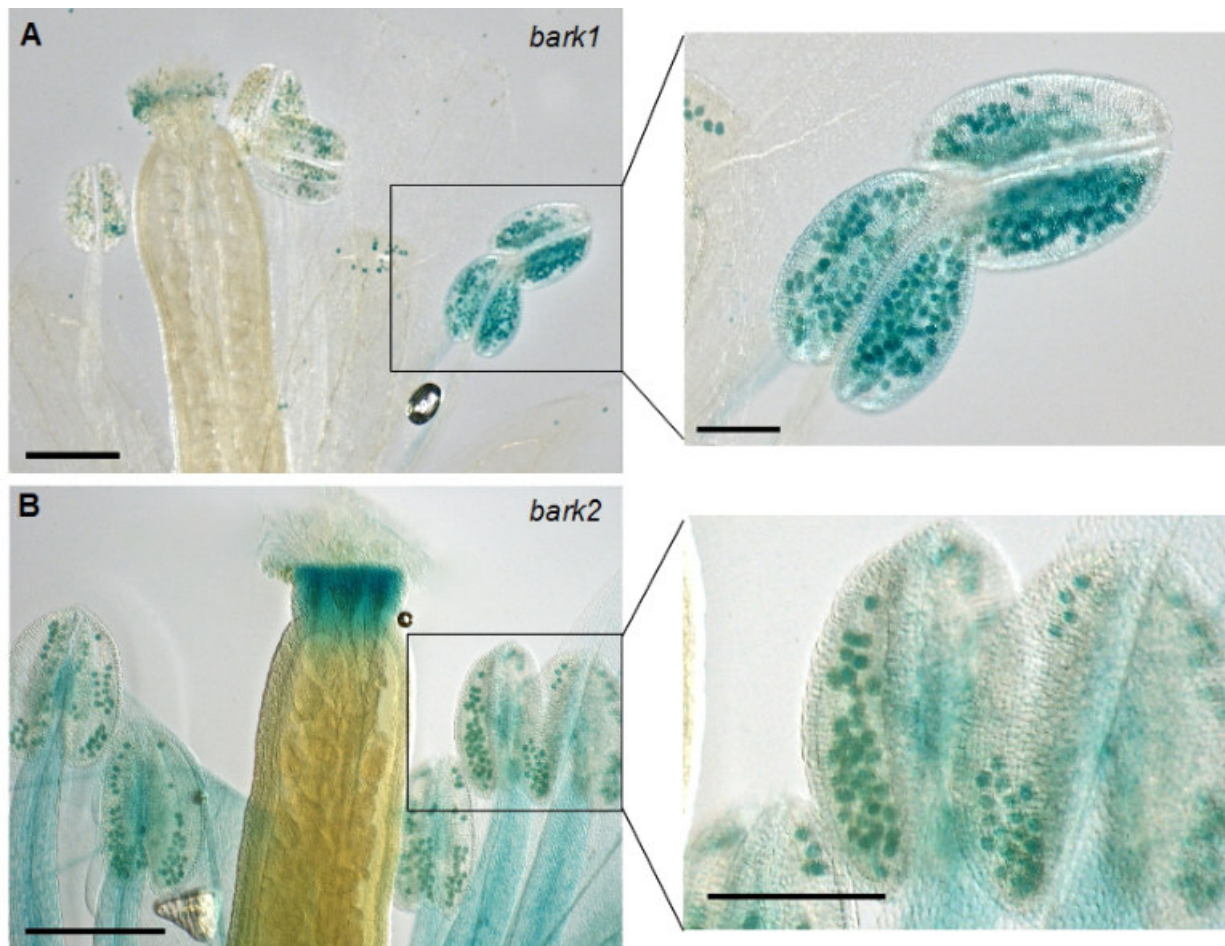


Figure 24: Macroscopic imaging of β -glucuronidase activity under *bark*-promotor control.

Five-week-old flowers of *bark1*-GUS (A) and *bark2*-GUS lines (B) were used for GUS staining. For *bark1*, a strong blue staining of the pollen was visible (left: scale bar = 400 μ m, right: scale bar = 200 μ m). In addition to the strong staining of the pollen, the stylus and the filaments were also stained blue for *bark2* (left: scale bar = 400 μ m, right: scale bar = 200 μ m).

In this so-called GUS staining, five out of five *bark1*-GUS and *bark2*-GUS lines showed a strong *bark1* (Figure 24A) and *bark2* (Figure 24B) promotor activity in pollen. In addition to these results, a *bark2* promotor activity was detected in the style and in the filaments.

4.3.2 *Homozygous bark1-1 plants show aborted pollen grains and modifications in pollen tube development*

Due to the strong expression of *bark1* and *bark2* in pollen, the T-DNA insertion lines *bark1-1*, *bark2-1* and *bark2-2* (Figure 8, listed Table 4) were analyzed concerning a pollen phenotype. All plants were genotyped for a comparison of homozygous and segregating wild-type plants of the *bark* T-DNA insertion lines and Col-0 plants (appendix: Figure 69). The plants were grown on soil until they flowered. At this time, pollen was collected for pollen germination assays. Pollen development was observed on agar by bright field microscopy (Figure 25).

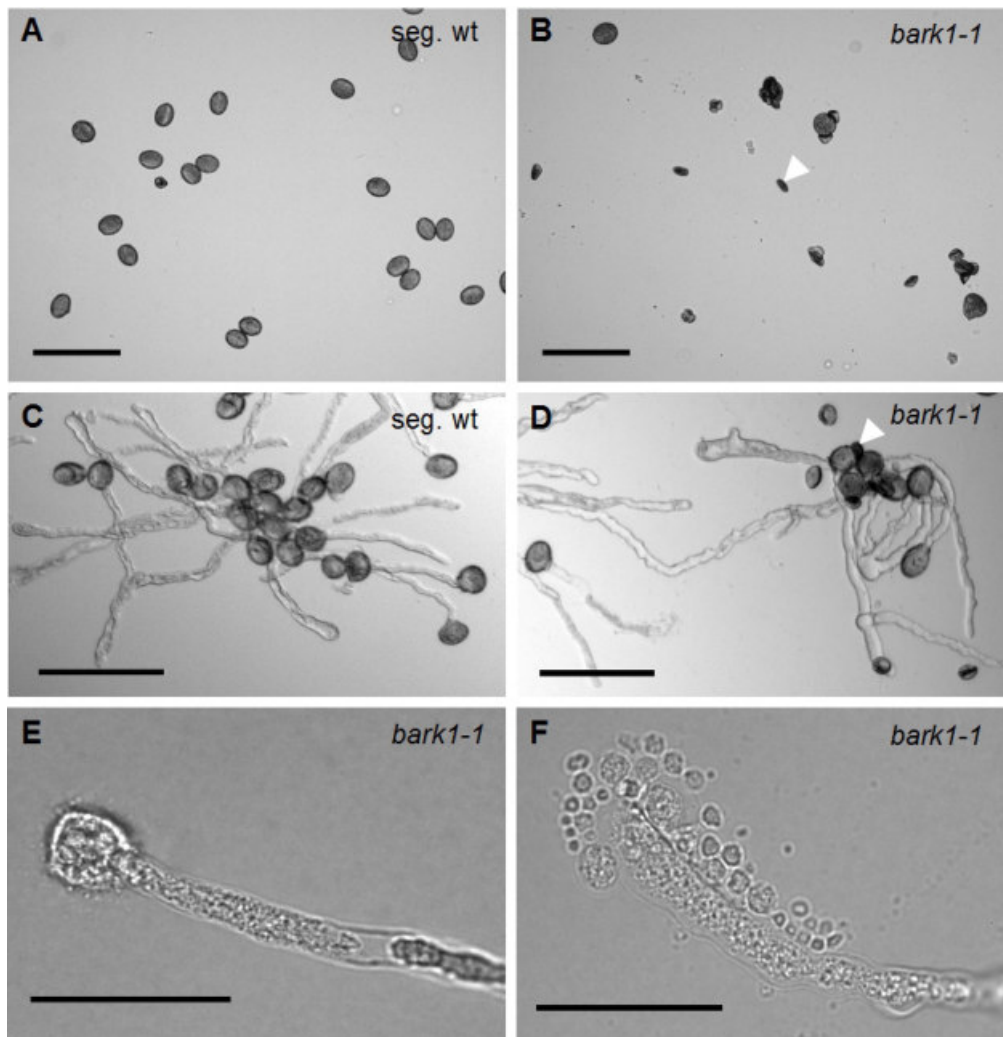


Figure 25: Pollen development of homozygous *bark1-1* and segregating wild-type plants.

(A) Pollen grains of segregating wild-type plants. They had an oval form and a mostly consistent size (scale bar = 100 μ m).

(B) Pollen grains of homozygous *bark1-1* plants. Some pollen grains looked similar to the segregating wild-type pollen. Other pollen grains were significantly smaller and bulky (white arrow, scale bar = 100 μ m).

(C) Pollen germination of segregating wild-type plants. Almost all pollen showed the formation of pollen tubes 22 h after application on agar (scale bar = 100 μ m).

(D) Pollen germination of homozygous *bark1-1* plants. Pollen grains with the same appearance as the segregating wild-type pollen germinated and developed pollen tubes 22 h after application on agar. Pollen grains, which looked smaller and bulky, did not to germinate (white arrow, scale bar = 100 μ m).

(E, F) Pollen tube development of homozygous *bark1-1* plants. Several pollen grains showed tip swelling and partially burst of the pollen tip, which terminated the growth process (E). Other pollen tubes, which were still intact, showed the building of vesicles around the pollen tube (F) (scale bar = 30 μ m).

The comparison of segregating wild-type and homozygous *bark1-1* pollen showed a difference concerning pollen development. Most pollen of segregating wild-type plants had an oval form and a mostly consistent size, comparable with Col-0 pollen (Figure 25A). By contrast, homozygous *bark1-1* plants showed two different kinds of pollen. On one hand, there were pollen grains, which looked similar to the segregating wild-type pollen. On the other hand, there were aborted pollen grains, which looked significantly smaller and bulky (Figure 25B, white arrow). In addition, it was observed that modified pollen grains did not germinate on agar during a period of 22 h (Figure 25D, white arrow). The situation was

different for the pollen of homozygous *bark1-1* plants, which looked similar to the segregating wild-type pollen (Figure 25D), and for the segregating wild-type pollen itself (Figure 25C). These pollen grains germinated and developed pollen tubes on the same germination agar. Some pollen tubes of homozygous *bark1-1* plants developed similarly to the segregating wild-type line. Others showed tip swelling and burst of the pollen tube tip, which terminated pollen tube growth (Figure 25E). Additionally, pollen tubes were observed, which showed vesicle formation around the growing pollen tube tip (Figure 25F).

In order to analyze whether *bark* was expressed in the T-DNA insertion lines, RNA was purified from flowers. cDNA was generated from this RNA in a two-step RT-PCR. PCR analyses were performed on the cDNA to prove a successful knockout. These analyses showed that the *bark2-1* line was a knockout line. By contrast, the *bark2-2* line was no knockout line. The T-DNA insertion in the promotor region of *bark1* seemed to lead to a reduced expression level but not to a complete knockout in the *bark1-1* line (appendix: Figure 70).

To verify that the observed pollen phenotypes were caused by the reduced *bark1* expression in the *bark1-1* line, a complementation line (*cbark1-1*) was established (by Melanie Schulz) and analyzed. *cbark1-1* plants did not show aborted pollen, tip swelling, and vesicle formation around the pollen tube tip during pollen germination assays. The majority of pollen grains germinated and grew long pollen tubes (Figure 26A).

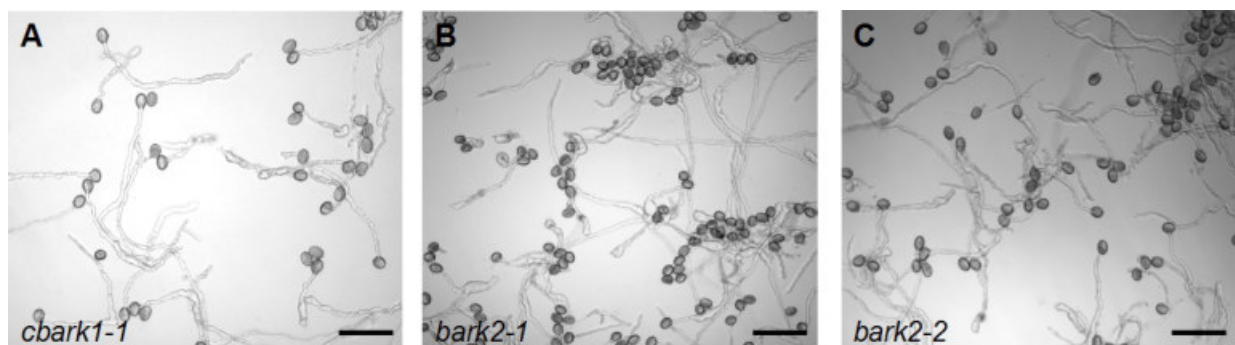


Figure 26: Pollen development of the complementation line *cbark1-1* and the homozygous lines *bark2-1* and *bark2-2*.

(A) Plants of the complementation line *cbark1-1* did not show aborted pollen, tip swelling or vesicle formation around the pollen tube (scale bar = 100 μm).

(B, C) Homozygous *bark2-1* (B) and *bark2-2* plants (C) showed aforementioned modifications only to a very low extent in comparison to homozygous *bark1-1* plants (scale bar = 100 μm).

The phenotypes of homozygous *bark1-1* plants were only shown to a very low extent in pollen germination assays of homozygous *bark2-1* plants. Comparably to the complementation line, the majority of pollen grains germinated and developed long pollen tubes (Figure 26B).

4.3.3 *Oryzalin impairs pollen tube development in a similar way as the bark1-1 line*

The dinitroaniline herbicide oryzalin is already known to inhibit plant microtubule polymerization due to its binding to tubulin dimers in a reversible, pH-dependent manner [86-88]. When oryzalin was added to the pollen germination agar in different concentrations, it had an effect on the germination of Col-0 pollen (Figure 27).

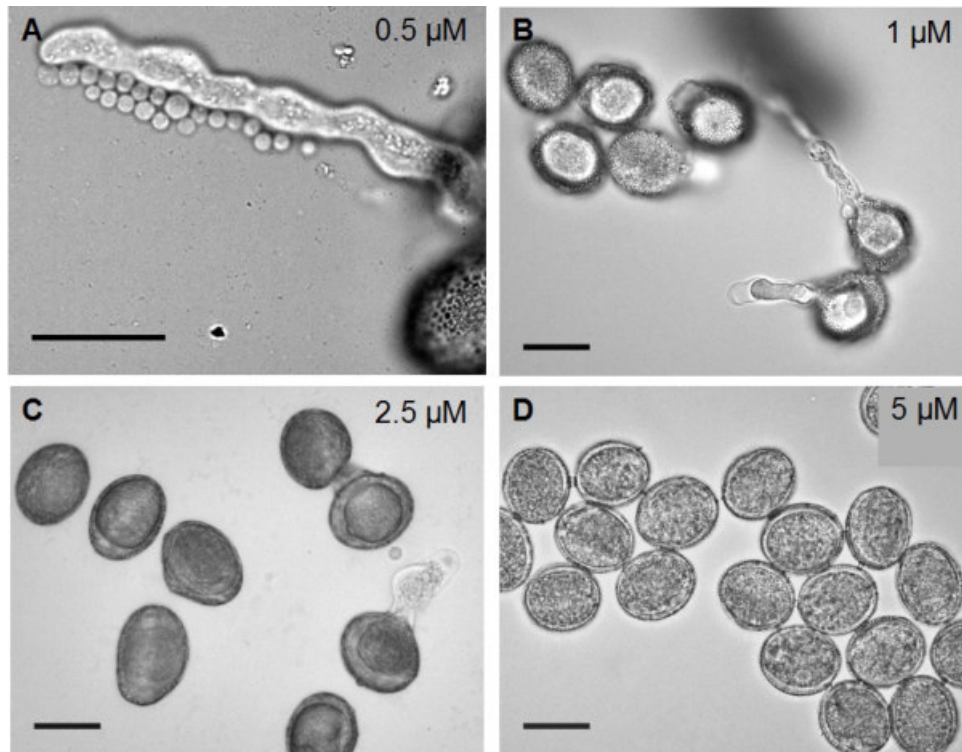


Figure 27: Influence of oryzalin on pollen germination.

(A) Col-0 pollen germination in presence of 0.5 μM oryzalin. Several germinating pollen grains showed vesicle formation around the growing pollen tube (scale bar = 20 μm).

(B, C) Col-0 pollen germination in presence of 1 μM (B) and 2.5 μM oryzalin (C). Higher oryzalin concentrations led to a strong decrease of pollen germination. Germinating pollen grains were very short (scale bar = 20 μm).

(D) Col-0 pollen germination in presence of 5 μM oryzalin. Germination was prevented (scale bar = 20 μm).

In presence of 0.5 μM oryzalin, Col-0 pollen germination and pollen tube development were still possible. Interestingly, the formation of vesicles at the tip of the growing pollen tube was observed (Figure 27A). This phenomenon was similar to the phenotype of homozygous *bark1-1* plants (Figure 25F). At higher oryzalin concentrations - between 1 μM and 2.5 μM - the Col-0 pollen germination rate decreased. Germinating pollen grains formed very short pollen tubes, which often burst (Figure 27B, C). A concentration of 5 μM oryzalin completely prevented pollen germination (Figure 27D).

4.3.4 *Multiple punctuated, motile AtBARK signals were detected in growing pollen tubes*

In order to analyze the intracellular distribution of *AtBARK1* in pollen tubes, the construct 35S-pMDC85-BARK1-GFP (appendix: Figure 66) was transformed into Col-0 plants through

A. tumefaciens. A successful transformation was proven with PCR analyses (appendix: Figure 68). Pollen germination assays were performed and analyzed by TIRF microscopy (Figure 28).

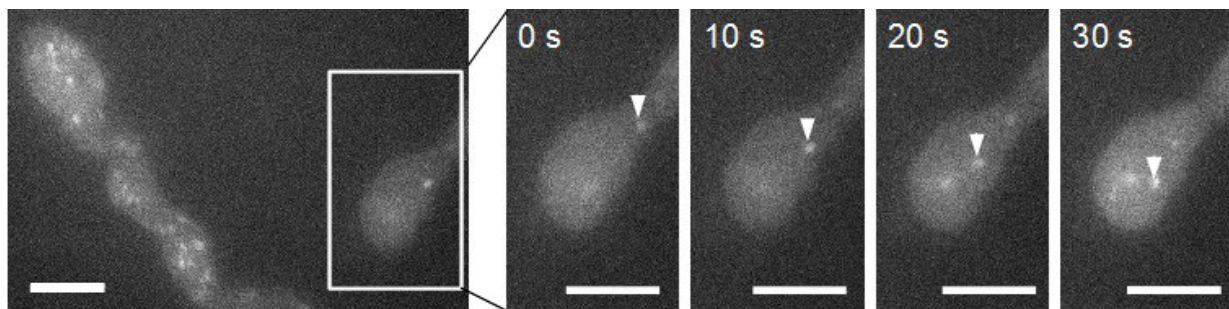


Figure 28: Intracellular distribution of *AtBARK1* in pollen tubes of *A. thaliana*.

TIRF images of pollen tubes from Col-0 plants, which contained the 35S-pMDC85-BARK1-GFP construct. Time-lapse imaging showed multiple punctuated, motile *AtBARK1*-GFP signals in growing pollen tubes (scale bar = 20 μ m). A moving *AtBARK1*-GFP signal was marked by white arrowheads.

Time-lapse imaging showed multiple punctuated, motile *AtBARK1*-GFP signals spread over the total length of pollen tubes (Figure 28).

4.3.5 Homozygous bark1-1 plants show an increased number of smaller siliques and a reduced seed number per silique

Based on aforementioned data concerning pollen phenotypes in consequence of impaired *bark1* expression (*bark1-1* plants) or impaired microtubule dynamics (oryzalin treatment), it seemed interesting to explore whether these modifications have an influence on fertilization and the development of siliques and the number of seeds.

For morphological analyses, homozygous *bark1-1* plants, segregating wild-type plants, and Col-0 plants were seeded, genotyped (appendix: Figure 69), and grown under standard cultivation conditions. Plant growth was similar between segregating wild-type and Col-0 plants over seven weeks. Several homozygous *bark1-1* plants showed an increased number of underdeveloped siliques (Figure 29).

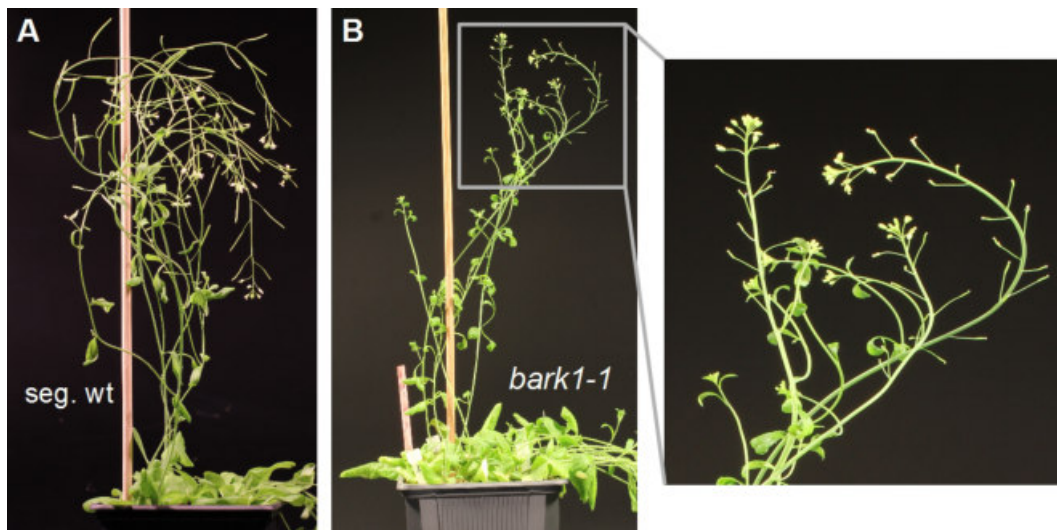


Figure 29: Silique development of segregating wild-type and homozygous *bark1-1* plants.

Several homozygous *bark1-1* plants (B) showed the development of less and underdeveloped siliques in comparison to segregating wild-type plants (A).

Due to the silique phenotype of homozygous *bark1-1* plants, siliques were collected, decolorized, and the refraction index was adapted to count the seeds inside (Figure 30) [89].

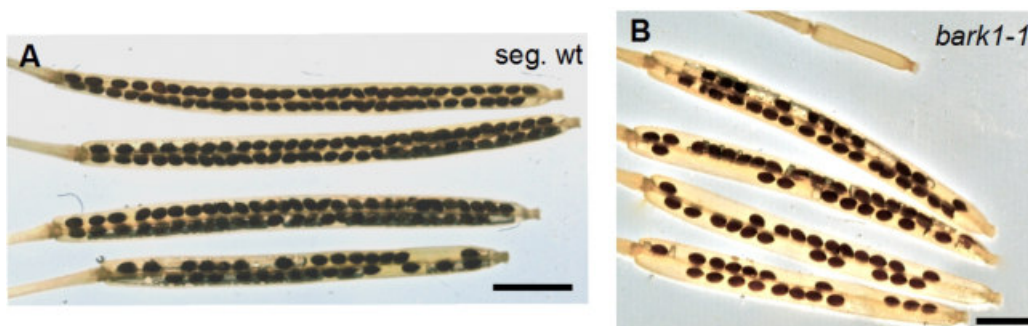


Figure 30: Siliques of homozygous *bark1-1* plants and segregating wild-type plants.

(A) Siliques of segregating wild-type plants showed a normal development of seeds (scale bar = 2 mm).

(B) Siliques of homozygous *bark1-1* plants showed a decreased number of seeds per silique (scale bar = 2 mm).

Homozygous *bark1-1* plants developed several siliques with a decreased number of seeds inside (Figure 30B) in comparison to segregating wild-type plants (Figure 30A).

4.3.6 The pollen, silique, and seed phenotypes of homozygous *bark1-1* plants are temperature-independent

In order to obtain statistic evidence of the observed difference in seed number, it was necessary to collect and count a specific number of siliques of each plant line and compare these values. In addition to this statistical evaluation, plants were grown under different temperature and humidity conditions during following experiments to possibly favor occurred phenotypes.

First, homozygous *bark1-1* plants, segregating wild-type plants, and Col-0 plants were analyzed under different temperature conditions. Plants were grown under long day conditions with approximately 60 % humidity at 17 °C, 22 °C, and 27 °C and genotyped (appendix: Figure 69). Plant growth was documented over the period of seven weeks for morphological analyses. During this time, it was similar between homozygous *bark1-1*, segregating wild-type and Col-0 plants at the same temperature (Figure 31). However, there were growth variations between plants at different temperatures. Plants cultured at 17 °C grew slower, while plants at 22 °C and 27 °C grew faster (Figure 31). Finally, all plants reached a similar growth stage. Many homozygous *bark1-1* plants showed an increased number of smaller siliques (as shown in Figure 29).

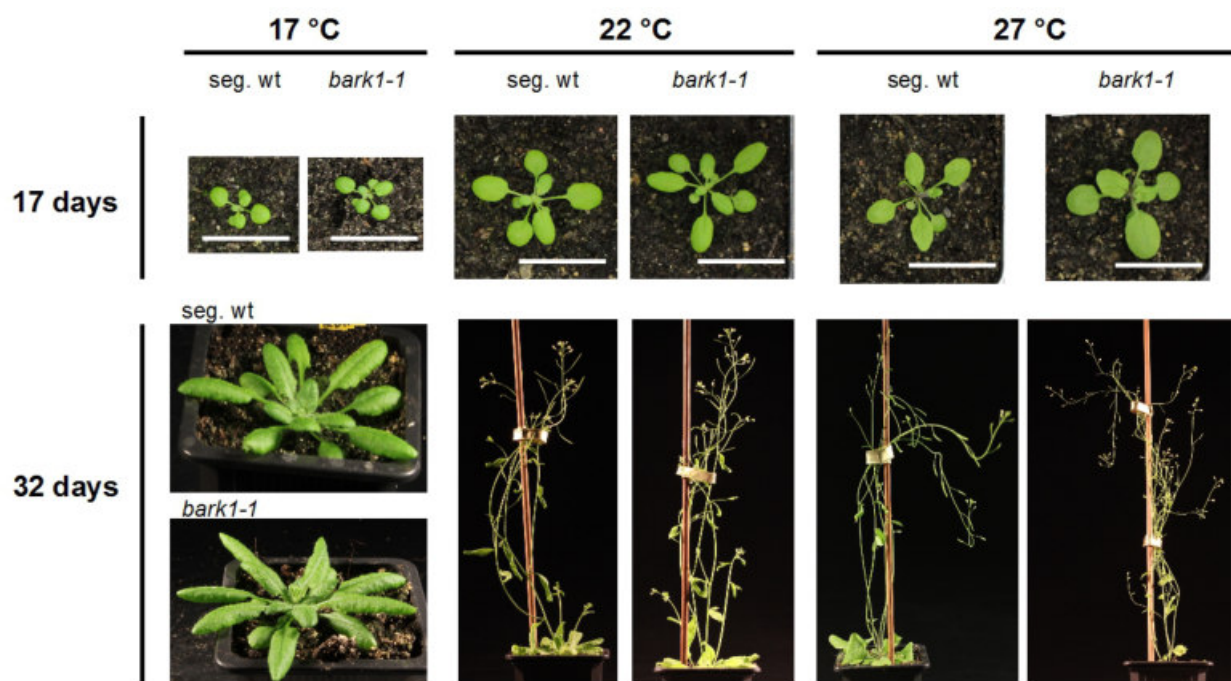


Figure 31: Plant growth of homozygous *bark1-1* plants and segregating wild-type plants under different temperature conditions.

Plant growth was similar between homozygous *bark1-1* and segregating wild-type plants at the same temperature. However, there were differences between the temperatures groups. Plants cultured at 17 °C grew slower, while plants at 27 °C grew faster. Finally, all plants reached a similar growth stage (scale bar = 1.8 cm).

In order to analyze silique and seed development, siliques of all plant groups were collected at a similar growth stage of the plants. These siliques were decolorized and the refraction index was adapted for seed counting [89] (Figure 32).

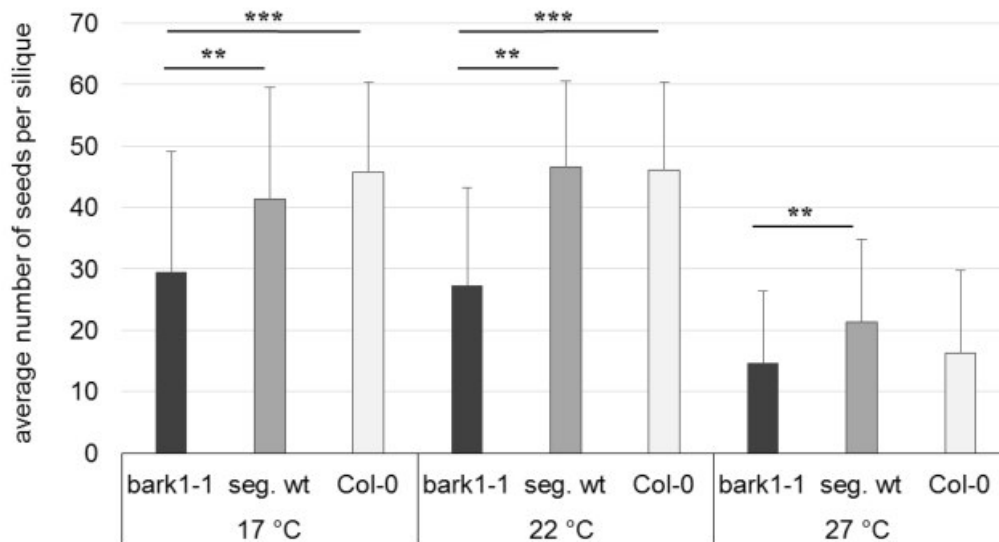


Figure 32: Seed development of homozygous *bark1-1* plants, segregating wild-type plants, and Col-0 plants at different temperatures.

Graphic chart of the mean number of seeds per silique for homozygous *bark1-1* plants, segregating wild-type plants, and Col-0 plants at different temperatures (17 °C, 22 °C, 27 °C, mean \pm s.d., N = 28-61, $p < */**/** = 5\% / 1\% / 0.1\%$).

Comparing the three lines of one temperature group, homozygous *bark1-1* plants, grown at 17 °C and 22 °C, had in each case a significantly lower mean number of seeds per silique in comparison to segregating wild-type plants and Col-0 plants. Segregating wild-type plants and Col-0 plants at 17 °C and 22 °C did not show significant differences. For the three lines grown at 27 °C a significant difference between homozygous *bark1-1* plants and segregating wild-type plants was detected. It was notable that the mean number of seeds per silique was generally very low at 27 °C.

The comparison of seed development of all lines at different temperatures showed that a higher temperature led to a worse development of siliques and seeds in general. The exact mean \pm s.d. values were listed in the appendix Table 22.

First, the three lines of one temperature group were compared. Homozygous *bark1-1* plants, grown at 17 °C and 22 °C, had a significantly lower mean number of seeds per silique in comparison to segregating wild-type plants and Col-0 plants. By contrast, segregating wild-type plants and Col-0 plants at 17 °C and 22 °C did not show a significant difference in the mean seed number per silique. The three lines grown at 27 °C showed a significant difference between homozygous *bark1-1* plants and segregating wild-type plants (Figure 32).

The comparison of silique and seed development of all three lines at different temperatures showed that a higher temperature (27 °C) led to an overall worse development of siliques and seeds in general (Figure 32).

Although segregating wild-type plants and Col-0 plants had aborted pollen, too, the extent of aborted pollen, combined with the impaired tube growth of homozygous *bark1-1* plants, indicate a significant decrease in seed number per silique. The detected phenotypes of homozygous *bark1-1* plants were not temperature-dependent.

4.3.7 The pollen, silique, and seed phenotypes of homozygous *bark1-1* plants are humidity-independent

In the next step, homozygous *bark1-1* and *bark2-1* plants were compared with segregating wild-type plants under different humidity conditions. The plants were grown under long day conditions at 22 °C with 50 %, 60 %, and 90 % humidity and genotyped (appendix: Figure 69). Plant growth was observed over the period of seven weeks for morphological analyses. It was similar between homozygous *bark2-1* and segregating wild-type plants at the same humidity. Homozygous *bark1-1* plants showed an increased number of smaller siliques in comparison to segregating wild-type plants (as shown in Figure 29). Siliques of all plant groups were collected in an approximately similar growth stage of the plants, decolorized and the refraction index was adapted for seed counting [89] (Figure 33, 34).

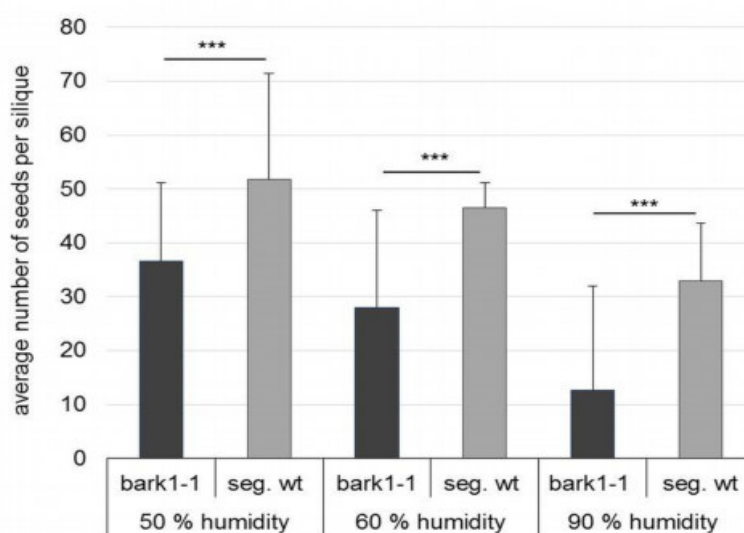


Figure 33: Seed development of homozygous *bark1-1* plants and segregating wild-type plants at different humidity.

Graphic chart of the mean number of seeds per silique for homozygous *bark1-1* plants and segregating wild-type plants at 50 %, 60 %, and 90 % humidity (mean \pm s.d., N = 15-80, $p < */**/** = 5\% / 1\% / 0.1\%$).

Comparing the two lines of one humidity group, homozygous *bark1-1* plants had in each case a significantly lower mean number of seeds per silique in comparison to segregating wild-type plants at each humidity.

The comparison of seed development of all lines at different humidity showed that a higher humidity led to a worse development of siliques and seeds in general. The exact mean \pm s.d. values were listed in the appendix Table 23.

First, homozygous *bark1-1* and segregating wild-type plants of one humidity group were compared. Homozygous *bark1-1* plants, grown at 50 %, 60 %, and 90 % humidity, had a significantly lower mean number of seeds per silique in comparison to segregating wild-type plants (Figure 33).

Comparing homozygous *bark1-1* plants and segregating wild-type plants at different humidity, the mean number of seeds per silique decreased with increasing humidity (Figure 33).

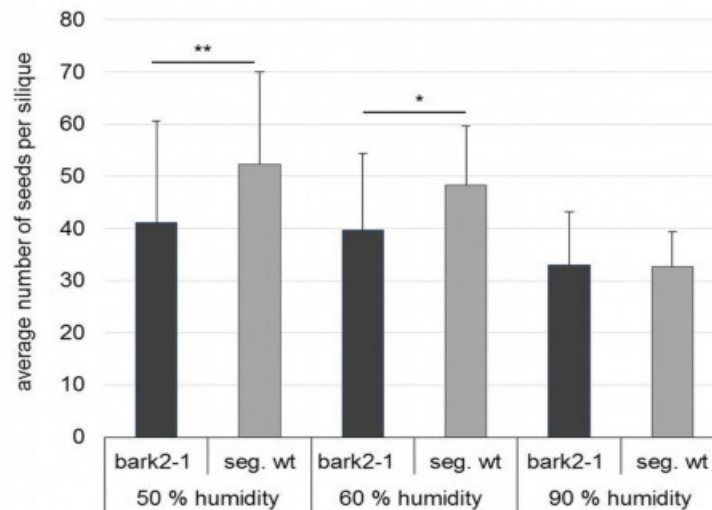


Figure 34: Seed development of homozygous *bark2-1* plants and segregating wild-type plants at different humidity.

Graphic chart of the mean number of seeds per silique for homozygous *bark2-1* plants and segregating wild-type plants at 50 %, 60 %, and 90 % humidity (mean \pm s.d., N = 15-80, $p < */**/** = 5\% / 1\% / 0.1\%$).

Comparing the two lines of one humidity group, homozygous *bark2-1* plants had a significantly lower mean seed number per silique at 50 % and 60 % humidity in comparison to segregating wild-type plants.

The comparison of silique and seed development of all lines at different humidity showed that a higher humidity led to a worse development of siliques and seeds in general. The exact mean \pm s.d. values were listed in the appendix Table 23.

Homozygous *bark2-1* plants did not show such a clear phenotype as *bark1-1* plants. Homozygous *bark2-1* plants, grown at 50 % and 60 % humidity, had a significantly lower mean number of seeds per silique in comparison to segregating wild-type plants. Consistent with the lower number of aborted pollen during pollen germination assays, the number of missing seeds per silique also decreased (Figure 34).

Comparing *bark2-1* plants and their segregating wild-type at different humidity, the mean number of seeds per silique decreased with an increasing humidity (Figure 34).

The phenotypes of homozygous *bark1-1* plants, which were found in the temperature experiment, were also observed in the humidity experiment. Plants showed aborted pollen, pollen with impaired tube formation, and the development of siliques with a significantly lower number of seeds. These phenotypes were not as pronounced and highly significant for homozygous *bark2-1* plants. It was also found that the detected phenotypes were not humidity-dependent.

4.4 Discussion

At1g73860 and *At1g18410* represent two interesting kinesin-14 genes because they both code for kinesins characterized by a specific N-terminal F-BAR domain. At present, there are no other F-BAR kinesins described in the literature. The F-BAR domains were detected by analyses of the whole amino acid sequence of different *A. thaliana* kinesins. These analyses also showed further comparable domains and domain arrangement (Figure 9). Additionally, *bark1* and *bark2* offered a highly similar gene organization (Figure 8). Therefore, it is fair to assume that both genes originate from gene duplication. Literature studies mentioned a high redundancy during the development of the kinesin-14 family. It probably arose from processes like sequence mutations, complete gene duplication, or alternative splicing [3].

In order to gain an insight into the biophysical properties of *AtBARK* proteins, expression constructs were cloned, expressed in bacteria, and purified by affinity chromatography for *in vitro* analyses.

4.4.1 *The influence of motor functionality on gliding and stepping assays with AtBARK proteins*

First, *AtBARK* proteins were tested in gliding and stepping assays. Gliding assays showed mostly stiff and rarely diffusive *AtBARK* interactions with microtubules (Figure 12). Stepping assays showed very bright, diffusing *AtBARK* signals on microtubules (Figure 13). Conditions like buffer composition, pH-value, ionic strength, and temperature have an effect on protein conformation, protein interactions, and the gliding performance [90]. A variation of these aforementioned conditions did not promote a constant microtubule movement in gliding assays or non-processive motor interactions in stepping assays. These kinds of motions were expected for *AtBARK* proteins because they were also shown for other members of the *Atkinesin-14* family and the close relative *OsKCH1* [34, 43, 91].

Hereafter, hypotheses are proposed to explain observed results (Figure 35).

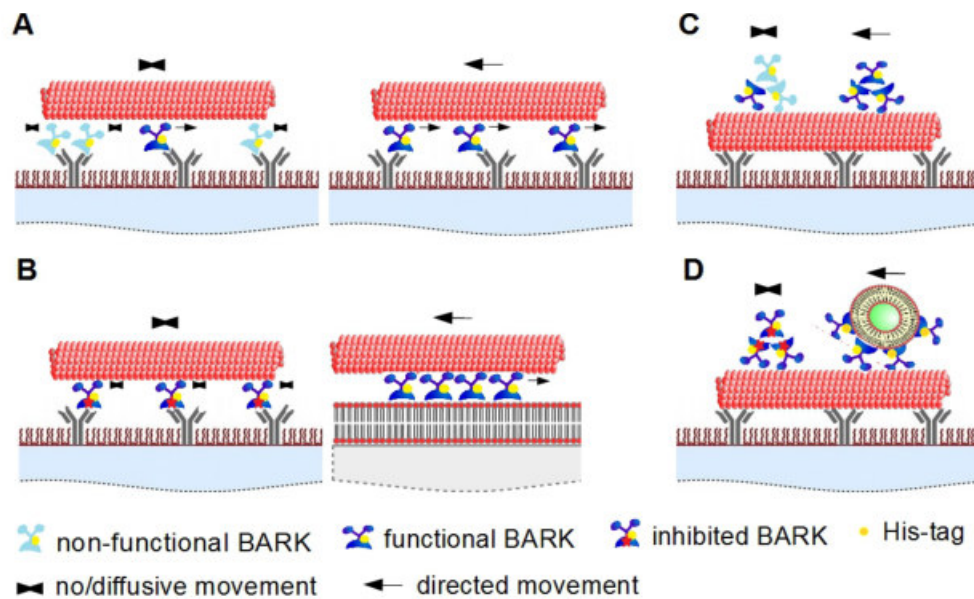


Figure 35: Proposed models showing the influence of motor functionality on gliding and stepping assays with *AtBARK* proteins.

(A, B) Missing directed movement of microtubules in gliding assays can be explained by a high concentration of non-functional motor proteins (A, left) or an intramolecular inhibition of motors (B, left). A higher concentration of functional motor (A, right) or cargo interaction (B, right) might enable gliding processes.

(C, D) Complexes comprising functional and non-functional motors (C, left) or complexes comprising inhibited motors - without cargo interaction - (D, left) can trigger diffusive movement in stepping assays. A higher concentration of functional motors (C, right) or cargo interaction (D, right) might enable transport processes.

On one hand, the concentration of functional *AtBARK* proteins could be lower than the concentration of non-functional motors in performed motility assays. If many non-functional motors bind microtubules in gliding assays, they impair directed movement. This could explain the predominant number of stably bound microtubules (Figure 35A). The diffusive movement of bright *AtBARK* signals in performed stepping assays might indicate the formation of *AtBARK* complexes. If these complexes compromise functional and non-functional motors, *AtBARK*-microtubule interactions could be impaired, which caused observed diffusive motion (Figure 35C). A detailed look at the purification gels (Figure 11) shows many impurities, which could be degradation products (= non-functional motors). This was an ongoing problem despite expression tests, construct design, and affinity chromatography, which supports the hypothesis of a high concentration of non-functional, disturbing motors.

The second hypothesis is based on intramolecular motor inhibition (Figure 35B, D). The absence of cargo molecules for the F-BAR domain of *AtBARK* proteins in performed motility assays might cause the unexpected motor-microtubule interactions. Various examples of intramolecular inhibition of BAR and F-BAR proteins were described in the literature. Some examples are posttranslational modifications [40, 60], inhibition through SH3 domains [40,

60, 92], or missing oligomerization [57, 60, 63], as well as the preferred binding to specific lipid compositions or membrane curvatures [40, 57, 59-61, 64].

A termination of possible intramolecular *AtBARK* inhibition was analyzed by gliding assays on SLBs.

4.4.2 *The influence of membrane fluidity, motor density, and motor functionality on membrane gliding assays with AtBARK proteins*

The SLB membrane was used as a binding partner for the F-BAR domain. Self-performed membrane gliding assays with *AtBARK* proteins showed many diffusively moving microtubules instead of expected microtubule gliding (Figure 15). There are again different reasons, which could explain these results (Figure 36).

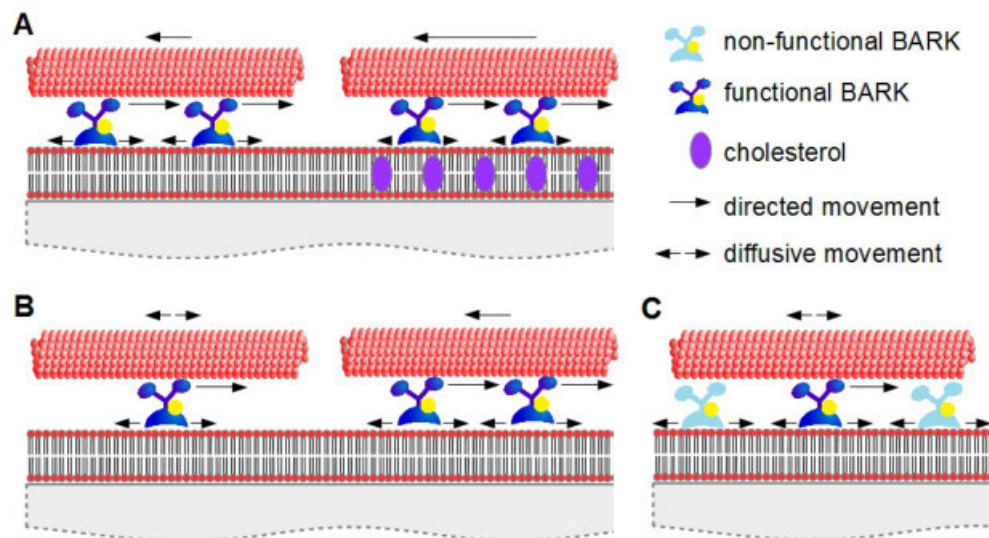


Figure 36: Proposed models showing the influence of membrane fluidity, motor density, and motor functionality on membrane gliding assays with *AtBARK* proteins.

(A) Diffusive movement of motors – more precisely of their tail domain - on fluid membranes can reduce the transport efficiency (left). An increasing viscosity of the membrane - for example, due to an increased cholesterol concentration - can reduce motor diffusion (right), which might improve microtubule gliding.

(B, C) Diffusive movement of microtubules on SLB can be explained by a low density of functional motors (B, left). By contrast, a higher density can enable directed movement (B, right). If the amount of non-functional motors strongly increases, they could additionally impair transport processes (C).

First, it is necessary to determine that there is a steric difference between gliding and membrane gliding assays. In gliding assays, motors are stably bound to the surface by antibodies. Conversely, membrane gliding assays offer fluid membranes, which enable motor tails to diffuse by slipping in the lipid bilayer (Figure 36A, left) [81]. Literature studies have shown that the transport efficiency of different motors on SLB depends on cargo properties, motor density and diffusivity [81, 93]. The experiments of Grover et al. showed a gradual shift from diffusive to directed microtubule motion with an increasing motor density in membrane gliding assays [81]. Furthermore, they showed that an increasing cholesterol

concentration reduced membrane fluidity. Membranes with an increased viscosity enabled reduced motor diffusivity and an increased microtubule transport efficiency and velocity in their experiments [81, 93]. In this study, an increasing cholesterol concentration did not change the kind of microtubule movement in membrane gliding assays. Accordingly, the diffusive movement of microtubules does not seem to be a problem of motor slipping alone (Figure 36A). The hypothesis of a low density of functional motors (Figure 36B), possibly in combination with disturbing, non-functional motors (Figure 36C), remains.

A further problem could be steric hindrances and intramolecular motor inhibitions through missing F-BAR domain interactions. The relevance of F-BAR oligomerization in tubulation processes was indicated in literature studies because the surface coverage of a single F-BAR domain is limited [57, 60, 63]. The vesicle transport assay was used in this study to test a cargo-based transport system with potential F-BAR oligomerization.

4.4.3 The influence of roadblocks on minus end-directed vesicle transport by AtBARK proteins

Cargo vesicles can be generated with various phospholipid compositions. Due to the specificity of several F-BAR proteins to PS [61], vesicles with different phospholipid compositions were tested in binding assays with *AtBARK* proteins (Figure 16). In contrast to the literature, performed experiments did not show an increased specificity of *AtBARK* proteins to PS. Therefore, vesicles with 20 % PS were used for further analyses.

In this study, vesicle assays showed a colocalization of microtubules and vesicles in the presence of *AtBARK* proteins (Figure 17). Variation of the motor concentration in these experiments showed diffusive vesicle motion at a low motor concentration and directed vesicle movement with an increasing motor concentration (Figure 18). Additionally, it was observed that vesicles of different sizes changed their kind of movement with an increasing motor concentration. This suggests that vesicle size and the exact number of bound motors had no influence on the transport. In this case, not only a minimum motor concentration but rather a minimum density or distribution of functional motor is important for directed movement. This conclusion can be supported by the results of Grover et al. [81].

The density effect and the observation of brightly shining, motile *AtBARK1*-GFP signals in growing pollen tubes in this study (Figure 25) support the hypothesis that *AtBARK* motor ensembles performed vesicle transport processes. It has been also shown in the literature that directed transport by minus end-directed, non-processive kinesins requires motor ensembles or motor oligomerization [20, 33, 42]. Complex formation is also known for plus end-directed

kinesins, which are processive and thus able to transport cargo vesicles as single molecules. However, motor ensembles have more power for a faster and prolonged transport [94-97].

Directly transported vesicles moved to the microtubule minus end (Figure 19). This fact proves that *AtBARK* proteins are minus end-directed motor proteins [1, 4, 6, 41]. The mean vesicle transport velocity and run length were comparable for *AtBARK1* ($45 \text{ nm}\cdot\text{s}^{-1}$, 615 nm) and *AtBARK2* ($42 \text{ nm}\cdot\text{s}^{-1}$, 635 nm) in this study (Figure 20). In comparison to many plus end-directed motor proteins, this velocity seems to be slow. However, it is also described in the literature that several minus end-directed kinesin-14 proteins show a slower velocity than plus end-directed motors [16, 98, 99].

It was conspicuous that the vesicle transport stopped at some point during each performed experiment. In order to prolong the run length of motor ensembles, different assay parameters and cargo properties with an effect on the transport efficiency were tested [81, 90, 93]. Although a variation of temperature, salt concentration, and vesicle-membrane viscosity partially showed a small effect on the mean run length in own experiments (Figure 21), vesicle transport still stopped after 600 - 700 nm. A further increase of motor concentration caused an immediate vesicle transport stop. These results refer to a maximum motor density in vesicle transport assays, besides the described minimum motor density, needed for directed movement. If the maximum density was achieved, excessed motors had a negative influence on the vesicle transport velocity and run length. This has been also shown in different literature studies [90, 93, 100, 101]. The negative influence could arise due to ‘traffic jam’, permanent roadblocks, or a combination of both (Figure 37).

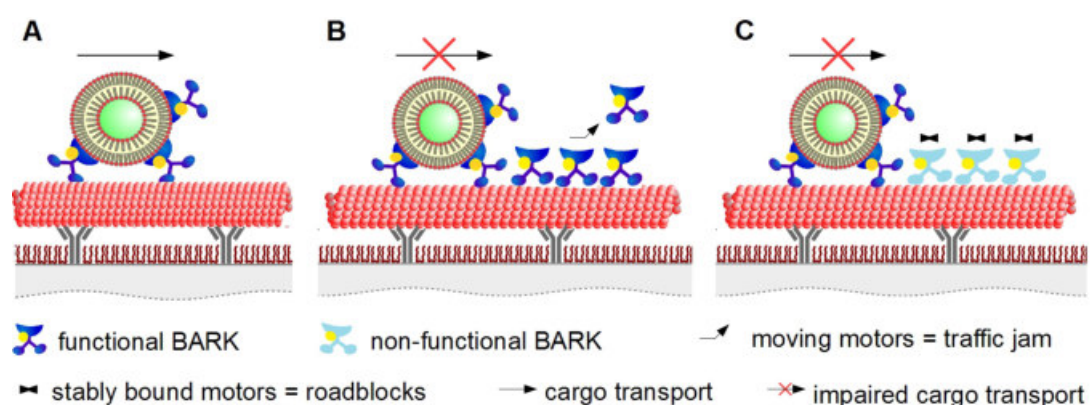


Figure 37: Proposed models for the ‘traffic jam’ and the roadblock effect during vesicle transport assays with *AtBARK* proteins.

(A) Functional vesicle transport assay.

(B) ‘Traffic jam’ during vesicle transport assays is caused by an excess of functional motor proteins, which bind to microtubules. They block tubulin-binding sites, which are probably required by motors that transport cargo molecules along the microtubule.

(C) Motor molecules turn into permanent roadblocks if they are non-functional and enable stable binding to microtubules. Usually, motor proteins, which transport cargo molecules, can circumvent these roadblocks. However, if the concentration of functional or non-functional motors increases they can block most tubulin-binding sites and prevent transport processes.

In the ‘traffic jam’ model, a vesicle transport stop is caused by an excess of functional motors that bind to microtubules (Figure 37B). They block tubulin-binding sites required by motors that transport cargo molecules [93, 94, 101]. If many non-functional motors stably bind to microtubules, they are no longer a part of moving motors in the ‘traffic jam’ but permanent roadblocks (Figure 37C).

It is known that motor proteins operate in crowded environments with the help of molecular properties to deal with roadblocks [101]. Processive motors can pause in front of roadblocks and circumvent them by side steps [94, 101-107]. The probability for pausing or circumvention events is thought to be partially regulated by the flexibility of the neck linker. Therefore, it differs between different processive kinesins [108]. Probably, circumvention mechanisms could be also expected for ensembles of non-processive motors that enable long-distance transport [20, 33, 42]. Nevertheless, molecular properties of *AtBARK* proteins, as well as improved cargo properties, did not prevent a transport stop in performed vesicle transport assays. Therefore, it seems promising that a high concentration of non-functional motors blocked most microtubule-binding sites and stopped the vesicle transport over time. This hypothesis can be supported by stepping assays analyses with a high *AtBARK* concentration. These experiments showed that the whole microtubule was blocked by moving and stably bound molecules over time (Figure 22).

Taken together, an intramolecular *AtBARK* inhibition in gliding, stepping, and membrane gliding assays cannot be completely excluded. However, a major problem of performed *in vitro* assays is probably caused by a high concentration of non-functional motors after purification. Therefore, the expression system should be improved. Although many animal proteins, as well as some plant proteins, were successfully expressed in prokaryotic cells, this system was not promising for the expression of *AtBARK* proteins. Expression tests (Figure 54), expression construct design, and purification with affinity chromatography did not show an improvement in this study. It has to be considered that the prokaryotic expression systems could impair the formation of functional eukaryotic proteins due to the absence of eukaryotic chaperons for folding processes, an early stop of translation, or missing posttranslational modifications [109-111]. Therefore, it might be helpful to use a eukaryotic expression system. A study by Korten et al. [109] analyzed a promising eukaryotic system: insect cells. They showed that kinesin-1, which was expressed in insect cells, had an improved purity, functionality, and long-term stability in comparison with the same protein expressed in bacterial cells. Further tests with this system might improve *AtBARK* functionality after purification. Therefore, it will be tested soon.

Thus far, *in vitro* analyses of this study have shown that minus end-directed *AtBARK1* and *AtBARK2* interact with membranes and microtubules simultaneously and enable directed vesicle transport along microtubules by motor ensembles.

Furthermore, it was interesting to gain an idea of the physiological role of *AtBARK* proteins.

4.4.4 The potential role of *AtBARK* proteins and microtubules during pollen development

Existing gene expression data from *GeneVestigator* (Figure 23) [83, 84] and own β -glucuronidase reporter gene assays (Figure 24) showed a high expression and promoter activity of *bark1* and *bark2* in pollen. Therefore, further analyses of pollen development in *bark* T-DNA insertion lines were performed.

As the project started, three T-DNA lines for both genes (*bark1-1*, *bark2-1* *bark2-2*) were available. During four years of research, new lines became available, which are currently analyzed. Thus far, it was possible to detect phenotypes for homozygous *bark1-1* plants in this study. They showed aborted pollen grains and modifications in pollen tube development (Figure 25). Furthermore, a reduced number of seeds was detected for *bark1-1* plants in this study (Figure 30, 32, 33). It is liable that impaired pollen development also affects silique and seed development. Viable seeds need a coordinated growth of the diploid embryo and the triploid endosperm, as well as a coordinated growth of the seed coat. Each change has an influence on the seed size, which often correlates with the number of seeds [112-114].

According to PCR analyses, which were performed with cDNA of analyzed *bark* T-DNA insertion lines, the *bark1-1* T-DNA insertion line was not a knockout line (appendix: Figure 70). However, it seemed that the T-DNA insertion in the promoter region of *bark1* led to a reduced expression level in the *bark1-1* line. For instance, it could affect the promoter itself or regulatory elements of the promoter. The detailed analysis of the *bark1* expression level in the *bark1-1* line has to be performed by qPCR. However, plants of the *bark1-1* complementation line (generated by Melanie Schulz) did not show any phenotype. This supports the result of a *bark1* knockdown in the *bark1-1* T-DNA insertion line.

In contrast to *bark1-1*, the *bark2-1* T-DNA insertion line did not show the pollen, silique and seed phenotypes in a comparable extent in this study. It has been shown in the literature that proteins with highly similar domain organization and localization did not show the same phenotype [115-117]. This could be explained by different expression levels of the proteins. Interestingly, the expression level of *bark1* in pollen is higher than the expression level of *bark2* (Figure 24). If both proteins have similar functions, *AtBARK1* could assume most processes of *AtBARK2* in single knockout plants of the *bark2-1* line. Therefore, no

pronounced phenotypes occurred. By contrast, *AtBARK2* could possibly not assume all processes of *AtBARK1* in single knockout plants of the *bark1-1* line. Therefore, specific phenotypes were detected in this study (Figure 25, 29, 30).

Taken together, *bark1-1* plants showed pollen phenotypes, which should be discussed. The aborted pollen grains looked smaller and bulky and did not germinate in comparison with the pollen of segregating wild-type plants (Figure 25). Other *bark1-1* pollen grains, which had a shape like wild-type pollen, partially developed pollen tubes with swelling tips or vesicle accumulation around the growing pollen tube (Figure 25). There are different components and signaling pathways, which have an influence on development and germination of pollen grains. Mutations, which change cell wall composition [118, 119], tryphine composition [120-122], or subunits of the TPLATE complex [123, 124], often lead to poor germination rates and partially or completely sterile plants. One example of the strong influence of aforementioned factors on pollen development in the literature relates to TML mutations. TML is a subunit of the TPLATE complex and important for the clathrin-dependent endocytosis. If this complex is affected by mutations, it often results in the formation of unviable pollen [124]. It seems to be interesting to gain a closer insight into the process of pollen tube growth.

The angiosperm pollen tube is highly polarized and elongates to form a cellular channel for the transport of the sperm cells from the pollen grain to the embryo sac for double fertilization [39, 125]. The growing pollen tube is sub-divided in the shank near the pollen grain, the sub apex, and the apex/ clear zone at the pollen tube tip [126, 127]. Polarization, tip growth, and transport processes in the vegetative cell are influenced by different processes. In a first step, the cytoskeleton is reorganized. Microtubules and actin fibers show a longitudinal orientation in the shank, an actin fringe in the sub apex, and a dynamic network of actin filaments and microtubules in the apex [38, 127, 128]. Furthermore, myosins interact with actin filaments and generate cytoplasmic streaming through ATP hydrolysis. The cytoplasmic streaming is - among others - necessary for the transport of vesicles and organelles [39, 126, 127]. The mechanism of tip growth requires exocytosis in the apical tip region. Secretory vesicles fuse with the apex membrane and release material for further tube elongation [125, 127, 129-131]. The growth direction is - among others - regulated by membrane-binding proteins, which modulate cellulose synthesis and cell wall deposition [125, 127, 131-133]. Exocytosis provides more membrane lipids than needed for the regular growth process. Therefore, the membrane excess is recycled by endocytosis and transport processes of endocytotic vesicles to degradation or recycling areas [125-127, 134, 135]. This brief overview shows that pollen

tube growth is regulated by different processes. At least one of them has to be disturbed to obtain results like the tip swelling and the vesicle accumulation phenotypes in this study.

In order to obtain a hint, which process might be disturbed, it has to be considered that *AtBARK1* and *AtBARK2* contain an F-BAR domain that binds and deforms membranes [37, 40, 53, 55, 57, 58]. Furthermore, both of them are kinesins, which are known as microtubule-binding proteins [1, 4, 6]. Therefore, it is interesting to find processes during pollen development, which require membrane deformation and microtubule-based interactions.

In order to analyze the role of microtubules in pollen development, pollen can be treated with microtubule polymerization inhibitors. Oryzalin, a dinitroaniline herbicide, is a highly potent microtubule polymerization inhibitor in plants. It forms reversible tubulin-oryzalin complexes, which prevent further microtubule polymerization and thus support their depolymerization [86-88]. These dynamic changes affect the ordinary microtubule organization. The phenotype, which was detected during oryzalin treatment of *A. thaliana* Col-0 pollen in this study (Figure 28), was similar to the phenotype of the *bark1-1* mutant pollen (Figure 25). The pronounced tip swelling and vesicle accumulation support the hypothesis that microtubules and microtubule-associated *AtBARK* proteins are important effectors involved during pollen tube formation.

The role of microtubules and microtubule-binding proteins in pollen development is discussed controversially in the literature [38, 39, 136]. It is known that both of them occur in growing pollen tubes of *A. thaliana*. They are localized at different areas, indicating different functions [38, 39]. Previous studies have apportioned microtubules and kinesins a role during dynamic transport processes like the positioning of the generative cell and the vegetative nucleus [39, 137-139], pulsatory growth [39, 140], and the accumulation of vacuoles in the pollen tube [39, 141]. Further studies proposed a role in the regulation of pollen tube growth direction through localization and activity regulation of the callose and cellulose synthesis [38, 132, 133]. These functions are not sufficient to explain the *bark1* phenotypes found in this study (Figure 25). The vesicle accumulation rather indicates a problem of membrane excess in the tip, which is normally regulated by endocytosis and vesicle transport processes to degradation or recycling areas [126, 127, 134].

However, many literature studies assume that actin filaments and myosins play the major role in endomembrane traffic to the growth region and degradation areas of pollen tubes [39, 135, 142-144]. This hypothesis is mainly based on actin inhibitor studies. Experiments of these studies showed that organelle and vesicle transport-dependent processes like cytoplasmic streaming and pollen tube growth were strongly affected by actin inhibitors [135, 144-148].

Additionally, a study by Moscatelli et al. [149] identified endocytosis internalization pathways in tobacco pollen tubes with different sensitivity to latrunculin B (actin-polymerization inhibitor). Their experiments indicate an actin involvement in endocytosis. Certainly, the role of the cytoskeleton and its connection to vesicles during secretion and endocytosis in the apex is not known in detail [125, 135, 144]. These facts leave room for studies opening the discussion about microtubule and microtubule-associated protein involvement during intracellular transport and endocytosis in pollen tubes [38, 39, 42, 125, 135, 143].

Similar to actin-binding myosins, microtubule-binding kinesins interact with organelles and vesicles purified from tobacco [39] or mosses [42] and transport them along microtubules *in vitro*. Further literature experiments concerning organelle transport on microtubules and actin filaments in tobacco showed a functional cooperation between actin filaments, microtubules, and their connected proteins during transport processes. This cooperation was hypothesized as a velocity-regulating process for exact organelle and vesicle positioning [38, 39, 135, 136, 150-155]. If vesicle transport or vesicle positioning are interrupted during pollen tube growth, tip swelling and vesicle accumulation could be a possible reaction. However, the vesicle accumulation would be expected within the pollen tube and not around the pollen tube, as shown in this study. The phenotype of vesicle accumulation within the pollen tube of *A. thaliana* has been described in the literature. A double knockout of KCBP and one of its suppressors (*suz1*) showed reduced pollen germination and deformed pollen tubes with an accumulation of numerous ‘spherical bodies’ in the pollen tube. This phenotype was hypothesized as being the result of incorrectly running transport or exocytosis processes [156]. Therefore, a vesicle accumulation around the pollen tube, as shown in this study, could indicate an involvement of *AtBARK* proteins during a related process: endocytosis. This hypothesis is supported by the facts that endocytosis deals with membrane transformation and is connected to different BAR and F-BAR proteins at various time points in eukaryotic organisms [55, 57, 157, 158]. The analyzed *AtBARK* proteins contain an F-BAR domain, which also interacts with vesicle membranes *in vitro* (Figure 17).

In plant cells, many endocytotic processes are carried out by clathrin-mediated endocytosis (CME). CME is divided into five steps starting with the nucleation [115, 126, 159, 160]. The ancestral adaptor complex TPLATE interacts with the membrane, adaptor protein 2 (AP2), clathrin, proteins with ANTH domains, and dynamin-related proteins to initiate and advance CME [53, 115, 123, 124, 161]. In the next step, cargo molecules were selected depending on endocytotic sorting signals (e.g. linear amino acid motifs, conformational motifs, posttranslational modifications) [115, 162]. After cargo selection, clathrin-coated pits are

formed, which enable membrane stabilization and recruiting of proteins for membrane invagination [115, 163]. Membrane fission starts with the recruitment of dynamin through the TPLATE subunits TASH3 and TML. Both subunits assemble into multimeric helical arrays located at the neck of the clathrin-coated pits. Dynamin constricts the endocytotic vesicle through GTP hydrolysis and with the help of further proteins [115, 164]. Membrane fission is followed by the destruction of the clathrin coat with the help of SH3P1 an auxilin-like protein and recruited heat shock proteins. After this process, endocytotic vesicles fuse with the trans-Golgi network and multivesicular endosomes for sorting and recycling processes. Degradation mostly occurs in the vacuole [115].

Comparing the CME of plants with other organisms like yeast or animals, there are many similarities but also some differences. For instance, the function of the TPLATE complex in plant systems is adopted by the AP2 complex in animal or yeast systems. Therefore, the AP2 complex is essential for the initial nucleation [70, 115]. Mutations in this complex often have a fatal outcome in animals, while in plants the cells remain viable [165-167]. A further difference relates to sorting, degradation, and recycling processes. In plant systems, sorting and recycling processes are performed by the trans-Golgi network and multivesicular endosomes. The vacuole enables degradation pathways. By contrast, these processes are enabled by early and late endosomes or lysosomes in yeast and animal systems [115]. Therefore, it is possible to compare proteins and processes in-between these systems for possible working hypotheses, but it has to be considered with caution.

Research concerning localization and function of F-BAR proteins in endocytosis in yeast and animal systems is advanced in contrast to plant systems. FCHo proteins, which contain an F-BAR domain [64], are known as activators for the AP2 complex [70, 115]. In addition, they are described as clathrin-coated pit nucleators due to their binding at slightly curved membranes for further protein recruitment and deepening of the membrane curvature [68]. Other F-BAR proteins like the FBP17/ Toca-2 and the CIP4/ Toca-3 bind after the formation of the clathrin-coated pit and oligomerize to support further membrane curvature, stabilization, and deformation [53, 57, 61]. Their SH3 domain also binds dynamin, which is important for membrane fission [53, 57, 61]. Similar to these examples, *AtBARK1* and *AtBARK2* could be two of these F-BAR proteins involved in vesicle formation during endocytosis in *A. thaliana*.

4.4.5 Proposed model for *AtBARK* involvement during endocytosis in angiosperm pollen tube development

Here, two hypotheses concerning *AtBARK*'s function and localization in specific endocytotic stages are proposed (Figure 38).

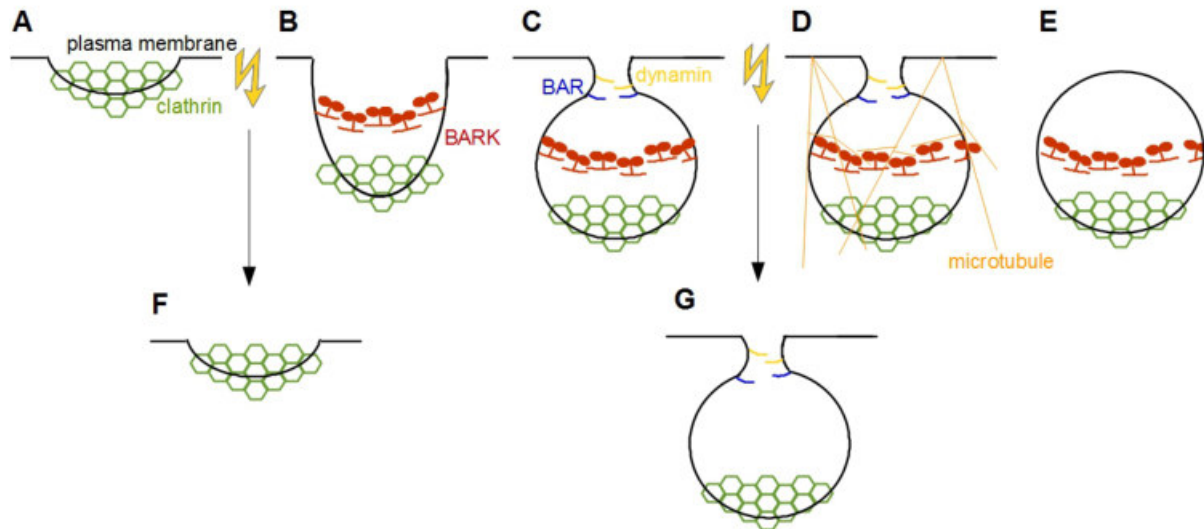


Figure 38: Proposed model for the involvement of *AtBARK* proteins during endocytosis.

(A) Formation of the clathrin-coated pit.

(B) Formation of the endocytotic vesicle due to further membrane invagination.

(C, D) Fission of the endocytotic vesicle with the involvement of BAR proteins and dynamin.

(E) Release of the endocytotic vesicle.

(F) *AtBARK* could be mainly involved in membrane invagination (B). The absence of *AtBARK* proteins in this stage might terminate further membrane curvature.

(G) *AtBARK* could be mainly involved in vesicle separation from the membrane through microtubule interactions (D). The absence of *AtBARK* proteins and/ or microtubules in this stage might interrupt complete vesicle release.

In the first hypothesis, *AtBARK* proteins are mainly necessary to intensify membrane curvature of clathrin pits. In the absence of *AtBARK* proteins, the membrane undergoes structural changes through the formation of clathrin-coated pits. However, further membrane curvature and vesicle formation might be impaired. Therefore, endocytosis is interrupted briefly after initiation (Figure 38F). Despite this interruption, exocytotic vesicles fuse with the membrane to provide material for the pollen tube growth. The excess of membrane lipids, which cannot be prevented by impaired endocytosis, could lead to tip swelling and external lipid vesicle release.

In the second hypothesis, *AtBARK* proteins provide membrane curvature together with other proteins at the beginning of endocytosis. However, they are mainly necessary to separate vesicles from the plasma membrane in a later stage. It was shown by colocalization experiments that dynamin, BAR proteins, and actin play a role in membrane fission in yeast and animals [57, 61, 69, 168-172]. If microtubule-binding F-BAR proteins like *AtBARK1/2* are involved in this process in *A. thaliana*, they possibly support or replace the role of actin.

This means that they could pull vesicles from the membrane due to microtubule interactions. Based on this hypothesis, the absence of microtubules or interacting *AtBARK* proteins could prevent vesicle separation from the membrane (Figure 38G). Furthermore, the excess of membrane lipids could cause tip swelling or external lipid vesicle release in the pollen tube tip.

The general hypothesis of microtubule involvement in controlling processes of exo- and endocytosis in pollen tube tips is supported by an inhibitor study by Idilli et al. [125]. They showed that impaired microtubule dynamics in tobacco negatively affected plasma membrane internalization at the tip and the migration of endocytotic vesicles from the apex to the shank. Another interesting point mentioned in that study considers the location of endocytosis. Several models of tip growth in pollen tubes suggest that exocytosis and growth occur at the pollen tube tip, while endocytosis occurs in the shank [173]. However, recent studies indicate that exocytosis occurs in the sub-apical region and endocytosis occurs in the shank and in the apex of the pollen tube of tobacco and lily [125, 126, 129, 130, 134, 174, 175]. In the apex, the endocytosis rate is not as high as in the shank. Nevertheless, small vesicles are formed, constricted, and recycled there [125, 126, 130, 134, 173, 174, 176].

Both hypotheses proposed in this study and the question of whether *AtBARK* proteins are involved during endocytosis in the tip or in the shank could be checked by localization studies in *A. thaliana*. Colocalization of *AtBARK* proteins and microtubules with CME components like the TPLATE complex, clathrin, or dynamin could show whether *AtBARK* involvement is necessary for membrane deformation in early endocytosis or for vesicle separation in later steps. The participation of *AtBARK* proteins during endocytosis in the shank or in the tip could be further analyzed by *in vivo* localization of *AtBARK1/2*-GFP expressed under its own promoter. Moreover, analyzes of microtubule dynamics during inhibitor studies in Col-0 or in *bark* T-DNA insertion lines - containing fluorescence marked microtubules - might be helpful. Some of these aforementioned experiments remain in progress.

4.4.6 Conclusion

In this study, two novel *Atkinesin-14* motors with an F-BAR domain were characterized for the first time. The implementation of different *in vitro* assays showed that *AtBARK1* and *AtBARK2* are minus end-directed motor proteins that bind vesicles and transports them along microtubule tracks with the help of motor ensembles. These properties, the high expression in pollen, and the described pollen, silique, and seed phenotypes of a *bark1* T-DNA insertion line support the hypothesis that *AtBARK* proteins are involved in endocytosis during pollen tube development.

5 A novel microtubule segregating kinesin in *Arabidopsis thaliana*

5.1 Introduction

The kinesin-14 class is the largest kinesin subfamily in *A. thaliana* [1, 4, 6, 43]. According to the classical description of the kinesin-14 family by Lawrence et al. [43], members should be minus end-directed proteins with a C-terminal motor domain.

Most publications analyzing these minus end-directed kinesin-14 proteins with a C-terminal motor domain in different organisms indicate an involvement in cell division [11, 16, 32, 42, 50, 51, 177-179]. The mitotic spindle is a microtubule-based, bipolar machinery for mitosis and meiosis in eukaryotes [50, 180]. Its function and organization depend - among others - on a balance of complementary and antagonistic forces of different motor proteins [32, 177, 180]. Some of these motors are kinesin-14 members, which use different mechanisms to enable spindle dynamics. They crosslink microtubules or slide them either against each other in the spindle midzone to generate an inward force that pulls spindle poles together, or against other structures like the cell cortex for focusing microtubules at the pole regions [32, 50, 51, 177, 180]. In contrast to various other organisms, plants show differences concerning mitotic mechanisms and participating motors. For instance, flowering plants lack centrosomes and microtubule minus end-directed dyneins [20, 177, 181]. In addition, preprophase band, phragmoplast, and cell plate formation occur during plant mitosis and cytokinesis [32, 177, 182, 183]. Therefore, it is supposed that minus end-directed *At*kinesin-14 proteins have a special role during cell division. ATK1 and ATK5 are two examples of minus end-directed C-terminal kinesin-14 proteins in *A. thaliana*, which take part in the alignment of microtubules by regulating the spindle length, width, and integrity [50-52]. Their rice homolog *OsDLK* is also expressed during mitosis, where it was repartitioned between spindle and phragmoplast. Experiments for *OsDLK* characterization were performed during a cooperation project with Prof. Dr. Peter Nick from Karlsruhe Institute of Technology. The results have been published in 'Scientific Reports' (Paper see appendix).

As mentioned at the beginning, the classical description of the kinesin-14 family does not fit to all members of the *At*kinesin-14 family [43]. Structural analyses showed that many of these kinesins have further characteristic domains and partially different domain organizations [1, 5, 6]. Although these motors are not studied well in *A. thaliana* thus far, some of them have specific tails, which provide a hint for possible motor functions.

The kinesin-14 members *AtBARK1* and *AtBARK2*, for example, contain an internal motor domain flanked by two coiled-coil domains and an F-BAR domain as cargo-binding site. According to literature studies and own analyses in *A. thaliana* (**Chapter 4**), F-BAR domains have membrane sensing, binding, and deforming properties with functions in endocytosis [37, 40, 53, 55, 57, 58].

Seven further *Atkinesin-14* members (KCHs) contain an internal motor domain and an actin-binding calponin homology domain. KCH proteins are partially characterized in plant organisms like cotton, tobacco, and rice [34, 184-188]. As a side project during this thesis, the rice kinesin-14 *OsKCH1* was analyzed. The experiments showed that *OsKCH1* is a minus end-directed, non-processive motor, which transports actin filaments along microtubules with two distinct velocities. The respective velocity depends on the relative orientation of the actin filament on the microtubule. These results, which indicate for a role in the orientation of the cytoskeleton, were published in Nature Plants (Paper see appendix) [34]. There is only little information about KCHs in *A. thaliana*. However, it is possible that their function is also connected to the cytoskeletal organization. Schneider et al. [184] assumed a function during gametophyte or floral development for five KCH genes and a role in vascular tissue development or secondary cell wall formation for two KCH genes. These hypotheses were based on gene expression data analyses.

These examples show that surveying, existing structural characteristics and homolog proteins in other organisms can be helpful starting points for protein characterization and subsequent connection to physiological functions.

Besides these members, there are also two *Atkinesin-14* genes (*misk1*: *At1g5550*, *misk2*: *At5g27950*), which encode for plant-specific motors with characteristics of a non-processive, minus end-directed kinesin-14 with an N-terminal motor domain (*AtMISK*). In the literature, only plus end-directed motors are described with an N-terminal motor domain to date [43]. According to missing information about specific tail domain functions, it is difficult to establish hypotheses concerning biophysical properties and the physiological role of *AtMISK*. However, the peculiar motor domain localization offers a good incentive for an *in vitro* and *in vivo* characterization of *AtMISK* proteins.

5.2 Results of the *in silico* and *in vitro* experiments

5.2.1 *misk1* and *misk2* show a similarity in gene organization

The gene organizations of *misk1* (*At1g55550*) and *misk2* (*At5g27950*) were generated on gene information obtained from TAIR (The Ohio State University [73]) (Figure 39A, B).

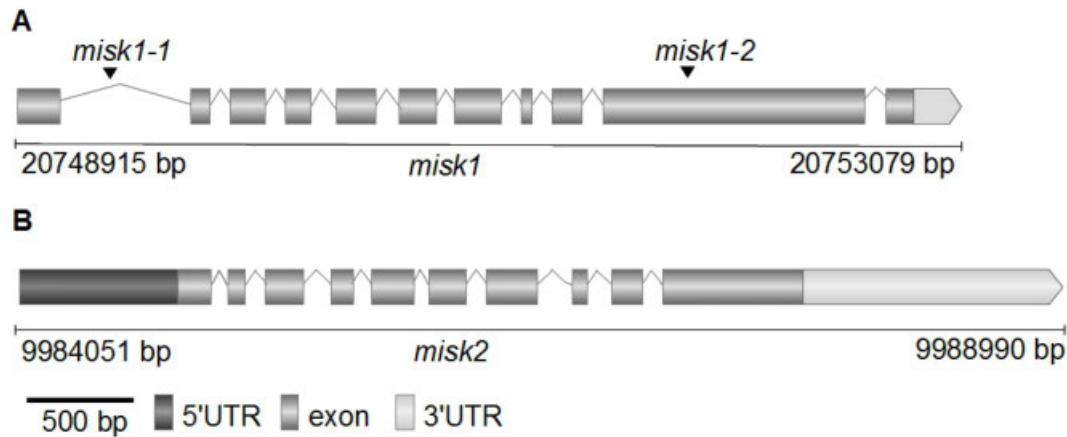


Figure 39: Gene organization of *misk1* and *misk2*.

The gene organizations of *misk1* (*At1g55550*) (A) and *misk2* (*At5g27950*) (B) were generated on gene information obtained from TAIR (The Ohio State University [73]) and marked with experimentally relevant T-DNA insertion lines.

Comparing the gene structures of *misk1* and *misk2*, a resemblance of gene organization was found. According to an amino acid similarity comparison over 416 amino acids with the EMBOSS Matcher (EMBL-EBI) [74], *misk1* and *misk2* have an amino acid sequence identity of 45 % and an amino acid sequence similarity of 67 %. Based on the amino acid sequence different algorithms (DELTA-BLAST algorithm, National Library of Medicine, USA [76]; ExPASy COILS algorithm [77]) were used to identify specific *AtMISK* domains (Figure 40).



Figure 40: Structural features of *AtMISK* proteins.

General domain structure of *AtMISK* proteins based on their amino acid sequences.

Besides the coiled-coil domain, only the N-terminal kinesin-14 motor domain was found as a defined structure for both proteins. The structure and function of the C-terminal tail domain are unknown thus far (Figure 40).

5.2.2 Expression and purification of *AtMISK1* for *in vitro* analyses

The *in vitro* characterization of *AtMISK1* was performed with two constructs: *AtMISK1*(aa3-462)-EGFP-6xHis comprising the N-terminal motor domain and the following coiled-coil domain sequences and *AtMISK1*(aa3-415)-EGFP-6xHis comprising the motor domain sequence. An EGFP-6xHis-tag was C-terminally fused to both constructs for motor visualization and purification (Figure 41).

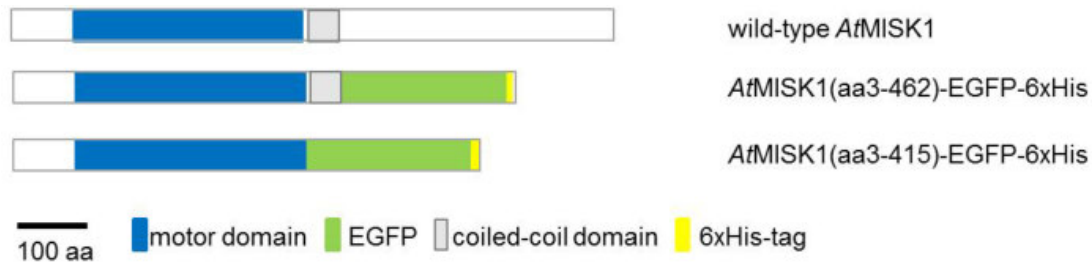


Figure 41: Schematic representation of the domain organization in wild-type *AtMISK1* and in the recombinant expression constructs used for *in vitro* characterization.

The *AtMISK1* wild-type protein has a sequence of 859 amino acids with an N-terminal motor domain followed by a coiled-coil domain. One construct of *AtMISK1* contains the sequence of the N-terminal motor domain (aa3-415), the second one additionally the sequence of the coiled-coil domain (aa3-462). An EGFP-6xHis-tag was C-terminally fused to both constructs for motor visualization and purification.

The expression constructs (Figure 41) were transformed into different *E.coli* strains for an expression test. This test showed the best expression results in *E.coli* BL21(DE3) pRARE cells with expression conditions listed in Table 16. Both constructs were expressed, and purified by affinity chromatography. The purification fractions were analyzed by SDS-PAGEs. The gels were stained with colloidal Coomassie (Figure 42).

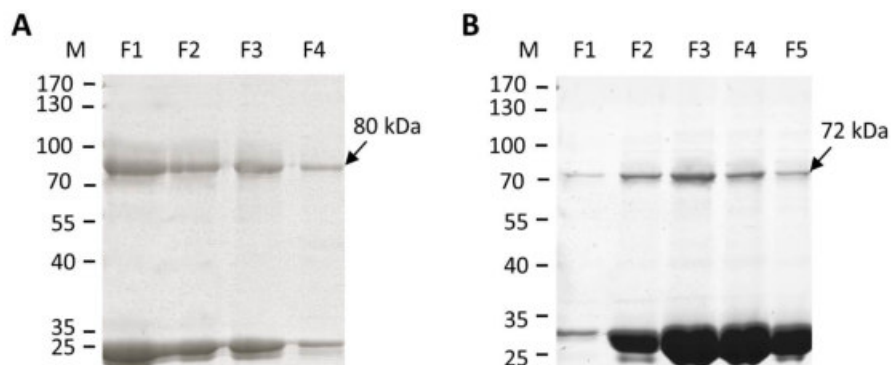


Figure 42: SDS-PAGEs of the protein purification fractions after affinity chromatography for *AtMISK1*.

Both proteins were expressed and purified, proved by a protein band on the right marker level (black arrow):

AtMISK1(aa3-462)-EGFP-6xHis (A, 80 kDa), *AtMISK1*(aa3-415)-EGFP-6xHis (B, 72 kDa).

A second strong protein band was detected at 25-30 kDa, which could correspond to EGFP fragments. (Legend: M = marker, F1-F5 = elution fractions 1-5).

The Coomassie gels showed a strong protein band for each construct on the right marker level (Figure 42). Additionally, a second strong band was detected at 25 - 30 kDa, which might correspond to EGFP fragments. Purified proteins were used for further *in vitro* analyses.

5.2.3 The minus end-directed *AtMISK1* transports microtubules with a distinct velocity

The gliding assay was used to determine the velocity and direction of protein movement [78-80]. Experiments were performed in flow cells constructed as described before (see 4.2.3). The interactions of fluorescence-labeled microtubules with immobilized *AtMISK1*(aa3-462)-EGFP-6xHis were detected by epifluorescence microscopy (Figure 43A).

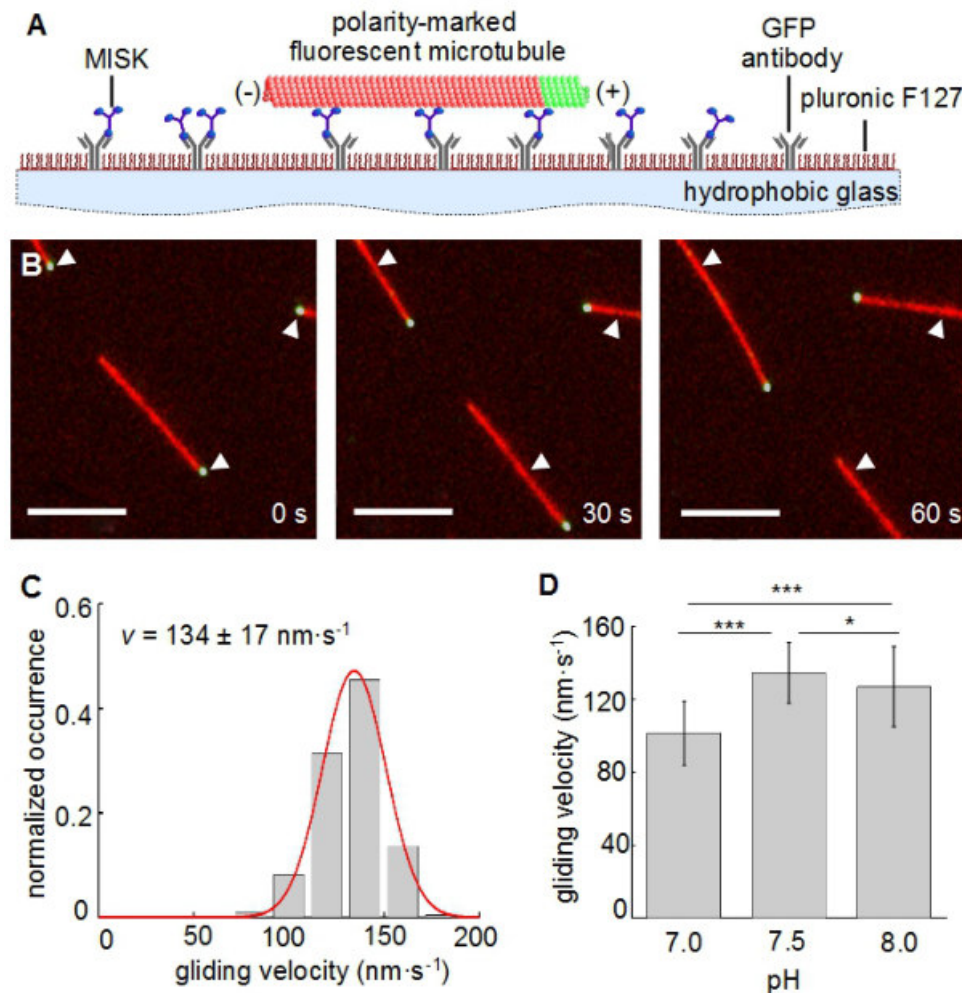


Figure 43: Gliding assay and velocity analyses of *AtMISK1*.

(A) Schematic representation of a gliding assay with *AtMISK1*. The interactions of fluorescence-labeled microtubules with immobilized motors were detected by epifluorescence microscopy.

(B) Time-lapse imaging of a gliding assay with *AtMISK1*(aa3-462)-EGFP-6xHis. Microtubules (red) were transported in the direction of the polarity-marked plus end (gray) by *AtMISK1*. Therefore, *AtMISK1* was identified as a minus end-directed motor. The starting position of each microtubule was marked by white arrowheads.

(C) Histogram of the mean transport velocity for 220 microtubules transported by *AtMISK1*(aa3-462)-EGFP-6xHis at pH 7.5. A mean transport velocity $134 \pm 17 \text{ nm}\cdot\text{s}^{-1}$ (mean \pm s.d.) was measured.

(D) Velocity analyses of *AtMISK1*(aa3-462)-EGFP-6xHis gliding assays at different pH values: $v_{\text{pH } 7.0} = 101 \pm 18 \text{ nm}\cdot\text{s}^{-1}$ (mean \pm s.d., N = 95), $v_{\text{pH } 7.5} = 134 \pm 17 \text{ nm}\cdot\text{s}^{-1}$ (mean \pm s.d., N = 220), $v_{\text{pH } 8.0} = 127 \pm 22 \text{ nm}\cdot\text{s}^{-1}$ (mean \pm s.d., N = 121).

Gliding assays showed that *AtMISK1* propelled 100 out of 107 microtubules with a leading polarity-marked plus end. Therefore, *AtMISK1* was identified as a minus end-directed motor (Figure 43B). The gliding performance was analyzed under different buffers conditions. From

pH 7.0 up to pH 8.0 directedly transported microtubules were detected. Lower pH values led to stably bound microtubules, while higher pH values caused a substantially decreased binding efficacy of microtubules. Microtubules were tracked with FIESTA [82] and the gliding velocities were evaluated with MATLAB (Figure 43D). The best gliding conditions were observed at pH 7.5 with $134 \pm 17 \text{ nm} \cdot \text{s}^{-1}$ ($N = 220$, Figure 43C). Therefore, these conditions and parameters were adopted for following analyses.

5.2.4 *AtMISK1* shows diffusive and non-processive interactions with microtubules

The stepping assay was used to characterize the velocity, direction, and processivity of single molecule movement [78, 80]. Experiments were performed in flow cells constructed as described before (see 4.2.3). The interactions of fluorescence-labeled *AtMISK1*(aa3-462)-EGFP-6xHis with immobilized, fluorescence-labeled microtubules were detected by TIRF microscopy (Figure 44A).

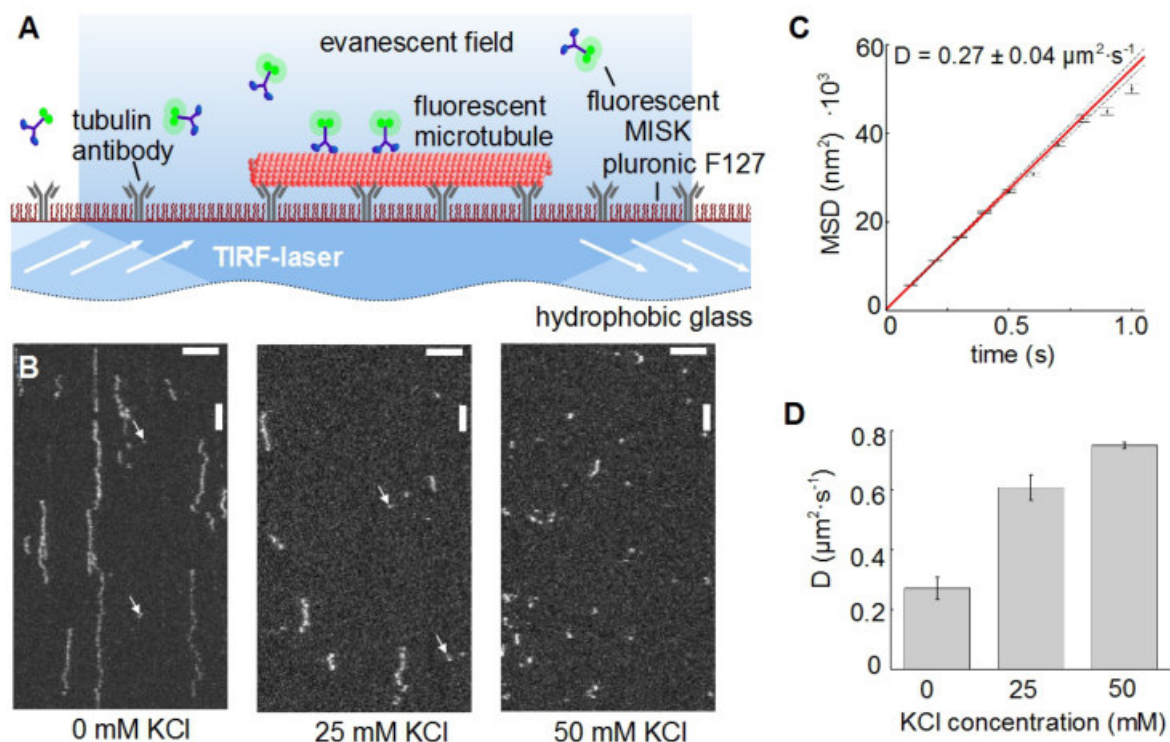


Figure 44: Stepping assay and diffusion analyses of *AtMISK1*.

(A) Schematic representation of a stepping assay with *AtMISK1*. The interactions of fluorescence-labeled motors with immobilized, fluorescence-labeled microtubules were detected by TIRF microscopy.

(B) Kymographs of *AtMISK1*(aa3-462)-EGFP-6xHis in stepping assays with 0 mM, 25 mM, and 50 mM KCl. At low salt concentration (0 mM KCl), many diffusing and some transient (white arrowheads) interactions were visible. With an increasing salt concentration, the interaction period between diffusing molecules and microtubules decreased (horizontal scale bar = 5 μm , vertical scale bar = 60 s).

(C) The MSD data of *AtMISK1*(aa3-462)-EGFP-6xHis stepping assays with 0 mM KCl could be linearly fitted.

(D) The diffusion coefficient of *AtMISK1*(aa3-462)-EGFP-6xHis in stepping assays increased with an increasing salt concentration: $D_{0\text{mM KCl}} = 0.27 \pm 0.04 \mu\text{m}^2 \cdot \text{s}^{-1}$ ($N = 1089$), $D_{25\text{mM KCl}} = 0.61 \pm 0.04 \mu\text{m}^2 \cdot \text{s}^{-1}$ ($N = 2262$), $D_{50\text{mM KCl}} = 0.75 \pm 0.01 \mu\text{m}^2 \cdot \text{s}^{-1}$ ($N = 989$) (mean \pm s.d.).

The kind of interaction between *AtMISK1* and microtubules was analyzed by kymographs (Figure 44B). The buffer, which was used for the experiments, contained 4 mM MgCl₂. At low salt concentration - without additional KCl (0 mM KCl) -, many diffusive and some transient motor interactions were detected (Figure 44B, left). With an increasing salt concentration (25 mM and 50 mM KCl), the interaction period between diffusing motors and microtubules decreased (Figure 44B, middle, right). Molecules were tracked with FIESTA [82]. Further, MSD analyses at different salt concentrations were performed with MATLAB to prove the kind of movement and calculate the diffusion coefficient. The linearly fitted MSD data plots for 0 mM, 25 mM, and 50 mM KCl clearly proved the diffusive nature of most observed interactions (Figure 42C). The diffusion coefficient increased with increasing salt concentration (Figure 44D). These results showed that *AtMISK1* dimers enabled diffusive and non-processive motor-microtubule interactions.

In a next step, the construct *AtMISK1*(aa3-415)-EGFP-6xHis, which only contains the motor domain, was analyzed in stepping assays (Figure 45A). Due to the missing coiled-coil domain, the proteins existed as monomers to analyze whether diffusive and transient interactions were caused by single motor heads, too.

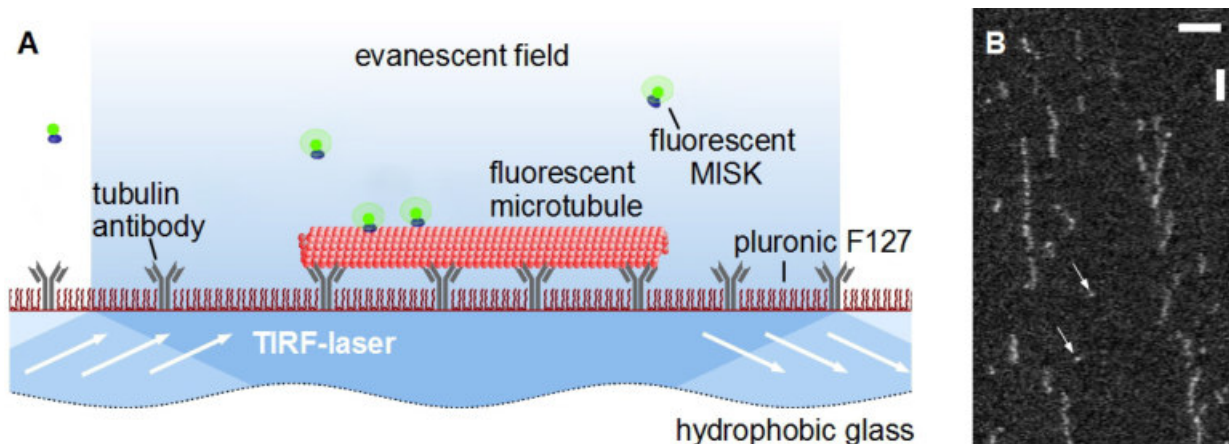


Figure 45: Stepping assay and diffusion analyses of *AtMISK1* monomers.

(A) Schematic representation of a stepping assay with *AtMISK1* monomers.

(B) Kymographs of *AtMISK1*(aa3-415)-EGFP-6xHis in stepping assays. Diffusive and some transient (white arrowheads) motor interactions were detected (horizontal scale bar = 5 μm, vertical scale bar = 60 s).

The kymographs of *AtMISK1* monomers showed similar results as the kymographs of *AtMISK1* with its dimerization domain: many diffusive and some transient motor interactions on microtubules (Figure 45B). These results showed that single motor heads enabled both kinds of interactions.

5.2.5 *AtMISK1* crosslinks or slides microtubules along each other dependent on microtubule polarity

As *AtMISK1* - without its tail domain - enabled two kinds of microtubule interactions, it was tested whether it crosslinks microtubules. Therefore, sliding assays were performed. The flow cells for the experiments were constructed as described before (see 4.2.3). The interactions of fluorescence-labeled cargo- and template-microtubules with *AtMISK1*(aa3-462)-EGFP-6xHis were analyzed by epifluorescence microscopy (Figure 46A).

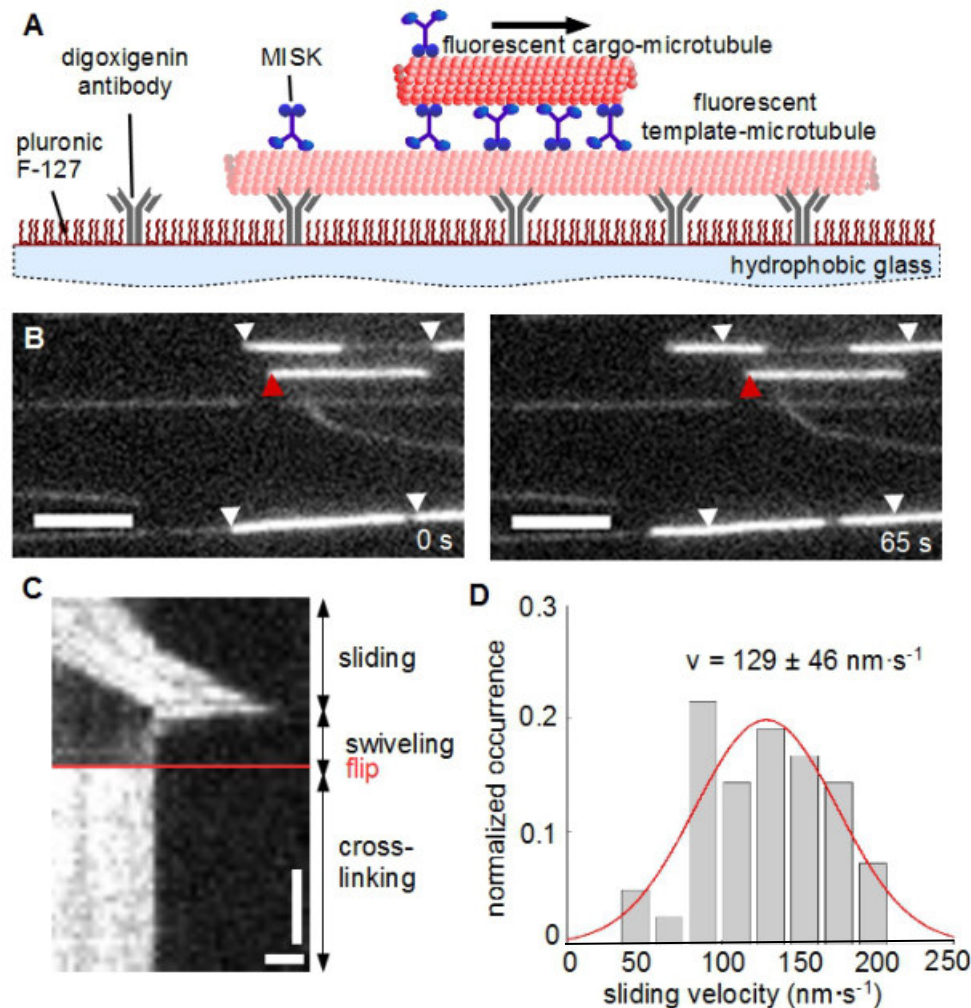


Figure 46: Sliding assay and velocity analysis of *AtMISK1*.

(A) Schematic representation of a sliding assay with *AtMISK1*. The interactions of fluorescence-labeled cargo- and template-microtubules with motors were analyzed by epifluorescence microscopy

(B) Time-lapse imaging of sliding assays with *AtMISK1*(aa3-462)-EGFP-6xHis. Two distinct populations of motor-microtubule interaction were detected: in population one, microtubules (gray) slid along each other (white arrowheads); in population, two microtubules were stably crosslinked (red arrowheads, scale bar = 5 μm).

(C) Kymograph of a flipping cargo-microtubule during a sliding assay with *AtMISK1*(aa3-462)-EGFP-6xHis. The cargo-microtubule was transported along the template-microtubule by *AtMISK1* in the upper part of the picture. After the flip, the cargo-microtubule transport was stopped due to stable crosslinking on the template-microtubule (horizontal scale bar = 1 μm , vertical scale bar = 30 s).

(D) Histogram for 42 cargo microtubules transported by *AtMISK1*(aa3-462)-EGFP-6xHis in sliding assays at pH 7.5. A velocity of $129 \pm 46 \text{ nm}\cdot\text{s}^{-1}$ was measured (mean \pm s.d.).

The sliding assays showed that *AtMISK1* - without its tail domain - interacted with template- and cargo-microtubules simultaneously. Concerning the kind of interaction between motors and microtubules, two different populations were detected. On one hand, *AtMISK1* slid the microtubules along each other and on the other hand, it stably crosslinked microtubules without sliding activity (Figure 46B). In some experiments, flipping cargo-microtubules were observed (Figure 46C). In the beginning, these flipping cargo-microtubules were transported over the template-microtubules. When they reached the end of the template-microtubule, their ends remained fixed, while their main parts swiveled a few minutes until they were inversely and stably bound at the same template-microtubule again. This phenomenon indicated that the aforementioned populations of slid and crosslinked microtubules were linked to the different microtubule polarities.

Additionally, microtubules were detected with FIESTA [82] and the transport velocity was analyzed with MATLAB. The microtubules were transported with $129 \pm 46 \text{ nm}\cdot\text{s}^{-1}$ (mean \pm s.d., N = 42, Figure 46D), which approximately corresponded to the observed gliding velocity of *AtMISK1* (Figure 43C).

5.3 Results of the *in vivo* experiments

5.3.1 *misk1* is strongly expressed in the vascular tissue of growing roots

The expression pattern of genes can provide information on their physiological role. In order to visualize the tissue-specific promoter activity of *misk1*, β -glucuronidase staining was performed. Therefore, the *misk1* promoter was cloned into a vector in front of the β -glucuronidase gene (appendix: Figure 66). The resulting vector was transformed into Col-0 plants through *A. tumefaciens*. A successful transformation was proven by PCR analyses (appendix: Figure 67). The *misk1* promoter activity was observed (Figure 47).

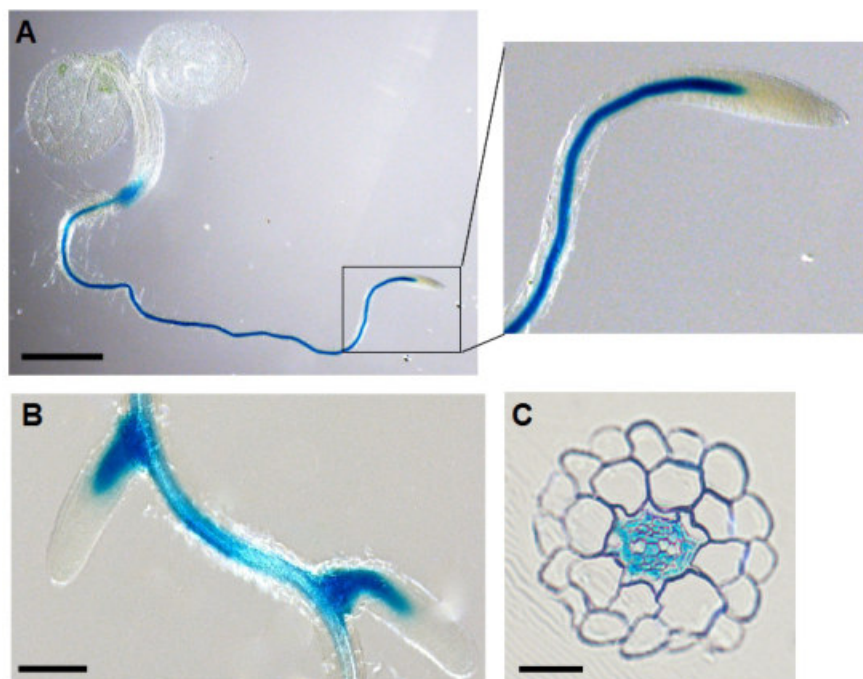


Figure 47: Macroscopic and microscopic imaging of β -glucuronidase activity under *misk1*-promoter control.

β -glucuronidase staining of five- to seven-days-old seedlings, which contained the pMDC162-MISK1-GUS construct.

(A) Five-days-old seedlings showed a strong blue staining of the vascular tissue in the root (scale bar = 500 μ m).

(B) Seven-days-old seedlings showed the same staining pattern. Additionally, a blue staining of the vascular tissue in the initial developing side roots was detected (scale bar = 100 μ m).

(C) Cross sections of the stained roots proved that only the vascular tissue was stained (scale bar = 25 μ m).

For the analyses of *misk1* promoter activity, seedlings of five independent successfully transformed plant lines were stained. Five-days-old seedlings showed a consistent and distinct staining of the vascular tissue in growing roots (Figure 47A). In seven-days-old seedlings, an additional staining of the vascular tissue in the initial developing side roots was detected (Figure 47B). Cross sections of the stained roots proved that the vascular and no surrounding tissue was stained (Figure 47C). The promoter activity of *misk1* in the vascular tissue of roots matched with *GeneVestigator* data [83, 84], which showed a *misk1* expression in xylem tissue.

5.3.2 Homozygous T-DNA insertion lines of *mask1* do not show a root or annular xylem phenotype

For the following phenotype analyses, the T-DNA insertion lines *mask1-1* and *mask1-2* (Figure 39, Table 5) were used. All plants were genotyped for a comparison of homozygous and segregating wild-type plants (appendix: Figure 69). RNA was gained from the roots of these lines and used for a two-step RT-PCR to generate cDNA. PCR analyses were performed on the cDNA to prove a successful knockout (appendix: Figure 71). Due to the expression data of *mask1* and *mask2*, a special attention was directed at the root development. Homozygous and segregating wild-type plants were seeded on plant agar and grown for ten days (Figure 48A).

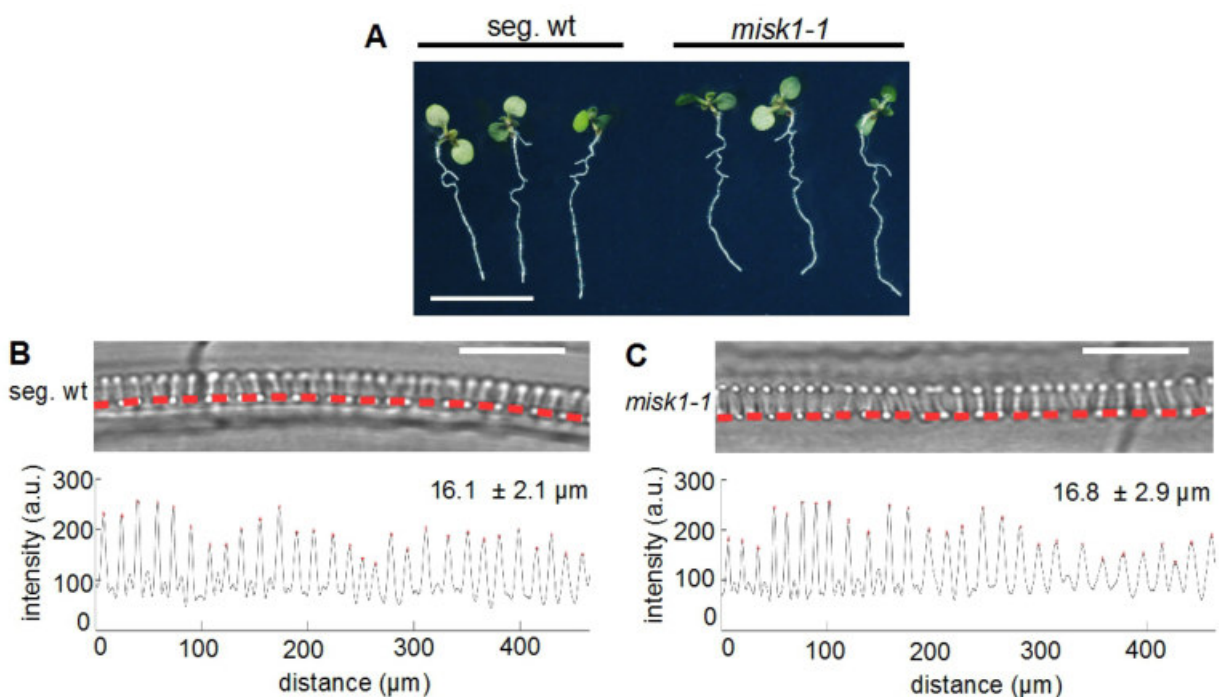


Figure 48: Phenotype analyses of the homozygous *mask1* T-DNA insertion lines.

(A) Homozygous *mask1-1* and segregating wild-type plants grown on agar over a period of ten days. The root growth stage and development looked similar for all plants.

(B, C) Annular xylem scans of homozygous *mask1-1* (C) and segregating wild-type plants (B) grown on agar over a period of ten days. Roots were decolorized and the refraction index was adapted [89]. The analyzed pictures did not show a structural difference between the secondary cell wall pitch p of homozygous and segregating wild-type plants ($p_{\text{seg. wt}} = 16.1 \pm 2.1 \mu\text{m}$, $p_{\text{mask1-1}} = 16.8 \pm 2.9 \mu\text{m}$ (mean \pm s.d.)).

Morphological analyses of the roots did not show a difference in growth stage and development between homozygous and segregating wild-type plants of both *mask1* T-DNA insertion lines (example: *mask1-1* Figure 48A). Therefore, the xylem tissue was analyzed in detail. Roots were decolorized and the refraction index was adapted [89] to visualize the xylem tissue via microscopy. The structure of the annular xylem tissue was homogeneous and pitches were similar for all plants (example: *mask1-1* Figure 48B, C). Thus far, it was not possible to detect a phenotype.

5.4 Discussion

At1g55550 and *At5g27950* represent a second interesting subgroup of kinesin-14 genes because they both code for plant-specific minus end-directed kinesins with an N-terminal motor domain (Figure 5, 41) [1, 6]. According to this structural variation, *AtMISK1* constructs were cloned, expressed in bacteria, and purified by affinity chromatography for *in vitro* characterization. Performed *in vitro* assays provide an insight into the biophysical properties of *AtMISK1*.

5.4.1 *The N-terminal motor domain of AtMISK1 probably contains a neck linker for minus end-directed movement*

AtMISK1 gliding assays were performed under different conditions because distinct parameters like pH value, ionic strength, or temperature can influence the protein conformation, protein interaction, and gliding velocity [90]. In this study, constant microtubule transport was observed under defined conditions with a velocity of $134 \pm 17 \text{ nm} \cdot \text{s}^{-1}$ (Figure 43). Interestingly, these gliding assays showed the motor activity of a minus end-directed kinesin with an N-terminal motor domain for the first time to our best knowledge. To date, N-terminal motor domains were only described for plus end-directed kinesin families in the literature [43].

The directionality of movement is determined by the neck linker, whose sequence and structural elements differ between plus and minus end-directed motor proteins [9]. It seems promising that *AtMISK1* has an N-terminal motor domain, which contains a neck linker structure for minus end-directed movement.

5.4.2 *AtMISK1 probably forms a tetrameric or a flexible, dimeric structure in in vitro assays*

Stepping assays and kymograph evaluations showed mostly diffusive and some non-processive interactions between *AtMISK1* and microtubules in this study. With an increasing salt concentration diffusion rates increased as expected (Figure 44) [90].

Non-processive interactions of homo- or heterodimeric motor domains with microtubules have been described for members of the kinesin-14 family in different organisms [20, 33, 34, 189]. Furthermore, diffusive interactions of these proteins with microtubules are already known. Ncd (*Drosophila melanogaster*) is a well-studied protein of this family. Fink et al. [33] performed experiments with truncated Ncd constructs. These experiments showed that non-processive Ncd interactions depended on the motor domain, while diffusive Ncd interactions depended on the tail domain. Both kinds of interaction as well as sliding and

crosslinking activity were only possible with full-length Ncd containing the motor and the tail domain [16, 33]. In comparison to the Ncd full-length construct, the *AtMISK1*(aa3-462)-EGFP-6xHis construct of this study only comprises the motor and the coiled-coil domain. The coiled-coil domain was included because it is necessary for dimerization [190, 191]. Despite tail elimination, it was possible to detect diffusive and transient (non-processive) *AtMISK1*-microtubule interactions (Figure 44). These findings raise the question of whether the motor domain enables both kinds of interactions.

In order to clarify this question, a single-headed construct of *AtMISK1* - without the dimerization domain - was analyzed in stepping assays. Comparable to the dimeric *AtMISK1* construct, single-motor heads also enabled many diffusive and some transient interactions in this study (Figure 45). These results prove that the motor domain enables both kinds of interactions.

In a next step, it was tested whether *AtMISK1* crosslinks and slides microtubules. Implemented sliding assays showed that *AtMISK1* crosslinked microtubules or slid them along each other (Figure 46). Two scenarios remain, which could explain microtubule sliding and crosslinking by *AtMISK1*(aa3-462)-EGFP-6xHis in this case (Figure 49).

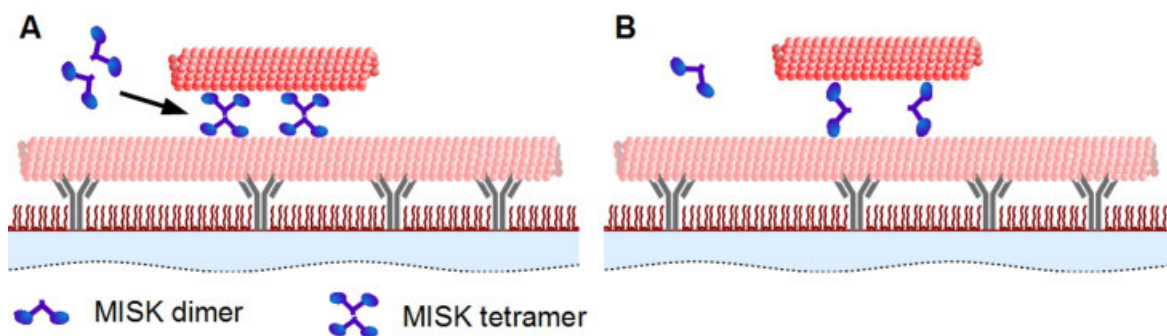


Figure 49: Proposed models for interactions of *AtMISK1* with microtubules.

(A) If both heads of the *AtMISK1* dimer are only able to bind at the same microtubule, the formation of motor tetramers could link microtubules.

(B) If each motor head of the *AtMISK1* dimer binds at different microtubules, the dimer itself could link microtubules.

It might be possible that both heads of a motor dimer could only bind to the same microtubule due to steric properties of the neck linker. In this case, the formation of *AtMISK1* tetramers is necessary to enable microtubule crosslinking or sliding (Figure 49A). Processive, microtubule-based transport through artificial or cargo-dependent clustering of minus end-directed, non-processive kinesins was already described in the literature for *Physcomitrella patens* [20], *Oryza sativa* [34] or *Drosophila melanogaster* [192].

Otherwise, it is also possible that a dimeric motor binds with each head at different microtubules for crosslinking and sliding processes (Figure 49B). This kind of microtubule-

crosslinking has not been described in the literature for kinesin-14 proteins thus far but for dyneins. A study by Tanenbaum et al. [190] investigated constructs of a dynein motor concerning their microtubule interactions: a full length and two truncated constructs, which comprised the motor domain dimerized by a GST-tag or by the native dimerization domain. All three constructs showed crosslinking of microtubules in the absence of ATP and sliding of anti-parallel microtubules in the presence of ATP. If the microtubule-binding site in the motor domain was mutated, no interaction was detected [190]. These results indicate a very flexible motor domain linker, which allows each head of the dimer to walk independently on different microtubules. Crosslinking and sliding processes by these dynein dimers do not require the tail domain, accessory subunits, regulatory proteins, or oligomerization processes. Further experiments with the aforementioned dynein constructs have shown that the processivity of the motor protein depended on the kind of binding between motors and microtubules. Dyneins binding with both heads at one microtubule showed processive movement, while dyneins binding with each head at different microtubules rather frequently moved bidirectionally [190]. In contrast to dynein, *AtMISK1* showed diffusive and non-processive movement on single microtubules.

A possibility to support one of these hypotheses is a bleaching experiment performed as described by Jonsson et al. [20]. Similar experiments remain in progress to prove whether fluorescence-marked *AtMISK1* molecules are bleached in two (dimer) or four steps (tetramer). Furthermore, structural analyses of the neck linker might be helpful.

Even if the exact mechanism is not entirely clarified, own experiments showed that *AtMISK1* crosslinked microtubules or slid them along each other (Figure 46). The kind of interaction was dependent on the relative polarity of the two microtubules to each other. This was proven by observed flipping events during self-performed sliding assays. After these flips of sliding cargo-microtubules on the same template-microtubules, they were stably crosslinked (Figure 46). The result that the orientation/ polarity of the microtubules determined stable crosslinking or sliding, was already shown for other minus end-directed motor proteins like Ncd (*Drosophila melanogaster*), XCTK2 (*Xenopus laevis*) or HSET (human) [33, 193, 194]. As mentioned for Ncd, these proteins have two microtubule-binding domains: one in the motor domain and the second in the tail domain. Fink et al. [33] described the following model mechanism for motor-microtubule interactions: Due to a loose binding of the motors to the microtubules, the motor domain and tail domain can switch between cargo- and template-microtubules. Thereby, the motors exert different forces on the cargo-microtubule: motors that are bound with their motor domain to the cargo-microtubule can push it in a specific

direction, while those that are bound with their tail domain to the cargo-microtubule can pull it in a specific direction (Figure 50).

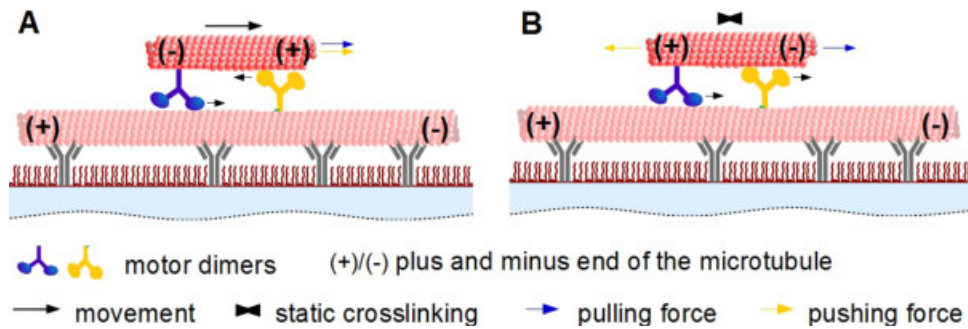


Figure 50: Models for the crosslinking and sliding mechanisms of microtubules by Ncd.

The motor domain and tail domain of Ncd can switch between cargo- and template-microtubules. Motors that are bound with their motor domain to the cargo-microtubule can push it in a specific direction, while motors that are bound with their tail domain to the cargo-microtubule can pull it in a specific direction.

(A) During anti-parallel linking of the microtubules, the motors push (yellow motor) and pull (blue motor) the cargo-microtubule in the same direction, which causes sliding. Modified from [33].

(B) During parallel linking of microtubules, motors push and pull the cargo-microtubule in the opposite direction. These counteracting motors slow down initial sliding of parallel microtubules. Modified from [33].

During anti-parallel linking of the microtubules, the motors push and pull the cargo-microtubule in the same direction, which causes sliding (Figure 50A). By contrast, during parallel linking of microtubules, motors push and pull the cargo-microtubule in the opposite direction (Figure 50B). These counteracting motors slow down initial sliding of parallel microtubules [33]. A similar mechanism is hypothesized for *At*MISK. However, the two microtubules are only linked by the four motor heads of tetramers (Figure 51A) or by the two motor heads of flexible dimers (Figure 51B).

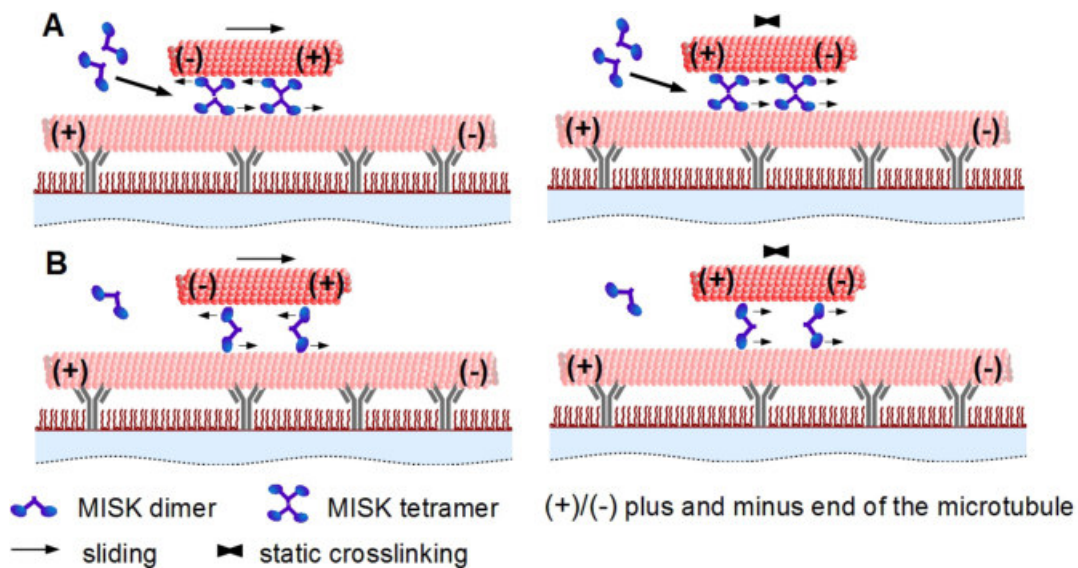


Figure 51: Proposed models for the crosslinking and sliding mechanisms of microtubules by *At*MISK1.

(A) If both heads of the motor dimer are only able to bind at the same microtubule, the formation of motor tetramers could enable crosslinking of parallel microtubules (right) or sliding of anti-parallel microtubules (left).

(B) If each motor head of the dimer binds at different microtubules, the dimer itself could enable crosslinking of parallel microtubules (right) or sliding of anti-parallel microtubules (left).

5.4.3 *The potential role of AtMISK1 during secondary cell wall development in xylem tissue*

The function of crosslinking and sliding by minus end-directed kinesin-14 motors is often connected to the assembly, structural organization, integrity, and maintenance of the mitotic spindle in the literature [32, 51, 177, 195]. Therefore, several minus end-directed kinesin-14 proteins of *A. thaliana* could be also necessary for cell division. This hypothesis is supported by the aforementioned facts that flowering plants lack centrosomes and dynein. Moreover, motor protein-based, plant-specific processes like the formation of the preprophase band, the phragmoplast and the cell plate occur during cell division [177, 181, 183]. However, only seven of twenty-one genes coding for minus end-directed kinesin-14 in *A. thaliana* are upregulated during mitosis [32]. Interestingly, *AtMISK1* is not one of these kinesins [32, 33].

GUS staining showed *misk1* promotor activity in growth regions of the vascular tissue in roots of *A. thaliana* (Figure 47). The vascular tissue comprises xylem rays with species-specific organization patterns, which reach up to the pericambium. The phloem - separated by the parenchymatic tissue - is embedded between these xylem rays. The vascular tissue enables structural stability as well as water, nutrient, and signal molecule transport [196-198]. In addition to the GUS data, *GeneVestigator* data showed *misk1* expression in the xylem tissue. *GeneVestigator* data for the closest relative of *misk1*, *misk2*, also showed expression in the xylem tissue. This fact was checked because the kinesin-14 family has a high redundancy [3]. Based on these data, the development of the xylem tissue was analyzed to find potential processes for *AtMISK1* involvement.

The xylem tissue develops in a spatiotemporal organized manner passing various differentiation steps [196-198]. The three types of matured xylem tissue are xylem trachearies (conducting cells), xylem fibers (structural support) and xylem parenchyma (lignification of neighboring tracheary elements) [196-198]. Tracheary elements exist as protoxylem or metaxylem. The protoxylem has annular or spiral secondary cell wall thickenings, which enable distinct stability but also a certain flexibility for rapid cell elongation. The metaxylem matures when surrounding organs completed their growth process. It develops a reticulate, scaliform, or pitted cell wall pattern to provide the cell shape. After secondary cell wall deposition in the metaxylem, the tonoplasts were destroyed. They release proteases and nucleases, which initiate apoptosis. Adult, hollow, dead tracheary elements are connected to a continuous system of long tubular xylem vessels for transport processes [196-202]. By contrast, xylem fibers develop a thick consistent secondary cell wall. It is arranged in three concentric layers with varying microfibril angles. Additionally, it contains a high percentage of lignin to provide structural support [196].

The xylem tissue differentiation in *A. thaliana* is regulated - among others - over a network of different transcription factors and hormones [196, 197, 200, 201, 203]. Furthermore, the cytoskeleton plays an important role in regulation and organization processes [196, 199, 200]. Experiments of *in vivo* studies concerning microtubule function during tracheary differentiation in *A. thaliana* showed that cortical microtubules supported and regulated the spatial secondary cell wall pattern generation [199, 200]. However, the mechanisms of cortical microtubule arrangement for the formation of specific secondary cell wall pattern is not completely analyzed [200]. Microtubule rearrangement could be connected to the touch-and-reorientation model observed *in vitro* and *in vivo* in root hairs in *A. thaliana* and in tobacco BY-2 cells. It postulates that collision of microtubules results in a shrinkage phase followed by a growing phase in another direction. Microtubule-bundling is possible if microtubules clash at a specific angle [198, 199, 204-206]. This model depends on polymerization and depolymerization kinetics, regulation of structural components (e.g. tubulin dimer concentration), specific spatiotemporal expression of microtubule-associated proteins (MAPs), and posttranslational modifications of MAPs or microtubules.

Several studies assumed that different MAPs are involved in the organization of cortical microtubules during secondary cell wall patterning in protoxylem and metaxylem [196, 198-200, 207-213] (Figure 52A).

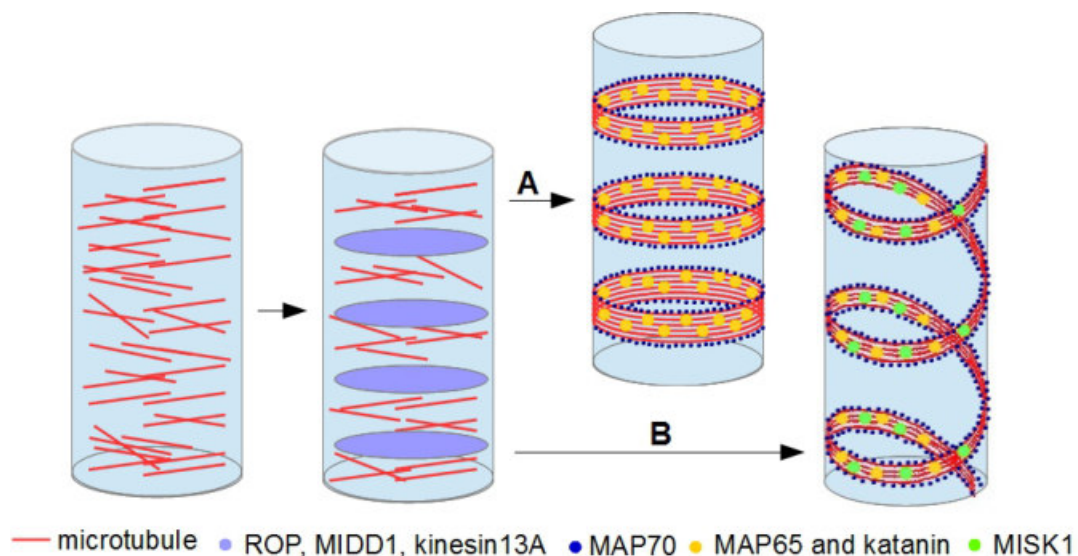


Figure 52: Proposed model for microtubule organization during secondary cell wall formation of the protoxylem tissue with and without MISK1.

ROPs may recruit MIDD1 to the plasma membrane, where it could promote local microtubule disassembly with the help of interaction partners like kinesin13A. MAP70 members could further organize microtubules at the boundary of secondary cell wall deposition, where the microtubules could be organized by proteins like katanin and MAP65 (A). If MISK is involved, it could further slide the microtubules along each other, which could be necessary for the development of a helically elongated shape (B). Modified from [200, 207].

One example of a MAP that is upregulated during secondary cell wall formation of *A. thaliana* tracheary elements is MIDD1. It is supposed that *AtMIDD1* is recruited to the

plasma membrane by Rac/Rho small GTPases (ROPs). Furthermore, it should regulate cell wall pit formation by locally destabilizing cortical microtubules, possibly with the help of *Atkinesin13A* [198, 200, 207]. By contrast, cell wall formation seems to be partially regulated by proteins like *AtMAP65* and *AtMAP70*. Two *AtMAP70* members were localized on secondary-cell-wall-pit-flanking microtubules. It is hypothesized that *AtMAP70-1* and *AtMAP70-5* localize and stabilize these subpopulations of cortical microtubules along the edge of secondary cell wall thickenings. This allocates them a role as a boundary marker of secondary cell wall deposition on the plasma membrane [198, 200, 207, 214]. Besides this localization, it is also known that cortical microtubules form bundles beneath the areas of accruing cell wall thickenings. It is supposed that *Atkatanin* and *AtMAP65* proteins are involved in this process. *AtMAP65* proteins are known to bundle, stabilize, and elongate microtubules [198, 200, 207-209]. Various secondary cell wall patterns seem to be the result of an interplay between aforementioned MAPs and their respective expression rate [207].

Regarding the crosslinking activity of *AtMISK1*, it could bundle and organize cortical microtubules possibly in cooperation with *AtMAP65* and *Atkatanin*. This could promote an annular secondary cell wall pattern in protoxylem (Figure 52A). In contrast to the other two MAPs, *AtMISK* can slide microtubules along each other. This property could be necessary developing a helically elongated, spiral structure of the microtubules and the accruing secondary cell wall (Figure 52B). The spiral elongation might be also supported by *AtMAP70* members because literature studies showed that an *AtMAP70-5* overexpression promoted the formation of spiral secondary cell wall patterns [214].

The hypothesis of *AtMISK* involvement can be proved with colocalization studies of *AtMISK*, microtubules, and *AtMAPs* during secondary cell wall formation of the protoxylem tissue.

If *AtMISK* is involved in xylem development, tissue-specific phenotypes could occur. However, own morphological analyses of the roots of *misK1* T-DNA insertion lines have not shown a phenotype in growth stage and development (Figure 48A). Confirming to these results, the microscopic analyses showed a homogenous annular xylem structure and similar pitches for the two lines (Figure 48B, C). These results would fit to the proposed model of secondary cell wall formation (Figure 52A). In this model, other proteins like *AtMAP65* are also mentioned to perform microtubule-bundling. Therefore, these proteins possibly replace the function of *AtMISK* to a certain extent and prevent strong specific phenotypes in the annular protoxylem. In contrast to annular protoxylem, the helical protoxylem needs a spiral shift, which could be caused by *AtMISK1*-sliding properties. Analyses concerning a helical protoxylem phenotype remain in process.

5.4.4 Conclusion

In this thesis, it was possible to describe a novel kinesin-14 motor with an N-terminal motor domain for the first time. *In vitro* assays showed that *AtMISK1* - without its tail domain - is a minus end-directed, non-processive and diffusive kinesin-14 motor protein with a velocity of $134 \pm 17 \text{ nm}\cdot\text{s}^{-1}$. The motor enables stable microtubule-crosslinking or microtubule-sliding depending on the polarity of linked microtubules. Despite the functional similarity to proteins with mitotic functions, *misk1* is not upregulated during mitosis. By contrast, *AtMISK* showed promoter activity in the xylem tissue. Taking *in vitro* and *in vivo* analyses together, it can be hypothesized that *AtMISK1* is involved in the rearrangement of the cytoskeleton for secondary cell wall development in growing xylem tissue.

6 General discussion

The archetypic kinesin-14 members are responsible for the general group description of minus end-directed, non-processive motor proteins with a C-terminal motor domain and a functional specification for processes in cell division. They are well investigated in different eukaryotic organisms [1-3, 6, 41]. This group comprises the members KatA-C, and Kin-14D in *A. thaliana* (Figure 5). However, there are further *At*kinesin-14 members with particular structural characteristics, whose functions have not been analyzed thus far.

This thesis deals with three members of the kinesin-14 family in *A. thaliana*. They were analyzed concerning their structure, properties, functions, and localization to gain insights into their physiological roles.

The two investigated minus end-directed, non-processive *At*BARK proteins have an internal motor-domain flanked by two coiled-coil domains and an N-terminal F-BAR domain. Both proteins have membrane sensing, binding, and deformation properties and transport vesicles along microtubules. The high sequence similarity and a similar expression pattern in pollen, combined with the pollen shape and pollen tube growth phenotypes of the *bark1-1* T-DNA insertion line indicate a relation to endocytosis in growing pollen tubes (see **Chapter 4**).

The other investigated minus end-directed, non-processive, diffusive *At*kinesin-14 protein *At*MISK1 has an N-terminal motor domain flanked by one coiled-coil domain. Its microtubule-crosslinking and sliding properties depend on the polarity of the linked microtubules. It is conspicuous that *At*MISK1 - without its tail domain - crosslinks and slides microtubules. This indicates that the protein forms a tetrameric or a flexible dimeric structure. The aforementioned properties and an expression in xylem tissue suggest a role in the rearrangement of the cytoskeleton for secondary cell wall formation in differentiating xylem tissue of the roots (see **Chapter 5**).

It has to be considered that kinesin-14 motors with an F-BAR domain (*At*BARK) and kinesin-14 motors with an N-terminal motor domain (*At*MISK) were characterized for the first time. In *A. thaliana*, these motors are arranged in deeper branches of the phylogenetic tree than the mitotic *At*kinesins-14 motors (Figure 5). This probably reflects not only structural differences but also different protein properties and functions. Therefore, a further sub-division of the large kinesin-14 family in *A. thaliana* can be considered. This was also undertaken for the large number of plus end-directed kinesins (group 1 to 12).

An initial sub-division was also mentioned by Miki et al. and Richardson et al. [1, 41]. Based on own structural analyses, which include the whole amino acid sequences of analyzed

*At*kinesins, and the created phylogenetic tree (Figure 5), the *At*kinesin-14 family could be subdivided into the following groups:

- (1) archetypic kinesin-14 motors with a C-terminal motor domain and putative functions in cell division (KatA-C and Kin-14D);
- (2) plant-specific kinesin-14 motors with an N-terminal (MISK1-2, Kin.14-S) or an internal motor domain (DGBLK, DGBK) flanked by one coiled-coil domain;
- (3) kinesins with an internal motor domain flanked by two coiled-coil domains (KCH1-7, BARK1-2).

Further analyses of kinesin-14 group members can improve the knowledge of functions and their participation in development processes of plants. This can lead to a better understanding of this multifunctional group and a better structural and functional classification.

7 Material and methods

7.1 Organisms

7.1.1 Bacterial strains

Table 1: Register of *E. coli* strains used for experiments in this thesis.

strain	genotype	reference
DH5 α	B F ⁻ endA1 glnV44 thi-1 recA1 relA1 gyrA96 deoR nupG purB20 ϕ 80dlacZ Δ M15 Δ (lacZYA-argF)U169, hsdR17(r _K -m _K ⁺), λ -	[215]
BL21 pRARE (DE3) = Rosetta2(DE3)	F-ompT Ion hsdSB (r _B ⁻ m _B ⁻) gal dcm (DE3) pRARE2 (Cam ^R)	Novagen
BL21 Gold (DE3)	B F ⁻ ompT hsdS(r _B ⁻ m _B ⁻) dcm ⁺ Tet ^r gal λ (DE3) endA I	Aligent Technologies
BL21(DE3) RIPL	B F ⁻ ompT hsdS(r _B ⁻ m _B ⁻) dcm ⁺ Tetr gal λ (DE3) endA The (argU proL Cam ^R) (argU ileY leuW Strep/Spec ^R)	Aligent Technologies
BL21 Rosetta Gami2 (DE3)	Δ (ara-leu)7697 Δ lacX74 Δ phoA PvuII phoR araD139 ahpC 73ale galK rpsL(DE3) F'(lac ⁺ lacI ^q pro) gor522::Tn10 trxB pRARE2 (Cam ^R , Str ^R , Tet ^R)	Novagen

Table 2: Register of *A. tumefaciens* strains used for experiments in this thesis.

strain	genotype	resistance	reference
C58C1	C58	hygromycin	[216]

7.1.2 Plant lines of *Arabidopsis thaliana*

Table 3: Register of *A. thaliana* ecotypes used for experiments in this thesis.

ecotype	reference
Columbia-0 (Col-0)	NASC The European Arabidopsis Stock Centre, Nottingham, Great Britain http://arabidopsis.info/ [217]

Table 4: Register of transgenic *A. thaliana* lines established in this thesis.

name	vector	agrobacterium	selection
<i>pbark1-GUS</i>	pMDC162-pBARK1-GUS	C58C1	hygromycin, kanamycin
<i>pbark2-GUS</i>	pMDC162-pBARK2-GUS	C58C1	hygromycin, kanamycin
<i>pmisk1-GUS</i>	pMDC162-pMISK1-GUS	C58C1	hygromycin, kanamycin
<i>35S-bark1-GFP</i>	35S-pMDC85-BARK1-GFP	C58C1	hygromycin, kanamycin

Table 5: Register of *A. thaliana* T-DNA insertion lines used for experiments in this thesis.

line	name	affected gene	coordinates insertion	reference
<i>bark1-1</i>	GK345B04	<i>At1g73860</i>	27776306 bp	www.gabi-kat.de [218, 219]
<i>bark2-1</i>	SALK_023598	<i>At1g18410</i>	6341149 bp	www.arabidopsis.org [73] http://arabidopsis.info/ [217]
<i>bark2-2</i>	SALK_135977	<i>At1g18410</i>	6342011 bp	
<i>misk1-1</i>	SALK_043700C	<i>At1g55550</i>	20749281 bp	
<i>misk1-2</i>	SALK_146972C	<i>At1g55550</i>	20751943 bp	

7.1.3 Vectors

Table 6: Register of vectors used in this thesis.

vector	promotor	N-terminus	C-terminus	resistance	reference
pET28a	T7	6xHis	-	kanamycin	Novagen
pET17b- <i>At</i> MISK1-FL-EGFP-6xHis	T7	6xHis	-	ampicillin	sequence see appendix
pET17b-rKin430-EFGP-6xHis	T7	EGFP-6xHis	-	ampicillin	sequence see appendix
pMDC85	2x35S	-	GFP-6xHis	kanamycin chloramphenicol, hygromycin	[220]
pMDC162	-	-	GUS	kanamycin chloramphenicol, hygromycin	[220]
pENTR TM /D-TOPO [®]	T7	-	-	kanamycin	Invitrogen by Life Technologies TM

Table 7: Register of expression vectors established in this thesis.

cloned vector	based on	selection
pET28a- <i>At</i> BARK1(aa1-1025)-6xHis	pET28a	kanamycin
pET28a- <i>At</i> BARK2(aa163-1140)-EGFP-6xHis	pET28a	kanamycin
pET17b- <i>At</i> MISK1(aa3-462)-EGFP-6xHis	pET17b- <i>At</i> MISK1-FL-EGFP-6xHis	ampicillin
pET17b- <i>At</i> MISK1(aa3-415)-EGFP-6xHis	pET17b- <i>At</i> MISK1(aa3-462)-EGFP-6xHis	ampicillin

Sequences of the cloned expression constructs were listed in the appendix.

7.2 Material

7.2.1 Chemicals

Table 8: Register of chemicals used in this thesis.

chemical	company, city, country
4-(2-aminoethyl)benzensulfonyl fluoride hydrochloride (AEBSF)	PanReac AppliChem GmbH, Darmstadt, Germany
1,1'-dioctadecyl-3,3',3'-tetramethylindodicarbocyanine perchlorate (DiD)	Life Technologies, Thermo Scientific, Waltham, USA
6xDNA loading dye	Thermo Scientific, Waltham, USA
N-2-hydroxyethylpiperazine-N'-2-ethane sulfonic acid (HEPES)	Carl Roth GmbH + Co. KG, Karlsruhe, Germany
2-(N-morpholino)-ethane sulfonic acid (MES)	Carl Roth GmbH + Co. KG, Karlsruhe, Germany
3-N-morpholinopropanesulfonic acid (MOPS)	PanReac AppliChem GmbH, Darmstadt, Germany
Adenosine 5'-triphosphate (ATP), Di-sodium salt trihydrate	Jena Bioscience, Jena, Germany
Adenosine 5'-triphosphate (ATP) solution	Jena Bioscience, Jena, Germany
α -D-glucose monohydrate	SERVA Electrophoresis GmbH, Heidelberg, Germany
Agar, Kolbe I	Carl Roth GmbH + Co. KG, Karlsruhe, Germany
Agarose powder	VWR Chemicals, Leuven, Belgium
Ammonium persulfate (APS)	Th.Geyer GmbH & Co. KG, Renningen, Germany
Ampicilin sodium salt (AMP)	PanReac AppliChem GmbH, Darmstadt, Germany
BioMücker WDG	Biofa AG, Münsingen Germany
Boric acid	CHEMSOLUTE [®] , Th.Geyer GmbH & Co. KG, Renningen, Germany
Brilliant blue R250	Carl Roth GmbH + Co. KG, Karlsruhe, Germany
Bromophenol blue sodium salt	PanReac AppliChem GmbH, Darmstadt, Germany
Calcium chloride (CaCl_2)	Merck KgaA, Darmstadt, Germany
Chloral hydrate	PanReac AppliChem GmbH, Darmstadt, Germany
Chloramphenicol (CAM)	Amresco [®] , Ohio, USA
Chloroform/Trichloromethane	Carl Roth GmbH + Co. KG, Karlsruhe, Germany
Cholesterol	PanReac AppliChem GmbH, Darmstadt, Germany
Cyanine 5-NHS ester	Enzo Life Science GmbH, Lörrach, Germany
Digoxiginin NHS-ester	Sigma-Aldrich, jetzt Merck KgaA, Darmstadt, Germany
Dimethyl sulfoxide (DMSO)	CHEMSOLUTE [®] , Th.Geyer GmbH & Co. KG, Renningen, Germany
Di-potassium hydrogen phosphate (K_2HPO_4)	PanReac AppliChem GmbH, Darmstadt, Germany
Di-sodium hydrogen phosphate anhydrous (Na_2HPO_4)	PanReac AppliChem GmbH, Darmstadt, Germany

Dithiothreitol (DTT)	PanReac AppliChem GmbH, Darmstadt, Germany
dNTP Set	Thermo Scientific, Waltham, USA
DyLight™ 594 NHS ester	Thermo Scientific, Waltham, USA
Ethanol absolute (EtOH)	CHEMSOLUTE®, Th.Geyer GmbH & Co. KG, Renningen, Germany
Ethidium bromide (EtBr)	Carl Roth GmbH + Co. KG, Karlsruhe, Germany
Ethylenediaminetetraacetic acid (EDTA)	Carl Roth GmbH + Co. KG, Karlsruhe, Germany
Ethylene glycol-bis-(β-aminoethyl ether)-N,N,N',N'-tetraacetic acid (EGTA)	PanReac AppliChem GmbH, Darmstadt, Germany
GeneRuler™ 1kb Plus DNA ladder	Thermo Scientific, Waltham, USA
Glacial acetic acid	VWR Chemicals, Fontenay-sous-Bois, France
Glycerol anhydrous	PanReac AppliChem GmbH, Darmstadt, Germany
Glycine	Carl Roth GmbH + Co. KG, Karlsruhe, Germany
Guanosine-5'((α,β)-methylene)triphosphate (GMPCPP) sodium salt	Jena Bioscience, Jena, Germany
Guanosine 5'-triphosphate (GTP) sodium salt	Jena Bioscience, Jena, Germany
Gum arabic	Carl Roth GmbH + Co. KG, Karlsruhe, Germany
Hydrochloric acid (HCl) 32 %	Merck KgaA, Darmstadt, Germany
Hygromycin B-solution	Carl Roth GmbH + Co. KG, Karlsruhe, Germany
Imidazole	Merck KgaA, Darmstadt, Germany
Isopropyl alcohol	CHEMSOLUTE®, Th.Geyer GmbH & Co. KG, Renningen, Germany
Isopropyl β-D-1-thiogalactopyranoside (IPTG)	PanReac AppliChem GmbH, Darmstadt, Germany
Kanamycin sulfate	AppliChem GmbH, Darmstadt, Germany
Lysogenic-broth (LB) (Luria/Miller), granulated	Carl Roth GmbH + Co. KG, Karlsruhe, Germany
Lecithin	Carl Roth GmbH + Co. KG, Karlsruhe, Germany
Lecithin SERIN <i>Aid</i> 20 P IP Phosphatidylserine 20 % sample	Lecico, Hamburg, Germany
Lecithin SERIN <i>Aid</i> 50 P IP Phosphatidylserine enriched soybean phospholipid sample	Lecico, Hamburg, Germany
LR white resin	Sigma-Aldrich, jetzt Merck KgaA, Darmstadt, Germany
Magnesium chloride hexahydrate (MgCl ₂)	VWR Chemicals, Leuven, Belgium
Magnesium sulfate heptahydrate (MgSO ₄ ·7H ₂ O)	PanReac AppliChem GmbH, Darmstadt, Germany
Mineral oil	Sigma-Aldrich, jetzt Merck KgaA, Darmstadt, Germany
Mucosol	Schülke & Mayr GmbH, Norderstedt, Germany
Murashige & Skoog (MS) Medium	Duchefa Biochemie, Haarlem, Netherlands
N-Ethylmaleimide (NEM)	Sigma-Aldrich, jetzt Merck KgaA, Darmstadt, Germany
N,N,N',N'-Tetramethylethylenediamine (Temed)	PanReac AppliChem GmbH, Darmstadt, Germany
Oryzalin	Sigma-Aldrich, jetzt Merck KgaA, Darmstadt, Germany

PageRuler™ prestained protein ladder	Thermo Scientific, Waltham, USA
peqGOLD TriFast™ Reagenz	PEQLAB, Erlangen, Germany
Phyto agar	Duchefa Biochemie, Haarlem, Netherlands
Piperazine-N, N'-bis-(2-ethane sulfonic acid) (PIPES)	PanReac AppliChem GmbH, Darmstadt, Germany Carl Roth GmbH + Co. KG, Karlsruhe, Germany
Pluronic®-127	Sigma-Aldrich, jetzt Merck KgaA, Darmstadt, Germany
Potassium acetate	PanReac AppliChem GmbH, Darmstadt, Germany
Potassium chloride (KCl)	Merck KgaA, Darmstadt, Germany
Potassium di-hydrogen phosphate (KH ₂ PO ₄)	PanReac AppliChem GmbH, Darmstadt, Germany
Potassium ferrocyanide	Sigma-Aldrich, jetzt Merck KgaA, Darmstadt, Germany
Potassium hydroxide (KOH)	CHEMSOLUTE®, Th.Geyer GmbH & Co. KG, Renningen, Germany
Previcur Energy	Bayer, Langenfeld, Germany
Protease inhibitor cocktail tablets	Roche Diagnostics GmbH, Mannheim, Germany
Rotiphorese® Gel 30	Carl Roth GmbH + Co. KG, Karlsruhe, Germany
Silwet-L77	Momentive, Leverkusen, Germany
Sodium chloride (NaCl)	CHEMSOLUTE®, Th.Geyer GmbH & Co. KG, Renningen, Germany
Sodium deoxycholate	PanReac AppliChem GmbH, Darmstadt, Germany
Sodium di-hydrogen phosphate monohydrate (NaH ₂ PO ₄)	Merck KgaA, Darmstadt, Germany
Sodium dodecyl sulfate (SDS) pellets	Carl Roth GmbH + Co. KG, Karlsruhe, Germany
Sodium hydroxide (NaOH)	Carl Roth GmbH + Co. KG, Karlsruhe, Germany
Sodium hypochlorite solution	CHEMSOLUTE®, Th.Geyer GmbH & Co. KG, Renningen, Germany
Streptomycin sulfate	PanReac AppliChem GmbH, Darmstadt, Germany
Sucrose	Carl Roth GmbH + Co. KG, Karlsruhe, Germany
Taxol (Paclitaxel))	VWR Chemicals, Leuven, Belgium
Terrific broth (TB)-medium-powder	PanReac AppliChem GmbH, Darmstadt, Germany
Tetracycline hydrochloride	Carl Roth GmbH + Co. KG, Karlsruhe, Germany
Trichloro(1H,1H,2H,2H-perfluorooctyl)silane	J&K Scientific, USA
Tris-(hydroxymethyl)-aminomethane (Tris)	VWR Chemicals, Leuven, Belgium
TritonX-100	SERVA Electrophoresis GmbH, Heidelberg, Germany
Tween®20	PanReac AppliChem GmbH, Darmstadt, Germany
Ultraviolet curing, Norland optical adhesive 63	Norland Products, Inc. NJ, USA
Urea pearls pure	PanReac AppliChem GmbH, Darmstadt, Germany
X-Gluc	X-Gluc Direct, England
Xylitol	Carl Roth GmbH + Co. KG, Karlsruhe, Germany

7.2.2 Kits

Table 9: Register of kits used in this thesis.

kit	company, city, country
pENTR™ /D-TOPO® Cloning Kit	Invitrogen by Life Technologies™, CA, USA
Gateway®LR Clonase™II enzyme mix	Invitrogen by Life Technologies™, CA, USA
HiYield® PCR Clean-up/GelExtraction Kit	SLG®, Gauting, Germany
HiYield® Plasmid Mini DANN Isolierungskit	SLG®, Gauting, Germany
QuikChange Lightning Site-Directed Mutagenesis Kit	Agilent Technologies, CA, USA
RevertAid First Strand cDNA Synthesis Kit	Thermo Scientific, Waltham, USA

7.2.3 Antibodies

Table 10: Register of antibodies used in this thesis.

antibody	company, city, country
Anti-digoxigenin antibody, produced in sheep	Roche, Mannheim, Germany
Anti-EGFP antibody, produced in mouse	Osenses, Keswick, Australia
Monoclonal Anti-β-Tubulin I clone SAP4G5, produced in mouse	Sigma-Aldrich, now Merck KgaA, Darmstadt, Germany

7.2.4 Enzymes

Table 11: Register of enzymes used in this thesis.

enzyme	company, city, country
Benzonase	Th.Geyer GmbH & Co. KG, Renningen, Germany
Catalase	Calbiochem®, Merck KgaA, Darmstadt, Germany
DpnI (FastDigest)	Thermo Scientific, Rockford, USA
DreamTaq DNA Polymerase Kit	Thermo Scientific, Rockford, USA
Glucose oxidase from <i>Aspergillus niger</i>	Sigma-Aldrich, jetzt Merck KgaA, Darmstadt, Germany
KpnI	New England Biolabs
Phusion High-Fidelity DNA Polymerase	Thermo Scientific, Waltham, USA
T4-DNA Ligase	Thermo Scientific, Rockford, USA

7.2.5 Equipment

Table 12: Register of equipment used in this thesis.

equipment	company, city, country
-----------	------------------------

Optima™ MAX-XP Ultracentrifuge	Beckman Coulter Life Science, IN, USA
PCR Thermocycler peqSTAR	VWR Chemicals, Leuven, Belgium
Percival	Plant Climatics, Wertingen, Germany
PerfectBlue™ Gelsystem	peQlab Biotechnologie GmbH, Erlangen, Germany
Plasma cleaner ZEPTO	Diener Electronic GmbH & Co. KG, Ebhausen, Germany
Purification pump FH10	Thermo Scientific, Thermo Electron LED GmbH, Harz, Germany
Shaker 3015	GFL mbH, Burgwedel, Germany
Sorvall ST 16R centrifuge	Thermo Scientific, Thermo Electron LED GmbH, Harz, Germany
TempController 2000-1	PeCon® GmbH, Erbach, Germany
Thermomixer compact	Eppendorf AG, Hamburg, Germany
ThermoStatC	Eppendorf AG, Hamburg, Germany
Tissue Lyser Qiagen	Retsch GmbH, Haan, Germany
Ultramicrotome Leica Reichert Ultracut S	Leica Microsystems, Wetzlar, Germany
Ultrasonic bath S30 Elmasonic	Elma-Hans Schmidbauer GmbH & Co. KG Singen, Germany
Vacuum pump	KNF LAB LABOPORT, Freiburg, Germany

7.3 Molecular biological methods

7.3.1 RNA-synthesis

100 - 200 mg required plant material was harvested in 2 ml tubes together with two steel balls and frozen in liquid nitrogen. Thereafter, samples were crushed in the Tissue Lyser for 2 min at 28 Hz. 1 ml peqGOLD TriFastTM was added and incubated for 5 min at 1400 rpm on the shaker (Thermomixer compact). 200 µl chloroform was added, mixed, and incubated for 8 min on ice. This step was followed by a centrifugation for 10 min at 4 °C and 13,500 x g (MIKRO 22R) for phase separation. The upper, aqueous phases were transferred in new 2 ml tubes together with 500 µl isopropyl alcohol for a 30-min precipitation at -20 °C. Subsequently, samples were centrifuged for 10 min at 4 °C and 13,500 x g (MIKRO 22R), the supernatant was discarded, and the pellet was washed with 1 ml 80 % ethanol. Ethanol was removed with a further centrifugation step for 5 min at 4 °C and 13,500 x g (MIKRO 22R). Pellets were dried under the fume hood. Thereafter, 50 µl RNase-free distilled water was added and resuspended on the shaker (Thermomixer compact) for a few minutes at 58 °C. RNA concentration was measured with the NanoDrop 2000 at 260 nm and RNA quality was proven with gel electrophoresis (1.5 % agarose gel, see 7.3.6). RNA was stored at -20 °C.

7.3.2 cDNA-synthesis

The RevertAid First Strand cDNA Synthesis Kit was used for cDNA-synthesis according to the manufacturer's instructions. cDNA was stored at -20 °C.

7.3.3 Verification of *Arabidopsis thaliana* knockout plant lines with PCR

The T-DNA insertion lines were ordered from the European Arabidopsis Stock Centre (NASC, Nottingham, Great Britain). In order to verify a specific gene knockout in these T-DNA insertion lines, RNA-synthesis (see 7.3.1) and cDNA-synthesis (see 7.3.2) were performed. The cDNA was used for PCR analyses with the DreamTaq DNA Polymerase Kit according to the manufacturer's instruction. The primers were designed with Clone Manager and listed in the appendix (see Table 21). Col-0 cDNA was used as a positive control. The PCR run was followed by an agarose gel electrophoresis (see 7.3.6). cDNA amplification should be only detected for the Col-0 positive control.

7.3.4 Genomic DNA isolation of *Arabidopsis thaliana* plants

Leaf material was cut from the respective plants and collected in 1.5 ml tubes. Lysis buffer (200 mM Tris-HCl pH 8, 250 mM NaCl, 25 mM EDTA, 0.5 % SDS) was added and the plant material was crushed with a drill and plastic pestles. The samples were centrifuged for 5 min at room temperature (RT) and 14,000 x g (Heraeus Fresco21). The supernatants were received in 150 µl isopropyl ethanol for precipitation at -20 °C. After 10 - 20 min the samples were centrifuged for 8 min at RT and 14,000 x g (Heraeus Fresco21). The pellets were washed in 70 % ethanol followed by a further centrifugation step for 3 min at RT and 14,000 x g (Heraeus Fresco21). The supernatants were discarded and the pellets were dried for 5 min at 50 °C. In the next step, pellets were resuspended in 50 µl distilled water and incubated on a shaker (Thermomixer compact) for 10 min at 50 °C and 1100 rpm. Isolated genomic DNA (gDNA) was used immediately for genotyping or stored at 4 °C.

7.3.5 Genotyping of *Arabidopsis thaliana* plants with PCR

After gDNA isolation (see 7.3.4), 2 µl gDNA each was used as a sample for the genotyping PCR with the DreamTaq DNA Polymerase Kit according to the manufacturer's instruction. Primers were designed with the T-DNA primer design tool of T-DNA express (<http://signal.salk.edu/tdnaprimers.2.html>). For the wild-type allele LP and RP primers were combined and for the T-DNA allele LP or RP and BP primers (Figure 53, appendix Table 20). Thereafter, agarose gel electrophoresis was performed (see 7.3.6).

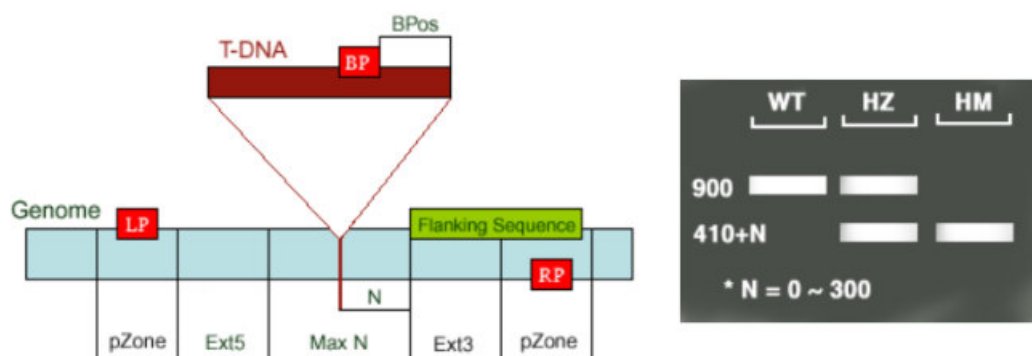


Figure 53: SALK T-DNA primer design.

N - Difference of the actual insertion site and the flanking sequence position, usually 0 - 300 bases

MaxN - Maximum difference of the actual insertion site and the sequence, default 300 bps

pZone - Regions used to pick up primers, default 100 bps

Ext5, Ext3 - Regions between the MaxN to pZone, reserved not for picking up primers

LP, RP - Left, Right genomic primer, BP - T-DNA border primer, LB - the left T-DNA border primer

BPos - The distance from BP to the insertion site (reference: <http://signal.salk.edu/tdnaprimers.2.html>)

WT - wild-type plant

HZ - heterozygous plant

HM - homozygous plant

7.3.6 Agarose gel electrophoresis

1 % agarose gels were prepared with agarose powder and 1x TAE buffer (50x TAE buffer: 242 g·l⁻¹ Tris, 57.1 ml·l⁻¹ glacial acetic acid, 9.3 g·l⁻¹ EDTA). The solution was boiled in the microwave to melt the agarose powder and filled in the gel chamber with ethidium bromide (0.5 µg·ml⁻¹). A gel comb was placed before the gel cooled down. After polymerization, the gel chamber was transferred into the electrophoresis chamber, which was filled with 1x TAE buffer. Samples, controls, and the GeneRuler™ 1kb plus DNA ladder were mixed with loading dye and filled in the gel pockets. Gel electrophoresis was performed for 1 h at 120 V with the PerfectBlue™ Gelsystem. Thereafter, gels were documented with the gel documentation system E-BOX VX2 with a P95Deprinter.

7.3.7 Overlap extension cloning

OEC is a method to create recombinant plasmids without restriction endonucleases or DNA ligases but with chimeric primers containing the plasmid sequence at the 5' ends and the insert sequence at the 3'ends [221]. Primer design and the first PCR were performed according to the instructions in the manual of Bryksin and Matsumura [222] to amplify the desired insertion sequence. Gel electrophoresis (see 7.3.6) was performed and the inserts were purified with the HiYield® PCR Clean-up/Gel Extraction Kit according to the manufacturer's instructions. The inserts were used as primers for the second PCR with a circular plasmid. The PCR was again performed according to the instructions in the manual of Bryksin and Matsumura [222]. Thereafter, the samples were digested with 5 units DpnI for 2 h at 37 °C to destroy the original plasmid templates. The overlap extension PCR products were used as DNA for the transformation of chemically competent *E.coli* DH5α cells (see 7.3.12).

7.3.8 Gateway cloning

During cDNA amplification with PCR, the bases CACC were attached to the 5'end of the sequence. This enabled a directed cloning in the output vector pENTR™/D-TOPO® with a topoisomerase. The output vector had flanking recombination sites (*attL1* and *attL2*), which were necessary for recombination of the respective gene in its destination vector. The destination vector comprised the two recombination sites *attR1* and *attR2*, which incorporate the *ccdB*-gene for selection. The LR-clonase was used to transfer the gene of interest from the output vector in different destination vectors for the creation of different fusion proteins [220]. The gateway cloning process was performed according to the manufacturer's instructions with the pENTR™/D-TOPO® Cloning Kit and the Gateway® LR Clonase™II enzyme mix Kit.

7.3.9 Site-directed mutagenesis

The site-directed mutagenesis was used for specific, intentional base changes in the DNA in order to generate additional vector restriction sites. It was performed with the QuickChange Lightning Site-Directed Mutagenesis Kit according to the manufacturer's instructions.

7.3.10 Preparation of chemically competent cells

The preparation of chemically competent cells was performed under sterile conditions. For the pre-culture 20 ml LB medium (25 g·l⁻¹ LB powder, autoclaved) was inoculated with required cells and antibiotics (Table 1) and incubated for 16 - 20 h at 37 °C and 180 rpm on the incubator shaker (MAXQ5000/6000). The main culture (250 ml LB medium) was inoculated with 10 ml of the pre-culture and with required antibiotics (Table 1) and incubated at 37 °C and 180 rpm on the incubator shaker (MAXQ5000/6000). Once the OD₆₀₀, which was measured with the photometer, reached 0.5, cells were transferred into 50 ml tubes and centrifuged 7 min at 4 °C and 2000 x g (Sorvall ST 16R). After eliminating the supernatants, the cells were gently resuspended in 75 ml pre-cooled TfbI buffer (30 mM potassium acetate, 50 mM MnCl₂, 100 mM KCl, 15 % glycerol pH 5.8, sterile filtrated) and incubated for 10 min on ice. The incubation was followed by a centrifugation step for 5 min at 4 °C and 1500 x g (Sorvall ST 16R). The supernatants were discarded and cells were gently resuspended in 10 ml pre-cooled TfbII buffer (10 mM MOPS, 75 mM CaCl₂, 10 mM KCl, 15 % glycerol pH 7, sterile filtrated). The suspension of chemically competent cells was split into 50 µl aliquots in sterile 1.5 ml tubes, frozen in liquid nitrogen, and stored at -80 °C.

7.3.11 Preparation of electrocompetent agrobacteria

In a first step, an overnight culture with 100 µl LB medium and the respectively required agrobacteria and antibiotics (Table 2) were prepared and placed on the incubator shaker (MAXQ5000/6000) at 28 °C. Next, the overnight culture was transferred to 50 ml tubes and incubated for 30 min on ice. Thereafter, various centrifugation steps were performed for 10 min at 4 °C and 4000 x g (Sorvall ST 16R), whereby the pellets were solved successively in a decreasing water solution with 10 % glycerol. The suspension of electrocompetent cells was split into 80 µl aliquots in sterile 1.5 ml tubes, frozen in liquid nitrogen, and stored at -80 °C.

7.3.12 Transformation of chemically competent cells

In order to transfect DNA vectors in different chemically competent *E.coli* cells, 1 µl DNA was added to 50 µl chemically competent cells (see 7.3.10). The cells were mixed gently and incubated for 10 min on ice, The heat shock was performed for 45 s at 42 °C (Thermomixer compact). After a short incubation on ice, 500 µl LB medium was added and the sample was incubated for 1 h at 37 °C and 500 rpm on a shaker (Thermomixer compact). Cells were plated on selection LB agar (25 g·l⁻¹ LB, 15 g·l⁻¹ agar, autoclaved) with required antibiotics (Table 1) and incubated for 16 - 20 h at 37 °C.

7.3.13 Electroporation of electrocompetent agrobacteria

In order to transfect DNA vectors in different electrocompetent agrobacteria, 1 µl DNA was added to 80 µL electrocompetent cells (see 7.3.11). The cells were mixed gently and transferred into an electroporation cuvette for an electroporation for 5 ms at 1440 V. 400 µl LB medium was added and the suspension was transferred to a tube, which was incubated for 3 h at 28 °C on a shaker (Thermomixer compact). The suspension was plated on selection LB agar with respectively required antibiotics (Table 2) and incubated for 2 - 3 days at 28 °C.

7.3.14 Colony PCR

Colony PCRs were performed to prove a successful transformation (see 7.3.12/13) of specific DNA vectors in bacterial cells. In contrast to ordinary PCRs, bacterial cells were used directly as DNA template instead of purified plasmid DNA or cDNA. Cells of grown colonies were picked and solved in 10 µl distilled water. 2 µl of each suspension was used as a template for PCR and added to the master mix. For the colony PCR, the DreamTaq DNA Polymerase was used. The master mix and the PCR run were prepared and performed according to the manufacturer's instructions with a prolonged initial denaturation of 5 min. Primers were designed with Clone Manager. Remaining bacterial suspension of each sample was transferred in LB medium with desired antibiotics (Table 1, 2) for subsequent plasmid preparation. The cultures were incubated at 37 °C (*E.coli*) or 28 °C (*agrobacteria*) on the shaker (Thermomixer compact). After colony PCR, gel electrophoresis (see 7.3.6) was performed to detect positive clones. For one of these positive clones, plasmid preparation was performed with the HiYield[®] Plasmid Mini DNA Isolierungskit according to the manufacturer's instructions.

7.3.15 Sequencing

Samples were prepared and sent to Eurofins Genomics (Ebersberg, Germany) for further sequencing analyses. The obtained sequencing results were evaluated with Clone Manager.

7.3.16 Molecular cloning of expression constructs for *in vitro* analyses

All coding sequences of established and used constructs in this study are listed in the appendix.

A. Molecular cloning of pET28a-*At*BARK1(aa1-1025)-6xHis

The complete coding sequence of *At*BARK1 was amplified from *A. thaliana* cDNA (RAFL19-19-I12, RIKEN BioResource Center) with the primers *At*BARK1_FL_OEC_fw and *At*BARK1_FL_OEC_rev (Table 13) and further cloned into the pET28a vector (Table 6) by overlap extension cloning (see 7.3.7) to generate the plasmid pET28a-*At*BARK1(aa1-1025)-6xHis. Successfully transformed *E. coli* DH5 α cells (see 7.3.12), growing on selection LB agar with kanamycin (50 $\mu\text{g}\cdot\text{ml}^{-1}$), were tested by colony PCR (see 7.3.14) with the primers pET17_fw and pET17_rev (Table 13). The DNA of positive tested clones was purified with the HiYield[®] Plasmid Mini DNA Isolierungskit according to the manufacturer's instructions and sequenced (see 7.3.15) with the primers T7, T7term, pET28a-BARK1_S1/S2 (Table 13).

B. Molecular cloning of pET28a-*At*BARK2(aa163-1140)-EGFP-6xHis

The main part of the *At*BARK2 coding sequence (aa163-1140) was amplified from cDNA with the primers *At*BARK2_FL_OEC_fw and *At*BARK2_FL_OEC_rev (Table 13) and further cloned into a pET28a vector (Table 6) by overlap extension cloning (see 7.3.7) to generate the plasmid pET28a-*At*BARK2(aa163-1140)-6xHis. The cDNA was gained from *A. thaliana* Col-0 pollen by RNA-synthesis (see 7.3.1) and following cDNA-synthesis (see 7.3.2). Transformation, selection (see 7.3.12), colony PCR (see 7.3.14), and DNA purification were performed as described before. The purified DNA was sequenced (see 7.3.15) with the primers T7, T7term, BARK2_S1/S2/S3 (Table 13). Thereafter, it was used as a vector for the generation of the plasmid pET28a-*At*BARK2(aa163-1140)-EGFP-6xHis.

The plasmid pET17b-rKin430-EFGP-6xHis (provided by Wim Walter) was used as a template for the amplification of an EFGP-6xHis-tag with the primers *At*BARK2_FL-EGFP_OEC_fw and *At*BARK2_FL-EGFP_OEC_rev (Table 13). This tag was further cloned into the plasmid pET28a-*At*BARK2(aa163-1140)-6xHis by overlap extension cloning (see 7.3.7). Transformation, selection (see 7.3.12), colony PCR (see 7.3.14), and DNA isolation were performed as described before. Thereafter, the DNA was sequenced (see 7.3.15) with the primers T7, T7term, pET28a-BARK2_S1/S2/S3 (Table 13).

digested with KpnI, and ligated with the T4 DNA ligase respectively according to the manufacturer's instructions. *E.coli* DH5 α cells were transformed with the ligation product (see 7.3.12). Successfully transformed bacteria, growing on selection LB agar with ampicillin (100 $\mu\text{g}\cdot\text{ml}^{-1}$), were tested by colony PCR (see 7.3.14) with the primers pET17_fw and pET17_rev (Table 14). The DNA of positive tested clones was purified as previously described and sequenced (see 7.3.15) with the primers T7 and T7term (Table 14).

D. Molecular cloning of pET17b-*AtMISK1*(aa3-415)-EGFP-6xHis

The expression construct pET17b-*AtMISK1*(aa3-415)-EGFP-6xHis contained the N-terminal motor domain of the coding sequence. The vector pET17b-*AtMISK1*(aa3-462)-EGFP-6xHis was used for a site-directed mutagenesis (see 7.3.9) with the primers *AtMISK1_KpnI_SDM1* and *AtMISK1_KpnI_SDM2* (Table 14) to generate a KpnI restriction site in front of the coiled-coil domain. The site-directed mutagenesis has been proven by sequencing (see 7.3.15) with the primers T7 and T7term (Table 14). *E.coli* DH5 α cells were transformed with successfully modified DNA (see 7.3.12) and grown on selection LB agar with ampicillin (100 $\mu\text{g}\cdot\text{ml}^{-1}$). The DNA was purified as described before, digested with KpnI, and ligated with the T4 DNA ligase according to the manufacturer's instructions. *E.coli* DH5 α cells were transformed with the ligation product (see 7.3.12). Successfully transformed bacteria, growing on selection LB agar with ampicillin (100 $\mu\text{g}\cdot\text{ml}^{-1}$), were tested by colony PCR (see 7.3.14) with the primers pET17_fw and pET17_rev (Table 14). The DNA of positive tested clones was purified as previously described and sequenced (see 7.3.15) with the primers T7 and T7term (Table 14).

Table 14: Oligonucleotides used for cloning, colony PCR, and sequencing during generation of *AtMISK* expression constructs for *in vitro* analyses.

Name	sequence	application
<i>AtMISK1_tr_SDM1</i>	GACGTTGGAGAACTCACTGGTACCCCTCATGTTATTG	cloning
<i>AtMISK1_tr_SDM2</i>	TAACATGAGGGGTACCAGTGAGTTTCTCCAACGTCTC	cloning
<i>AtMISK1_KpnI_SDM1</i>	CATTTAGGGGGTACCGAATCAACGGAAGAACAAGCG	cloning
<i>AtMISK1_KpnI_SDM2</i>	CGCTTGTTCTCCGTTGATTCGGTACCCCTAAATG	cloning
pET17_fw	TGACTTCCGCGTTTCCAGAC	colony PCR
pET17_rev	CAGCTTCCTTTCGGGCTTG	colony PCR
T7	TAATACGACTCACTATAGGG	sequencing
T7term	CTAGTTATTGCTCAGCGGT	sequencing

7.3.17 Molecular cloning of constructs for *in vivo* analyses

A. Molecular cloning of pMDC162-pBARK1/2-GUS and pMDC162-pMISK1-GUS

The sequence of the *bark1* promoter region was amplified from Col-0 gDNA with the primers *AtBARK1_Promotor_GUS_fw* and *AtBARK1_Promotor_GUS_rev* (Table 15) and further cloned into pMDC162 (Table 6) by gateway cloning (see 7.3.8).

The sequences of the *bark2* and *misk1* promoter regions were amplified from Col-0 gDNA with the primers *AtBARK2_Promotor_GUS_OEC_fw* / *AtMISK1_Promotor_GUS_OEC_fw* and *AtBARK2_Promotor_GUS_OEC_rev* / *AtMISK1_Promotor_GUS_OEC_rev* (Table 15) and further cloned into pMDC162 (Table 6) by overlap extension cloning (see 7.3.7).

Successfully transformed bacteria of all constructs (see 7.3.12), growing on selection LB agar with kanamycin (50 mg·ml⁻¹), were tested by colony PCR (see 7.3.14) with the primers M13_fw and M13_rev (Table 15). The DNA of positive tested clones was purified with the HiYield® Plasmid Mini DNA Isolierungskit according to the manufacturer's instructions and sequenced (see 7.3.15) with the primers M13_fw, M13_rev, and GUS_Sequ (Table 15). The vectors were listed in the appendix.

B. Molecular cloning of 35S-pMDC85-BARK1-GFP

The complete coding sequence of *AtBARK1* was amplified from *A. thaliana* cDNA with the primers *AtBARK1_GGFP_OEC_fw* and *AtBARK1_GGFP_OEC_rev* (Table 15) and further cloned into pMDC85 by overlap extension cloning (see 7.3.7).

Successfully transformed bacteria (see 7.3.12), growing on selection LB agar with kanamycin (50 mg·ml⁻¹), were tested by colony PCR (see 7.3.14) with the primers M13_fw and M13_rev (Table 15). The DNA of positive tested clones was purified with the HiYield® Plasmid Mini DNA Isolierungskit according to the manufacturer's instructions and sequenced (see 7.3.15) with the primers M13_fw, M13_rev, and *AtBARK1_Gen_S1/2/3/4/5/6* (Table 15). The vector was listed in the appendix.

Table 15: Oligonucleotides used for cloning, colony PCR, and sequencing during generation of *AtBARK* and *AtMISK in vivo* constructs.

name	sequence	application
<i>AtBARK1_Promotor_GUS_fw</i>	CACCATGACCCGCAACGCAGCGTGATAC	cloning
<i>AtBARK1_Promotor_GUS_rev</i>	CCGGTTGATCACGCATAGGATTC	cloning
<i>AtBARK2_Promotor_GUS_OEC_fw</i>	GAGGATCCCCGGGTACCGAGCTCGAATTATA CGTCTTAGAGCACGTTTTTCGTGTC	cloning
<i>AtBARK2_Promotor_GUS_OEC_rev</i>	GATTTACGGGTTGGGGTTTCTACAGGACGT AACATTGCTTCTGATAACCCTGCAAAC	cloning
<i>AtMISK1_Promotor_GUS_OEC_fw</i>	GAGGATCCCCGGGTACCGAGCTCGAATTATG CAGAGAACATGCTAATTCGTAATTTTC	cloning
<i>AtMISK1_Promotor_GUS_OEC_rev</i>	GATTTACGGGTTGGGGTTTCTACAGGACGT AACATTTATGCTCCGTCAAACCAAATC	cloning
<i>AtBARK1_GGFP_OEC_fw</i>	CAAACAAGTTTGTACAAAAAAGCTGAACGAG AAACATGAATCCTATGCGTGATCAACC	cloning
<i>AtBARK1_GGFP_OEC_rev</i>	CATTTTTTCTACCGGTACCGGGCCCCCCTCC CGCGCCCACCGTTTTGAAGAC	cloning
M13_fw	TGTA AACGACGGCCAGT	colony PCR sequencing
M13_rev	CAGGAAACAGCTATGACC	colony PCR sequencing
GUS_S	CGATCCAGACTGAATGCCACAGG	sequencing
<i>AtBARK1_Gen_S1</i>	GCCCTTGCCAGCTCTGGCCAATTA	sequencing
<i>AtBARK1_Gen_S2</i>	GGAAGTGGTGTAGAACACGAGGTATC	sequencing
<i>AtBARK1_Gen_S3</i>	AGCAGGCTCAAGGAACCTTGAAC	sequencing
<i>AtBARK1_Gen_S4</i>	CACAGGGTGCAGCAAACACAG	sequencing
<i>AtBARK1_Gen_S5</i>	CGCAAGCATGTATCCTGTGACATC	sequencing
<i>AtBARK1_Gen_S6</i>	GCGTCCCTTAAGGACACCATAGC	sequencing

7.4 Protein biochemical methods

7.4.1 Protein expression test

In order to ascertain optimal expression conditions for different protein constructs, expression tests were performed after the following scheme (Figure 54).

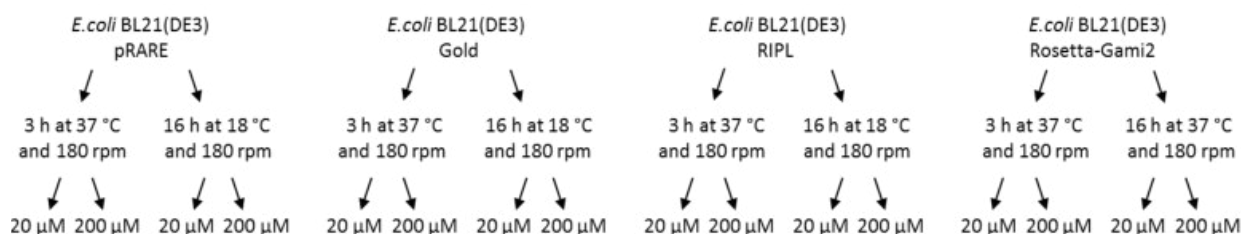


Figure 54: Schematic model of the performed expression tests.

Varying parameters: *E. coli* strains, medium (LB and TB), duration of expression, temperature, IPTG concentration (20 μM and 200 μM).

Four different chemically competent *E. coli* strains (Table 1) were transformed with one of the cloned expression vectors (Table 7) as described in 7.3.12. Pre-cultures were inoculated for the four expression strains in TB medium (36 g·l⁻¹ TB powder, 4 ml·l⁻¹ glycerol, 2.31 g·l⁻¹ KH₂PO₄, 12.54 g·l⁻¹ K₂HPO₄, autoclaved) with required antibiotics (Table 1, 7) and incubated for 16 - 20 h at 37 °C and 180 rpm on the shaker (MAXQ5000/6000). The main culture (30 ml LB medium) was inoculated with 500 μl of the pre-culture and required antibiotics (Table 1, 7) and incubated at 37 °C and 180 rpm on the shaker (MAXQ5000/6000). Once the OD₆₀₀, which was measured with the photometer, reached 0.6, respectively 3 ml of the main culture were transferred to four culture tubes for each *E. coli* strain. Two of them were induced with 20 μM IPTG, the others with 200 μM IPTG and afterward incubated on one hand for 3 h at 37 °C and 180 rpm (MAXQ5000/6000) and on the other hand for 16 h at 18 °C and 180 rpm (Shaker 3015). Additionally, 1 ml of each main culture was taken as a pre-induction sample.

These collected samples were centrifuged 1 min at RT and 14,000 x g (Heraeus Fresco21). The supernatants were discarded and pellets were frozen and stored at -20 °C. The same procedure was performed with the samples of each culture tube after induction and expression for the previously described timeframes.

Pellets were thawed for further analyses. 2 μl of the pellet suspension was added to 4 μl 6x sample buffer (62.5 mM Tris pH 6.9, 2.5 % SDS, 0.002 % bromophenol blue, 10 % glycerol) and 14 μl distilled water. These samples were incubated for 3 min at 95 °C (ThermoStatC) and loaded on the SDS gel (see 7.4.2). The best-performing expression cells and conditions for each construct were listed in Table 16.

Table 16: Register of *AtBARK* and *AtMISK* constructs of this thesis and their best-performing expression cells and conditions.

construct	<i>E.coli</i> strain	antibiotic resistance	expression conditions
pET28a- <i>AtBARK</i> 1(aa1-1025)-6xHis	<i>E.coli</i> BL21(DE3) pRARE	chloramphenicol, kanamycin	TB medium / 37 °C / 3 h / 200 µM IPTG
pET28a- <i>AtBARK</i> 2(aa163-1140)-EGFP-6xHis	<i>E.coli</i> BL21(DE3) RIPL	chloramphenicol, tetracyclin, streptomycin, kanamycin	TB medium / 18 °C / 16 h / 200 µM IPTG
pET17b- <i>AtMISK</i> (aa3-462)-EGFP-6xHis	<i>E.coli</i> BL21(DE3) pRARE	chloramphenicol, ampicillin	TB medium / 18 °C / 16 h / 200 µM IPTG
pET17b- <i>AtMISK</i> (aa3-415)-EGFP-6xHis	<i>E.coli</i> BL21(DE3) pRARE	chloramphenicol, ampicillin	TB medium / 37 °C / 3 h / 200 µM IPTG

7.4.2 SDS-PAGE

SDS-PAGEs were performed with a Mini-Protean[®] Tetra Vertical Electrophoresis Cell and its attachments.

The 10 % resolving gel solution (0.382 M Tris, 0.1 % SDS, 10 % Rotiphorese[®] Gel 30, 0.1 % APS, 0.1 % Temed) was prepared and filled in the gaps between the spacer glass plates and the short glass plates. Ethanol was filled on top of the resolving gels during polymerization for 30 min at RT. In the next step, ethanol was removed and the 5 % stacking gel solution (0.125 M Tris, 0.1 % SDS, 10 % Rotiphorese[®] Gel 30, 0.1 % APS, 0.1 % Temed) was prepared and filled in the gaps on top of the resolving gels. Thereafter, gel combs were inserted and the gels polymerized for 30 min at RT. After polymerization, the combs were removed and the gels were stored at 4 °C in plastic bags packed in wet papers.

The SDS-PAGE chamber for the gels was set up and filled with 1x SDS running buffer (25 mM Tris, 19.2 mM glycine, 0.1 % SDS). 10 µl of the boiled samples and 4 µl PageRuler[™] prestained protein ladder were loaded in the gel pockets. Subsequently, the tank was filled with 1x SDS running buffer and the electrophoresis was performed for 90 min at 140 V. The SDS gels were stained with colloidal Coomassie for 1 h at RT on a shaker (Shaker 3015). Documentation was performed via gel scanning (Epson Perfection V700 Photo).

7.4.3 *Protein expression*

Cells, medium, antibiotics, IPTG concentration, and expression conditions were used according to the results of the expression tests (listed in Table 16).

First, 20 ml LB medium with desired antibiotics was inoculated with one single colony of the cells and incubated overnight at 37 °C and 180 rpm on a shaker (MAXQ5000/6000). 8 ml of this pre-culture was used to inoculate 1 l main culture with desired antibiotics.

The main culture was incubated at 37 °C and 180 rpm on a shaker (MAXQ5000/6000) until the OD₆₀₀, which was measured with the photometer, reached 0.6. Thereafter, IPTG-induction and expression were performed.

7.4.4 *Protein purification*

The expression culture was centrifuged for 20 min at 4 °C and 7000 x g (Avanti[®]J-E centrifuge). The supernatant was removed, while the pellet was dissolved in 30 ml lysis buffer (2x phosphate buffered saline (PBS, 6x PBS: 822 mM NaCl, 16.2 mM KCl, 48.6 mM Na₂HPO₄·2 H₂O, 10.56 mM KH₂PO₄, 6 mM MgCl₂ pH 7.4), 3 % elution buffer (2x PBS, 500 mM imidazole, 1 mM ATP, 1 mM DTT), one protease inhibitor tablet, 1 mM ATP, 1 mM DTT) and disrupted with a high-pressure homogenizer Labor-Pilot2000/4. Disrupted cell components were separated from the proteins with a second centrifugation step for 20 min at 4 °C and 40,000 x g (Avanti[®]J-E centrifuge). Further protein purification was performed in the cooling chamber with a His Trap[™] FF crude immobilized metal affinity chromatography column connected to the purification pump FH10. The clarified bacterial supernatant was loaded on the affinity chromatography column, which was previously equilibrated with 10 column volumes of equilibration buffer (2x PBS, 3 % elution buffer, 1 mM ATP), with a rate of 1 ml·min⁻¹. After application, the column was washed with 10 column volumes of washing buffer (6x PBS, 6 % elution buffer, 1 mM ATP, 1 mM DTT). Thereafter, the protein was eluted with elution buffer. Fractions of 100 µl were collected and analyzed by NanoDrop 2000 measurement and SDS gel electrophoresis (see 7.4.2). The fraction with the highest amount of desired protein was aliquoted, frozen in liquid nitrogen, and stored at -80 °C. The protein concentration was measured in mg·ml⁻¹.

In most experiments, it was difficult to determine a specific concentration of the protein of interest because there were many impurities in the fractions, which might be also part of the total protein concentration.

7.4.5 Tubulin purification from porcine brain

Tubulin preparation was carried out after the protocol of Castoldi et al. [223]. Ten to twelve hemispheres of porcine brain were transported to the lab stored in cold 1x PBS. These hemispheres were cleaned, whereby all remaining blood and the cerebral membrane were removed. Thereafter, they were placed in a pre-cooled 1 l beaker. In the next step, the brain was weighed and the same amount of depolymerization buffer (50 mM MES pH 6.6, 1 mM CaCl₂, 1 mM DTT, 120 mM AEBSF) was added to homogenize the brain with an immersion blender. The mixture was balanced in centrifuge buckets and centrifuged at first for 30 min at 4 °C and 9000 x g (Avanti®J-E centrifuge) and in a second step for 30 min at 4 °C and 30,000 x g (Avanti®J-E centrifuge). Thereafter, the volume (V1) and concentration (NanoDrop 2000) were measured and the same volume of 2x HM-PIPES buffer (1 M PIPES pH 6.9, 10 mM MgCl₂, 20 mM EGTA, 20 % DMSO, 0.1 mM GTP, 1 mM ATP) was added. The sample was balanced in centrifuge buckets again and incubated for 60 min at 35 °C in a water bath, followed by a further centrifugation step for 30 min at 35 °C and 40,000 x g (Avanti®J-E centrifuge). The supernatants were discarded and the pellets were resuspended in 0.1 x V1 ice cold depolymerization buffer. The suspension was homogenized in an ice-cold 15 ml homogenizer and balanced in centrifuge buckets again for a 30-min depolymerization step on ice. Thereafter, samples were centrifuged for 30 min at 4 °C and 30,000 x g (Avanti®J-E centrifuge). The supernatants were collected in 50 ml tubes for volume (V2) and concentration (NanoDrop 2000) measurement. Thereafter, the same volume of 2x HM-PIPES buffer was added. The suspension was balanced in centrifuge buckets again for a 30-min incubation step in the water bath at 35 °C. After the last centrifugation step for 30 min at 35 °C and 40,000 x g (Avanti®J-E centrifuge), the tubulin pellet was ready for freezing in liquid nitrogen and storage at -80 °C or a subsequently labeling.

7.4.6 *Tubulin labeling*

The tubulin pellet from tubulin purification was resuspended in 0.06 x V1 (see 7.4.5) of ice-cold 1x BRB80 (80 mM PIPES pH 6.9, 1 mM MgCl₂, 1 mM EGTA, 120 mM AEBSF, 1 mM DTT) and the suspension was homogenized in a pre-cooled 15 ml homogenizer. Thereafter, depolymerization was performed for 30 min on ice and the sample was centrifuged for 30 min at 4 °C and 40,000 x g (Avanti®J-E centrifuge). The volume (V3) and concentration (NanoDrop 2000) of the supernatant were determined and the same volume 2x HM-PIPES were added. The sample was distributed in tubes and incubated in the water bath for 30 min at 35 °C for polymerization. Each tube was sub-layered with warm high pH cushion (0.1 M HEPES pH 8.6, 1 mM MgCl₂, 1 mM EGTA, 60 % glycerol) and balanced for a further centrifugation step for 45 min at 35 °C and 40,000 x g (Avanti®J-E centrifuge). The supernatants were removed and the pellets were solved in 1 ml pre-warmed labeling buffer (0.1 M HEPES pH 8.6, 1 mM MgCl₂, 1 mM EGTA, 40 % glycerol). A five-fold molar excess of labeling dye (Cy5, digoxigenin or DyLight594 solved in DMSO) was added and incubated for 1 h at 35 °C in the water bath. The same volume of quench solution (2x BRB80 pH 6,9, 100 mM K-glycin, 40 % glycerol) was added and further incubated for 5 min. The suspension was split and added on the top of 2 ml warm low pH cushion (1x BRB80 pH 6,9, 60 % glycerol) in centrifuge tubes. These tubes were balanced and centrifuged for 30 min at 35 °C and 40,000 x g (Avanti®J-E centrifuge). The supernatants were removed and the pellets were solved in 1 ml ice-cold IB (10 mM K-glycin, 5 mM MgCl₂ pH 7). The suspension was homogenized in an ice-cold homogenizer and depolymerized for 30 min on ice. Next, a further centrifugation step for 10 min at 4 °C and 80,000 x g (Optima™ MAX-XP Ultracentrifuge) was performed. The supernatants were mixed with 1x BRB80 containing 4 mM MgCl₂, 1 mM GTP, and 10 % DMSO. Tubulin polymerization was again performed for 30 min at 35 °C in the water bath before the suspension was distributed on ultracentrifuge tubes with 2 ml pre-warmed low pH cushion buffer. A further centrifugation step for 30 min at 35 °C and 40,000 x g was performed (Optima™ MAX-XP Ultracentrifuge). The supernatants were removed and the pellets were dissolved in 250 µl ice-cold IB buffer for a further depolymerization step for 30 min on ice followed by a centrifugation step for 10 min at 4 °C and 80,000 x g (Optima™ MAX-XP Ultracentrifuge). The volume and concentration (Nano Drop 2000) of the supernatant were determined. Thereafter, the concentration was adjusted to 4 mg·ml⁻¹ with IB buffer for further division in 5 µl aliquots. The aliquots were frozen in liquid nitrogen and stored at -80 °C.

7.4.7 Preparation of microtubules

A. Preparation of taxol-stabilized microtubules

Taxol-stabilized microtubules for motility assays were prepared by polymerization of DyLight594-labeled tubulin, which was purified from porcine brain (see 7.4.5/6). 1.25 μl polymerization mix (1x BRB80 pH 6.9, 5 % DMSO, 4 mM MgCl_2 , 1 mM GTP) was added to 5 μl tubulin (4 $\text{mg}\cdot\text{ml}^{-1}$), vortexed, spun down, and polymerized for 30 min at 37 °C (ThermoStatC). 100 μl 1x BRB80 pH 6.9 containing 10 μM taxol was added for microtubule stabilization. Thereafter, the sample was centrifuged for 10 min at 30 °C and 21,100 x g (Heraeus Fresco21) to remove unpolymerized tubulin dimers. After centrifugation, the supernatant was discarded and the microtubule pellet was resuspended in 200 μl 1x BRB80 pH 6.9 containing 10 μM taxol. Microtubules were stored at RT in the dark for 1 - 3 days.

B. Preparation of taxol-stabilized digoxigenin microtubules

Taxol-stabilized digoxigenin microtubules were also needed for sliding assays. They were prepared by polymerization of a mixture of DyLight594-labeled and digoxigenin-labeled tubulin, which were both purified from porcine brain (see 7.4.5/6). The preparation was performed as described for taxol-stabilized microtubules. Solely the amount of the polymerization mix and tubulin differed: 2.5 μl polymerization mix, 5 μl digoxigenin-labeled tubulin (4 $\text{mg}\cdot\text{ml}^{-1}$), and 1 μl DyLight594-labeled tubulin (4 $\text{mg}\cdot\text{ml}^{-1}$).

C. Preparation of taxol-stabilized polarity-marked microtubules

In order to determine the direction of motor movement, taxol-stabilized, polarity-marked microtubules were needed for motility assays. First, a mixture composed of 1x BRB80 pH 6.9 containing 2.5 mM GTP and 10 mM GMPCPP was prepared. 3.3 μl of this mixture was added to 5 μl Cy5-labeled tubulin (4 $\text{mg}\cdot\text{ml}^{-1}$), which was purified from porcine brain (see 7.4.5/6), and incubated for 20 min at 37 °C (ThermoStatC). During this incubation time, an elongation mix composed of 1x BRB80 pH 6.9 containing 0.5 mM NEM, 10 mM GMPCPP, and 100 mM MgCl_2 was prepared and stored for 30 sec at 37 °C (ThermoStatC). Thereafter, 6 μl of the mixture with Cy5-labeled tubulin was added to the elongation mix together with 1.5 μl DyLight594-labeled tubulin (4 $\text{mg}\cdot\text{ml}^{-1}$) and incubated for 20 min at 37 °C (ThermoStatC). In the next step, 100 μl 1x BRB80 pH 6.9 containing 20 μM taxol was added to stop the reaction and stabilize microtubules. Thereafter, the sample was centrifuged for 10 min at 30 °C and 21,100 x g (Heraeus Fresco21). The supernatant was discarded and the pellet was resuspended in 100 μl 1x BRB80 containing 10 μM taxol. Microtubules were stored at RT in the dark for 1 - 3 days.

7.5 Methods for characterization of kinesin motor proteins

7.5.1 Generation of unilamellar vesicles from an inverted emulsion

100 μl lipid solution ($100 \text{ mg}\cdot\text{ml}^{-1}$ in chloroform) was filled in a small glass vial and dried under constant air flow. Thereafter, the glass vial was placed on a heating plat for 30 min at $100 \text{ }^\circ\text{C}$ to remove remaining chloroform. 1 ml mineral oil solution was added and incubated on the heating plate for 1 h at $100 \text{ }^\circ\text{C}$. Next, this lipid suspension ($10 \text{ mg}\cdot\text{ml}^{-1}$) was sonicated (Ultrasonic bath S30 Elmasonic) for 15 min and stored at RT.

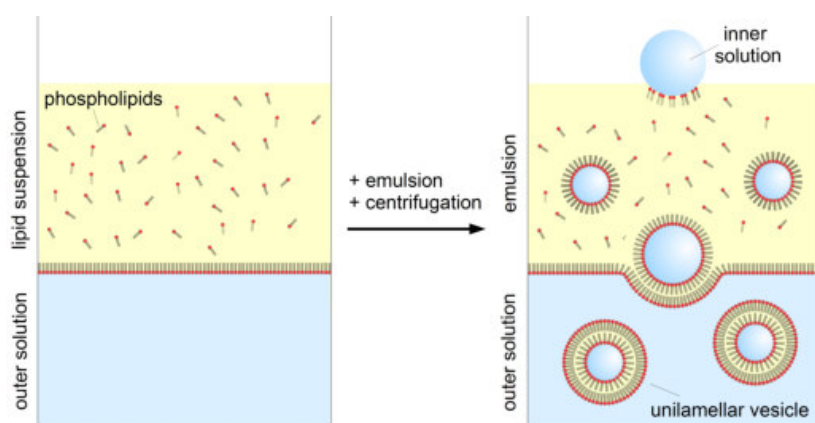


Figure 55: Schematic model of the generation of unilamellar vesicles from an inverted emulsion.

For vesicle formation, 10 μl inner solution (0.5 M sucrose in 1x BRB80 pH 6.9) was emulsified in 200 μl lipid suspension and kept for 2 h on ice. 200 μl lipid suspension was pipetted on the top of 600 μl outer solution (0.5 M glucose in 1x BRB80 pH 6.9) in a second tube and incubated at $85 \text{ }^\circ\text{C}$ (ThermoStatC) until the oil-water interface turned flat. Next, it was cooled on ice before the emulsion was added to the top. The sample was briefly centrifuged (Heraeus Fresco21) before the oil was removed and the vesicle solution was collected in a new tube. For vesicle illumination, 5 μl DyLight594-labeled tubulin ($4 \text{ mg}\cdot\text{ml}^{-1}$) were added to the inner solution. Vesicle membranes were labeled with the DiD. Vesicles were stored at $4 \text{ }^\circ\text{C}$.

7.5.2 Vesicle-binding assay

Binding assays were performed to investigate the binding efficiency between motors and vesicles. Vesicles were prepared as described in 7.5.1 with lecithin (97 % PC) or two phospholipid mixtures with 20 % or 50 % PS. 5 μl motor ($\sim 1.3 \text{ mg}\cdot\text{ml}^{-1}$) were incubated with 10 μl vesicle solution for 20 min on ice. During this process, vesicles and bound motor proteins accumulated at the top of the solution. The upper and lower phases were separated, mixed with 6x sample buffer, and boiled for 3 min at $95 \text{ }^\circ\text{C}$ (ThermoStatC). Thereafter, they were loaded on an SDS gel. SDS-PAGE was performed as described in 7.4.2.

7.5.3 Preparation of flow cell chambers for *in vitro* assays

Most assays for protein characterization were performed in flow cells. Gliding, sliding, stepping, and vesicle transport assays needed coverslips with a hydrophobic surface.

A. Cleaning procedure for coverslips with a hydrophobic surface

18x18 mm and 22x22 mm coverslips were placed in a rack and sonicated subsequently in different solutions in an ultrasonic bath (Ultrasonic bath S30 Elmasonic) for 15 min: 5 % mucasol, 2 M NaOH, distilled water, sodium hypochlorite, distilled water, 30 % ethanol with 1 M HCl, and distilled water. After each solution, they were rinsed with distilled water and after sonication with sodium hypochlorite, the coverslips were incubated further 45 min in the solution before the protocol went on. After the last washing step, coverslips were dried under compressed air flow and incubated in a plasma cleaner (Zepto, Diener electronic) for 3 min. For hydrophobic coating, the coverslips were placed in a desiccator with 100 μ l trichloro(1H,1H,2H,2H-perfluorooctyl)silane under vacuum for at least 12 h. The coverslips could be stored several days in closed glass containers with silica gel.

B. Preparation of flow cells

For flow cell preparation, three thin parafilm stripes were placed between a 22x22 mm bottom and a 18x18 mm top coverslip to form two approximately 2 mm wide flow channels. Thereafter, the flow cell was placed for a few minutes on a heating plate at 60 °C to press the melting parafilm gently to both coverslips. Overhanging parafilm was cut and the flow cell was placed into a metal holder ready to use for motility assays (Figure 56).

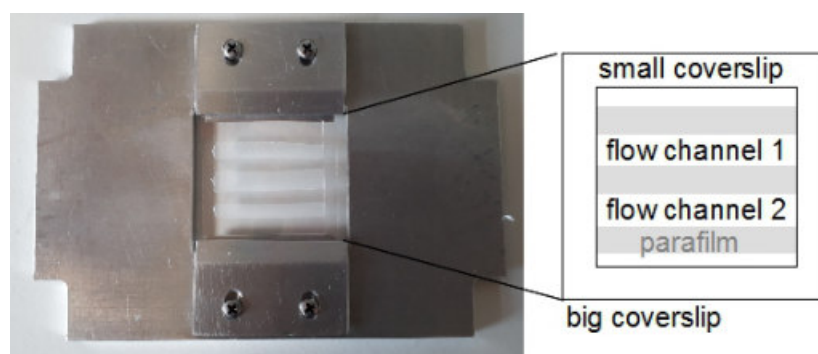


Figure 56: Flow cell chamber for *in vitro* assays.

7.5.4 Gliding assay

The gliding assay serves as a method to determine the velocity and direction of motor protein movement. If one end of the microtubules is specifically labeled, the directionality of motor movement can also be determined (Figure 57) [78-80].

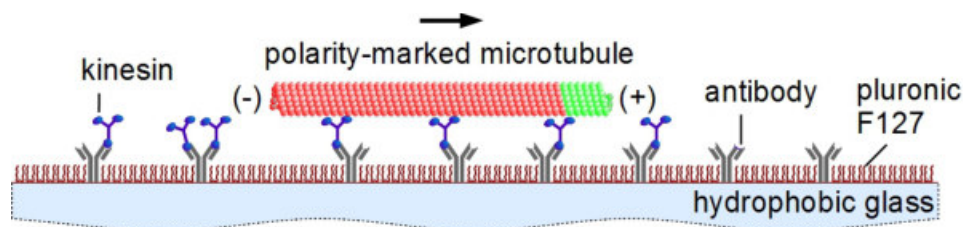


Figure 57: Schematic model of a gliding assay.

The channels of the flow cell were successively filled with different solutions. First, GFP or His antibodies, ($5 \mu\text{g}\cdot\text{ml}^{-1}$ or $10 \mu\text{g}\cdot\text{ml}^{-1}$ in 1x BRB80 pH 6.9) were filled in the channels with a vacuum pump and incubated for 10 min at RT. Thereafter, the channels were blocked for 1 h with 1 % Pluronic F127 in 1x BRB80 pH 6.9 at RT to prevent unspecific binding of proteins, and washed with 1x BRB80 pH 6.9 again. In the next step, the motors were immobilized by flushing the channels with a kinesin solution ($13 \mu\text{g}\cdot\text{ml}^{-1}$ kinesin in 1x BRB80 pH 6.9 - 8.0 containing 1 mM ATP and 10 mM DTT), which was incubated for 5 min at RT. DyLight594-labeled or polarity-labeled microtubules - diluted in 1x BRB80 pH 6.9 containing 10 μM taxol, 10 mM DTT, and 1 mM ATP - were filled in the channels. Finally, the imaging solution (1x BRB80 pH 6.9 - 8.0, containing 10 μM taxol, 10 mM DTT, 1 mM ATP, 40 mM glucose, 40 $\mu\text{g}\cdot\text{ml}^{-1}$ glucose oxidase, and 16 $\mu\text{g}\cdot\text{ml}^{-1}$ catalase) was added, to start the transport process. After applying of the imaging solution, the chamber was placed on an inverted fluorescence microscope (Nikon Eclipse Ti) with an APO TIRF 100x/1.49 oil immersion objective (intermediate lens 1.0x) and an objective heater (TempController 2000-1), which generated a constant temperature of 28 °C. The motility of DyLight594-labeled microtubules (562 nm) over the motor-coated surface was observed by epifluorescence. The emission was detected and analyzed by the software NIS-Elements AR4.40.00. Movies that were used for further velocity analyses were taken with an Andor iXon3 EMCCD camera with a detection rate of 1 frame per 5 s over 5 min.

FIESTA [82] was used for molecule tracking. This program tracked the middle of each structure, which was recognized as a microtubule, over the whole time frame and connected these points to a continuous track. With this time-distance track, the velocity of each continuously moving filament was calculated from the data and visualized with MATLAB. The mean motor velocity was determined with a Gaussian fit.

7.5.5 Sliding assay

The sliding assay serves as a method to determine the sliding velocity of motors that crosslink microtubules (Figure 58) [80].

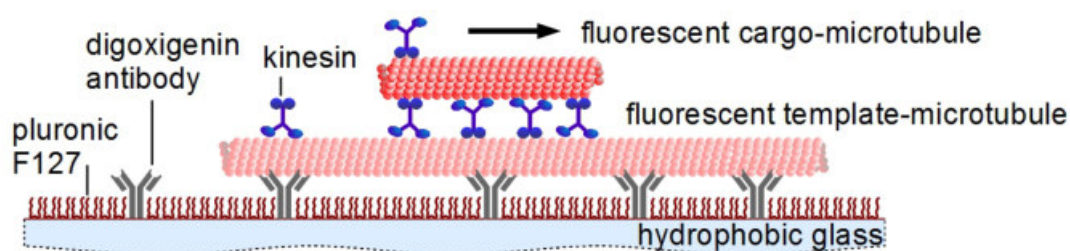


Figure 58: Schematic model of a sliding assay.

The channels of the flow cell were successively filled with different solutions. First, the digoxigenin antibodies ($20 \mu\text{g}\cdot\text{ml}^{-1}$ in 1x BRB80 pH 6.9) were filled in the channels with a vacuum pump and incubated for 5 min at RT. Thereafter, the channels were blocked for 1 h with 1 % Pluronic F127 in 1x BRB80 pH 6.9 at RT to prevent unspecific binding of proteins, and washed with BRB80 pH 6.9 again. In the next step, DyLight594-labeled digoxigenin microtubules - diluted in 1x BRB80 pH 6.9 containing $10 \mu\text{M}$ taxol - were filled in the channels and immobilized to the surface at RT. Subsequently, the motor was added by flushing the channels with a kinesin solution ($13 \mu\text{g}\cdot\text{ml}^{-1}$ kinesin in BRB80 pH 6.9 - 8.0 containing 10 mM DTT) without ATP and incubated for 5 min at RT. DyLight594-labeled or polarity-labeled microtubules - diluted in 1x BRB80 pH 6.9 containing $10 \mu\text{M}$ taxol and 10 mM DTT - were filled in the channels and incubated briefly at RT. Finally, the imaging solution (1x BRB80 pH 6.9 - 8.0 containing $10 \mu\text{M}$ taxol, 10 mM DTT, 1 mM ATP, 40 mM glucose, $40 \mu\text{g}\cdot\text{ml}^{-1}$ glucose oxidase, and $16 \mu\text{g}\cdot\text{ml}^{-1}$ catalase) was added. Thereafter, the prepared chamber was placed on an inverted fluorescence microscope (Nikon Eclipse Ti) with an APO TIRF 100x/1.49 oil immersion objective (intermediate lens 1.0x) and an objective heater (TempController 2000-1), which generated a constant temperature of $28 \text{ }^\circ\text{C}$. The motility of DyLight594-labeled cargo-microtubules (562 nm), which were transported along DyLight594-labeled template-microtubules (562 nm) by motors, was observed with epifluorescence. The emission was detected and analyzed by the NIS-Elements AR4.40.00. Movies that were used for further velocity analyses were taken with an Andor iXon3 EMCCD camera with a detection rate of 1 frame per 5 s over 5 min.

Velocity analyses were performed with FIESTA [82] and MATLAB as described in 7.5.4.

7.5.6 Stepping assay

The stepping assay is a method for the characterization of single motor molecules. It determines the velocity, direction, and processivity of motor protein movement (Figure 59) [78, 80].

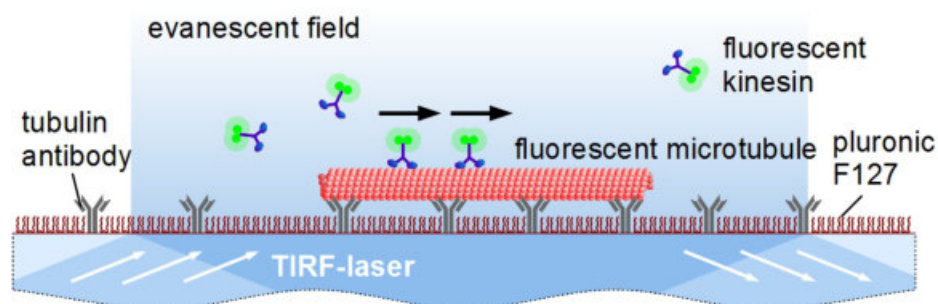


Figure 59: Schematic model of a stepping assay.

The channels of the flow cell were successively filled with different solutions. First, the tubulin antibodies ($25 \mu\text{g}\cdot\text{ml}^{-1}$ in 1x BRB80 pH 6.9) were filled in the channels with a vacuum pump and incubated for 10 min at RT. The channels were blocked for 1 h with 1 % Pluronic F127 in 1x BRB80 pH 6.9 at RT, and washed with 1x BRB80 pH 6.9 again. Next, DyLight594-labeled microtubules were immobilized by flushing the channels with a microtubule solution (microtubules in 1x BRB80 pH 6.9 containing $10 \mu\text{M}$ taxol), which was incubated briefly at RT. Finally, the imaging solution with motor (1x BRB80 pH 6.9 - 8.0 containing $10 \mu\text{M}$ taxol, 10 mM DTT, 1 mM ATP, 40 mM glucose, $40 \mu\text{g}\cdot\text{ml}^{-1}$ glucose oxidase, $16 \mu\text{g}\cdot\text{ml}^{-1}$ catalase, and $13 \text{ ng}\cdot\text{ml}^{-1}$ motor) was added. The prepared chamber was placed on an inverted fluorescence microscope (Nikon Eclipse Ti) with an APO TIRF 100x/1.49 oil immersion objective (intermediate lens 1.5x) and an objective heater (TempController 2000-1), which generated a constant temperature of $28 \text{ }^\circ\text{C}$. The interaction of GFP-labeled motors (488 nm) and DyLight594-labeled microtubules (562 nm) was observed by TIRF microscopy (see 7.5.9). The emission was detected and analyzed by the software NIS-Elements AR4.40.00. Movies that were used for analyses were taken with an Andor iXon3 EMCCD camera with a detection rate of 1 frame per 100 ms over 1 min.

Fiji [224] was used to create kymographs for the analysis of motor processivity. FIESTA [82] and MATLAB were used for molecule tracking and the evaluation of the MSD and the diffusion coefficient with a routine obtained from Dr. Friedrich Schwarz (TU Dresden). The MSD is often used for the measurement of undirected, random movements to calculate the distance, which is covered by a molecule on mean in a specific time frame [225].

7.5.7 Vesicle transport assay

Vesicle transport assays were performed to determine the transport velocity of the motors during cargo interaction (Figure 60).

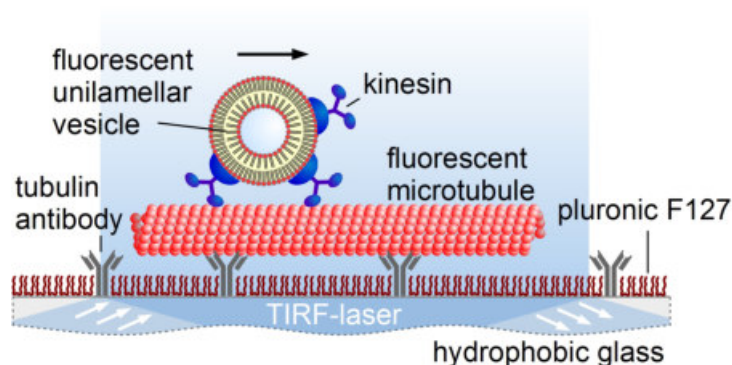


Figure 60: Schematic model of a vesicle transport assay.

The channels of the flow cell were successively filled with different solutions. First, the tubulin antibodies ($25 \mu\text{g}\cdot\text{ml}^{-1}$ in 1x BRB80 pH 6.9) were filled in the channels with a vacuum pump and incubated for 10 min at RT. Subsequently, the channels were blocked for 1 h with 1 % Pluronic F127 in 1x BRB80 pH 6.9 at RT to prevent unspecific binding of proteins, and washed with 1x BRB80 pH 6.9 again. DyLight594-labeled microtubules were immobilized to the surface by flushing the channel with a microtubule solution (microtubules in BRB80 pH 6.9 containing $10 \mu\text{M}$ taxol), which was incubated briefly at RT. Next, the imaging solution with diluted DiD-labeled vesicles (1x BRB80 pH 6.9 containing $10 \mu\text{M}$ taxol, 10 mM DTT, 1 mM ATP, 40 mM glucose, $40 \mu\text{g}\cdot\text{ml}^{-1}$ glucose oxidase, $16 \mu\text{g}\cdot\text{ml}^{-1}$ catalase, and $2 \mu\text{l}$ vesicles) was filled in the channel and incubated briefly at RT. Finally, the imaging solution with motor ($\sim 13 \mu\text{g}\cdot\text{ml}^{-1}$) was added. The prepared chamber was placed on an inverted fluorescence microscope (Nikon Eclipse Ti) with an APO TIRF 100x/1.49 oil immersion objective (intermediate lens 1.0x) and an objective heater (TempController 2000-1), which generated a constant temperature of $28 \text{ }^\circ\text{C}$. The transport of DiD-labeled vesicles (640 nm) along DyLight594-labeled microtubules (562 nm) by motors was observed with TIRF microscopy (see 7.5.9). The emission was detected and analyzed by the software NIS-Elements AR4.40.00. Movies that were used for further analyses were taken with an Andor iXon3 EMCCD camera with a detection rate of 1 frame per 1 s over 5 min.

Fiji [224] and FIESTA [82] were used as described in 7.5.6 for motor processivity and MSD analyses. For velocity analyses, vesicles were tracked with FIESTA. The mean velocity of each moving vesicle was calculated and visualized in MATLAB. The mean transport velocity was determined with a Gaussian fit.

7.5.8 Components used for the solutions of the motility assays

The main components of the solutions that were filled in the flow channels during motility assays had specific functions:

ATP is bound and hydrolyzed by the motor to convert chemical energy into mechanical work for the transport of microtubules along the surface [1, 4, 5].

Other listed components were added to suppress photobleaching of the fluorescent dye. **Glucose**, **catalase**, and **glucose oxidase** are agents, which reduce oxygen concentration. A reduced oxygen concentration impairs building of harmful reactive oxygen species. **DTT** reduces free radicals and is part of the repairing system of fluorophores, which were damaged by reactive oxygen species [78].

Taxol stabilizes microtubules by preventing depolymerization [10].

7.5.9 Total internal reflection fluorescence microscopy

Epifluorescence microscopy, which was used for gliding and sliding assays, cannot illuminate single molecules due to a strong, disturbing background fluorescence. However, it was necessary to illuminate single molecules in stepping and vesicle transport assays. Therefore, TIRF microscopy was used.

The TIRF-laser shines in a specific angle (α) on the glass-sample-boundary and is totally reflected. This leads to the formation of an evanescent wave in the sample behind the glass. The intensity of this evanescent wave exponentially decreases the more the light enters the sample. Therefore, it is possible to illuminate a very thin area very close to the glass surface. (Figure 61) [226-228]. In this area, single molecules interact with immobilized microtubules and can be detected.

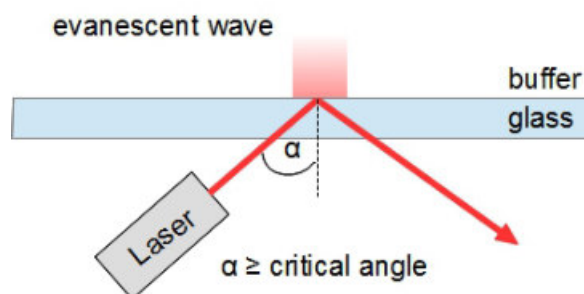


Figure 61: Principle of TIRF microscopy.

7.5.10 Generation of supported lipid bilayers

A. Preparation of multilamellar vesicles

A $0.5 \mu\text{g}\cdot\mu\text{l}^{-1}$ lipid suspension (lipids in chloroform with 0.0005 mol% DiD) was prepared. 100 μl of this lipid mixture were pipetted in a glass vial and dried under compressed air flow. The glass vial was placed on a heating plate for 30 min at 100 °C. Thereafter, 200 μl HEPES buffer (20 mM HEPES, 75 mM NaCl pH 7.2) was added and incubated for 15 min on the heating plate. Finally, the lipid suspension was vortexed for 10 min and divided in 20 μl aliquots, which were frozen in liquid nitrogen and stored at -20 °C.

B. Cleaning procedure of coverslips for supported lipid bilayers

Coverslips (22x22 mm) were washed with warm water, rubbed with mucasol, and washed with warm water and distilled water again. Subsequently, they were placed in racks and sonicated in ethanol and distilled water, each time for 10 min in an ultrasonic bath (Ultrasonic bath S30 Elmasonic). Further washing steps were performed in distilled water, ethanol, acetone, ethanol, and distilled water. The cleaned coverslips were dried under compressed air flow. They could be stored several days in closed glass containers with silica gel.

C. Preparation of supported lipid bilayers

Coverslips (22x22 mm) were plasma treated for 5 min (plasma cleaner ZEPTO). Meanwhile, an aliquot of multilamellar vesicles (MLVs) was mixed with 140 μl HEPES buffer (20 mM HEPES, 75 mM NaCl pH 7.2) and sonicated for 10 min in an ultrasonic bath (Ultrasonic bath S30 Elmasonic). The chambers for SLBs were prepared with PCR tubes, which were cut in the middle and stuck on the coverslip with ultraviolet (UV)-curable glue (Figure 62).

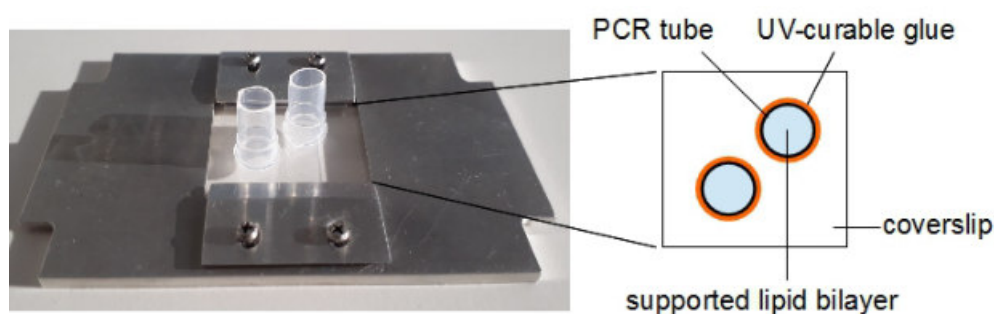


Figure 62: Supported lipid bilayer chambers for membrane assays.

The glue was cured under UV-light for 10 min. 40 μl vesicle solution, 3 μl 0.1 M CaCl_2 and 57 μl HEPES buffer were filled in each chamber and incubated for 20 min at RT for lipid-layer formation. Thereafter, the chambers were washed with 750 μl desired buffer in ten steps of 75 μl to remove remaining vesicles.

7.5.11 Fluorescence recovery after photobleaching microscopy

FRAP microscopy was used as described by Grover et al. [81] to test the integrity of the generated SLBs. For the FRAP test, the lipophilic dye DiD (640 nm) was added to the SLB as fluorescence marking. For photobleaching, a rectangular area was bleached with a high-intensity UV-laser. Subsequently, the bleached area was observed by TIRF-laser microscopy. In case of an intact membrane, the lipophilic dye diffuses through the membrane and enables an increase of fluorescence intensity in the bleached area. This method was performed with an inverted fluorescence microscope (Nikon Eclipse Ti) with an Andor spinning disk and FRAPPA unit, and an APO TIRF 100x/1.49 oil immersion object (intermediate lens 1,5x). The emission was detected and analyzed by the software NIS-Elements AR4.40.00. Movies that were used for further analyses were taken with an Andor iXon3 EMCCD camera with a detection rate of 1 frame per 1 s over 5 min.

7.5.12 Membrane gliding assay

The membrane gliding assay was performed to determine the microtubule-transport velocity of motors that interact with membranes (Figure 63) [81].

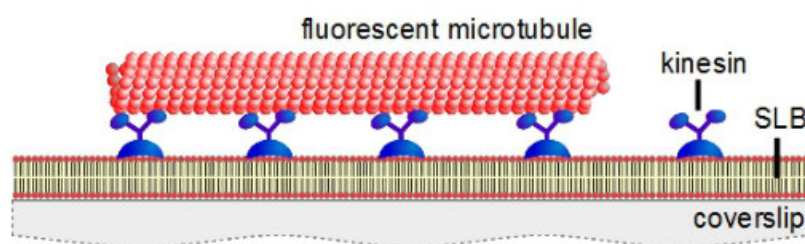


Figure 63: Schematic model of a membrane gliding assay.

The SLB chambers were filled with 25 μl 2x imaging solution (1x BRB80 pH 6.9 containing 20 μM taxol, 20 mM DTT, 2 mM ATP, 80 mM glucose, 80 $\mu\text{g}\cdot\text{ml}^{-1}$ glucose oxidase, and 32 $\mu\text{g}\cdot\text{ml}^{-1}$ catalase) containing motor (13 $\mu\text{g}\cdot\text{ml}^{-1}$) and DyLight594-labeled microtubules (562 nm). After a short incubation time at RT, the samples chambers were placed on an inverted fluorescence microscope (Nikon Eclipse Ti) with an APO TIRF 100x/1.49 oil immersion object (intermediate lens 1.0x) and an objective heater (TempController 2000-1), which generated a constant temperature of 28 $^{\circ}\text{C}$. The motility of microtubules over the motor-coated surface was observed by epifluorescence. The emission was detected and analyzed by the software NIS-Elements AR4.40.00. Movies that were used for further velocity analyses were taken with an Andor iXon3 EMCCD camera with a detection rate of 1 frame per 1 s over 5 min.

Velocity analyses were performed as described in 7.5.4.

7.6 Methods for cultivation and analysis of *Arabidopsis thaliana* plants

7.6.1 Cultivation of *Arabidopsis thaliana* plants

A. Sowing on soil

Seeds were sown on a composition of soil/sand/swelling clay (6.5/2.5/1) for plant cultivation. The soil was pretreated 2 h with BioMückk ($1 \text{ ml} \cdot \text{l}^{-1}$) and briefly with Previcur ($2.5 \text{ ml} \cdot \text{l}^{-1}$) to avoid pest infestation. Seeds were sowed and covered with a cap. They were stored 3 - 5 days in the cooling chamber ($8 \text{ }^\circ\text{C}$) for stratification. Thereafter, pots were transferred into the climate chamber or the climate cabinet (Percival) for further growth processes.

B. Sowing on agar plates

Seeds were sterilized with chloric gas (50 ml sodium hypochlorite and 2.3 ml 32 % HCl) in a desiccator for 4 - 6 h. Sterilized seeds were evaporated briefly under the sterile bench and sowed on MS-agar plates (0.5 % MS powder, 1 % sucrose, 0.8 % phyto agar, pH 5.7) with sterile toothpicks. Subsequently, the plates were sealed with a tape and stored for 2 days at $4 \text{ }^\circ\text{C}$. Thereafter, they were shifted in a tilted position in the climate cabinet (Percival).

The selection of transformed seeds on agar plates was performed by the addition of respective antibiotics to the MS-agar.

C. General cultivation conditions

A. thaliana plants were cultured in climate cabinets (Percival) or climate chambers under following long day conditions (Table 17).

Table 17: Growth conditions in climate chambers and cabinets for *A. thaliana* plant cultivation.

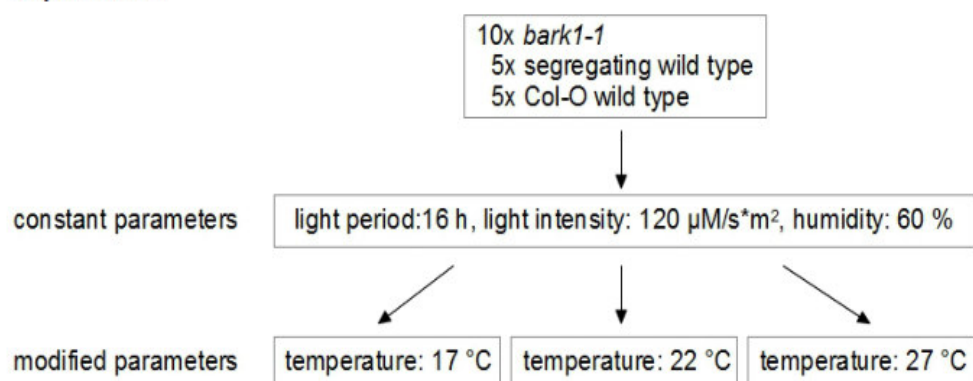
temperature	22 - 24 $^\circ\text{C}$
humidity	60 %
light intensity	$120 \mu\text{M} \cdot \text{s}^{-1} \cdot \text{m}^{-2}$
light period	16 h

Temperature and humidity were documented with data loggers (OM-EL-USB-2-LCD-PLUS) and the light was measured with the LI-250A light meter with a quantum sensor.

7.6.2 Phenotype analyses of bark T-DNA insertion lines

Morphological analyses of *bark* T-DNA insertion plants were performed as well as pollen germination and silique analyses. In order to enhance possible phenotypes, plants were sowed and grown on soil (see 7.6.1) under different temperature and humidity conditions according to the following scheme (Figure 64).

experiment 1



experiment 2

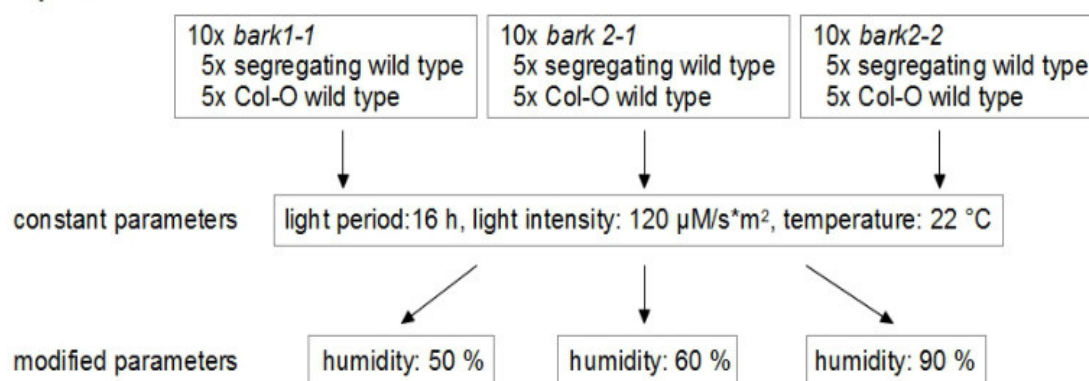


Figure 64: Cultivation conditions during phenotype analyses of the *bark* T-DNA insertion lines.

All plants for the experiments were genotyped (see 7.3.5), whereby it was possible to compare homozygous and segregating wild-type plants of the *bark* T-DNA insertion lines and Col-0 plants.

A. Morphological analyses

Plant growth was documented with photography (Canon EOS600d) weekly over a period of seven weeks for morphological analyses of different plant groups in the temperature and humidity experiment.

B. Pollen germination assays

In order to analyze the pollen germination and further pollen tube growth of different plant groups in the temperature and humidity experiments, pollen germination assays were performed.

In a first step, the pollen germination medium composed of 5 mM MOPS with 1.62 mM boric acid, 4 mM CaCl₂, 1 mM KCl, 1 mM MgCl₂ and 18 % sucrose was prepared and adjusted to pH 7 with 1 M Tris. In the next step, 0.5 % agarose was melt in the pollen germination medium at 95 °C. The generated pollen germination agar was divided into 500 µl aliquots, which were stored at 4 °C until further application.

The pollen germination agar was melted at 95 °C, and 50 µl were pipetted in a round area of breathable film surrounded by an adhesive film. If pollen germination assays were performed with oryzalin, it was added freshly to the pollen germination agar with a final concentration of 0.5 µM, 1 µM, 2.5 µM and 5 µM. After a few minutes, the agar solidified. Next, the pollen could be carefully applied to the top. Therefore, the pollen was harvest from the anthers of desired flowering plants and applied on agar (Leica S4 E). In order to obtain a closed chamber, the adhesive film around the agar was stuck to an object slide or coverslip. The single pollen grains or tubes were visualized by microscopy through the object slide or coverslip (Figure 65).

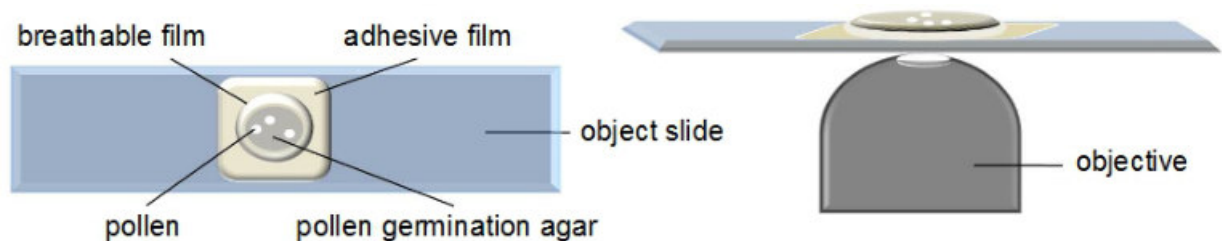


Figure 65: Schematic model of chambers for pollen germination assays.

The prepared chamber was placed on an inverted Nikon Eclipse Ti with a CIF Plan Fluor 40x/1.30 oil immersion objective or an APO TIRF 100x/1.49 oil immersion objective (intermediate lens 1.0x or 1.5x). Movies that were used for further analyses were taken with a ProgRes CT5 camera with a detection rate of 1 frame per 10 min over 12 - 24 h.

In order to visualize fluorescence-labeled constructs in pollen tubes, an APO TIRF 100x/1.49 oil immersion objective (intermediate lens 1,5x) was used and movies were taken with an Andor iXon3 EMCCD camera with a detection rate of 1 frame per 1 s over 5 min.

C. Silique and seed analyses

Five siliques of all plant groups in the temperature and humidity experiment were collected in an approximately similar growth stage of the plants. These collected siliques were decolorized and the refraction index was adapted for seed counting through the addition of 1 ml bleaching solution (25 % Urea, 15 % sodium deoxycholate, 10 % Xylitol) [89] for a few days. Transparent siliques were documented by pictures with the macroscope (Olympus MVX10) for further analyses like seed counting. The seeds of five siliques of three to ten biological replicates were counted and the seed number (mean \pm s.d.) was used for further statistical analyses. The two-sample t-test for independent samples with unequal standard deviations was performed. This statistical significance test investigates the relation between the mean values of two basic populations with the help of the mean values of two independent samples. The level of significance was specified with $p < 5\%$, 1% , and 0.1% .

7.6.3 *Phenotype analyses of *misk1* T-DNA insertion lines*

The *misk1* T-DNA insertion lines (Table 5) were analyzed concerning morphological structure abnormalities of the roots. All plants for the experiments were genotyped (see 7.3.5) to compare homozygous and segregating wild-type plants.

Seeds of required plants were sown on plant agar (see 7.6.1) and growth was documented constant via scanning over a period of ten days. With these pictures, morphological analyses of the roots were performed concerning parameters like root size, growth, and development state. After 7 - 10 days, some of these plants were removed from the agar and transferred into 2 ml tubes for further detailed xylem tissue analyses. Therefore, roots were decolorized and the refraction index was adapted through the addition of 1 ml bleaching solution (25 % Urea, 15 % sodium deoxycholate, 10 % Xylitol) [89]. The annular xylem tissue was documented via microscopy (Nikon Eclipse Ti, CFI Plan Fluor 40x/1.30 or APO TIRF 100x/1.49 oil immersion object (intermediate lens 1.0x)). Pictures of the annular xylem tissue were taken with a ProgRes CT5 camera and analyzed concerning structural abnormalities with Fiji and MATLAB. The program determined the pitch of the helical secondary cell wall of xylem cells from analyses of a line scan on light microscopic bright-field illuminated images. The calculated mean distances (mean \pm s.d.) were further compared between homozygous and segregating wild-type plants to evaluate possible morphological differences.

7.6.4 Floral painting and selection of transgenic plants

An overnight culture was prepared with 20 ml LB medium and the respectively required agrobacteria (Table 2) and antibiotics (Table 4) and placed on the incubator shaker (MAXQ5000/6000) at 28 °C. The Col-0 plants should be in the stage of bud building and watered well for the painting process. On the next day, the painting solution was prepared. Therefore, the overnight culture was centrifuged in 50 ml tubes for 10 min at RT and 4700 x g (Sorvall ST 16R) and solved in 20 ml sucrose-silwett-77 solution (5 % sucrose, 0.05 % silwett-77 in distilled water). This bacterial suspension was painted on the buds of the Col-0 plants three times. Thereafter, painted plants were covered with plastic bags to retain the humidity for a better infiltration. Plants were grown in the climatic chambers (see 7.6.1) until the seeds were harvested.

7.6.5 Generation of promotor-GUS lines and 35S-bark1-GFP lines

In order to establish the promotor-GUS lines of *bark1*, *bark2*, and *misk1* as well as 35S-*bark1*-GFP lines, agrobacteria (Table 2) were transformed with one of the prepared vector constructs (see 7.3.13) for following infiltration of Col-0 plants via floral painting (see 7.6.4). Harvest seeds were sowed and cultured as described in 7.6.1 on MS-agar with hygromycin B (20 mg·l⁻¹) for the selection of transgenic plants. Resistant, growing plants were transferred to agar without antibiotics. Thereafter, gDNA was isolated (see 7.3.4) and plants were genotyped (see 7.3.5) to prove a successful infiltration again. The following primer combinations were used for the different lines: *AtBARK1_Prom_fw*/*AtBARK2_Prom_fw*/*AtMISK1_Prom_fw* and *GUS_rev* as well as 35S-*AtBARK1*-GFP_fw and 35S-*AtBARK1*-GFP_rev (see Table 18). The PCR was analyzed by gel electrophoresis (see 7.3.6).

Seeds of successfully infiltrated plants were collected for the new established transgenic line.

Table 18: Oligonucleotides used for genotyping of the promotor-GUS and the 35S-bark1-GFP lines.

name	sequence	application
<i>AtBARK1_Prom_fw</i>	TGTGGTGATATAGCGACGTGAC	genotyping
<i>AtBARK2_Prom_fw</i>	GTGTTTGTGGCTACCTGCTATC	genotyping
<i>AtMISK_Prom_fw</i>	GACTCGAACTCATGCCTCTTTG	genotyping
<i>GUS_rev</i>	CACCGAAGTTCATGCCAGTC	genotyping
35S- <i>AtBARK1</i> -GFP_fw	GTAATCCCAGCAGCTGTTAC	genotyping
35S- <i>AtBARK1</i> -GFP_rev	GGCAGCCCTTATGGAGATTC	genotyping

7.6.6 *β-glucuronidase staining*

The GUS staining was used to analyze tissue-specific expression of genes qualitatively by promoter activity [85]. Therefore, the promoter of the gene of interest was cloned into a vector in front of the β -glucuronidase gene (see 7.3.17). *Agrobacteria* (Table 2) were transformed with one of the prepared vector constructs (see 7.3.13) for following infiltration of Col-0 plants via floral painting (see 7.6.4). Seeds of successfully infiltrated plants were seeded for analyses.

The plant material of interest was harvested from the respective plants and collected in 2 ml tubes with 0.1 M sodium phosphate buffer pH 7. The buffer was exchanged by 500 μ l of the GUS staining solution (20 mM phosphate buffer, 3 mM ferrocyanide, 0.5 % TritonX-100, 0.001 $\text{g}\cdot\text{ml}^{-1}$ X-Gluc in DMSO). Samples were placed in the vacuum infiltrator (Concentrator plus) for 10 min at RT. Thereafter, the samples were placed in the dark 37 °C incubator for specific time frames (4 - 24 h). Col-0 plants were carried along as staining controls. If the promoter was active and the enzyme β -glucuronidase was produced, it hydrolyzed 5-bromo-4-chloro-3-indolyl glucuronide (X-Gluc) to glucuronic acid and 5-bromo-4-chloro-indoxyl, which was oxidized to a blue dye (5,5'-dibromo-4,4'-dichloro-indigo) [85]. This dye could be observed in the tissue by microscopy. After the staining period, samples were destained with 500 μ l ethanol-glacial acetic acid two times for 30 min and stored in this solution until macroscopic analysis. For macroscopic analysis, samples were prepared on slides in distilled water and covered with a coverslip. Subsequently, samples were analyzed by the MV Plapo 1x objective of the microscope (Olympus MVX10). Photos were taken with camera DP73 and edited with the software Olympus cellSens Standard.

In order to gain an insight into the vascular bundles of the plant, root cross sections were performed after GUS staining. Therefore, stained roots were washed three times with 50 mM MBS pH 6.8 (100 mM PIPES, 10 mM EGTA, 5 mM $\text{MgSO}_4\cdot 7\text{H}_2\text{O}$). Thereafter, samples were introduced into 2 % agar with 50 mM MSB pH 6.8. The dehydrating process was performed with an increasing ethanol line on ice. The agar-enclosed roots were successively incubated in 30 %, 50 %, 70 %, and 90 % ethanol for 15 min and finally in 100 % ethanol for 30 min. In the next step, the LR-white resin medium grade acrylic resin infiltration was performed in four steps. The first approach occurred with ethanol and LR-white in the proportion 2:1 followed by 1:1 and 1:2, each approach for 1 h at RT. Thereafter, the samples were incubated in 100 % LR-white overnight. On the next day, samples were embedded in gelatine capsules. Polymerization was performed for 2 h at RT and 36 h at 50 °C (both incubations in an oxygen-free atmosphere). 5 μ m cross sections were performed with the

ultramicrotome (Leica Reichert Ultracut S).

7.7 Software and databases

Table 19: Register of software and databases used for this thesis.

software/databases	reference
Clone Manager 9 Professional Edition	Scientific and Educational Software, Morrisville, USA
Clustal Omega	[46-48]
ExPASy Coils algorithm	[77]
DELTA-BLAST algorithm	National Library of Medicine, USA [76]
eFP Browser	[229]
EMBOSS Matcher	[74]
FIESTA	[82]
Fiji	[224]
Genevestigator	NEBION AG, Zürich, Schweiz [83, 84]
interactive tree of life (iTOL)	[49]
MATLAB	MATLAB version R2013a. Natick, Massachusetts: The MathWorks Inc., 2010.
Microsoft Office (Excel, Word, PowerPoint)	Microsoft Corporation, Redmond, USA
NIS-Elements AR4.40.00	Nikon, Amsterdam, Netherlands
Olympus cellSens Standard	Olympus Corporation Tokyo, Japan
SWISS-MODEL	[75]
TAIR (Arabidopsis Information Resource)	www.arabidopsis.org [73]
Vector NTI®	Thermo Fisher Scientific, Waltham, USA

8 References

1. Richardson, D.N., M.P. Simmons, and A.S. Reddy, *Comprehensive comparative analysis of kinesins in photosynthetic eukaryotes*. BMC Genomics, 2006. **7**: p. 18.
2. Reddy, A.S., *Molecular motors and their functions in plants*. Int Rev Cytol, 2001. **204**: p. 97-178.
3. Vale, R.D., *The molecular motor toolbox for intracellular transport*. Cell, 2003. **112**(4): p. 467-80.
4. Lee, Y.R. and B. Liu, *Cytoskeletal motors in Arabidopsis. Sixty-one kinesins and seventeen myosins*. Plant Physiol, 2004. **136**(4): p. 3877-83.
5. Zhu, C. and R. Dixit, *Functions of the Arabidopsis kinesin superfamily of microtubule-based motor proteins*. Protoplasma, 2012. **249**(4): p. 887-99.
6. Reddy, A.S. and I.S. Day, *Kinesins in the Arabidopsis genome: a comparative analysis among eukaryotes*. BMC Genomics, 2001. **2**: p. 2.
7. Vale, R.D., T.S. Reese, and M.P. Sheetz, *Identification of a novel force-generating protein, kinesin, involved in microtubule-based motility*. Cell, 1985. **42**(1): p. 39-50.
8. Vale, R.D. and R.J. Fletterick, *The design plan of kinesin motors*. Annu Rev Cell Dev Biol, 1997. **13**: p. 745-77.
9. Endow, S.A., *Determinants of molecular motor directionality*. Nat Cell Biol, 1999. **1**(6): p. E163-7.
10. Lodish, H., et al., *Cell Organization and Movement II: Microtubules and Intermediate Filaments*, in *Molecular Cell Biology 7th Edition*. 2013, Ahr Parker, K.: New York. p. 821-872.
11. Welburn, J.P., *The molecular basis for kinesin functional specificity during mitosis*. Cytoskeleton (Hoboken), 2013. **70**(9): p. 476-93.
12. Rank, K.C. and I. Rayment, *Functional asymmetry in kinesin and dynein dimers*. Biol Cell, 2013. **105**(1): p. 1-13.
13. Yildiz, A., et al., *Kinesin walks hand-over-hand*. Science, 2004. **303**(5658): p. 676-8.
14. Zhang, P., et al., *Drosophila Ncd reveals an evolutionarily conserved powerstroke mechanism for homodimeric and heterodimeric kinesin-14s*. Proc Natl Acad Sci U S A, 2015. **112**(20): p. 6359-64.
15. Sack, S., F.J. Kull, and E. Mandelkow, *Motor proteins of the kinesin family. Structures, variations, and nucleotide binding sites*. Eur J Biochem, 1999. **262**(1): p. 1-11.
16. She, Z.Y. and W.X. Yang, *Molecular mechanisms of kinesin-14 motors in spindle assembly and chromosome segregation*. J Cell Sci, 2017. **130**(13): p. 2097-2110.
17. Shao, Q. and Y.Q. Gao, *On the hand-over-hand mechanism of kinesin*. Proc Natl Acad Sci U S A, 2006. **103**(21): p. 8072-7.
18. Foster, K.A. and S.P. Gilbert, *Kinetic studies of dimeric Ncd: evidence that Ncd is not processive*. Biochemistry, 2000. **39**(7): p. 1784-91.
19. Foster, K.A., A.T. Mackey, and S.P. Gilbert, *A mechanistic model for Ncd directionality*. J Biol Chem, 2001. **276**(22): p. 19259-66.
20. Jonsson, E., et al., *Clustering of a kinesin-14 motor enables processive retrograde microtubule-based transport in plants*. Nature Plants, 2015. **1**: p. Article number: 15087.
21. Weinger, J.S., et al., *A nonmotor microtubule binding site in kinesin-5 is required for filament crosslinking and sliding*. Curr Biol, 2011. **21**(2): p. 154-60.
22. Cai, D., et al., *Kinesin-1 structural organization and conformational changes revealed by FRET stoichiometry in live cells*. J Cell Biol, 2007. **176**(1): p. 51-63.
23. Coy, D.L., et al., *Kinesin's tail domain is an inhibitory regulator of the motor domain*. Nat Cell Biol, 1999. **1**(5): p. 288-92.
24. Friedman, D.S. and R.D. Vale, *Single-molecule analysis of kinesin motility reveals regulation by the cargo-binding tail domain*. Nat Cell Biol, 1999. **1**(5): p. 293-7.

25. Hammond, J.W., et al., *Autoinhibition of the kinesin-2 motor KIF17 via dual intramolecular mechanisms*. J Cell Biol, 2010. **189**(6): p. 1013-1025.
26. Espeut, J., et al., *Phosphorylation relieves autoinhibition of the kinetochore motor Cenp-E*. Mol Cell, 2008. **29**(5): p. 637-43.
27. Kim, Y., et al., *Aurora kinases and protein phosphatase 1 mediate chromosome congression through regulation of CENP-E*. Cell, 2010. **142**(3): p. 444-55.
28. Cahu, J., et al., *Phosphorylation by Cdk1 increases the binding of Eg5 to microtubules in vitro and in Xenopus egg extract spindles*. PLoS One, 2008. **3**(12): p. e3936.
29. Lan, W., et al., *Aurora B phosphorylates centromeric MCAK and regulates its localization and microtubule depolymerization activity*. Curr Biol, 2004. **14**(4): p. 273-86.
30. Moore, A.T., et al., *MCAK associates with the tips of polymerizing microtubules*. J Cell Biol, 2005. **169**(3): p. 391-7.
31. Tanenbaum, M.E. and R.H. Medema, *Localized Aurora B activity spatially controls non-kinetochore microtubules during spindle assembly*. Chromosoma, 2011. **120**(6): p. 599-607.
32. Vanstraelen, M., D. Inze, and D. Geelen, *Mitosis-specific kinesins in Arabidopsis*. Trends Plant Sci, 2006. **11**(4): p. 167-75.
33. Fink, G., et al., *The mitotic kinesin-14 Ncd drives directional microtubule-microtubule sliding*. Nat Cell Biol, 2009. **11**(6): p. 717-23.
34. Walter, W.J., et al., *The non-processive rice kinesin-14 OsKCH1 transports actin filaments along microtubules with two distinct velocities*. Nature Plants, 2015. **1**(2015.111): p. 2015.111.
35. Eckerdt, F., et al., *Spindle pole regulation by a discrete Eg5-interacting domain in TPX2*. Curr Biol, 2008. **18**(7): p. 519-25.
36. Ma, N., et al., *Poleward transport of TPX2 in the mammalian mitotic spindle requires dynein, Eg5, and microtubule flux*. Mol Biol Cell, 2010. **21**(6): p. 979-88.
37. Ahmed, S., et al., *F-BAR domain proteins: Families and function*. Commun Integr Biol, 2010. **3**(2): p. 116-21.
38. Cai, G. and M. Cresti, *Microtubule motors and pollen tube growth--still an open question*. Protoplasma, 2010. **247**(3-4): p. 131-43.
39. Romagnoli, S., G. Cai, and M. Cresti, *In vitro assays demonstrate that pollen tube organelles use kinesin-related motor proteins to move along microtubules*. Plant Cell, 2003. **15**(1): p. 251-69.
40. Mim, C. and V.M. Unger, *Membrane curvature and its generation by BAR proteins*. Trends Biochem Sci, 2012. **37**(12): p. 526-33.
41. Miki, H., Y. Okada, and N. Hirokawa, *Analysis of the kinesin superfamily: insights into structure and function*. Trends Cell Biol, 2005. **15**(9): p. 467-76.
42. Yamada, M., et al., *Multiple kinesin-14 family members drive microtubule minus end-directed transport in plant cells*. J Cell Biol, 2017. **216**(6): p. 1705-1714.
43. Lawrence, C.J., et al., *A standardized kinesin nomenclature*. J Cell Biol, 2004. **167**(1): p. 19-22.
44. Shen, Z., et al., *Phylogenetic analysis of the Kinesin superfamily from physcomitrella*. Front Plant Sci, 2012. **3**: p. 230.
45. Meinke, D.W., et al., *Arabidopsis thaliana: a model plant for genome analysis*. Science, 1998. **282**(5389): p. 662, 679-82.
46. Sievers, F., et al., *Fast, scalable generation of high-quality protein multiple sequence alignments using Clustal Omega*. Mol Syst Biol, 2011. **7**: p. 539.
47. Sievers, F. and D.G. Higgins, *Clustal omega*. Curr Protoc Bioinformatics, 2014. **48**: p. 3 13 1-16.
48. Sievers, F. and D.G. Higgins, *Clustal Omega, accurate alignment of very large numbers of sequences*. Methods Mol Biol, 2014. **1079**: p. 105-16.

49. Letunic, I. and P. Bork, *Interactive tree of life (iTOL) v3: an online tool for the display and annotation of phylogenetic and other trees*. Nucleic Acids Res, 2016. **44**(W1): p. W242-5.
50. Ambrose, J.C., et al., *A minus-end-directed kinesin with plus-end tracking protein activity is involved in spindle morphogenesis*. Mol Biol Cell, 2005. **16**(4): p. 1584-92.
51. Ambrose, J.C. and R. Cyr, *The kinesin ATK5 functions in early spindle assembly in Arabidopsis*. Plant Cell, 2007. **19**(1): p. 226-36.
52. Marcus, A.I., et al., *A kinesin mutant with an atypical bipolar spindle undergoes normal mitosis*. Mol Biol Cell, 2003. **14**(4): p. 1717-26.
53. Itoh, T. and P. De Camilli, *BAR, F-BAR (EFC) and ENTH/ANTH domains in the regulation of membrane-cytosol interfaces and membrane curvature*. Biochim Biophys Acta, 2006. **1761**(8): p. 897-912.
54. McMahan, H.T. and J.L. Gallop, *Membrane curvature and mechanisms of dynamic cell membrane remodelling*. Nature, 2005. **438**(7068): p. 590-6.
55. Qualmann, B., D. Koch, and M.M. Kessels, *Let's go bananas: revisiting the endocytic BAR code*. EMBO J, 2011. **30**(17): p. 3501-15.
56. Zimmerberg, J. and M.M. Kozlov, *How proteins produce cellular membrane curvature*. Nat Rev Mol Cell Biol, 2006. **7**(1): p. 9-19.
57. Shimada, A., et al., *Curved EFC/F-BAR-domain dimers are joined end to end into a filament for membrane invagination in endocytosis*. Cell, 2007. **129**(4): p. 761-72.
58. Frost, A., V.M. Unger, and P. De Camilli, *The BAR domain superfamily: membrane-molding macromolecules*. Cell, 2009. **137**(2): p. 191-6.
59. Peter, B.J., et al., *BAR domains as sensors of membrane curvature: the amphiphysin BAR structure*. Science, 2004. **303**(5657): p. 495-9.
60. Roberts-Galbraith, R.H. and K.L. Gould, *Setting the F-BAR: functions and regulation of the F-BAR protein family*. Cell Cycle, 2010. **9**(20): p. 4091-7.
61. Itoh, T., et al., *Dynamin and the actin cytoskeleton cooperatively regulate plasma membrane invagination by BAR and F-BAR proteins*. Dev Cell, 2005. **9**(6): p. 791-804.
62. Frost, A., P. De Camilli, and V.M. Unger, *F-BAR proteins join the BAR family fold*. Structure, 2007. **15**(7): p. 751-3.
63. Frost, A., et al., *Structural basis of membrane invagination by F-BAR domains*. Cell, 2008. **132**(5): p. 807-17.
64. Henne, W.M., et al., *Structure and analysis of FCHo2 F-BAR domain: a dimerizing and membrane recruitment module that effects membrane curvature*. Structure, 2007. **15**(7): p. 839-52.
65. Habermann, B., *The BAR-domain family of proteins: a case of bending and binding?* EMBO Rep, 2004. **5**(3): p. 250-5.
66. Millard, T.H., et al., *Structural basis of filopodia formation induced by the IRSp53/MIM homology domain of human IRSp53*. EMBO J, 2005. **24**(2): p. 240-50.
67. Farsad, K., et al., *Generation of high curvature membranes mediated by direct endophilin bilayer interactions*. J Cell Biol, 2001. **155**(2): p. 193-200.
68. Henne, W.M., et al., *FCHo proteins are nucleators of clathrin-mediated endocytosis*. Science, 2010. **328**(5983): p. 1281-4.
69. Tsujita, K., et al., *Coordination between the actin cytoskeleton and membrane deformation by a novel membrane tubulation domain of PCH proteins is involved in endocytosis*. J Cell Biol, 2006. **172**(2): p. 269-79.
70. Hollopeter, G., et al., *The membrane-associated proteins FCHo and SGIP are allosteric activators of the AP2 clathrin adaptor complex*. Elife, 2014. **3**.
71. Kessels, M.M. and B. Qualmann, *The syndapin protein family: linking membrane trafficking with the cytoskeleton*. J Cell Sci, 2004. **117**(Pt 15): p. 3077-86.
72. Lippincott, J. and R. Li, *Involvement of PCH family proteins in cytokinesis and actin distribution*. Microsc Res Tech, 2000. **49**(2): p. 168-72.

73. Lamesch, P., et al., *The Arabidopsis Information Resource (TAIR): improved gene annotation and new tools*. Nucleic Acids Res, 2012. **40**(Database issue): p. D1202-10.
74. Rice, P., I. Longden, and A. Bleasby, *EMBOSS: the European Molecular Biology Open Software Suite*. Trends Genet, 2000. **16**(6): p. 276-7.
75. Bordoli, L., et al., *Protein structure homology modeling using SWISS-MODEL workspace*. Nat Protoc, 2009. **4**(1): p. 1-13.
76. Boratyn, G.M., et al., *Domain enhanced lookup time accelerated BLAST*. Biol Direct, 2012. **7**: p. 12.
77. Lupas, A., M. Van Dyke, and J. Stock, *Predicting coiled coils from protein sequences*. Science, 1991. **252**(5009): p. 1162-4.
78. Nitzsche, B., et al., *Studying kinesin motors by optical 3D-nanometry in gliding motility assays*. Methods Cell Biol, 2010. **95**: p. 247-71.
79. Tao, L. and J.M. Scholey, *Purification and assay of mitotic motors*. Methods, 2010. **51**(2): p. 233-41.
80. Rogers, S.L. and J.M. Scholey, *Motility Assays for Microtubule Motor Proteins*. In: eLS. John Wiley & Sons Ltd, Chichester. <http://www.els.net> [doi: 10.1038/npg.els.0002621], 2004.
81. Grover, R., et al., *Transport efficiency of membrane-anchored kinesin-1 motors depends on motor density and diffusivity*. Proc Natl Acad Sci U S A, 2016. **113**(46): p. E7185-E7193.
82. Ruhnaw, F., D. Zwicker, and S. Diez, *Tracking single particles and elongated filaments with nanometer precision*. Biophys J, 2011. **100**(11): p. 2820-8.
83. Hruz, T., et al., *Genevestigator v3: a reference expression database for the meta-analysis of transcriptomes*. Adv Bioinformatics, 2008. **2008**: p. 420747.
84. Zimmermann, P., et al., *GENEVESTIGATOR. Arabidopsis microarray database and analysis toolbox*. Plant Physiol, 2004. **136**(1): p. 2621-32.
85. Jefferson, R.A., T.A. Kavanagh, and M.W. Bevan, *GUS fusions: beta-glucuronidase as a sensitive and versatile gene fusion marker in higher plants*. EMBO J, 1987. **6**(13): p. 3901-7.
86. Hugdahl, J.D. and L.C. Morejohn, *Rapid and Reversible High-Affinity Binding of the Dinitroaniline Herbicide Oryzalin to Tubulin from Zea mays L*. Plant Physiol, 1993. **102**(3): p. 725-740.
87. Morejohn, L.C., et al., *Oryzalin, a dinitroaniline herbicide, binds to plant tubulin and inhibits microtubule polymerization in vitro*. Planta, 1987. **172**(2): p. 252-64.
88. Morejohn, L.C. and D.E. Fosket, *The biochemistry of compounds with anti-microtubule activity in plant cells*. Pharmacol Ther, 1991. **51**(2): p. 217-30.
89. Kurihara, D., et al., *ClearSee: a rapid optical clearing reagent for whole-plant fluorescence imaging*. Development, 2015. **142**(23): p. 4168-79.
90. Böhm, K.J.S., R.; Unger, E., *Speeding up kinesin-driven microtubule gliding in vitro by variation of cofactor composition and physicochemical parameters*. Cell Biology International, 2000. **24**(6): p. 336-341.
91. Marcus, A.I., et al., *Arabidopsis thaliana protein, ATK1, is a minus-end directed kinesin that exhibits non-processive movement*. Cell Motil Cytoskeleton, 2002. **52**(3): p. 144-50.
92. Rao, Y., et al., *Molecular basis for SH3 domain regulation of F-BAR-mediated membrane deformation*. Proc Natl Acad Sci U S A, 2010. **107**(18): p. 8213-8.
93. Nelson, S.R., K.M. Trybus, and D.M. Warshaw, *Motor coupling through lipid membranes enhances transport velocities for ensembles of myosin Va*. Proc Natl Acad Sci U S A, 2014. **111**(38): p. E3986-95.
94. Conway, L., et al., *Motor transport of self-assembled cargos in crowded environments*. Proc Natl Acad Sci U S A, 2012. **109**(51): p. 20814-9.
95. Jamison, D.K., et al., *Two kinesins transport cargo primarily via the action of one motor: implications for intracellular transport*. Biophys J, 2010. **99**(9): p. 2967-77.

96. Vershinin, M., et al., *Multiple-motor based transport and its regulation by Tau*. Proc Natl Acad Sci U S A, 2007. **104**(1): p. 87-92.
97. Beeg, J., et al., *Transport of beads by several kinesin motors*. Biophys J, 2008. **94**(2): p. 532-41.
98. Endow, S.A. and K.W. Waligora, *Determinants of kinesin motor polarity*. Science, 1998. **281**(5380): p. 1200-2.
99. Furuta, K., et al., *Diffusion and directed movement: in vitro motile properties of fission yeast kinesin-14 Pkl1*. J Biol Chem, 2008. **283**(52): p. 36465-73.
100. Klumpp, S. and R. Lipowsky, *Cooperative cargo transport by several molecular motors*. Proc Natl Acad Sci U S A, 2005. **102**(48): p. 17284-9.
101. Leduc, C., et al., *Molecular crowding creates traffic jams of kinesin motors on microtubules*. Proc Natl Acad Sci U S A, 2012. **109**(16): p. 6100-5.
102. Telley, I.A., P. Bieling, and T. Surrey, *Obstacles on the microtubule reduce the processivity of Kinesin-1 in a minimal in vitro system and in cell extract*. Biophys J, 2009. **96**(8): p. 3341-53.
103. Schneider, R., et al., *Kinesin-1 motors can circumvent permanent roadblocks by side-shifting to neighboring protofilaments*. Biophys J, 2015. **108**(9): p. 2249-57.
104. Dreblow, K., N. Kalchishkova, and K.J. Bohm, *Kinesin passing permanent blockages along its protofilament track*. Biochem Biophys Res Commun, 2010. **395**(4): p. 490-5.
105. Korten, T. and S. Diez, *Setting up roadblocks for kinesin-1: mechanism for the selective speed control of cargo carrying microtubules*. Lab Chip, 2008. **8**(9): p. 1441-7.
106. Scharrel, L., et al., *Multimotor transport in a system of active and inactive kinesin-1 motors*. Biophys J, 2014. **107**(2): p. 365-372.
107. Schmidt, C., et al., *Tuning the "roadblock" effect in kinesin-based transport*. Nano Lett, 2012. **12**(7): p. 3466-71.
108. Hoepflich, G.J., et al., *Kinesin's neck-linker determines its ability to navigate obstacles on the microtubule surface*. Biophys J, 2014. **106**(8): p. 1691-700.
109. Korten, T., et al., *Kinesin-1 Expressed in Insect Cells Improves Microtubule in Vitro Gliding Performance, Long-Term Stability and Guiding Efficiency in Nanostructures*. IEEE Trans Nanobioscience, 2016. **15**(1): p. 62-9.
110. Kurland, C. and J. Gallant, *Errors of heterologous protein expression*. Curr Opin Biotechnol, 1996. **7**(5): p. 489-93.
111. Schmidt, F.R., *Recombinant expression systems in the pharmaceutical industry*. Appl Microbiol Biotechnol, 2004. **65**(4): p. 363-72.
112. Van Daele, I., et al., *A comparative study of seed yield parameters in Arabidopsis thaliana mutants and transgenics*. Plant Biotechnol J, 2012. **10**(4): p. 488-500.
113. Sun, X., et al., *Transcriptional and hormonal signaling control of Arabidopsis seed development*. Curr Opin Plant Biol, 2010. **13**(5): p. 611-20.
114. Alonso-Blanco, C., et al., *Natural allelic variation at seed size loci in relation to other life history traits of Arabidopsis thaliana*. Proc Natl Acad Sci U S A, 1999. **96**(8): p. 4710-7.
115. Valencia, J.P.G., K.; Otegui M. S. , *Endocytosis and Endosomal Trafficking in Plants*. Annu Rev Plant Biol, 2016. **67**: p. 309-335.
116. Holstein, S.E., *Clathrin and plant endocytosis*. Traffic, 2002. **3**(9): p. 614-20.
117. Kitakura, S., et al., *Clathrin mediates endocytosis and polar distribution of PIN auxin transporters in Arabidopsis*. Plant Cell, 2011. **23**(5): p. 1920-31.
118. Taylor, L.P. and P.K. Hepler, *Pollen Germination and Tube Growth*. Annu Rev Plant Physiol Plant Mol Biol, 1997. **48**: p. 461-491.
119. Mo, Y., C. Nagel, and L.P. Taylor, *Biochemical complementation of chalcone synthase mutants defines a role for flavonols in functional pollen*. Proc Natl Acad Sci U S A, 1992. **89**(15): p. 7213-7.

120. Hulskamp, M., et al., *Identification of genes required for pollen-stigma recognition in Arabidopsis thaliana*. Plant J, 1995. **8**(5): p. 703-14.
121. Preuss, D., et al., *A conditional sterile mutation eliminates surface components from Arabidopsis pollen and disrupts cell signaling during fertilization*. Genes Dev, 1993. **7**(6): p. 974-85.
122. Aarts, M.G., et al., *Molecular characterization of the CER1 gene of Arabidopsis involved in epicuticular wax biosynthesis and pollen fertility*. Plant Cell, 1995. **7**(12): p. 2115-27.
123. Van Damme, D., et al., *Somatic cytokinesis and pollen maturation in Arabidopsis depend on TPLATE, which has domains similar to coat proteins*. Plant Cell, 2006. **18**(12): p. 3502-18.
124. Gadeyne, A., et al., *The TPLATE adaptor complex drives clathrin-mediated endocytosis in plants*. Cell, 2014. **156**(4): p. 691-704.
125. Idilli, A.I., et al., *Microtubule depolymerization affects endocytosis and exocytosis in the tip and influences endosome movement in tobacco pollen tubes*. Mol Plant, 2013. **6**(4): p. 1109-30.
126. Onelli, E. and A. Moscatelli, *Endocytic Pathways and Recycling in Growing Pollen Tubes*. Plants (Basel), 2013. **2**(2): p. 211-29.
127. Munk, K., et al., *Taschenbuch Biologie - Botanik*, ed. K. Munk. 2009, Stuttgart, New York: George Thieme Verlag KG.
128. Geitmann, A. and A.M. Emons, *The cytoskeleton in plant and fungal cell tip growth*. J Microsc, 2000. **198**(Pt 3): p. 218-45.
129. Zonia, L. and T. Munnik, *Vesicle trafficking dynamics and visualization of zones of exocytosis and endocytosis in tobacco pollen tubes*. J Exp Bot, 2008. **59**(4): p. 861-73.
130. Moscatelli, A., *Endocytic pathways in pollen tube: Implications for in vivo growth regulation*. Plant Signal Behav, 2008. **3**(5): p. 325-7.
131. Chebli, Y., et al., *The cell wall of the Arabidopsis pollen tube--spatial distribution, recycling, and network formation of polysaccharides*. Plant Physiol, 2012. **160**(4): p. 1940-55.
132. Cai, G., *How do microtubules affect deposition of cell wall polysaccharides in the pollen tube?* Plant Signal Behav, 2011. **6**(5): p. 732-5.
133. Cai, G., et al., *Distribution of callose synthase, cellulose synthase, and sucrose synthase in tobacco pollen tube is controlled in dissimilar ways by actin filaments and microtubules*. Plant Physiol, 2011. **155**(3): p. 1169-90.
134. Moscatelli, A. and A.I. Idilli, *Pollen tube growth: a delicate equilibrium between secretory and endocytic pathways*. J Integr Plant Biol, 2009. **51**(8): p. 727-39.
135. Cai, G., L. Parrotta, and M. Cresti, *Organelle trafficking, the cytoskeleton, and pollen tube growth*. J Integr Plant Biol, 2015. **57**(1): p. 63-78.
136. Romagnoli, S., et al., *Microtubule- and actin filament-dependent motors are distributed on pollen tube mitochondria and contribute differently to their movement*. Plant Cell Physiol, 2007. **48**(2): p. 345-61.
137. Lloyd, C.W., Pearce, K.J., Rawlins, D.J., Ridge, R.W., and Shaw, and P.J., *Endoplasmic microtubules connect the advancing nucleus to the tip of legume root hairs, but F-actin is involved in the basipetal migration*. Cell Motil Cytoskeleton, 1987. **8**(1): p. 27-36.
138. Astrom, H., Sorri, O., and Raudaskoski, M., *Role of microtubules in the movement of the vegetative nucleus and generative cell in tobacco pollen tubes*. Sex Plant Reproduction, 1995. **8**(2): p. 61-69.
139. Miyake, T., Kuroiwa, H., and Kuroiwa, T., *Differential mechanisms of movement between a generative cell and a vegetative nucleus in pollen tubes of Nicotiana tabacum as revealed by additions of colchicine and nonanoic acid*. Sex Plant Reproduction, 1995(4): p. 228-230.

140. Geitmann, A., Li, Y.-Q., and Cresti, M., *The role of cytoskeleton and dictyosome activity in the pulsatory growth of Nicotiana tabacum and Petunia hybrida pollen tubes*. *Botanica Acta*, 1996. **109**(2): p. 102-109.
141. He, Y., Wetzstein, H.Y., and Palevitz, B.A., *The effect of a triazole fungicide, propiconazole, on pollen germination, the growth and cytoskeletal distribution in Tradescantia virginiana*. *Sex Plant Reproduction*, 1995. **8**(4): p. 210-216.
142. Heslop-Harrison, J., Heslop-Harrison, Y., Cresti, M., Tiezzi, A., and Moscatelli, A., *Cytoskeletal elements, cell shaping and movement in the angiosperm pollen tube*. *J Cell Sci*, 1988. **91**: p. 49-60.
143. Shimmen, T., *The sliding theory of cytoplasmic streaming: fifty years of progress*. *J Plant Res*, 2007. **120**(1): p. 31-43.
144. Cheung, A.Y., et al., *The dynamic pollen tube cytoskeleton: live cell studies using actin-binding and microtubule-binding reporter proteins*. *Mol Plant*, 2008. **1**(4): p. 686-702.
145. Mascarenhas, J.P., and Lafountain, J., *Protoplasmic streaming, cytochalasin B, and growth of the pollen tube*. *Tissue Cell*, 1972. **2**(1): p. 11-14.
146. Lancelle, S.A., and Hepler, P.K., *Cytochalasin-induced ultrastructural alterations in Nicotiana pollen tubes*. *Protoplasma*, 1988. **2**: p. 65-75.
147. Vidali, L. and P.K. Hepler, *Actin and pollen tube growth*. *Protoplasma*, 2001. **215**(1-4): p. 64-76.
148. Vidali, L., S.T. McKenna, and P.K. Hepler, *Actin polymerization is essential for pollen tube growth*. *Mol Biol Cell*, 2001. **12**(8): p. 2534-45.
149. Moscatelli, A., et al., *Inhibition of actin polymerisation by low concentration Latrunculin B affects endocytosis and alters exocytosis in shank and tip of tobacco pollen tubes*. *Plant Biol (Stuttg)*, 2012. **14**(5): p. 770-82.
150. Cai, G. and M. Cresti, *Are kinesins required for organelle trafficking in plant cells?* *Front Plant Sci*, 2012. **3**: p. 170.
151. Pierson, E.S.K., H. M. P.; Derksen, J., *Microtubules and actin filaments co-localize in pollen tubes of Nicotiana tabacum L. and Lilium longiflorum Thunb.* *Protoplasma*, 1989. **150**(1): p. 75-77.
152. Lancelle, S.A., and Hepler, P.K., *Association of actin with cortical microtubules revealed by immunogold localization in Nicotiana pollen tubes*. *Protoplasma*, 1991. **165**(1-3): p. 167-172.
153. Lancelle, S.A., and Hepler, P.K., *Ultrastructure of freeze-substituted pollen tubes of Lilium longiflorum*. *Protoplasma*, 1992. **167**(3-4): p. 215-230.
154. Romagnoli, S., et al., *Cytosolic proteins from tobacco pollen tubes that crosslink microtubules and actin filaments in vitro are metabolic enzymes*. *Cytoskeleton (Hoboken)*, 2010. **67**(12): p. 745-54.
155. Wang, J., et al., *AtFH16, [corrected] an Arabidopsis type II formin, binds and bundles both microfilaments and microtubules, and preferentially binds to microtubules*. *J Integr Plant Biol*, 2013. **55**(11): p. 1002-15.
156. Krishnakumar, S. and D.G. Oppenheimer, *Extragenic suppressors of the arabidopsis zwi-3 mutation identify new genes that function in trichome branch formation and pollen tube growth*. *Development*, 1999. **126**(14): p. 3079-88.
157. Ren, G., et al., *The BAR domain proteins: molding membranes in fission, fusion, and phagy*. *Microbiol Mol Biol Rev*, 2006. **70**(1): p. 37-120.
158. Kaksonen, M., C.P. Toret, and D.G. Drubin, *A modular design for the clathrin- and actin-mediated endocytosis machinery*. *Cell*, 2005. **123**(2): p. 305-20.
159. Onelli, E., et al., *Clathrin-dependent and independent endocytic pathways in tobacco protoplasts revealed by labelling with charged nanogold*. *J Exp Bot*, 2008. **59**(11): p. 3051-68.
160. McMahan, H.T. and E. Boucrot, *Molecular mechanism and physiological functions of clathrin-mediated endocytosis*. *Nat Rev Mol Cell Biol*, 2011. **12**(8): p. 517-33.

161. Zhang, Y., et al., *Change your TPLATE, change your fate: plant CME and beyond*. Trends Plant Sci, 2015. **20**(1): p. 41-8.
162. Traub, L.M. and J.S. Bonifacino, *Cargo recognition in clathrin-mediated endocytosis*. Cold Spring Harb Perspect Biol, 2013. **5**(11): p. a016790.
163. Tebar, F., et al., *Eps15 is a component of clathrin-coated pits and vesicles and is located at the rim of coated pits*. J Biol Chem, 1996. **271**(46): p. 28727-30.
164. Chappie, J.S. and F. Dyda, *Building a fission machine--structural insights into dynamin assembly and activation*. J Cell Sci, 2013. **126**(Pt 13): p. 2773-84.
165. Fan, L., et al., *Dynamic analysis of Arabidopsis AP2 sigma subunit reveals a key role in clathrin-mediated endocytosis and plant development*. Development, 2013. **140**(18): p. 3826-37.
166. Kim, S.Y., et al., *Adaptor protein complex 2-mediated endocytosis is crucial for male reproductive organ development in Arabidopsis*. Plant Cell, 2013. **25**(8): p. 2970-85.
167. Yamaoka, S., et al., *Identification and dynamics of Arabidopsis adaptor protein-2 complex and its involvement in floral organ development*. Plant Cell, 2013. **25**(8): p. 2958-69.
168. Merrifield, C.J., et al., *Imaging actin and dynamin recruitment during invagination of single clathrin-coated pits*. Nat Cell Biol, 2002. **4**(9): p. 691-8.
169. Merrifield, C.J., D. Perrais, and D. Zenisek, *Coupling between clathrin-coated-pit invagination, cortactin recruitment, and membrane scission observed in live cells*. Cell, 2005. **121**(4): p. 593-606.
170. Munn, A.L., *Molecular requirements for the internalisation step of endocytosis: insights from yeast*. Biochim Biophys Acta, 2001. **1535**(3): p. 236-57.
171. Engqvist-Goldstein, A.E. and D.G. Drubin, *Actin assembly and endocytosis: from yeast to mammals*. Annu Rev Cell Dev Biol, 2003. **19**: p. 287-332.
172. Ferguson, S.M., et al., *Coordinated actions of actin and BAR proteins upstream of dynamin at endocytic clathrin-coated pits*. Dev Cell, 2009. **17**(6): p. 811-22.
173. Zonia, L. and T. Munnik, *Uncovering hidden treasures in pollen tube growth mechanics*. Trends Plant Sci, 2009. **14**(6): p. 318-27.
174. Moscatelli, A., et al., *Distinct endocytic pathways identified in tobacco pollen tubes using charged nanogold*. J Cell Sci, 2007. **120**(Pt 21): p. 3804-19.
175. Bove, J., et al., *Magnitude and direction of vesicle dynamics in growing pollen tubes using spatiotemporal image correlation spectroscopy and fluorescence recovery after photobleaching*. Plant Physiol, 2008. **147**(4): p. 1646-58.
176. Helling, D., et al., *Pollen tube tip growth depends on plasma membrane polarization mediated by tobacco PLC3 activity and endocytic membrane recycling*. Plant Cell, 2006. **18**(12): p. 3519-34.
177. Bannigan, A., et al., *Emerging molecular mechanisms that power and regulate the anastral mitotic spindle of flowering plants*. Cell Motil Cytoskeleton, 2008. **65**(1): p. 1-11.
178. Endow, S.A., et al., *Mutants of the Drosophila ncd microtubule motor protein cause centrosomal and spindle pole defects in mitosis*. J Cell Sci, 1994. **107** (Pt 4): p. 859-67.
179. Wordeman, L., *How kinesin motor proteins drive mitotic spindle function: Lessons from molecular assays*. Semin Cell Dev Biol, 2010. **21**(3): p. 260-8.
180. Sharp, D.J., G.C. Rogers, and J.M. Scholey, *Microtubule motors in mitosis*. Nature, 2000. **407**(6800): p. 41-7.
181. Lawrence, C.J., et al., *Dyneins have run their course in plant lineage*. Traffic, 2001. **2**(5): p. 362-3.
182. Strompen, G., et al., *The Arabidopsis HINKEL gene encodes a kinesin-related protein involved in cytokinesis and is expressed in a cell cycle-dependent manner*. Curr Biol, 2002. **12**(2): p. 153-8.

183. Lee, Y.R. and B. Liu, *Identification of a phragmoplast-associated kinesin-related protein in higher plants*. *Curr Biol*, 2000. **10**(13): p. 797-800.
184. Schneider, R. and S. Persson, *Connecting two arrays: the emerging role of actin-microtubule cross-linking motor proteins*. *Front Plant Sci*, 2015. **6**: p. 415.
185. Preuss, M.L., et al., *A plant-specific kinesin binds to actin microfilaments and interacts with cortical microtubules in cotton fibers*. *Plant Physiol*, 2004. **136**(4): p. 3945-55.
186. Frey, N., J. Klotz, and P. Nick, *Dynamic bridges--a calponin-domain kinesin from rice links actin filaments and microtubules in both cycling and non-cycling cells*. *Plant Cell Physiol*, 2009. **50**(8): p. 1493-506.
187. Frey, N., J. Klotz, and P. Nick, *A kinesin with calponin-homology domain is involved in premitotic nuclear migration*. *J Exp Bot*, 2010. **61**(12): p. 3423-37.
188. Klotz, J. and P. Nick, *A novel actin-microtubule cross-linking kinesin, NtKCH, functions in cell expansion and division*. *New Phytol*, 2012. **193**(3): p. 576-89.
189. Popchock, A.R., et al., *The mitotic kinesin-14 KlpA contains a context-dependent directionality switch*. *Nat Commun*, 2017. **8**: p. 13999.
190. Tanenbaum, M.E., R.D. Vale, and R.J. McKenney, *Cytoplasmic dynein crosslinks and slides anti-parallel microtubules using its two motor domains*. *Elife*, 2013. **2**: p. e00943.
191. Hancock, W.O. and J. Howard, *Processivity of the motor protein kinesin requires two heads*. *J Cell Biol*, 1998. **140**(6): p. 1395-405.
192. Furuta, K., et al., *Measuring collective transport by defined numbers of processive and nonprocessive kinesin motors*. *Proc Natl Acad Sci U S A*, 2013. **110**(2): p. 501-6.
193. Walczak, C.E., S. Verma, and T.J. Mitchison, *XCTK2: a kinesin-related protein that promotes mitotic spindle assembly in *Xenopus laevis* egg extracts*. *J Cell Biol*, 1997. **136**(4): p. 859-70.
194. Mountain, V., et al., *The kinesin-related protein, HSET, opposes the activity of Eg5 and cross-links microtubules in the mammalian mitotic spindle*. *J Cell Biol*, 1999. **147**(2): p. 351-66.
195. Sharp, D.J., G.C. Rogers, and J.M. Scholey, *Cytoplasmic dynein is required for poleward chromosome movement during mitosis in *Drosophila* embryos*. *Nat Cell Biol*, 2000. **2**(12): p. 922-30.
196. Schuetz, M., R. Smith, and B. Ellis, *Xylem tissue specification, patterning, and differentiation mechanisms*. *J Exp Bot*, 2013. **64**(1): p. 11-31.
197. Kondo, Y., T. Tamaki, and H. Fukuda, *Regulation of xylem cell fate*. *Front Plant Sci*, 2014. **5**: p. 315.
198. Pesquet, E. and C. Lloyd, *Microtubules, MAPs and Xylem Formation*, in *The Plant Cytoskeleton, Advances in Plant Biology*. 2011, Springer New York: NY.
199. Oda, Y. and S. Hasezawa, *Cytoskeletal organization during xylem cell differentiation*. *J Plant Res*, 2006. **119**(3): p. 167-77.
200. Oda, Y. and H. Fukuda, *Secondary cell wall patterning during xylem differentiation*. *Curr Opin Plant Biol*, 2012. **15**(1): p. 38-44.
201. Zhang, J., A. Elo, and Y. Helariutta, *Arabidopsis as a model for wood formation*. *Curr Opin Biotechnol*, 2011. **22**(2): p. 293-9.
202. Nick, P., *Plant Microtubules, Development and Flexibility*. *Plant Cell Monographs*, ed. P. Nick. Vol. 2. 2008: Springer-Verlag Berlin Heidelberg. 269.
203. Dettmer, J., A. Elo, and Y. Helariutta, *Hormone interactions during vascular development*. *Plant Mol Biol*, 2009. **69**(4): p. 347-60.
204. Van Bruaene, N., G. Joss, and P. Van Oostveldt, *Reorganization and in vivo dynamics of microtubules during Arabidopsis root hair development*. *Plant Physiol*, 2004. **136**(4): p. 3905-19.

205. Dixit, R. and R. Cyr, *Encounters between dynamic cortical microtubules promote ordering of the cortical array through angle-dependent modifications of microtubule behavior*. *Plant Cell*, 2004. **16**(12): p. 3274-84.
206. Janson, M.E., M.E. de Dood, and M. Dogterom, *Dynamic instability of microtubules is regulated by force*. *J Cell Biol*, 2003. **161**(6): p. 1029-34.
207. Oda, Y. and H. Fukuda, *Spatial organization of xylem cell walls by ROP GTPases and microtubule-associated proteins*. *Curr Opin Plant Biol*, 2013. **16**(6): p. 743-8.
208. Fache, V., et al., *Arabidopsis kinetochore fiber-associated MAP65-4 cross-links microtubules and promotes microtubule bundle elongation*. *Plant Cell*, 2010. **22**(11): p. 3804-15.
209. Stoppin-Mellet, V., et al., *MAP65 coordinate microtubule growth during bundle formation*. *PLoS One*, 2013. **8**(2): p. e56808.
210. Zhong, R., et al., *A kinesin-like protein is essential for oriented deposition of cellulose microfibrils and cell wall strength*. *Plant Cell*, 2002. **14**(12): p. 3101-17.
211. Gardiner, J.C., N.G. Taylor, and S.R. Turner, *Control of cellulose synthase complex localization in developing xylem*. *Plant Cell*, 2003. **15**(8): p. 1740-8.
212. Gutierrez, R., et al., *Arabidopsis cortical microtubules position cellulose synthase delivery to the plasma membrane and interact with cellulose synthase trafficking compartments*. *Nat Cell Biol*, 2009. **11**(7): p. 797-806.
213. Wightman, R. and S. Turner, *Trafficking of the cellulose synthase complex in developing xylem vessels*. *Biochem Soc Trans*, 2010. **38**(3): p. 755-60.
214. Pesquet, E., et al., *The microtubule-associated protein AtMAP70-5 regulates secondary wall patterning in Arabidopsis wood cells*. *Curr Biol*, 2010. **20**(8): p. 744-9.
215. Hanahan, D., *Studies on transformation of Escherichia coli with plasmids*. *J Mol Biol*, 1983. **166**(4): p. 557-80.
216. Deblaere, R., et al., *Efficient octopine Ti plasmid-derived vectors for Agrobacterium-mediated gene transfer to plants*. *Nucleic Acids Res*, 1985. **13**(13): p. 4777-88.
217. Alonso, J.M., et al., *Genome-wide insertional mutagenesis of Arabidopsis thaliana*. *Science*, 2003. **301**(5633): p. 653-7.
218. Rosso, M.G., et al., *An Arabidopsis thaliana T-DNA mutagenized population (GABI-Kat) for flanking sequence tag-based reverse genetics*. *Plant Mol Biol*, 2003. **53**(1-2): p. 247-59.
219. Kleinboelting, N., et al., *GABI-Kat SimpleSearch: new features of the Arabidopsis thaliana T-DNA mutant database*. *Nucleic Acids Res*, 2012. **40**(Database issue): p. D1211-5.
220. Karimi, M., A. Depicker, and P. Hilson, *Recombinational cloning with plant gateway vectors*. *Plant Physiol*, 2007. **145**(4): p. 1144-54.
221. Bryksin, A.V. and I. Matsumura, *Overlap extension PCR cloning: a simple and reliable way to create recombinant plasmids*. *Biotechniques*, 2010. **48**(6): p. 463-5.
222. Bryksin, A. and I. Matsumura, *Overlap extension PCR cloning*. *Methods Mol Biol*, 2013. **1073**: p. 31-42.
223. Castoldi, M. and A.V. Popova, *Purification of brain tubulin through two cycles of polymerization-depolymerization in a high-molarity buffer*. *Protein Expression and Purification*, 2003. **32**(1): p. 83-88.
224. Schindelin, J., et al., *Fiji: an open-source platform for biological-image analysis*. *Nat Methods*, 2012. **9**(7): p. 676-82.
225. Michalet, X., *Mean square displacement analysis of single-particle trajectories with localization error: Brownian motion in an isotropic medium*. *Phys Rev E Stat Nonlin Soft Matter Phys*, 2010. **82**(4 Pt 1): p. 041914.
226. Funatsu, T., et al., *Imaging of single fluorescent molecules and individual ATP turnovers by single myosin molecules in aqueous solution*. *Nature*, 1995. **374**(6522): p. 555-9.

-
227. Vale, R.D., et al., *Direct observation of single kinesin molecules moving along microtubules*. *Nature*, 1996. **380**(6573): p. 451-3.
 228. Korten, T., et al., *Fluorescence imaging of single Kinesin motors on immobilized microtubules*. *Methods Mol Biol*, 2011. **783**: p. 121-37.
 229. Winter, D., et al., *An "Electronic Fluorescent Pictograph" browser for exploring and analyzing large-scale biological data sets*. *PLoS One*, 2007. **2**(8): p. e718.

9 Appendix

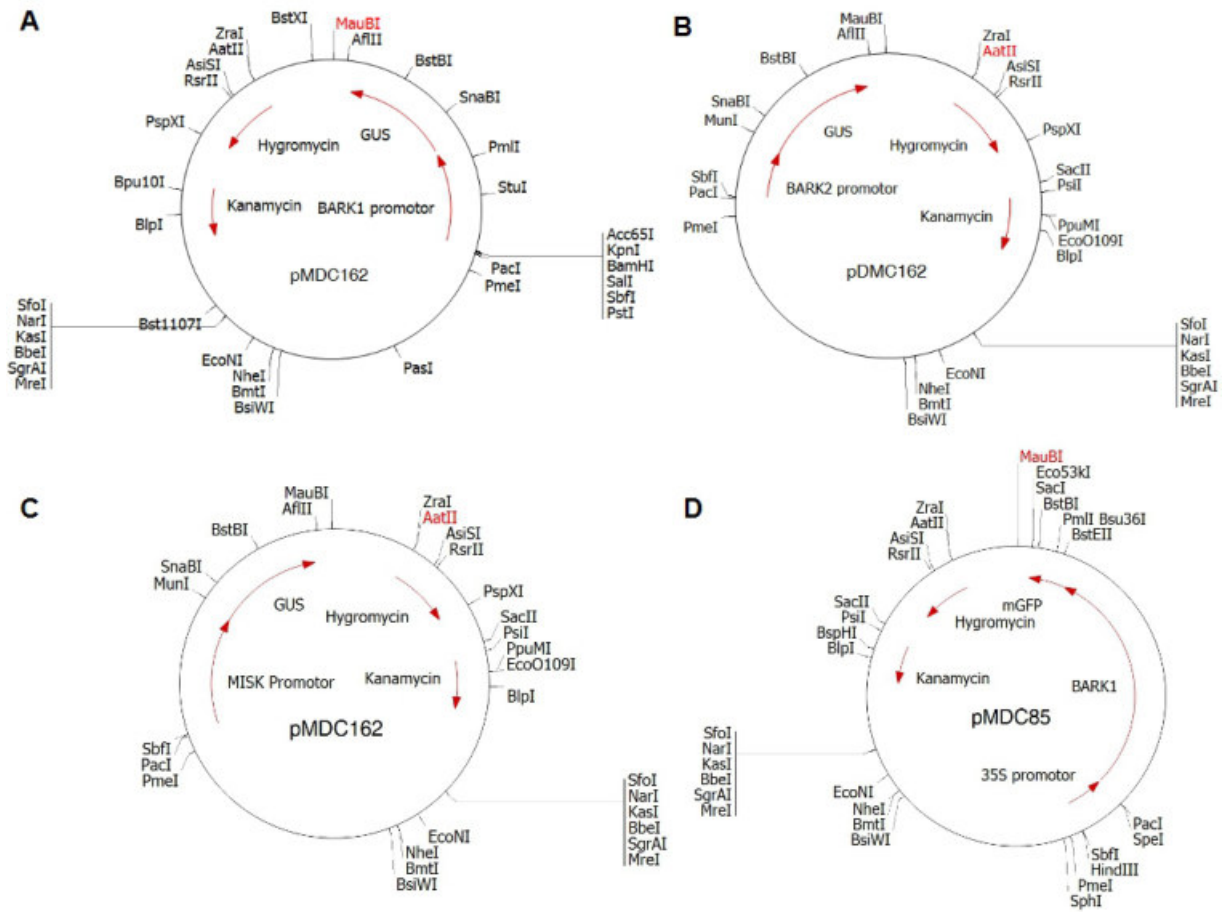


Figure 66: Vectors of the constructs pMDC162-pBARK1/2-GUS (A, B), pMDC162-pMISK1-GUS (C), and 35S-pMDC85-BARK1-GFP (D).

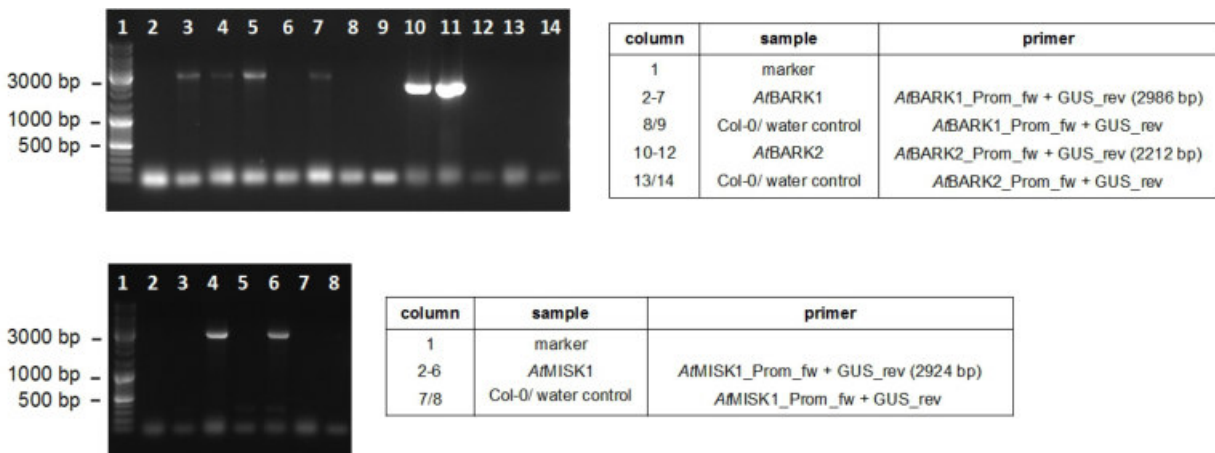


Figure 67: Agarose gel electrophoresis of genotyped *pbark1/2-GUS* and *pmisk-GUS* plants after bacterial transformation with pMDC162-pBARK1/2-GUS, pMDC162-pMISK1-GUS.

The result of the PCR showed a successful transformation for plant 3-5, 7 (*bark1*), for plant 10-11 (*bark2*) and for plant 4, 6 (*misk1*). Primers were listed in Table 15.

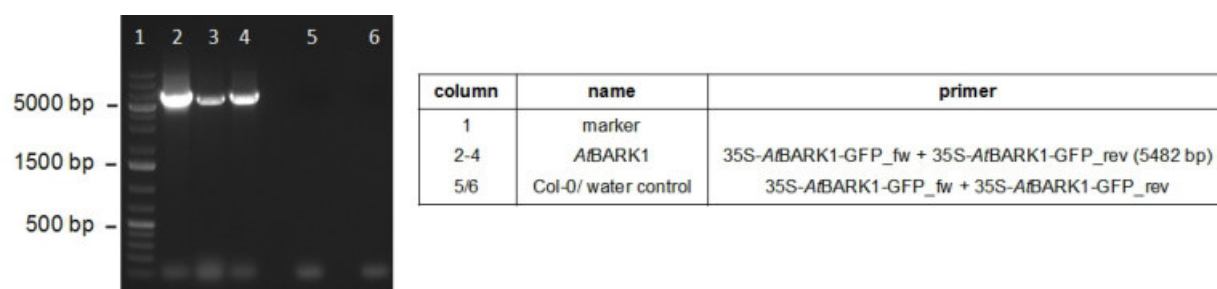


Figure 68: Agarose gel electrophoresis of genotyped 35S-*bark1*-GFP plants after bacterial transformation with pMDC85-BARK1-GFP.

The result of the PCR showed a successful transformation for plant 2-4. Primers were listed in Table 15.

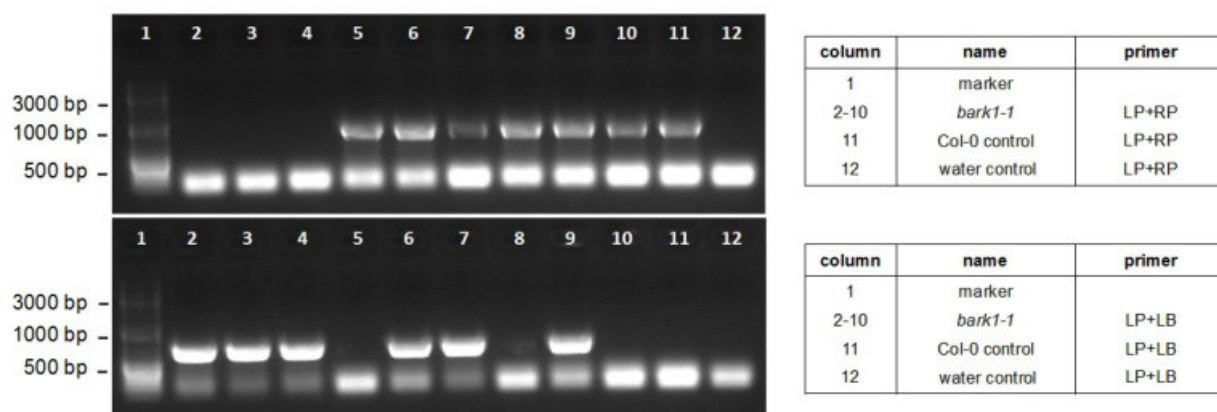


Figure 69: Exemplary agarose gel electrophoresis of the genotyped *bark1-1* line.

The result of the PCR showed homozygous plants (column 2-4), segregating wild-type plants (column 5,8,10) and heterozygous plants (column 6, 7, 9). The same procedure was performed for the *bark2* and the *misk1* lines. Primers were listed in Table 20.

Table 20: Oligonucleotides used for genotyping of the *bark1/2* and *misk1* T-DNA insertion lines.

name	sequence	application
<i>AtBARK345B04_LP</i>	ATACATAAGTAGGCACGCATTGAG	genotyping
<i>AtBARK345B04_RP</i>	AGACTTGTTAATTACTGCGCGTC	genotyping
T-DNA-GK_LB	ATAATAACGCTGCGGACATCTACATTTT	genotyping
<i>AtBARK023598_LP</i>	GCACGACTTTTCTCAGCAGAC	genotyping
<i>AtBARK023598_RP</i>	CTCTTGTTGCACAAAAGAGC	genotyping
<i>AtBARK135977_LP</i>	TTATTCGGCAAGATCAGATGC	genotyping
<i>AtBARK135977_RP</i>	GCTCTTTTGGTGCAACAAGAG	genotyping
LbB1.3	ATTTTGCCGATTTTCGGAA	genotyping
<i>AtMISK146972C_LP</i>	CTCTAAGCAATGGTGGAGCTG	genotyping
<i>AtMISK146972C_RP</i>	CGAGACGTTGGAGAACTCAC	genotyping
<i>AtMISK043700C_LP</i>	TCAGGTTGAAAACCTGTGCG	genotyping
<i>AtMISK043700C_RP</i>	TTCAAGATTTGGTTTTGACGG	genotyping

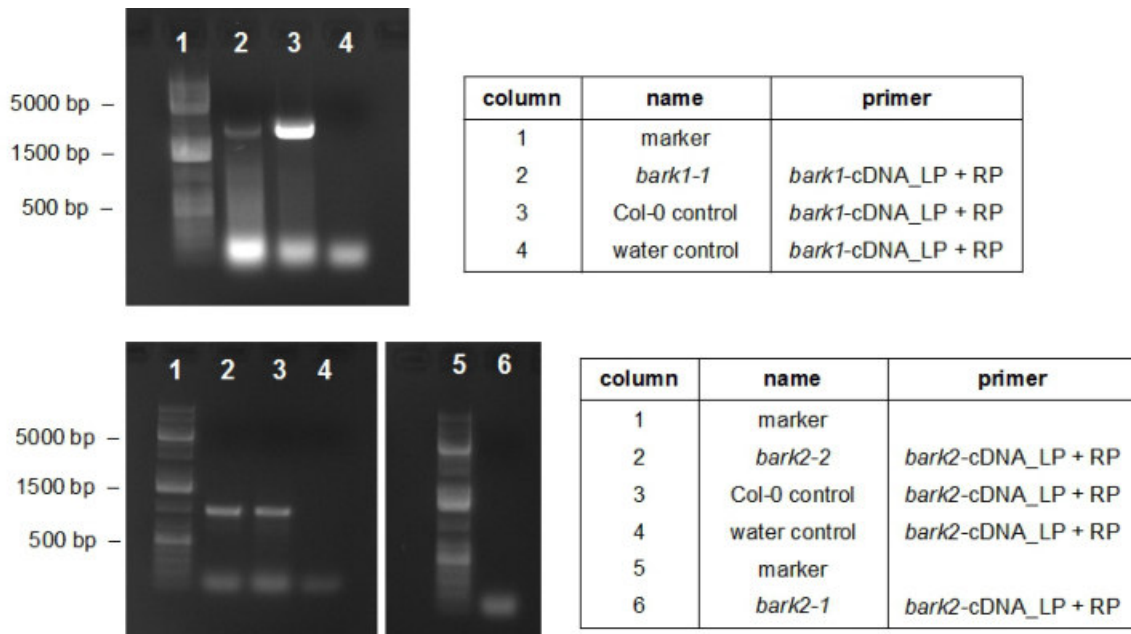


Figure 70: Agarose gel electrophoresis of the knockout PCR of *bark1* and *bark2* T-DNA insertion lines. The result of the PCR showed cDNA amplification of the coding *bark1* and *bark2* sequences for the *bark1-1* and the *bark2-2* T-DNA insertion lines, and for the Col-0 positive control after 30 PCR-cycles. There was no amplification for the *bark2-1* line after 30 PCR-cycles. Primers were listed in Table 21.

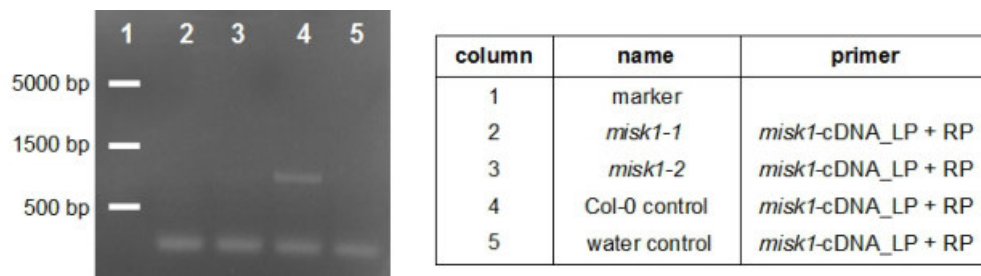


Figure 71: Agarose gel electrophoresis of the knockout PCR of *misk1* T-DNA insertion lines. The result of the PCR showed cDNA amplification of the coding *misk1* sequences for the Col-0 positive control but no amplification for the knockout lines *misk1-1* and *misk1-2* after 30 cycles. Primers were listed in Table 21.

Table 21: Oligonucleotides used for RT-PCRs of the *bark1/2* and *misk1* T-DNA insertion lines.

name	sequence	application
<i>bark1</i> -cDNA_LP	CTTTGGACCACGAGGCCAATTGAATCCTATGC	RT-PCR
<i>bark1</i> -cDNA_RP	CTCGAGTTACGCCACCGTTTTG	RT-PCR
<i>bark2</i> -cDNA_LP	TGGCAAGGACTTGAAGACTG	RT-PCR
<i>bark2</i> -cDNA_RP	TGACAACAAGGCTGACGTAG	RT-PCR
<i>misk1</i> -cDNA_LP	CCAACAGCTAGCAGCAACAG	RT-PCR
<i>misk1</i> -cDNA_RP	GTGAATCTCGCTCCCAATCC	RT-PCR

Table 22: Register of mean \pm s.d. values of the mean number of seeds per siliques in the temperature experiment of *bark1* T-DNA insertion line.

line	temperature	mean number of seeds per silique \pm s.d.
<i>bark1-1</i>	17 °C	29.5 \pm 19.6
	22°C	27.4 \pm 15.9
	27°C	14.6 \pm 11.7
seg. WT	17 °C	41.3 \pm 18.2
	22°C	46.6 \pm 13.9
	27°C	21.4 \pm 13.4
Col-0	17 °C	45.8 \pm 14.5
	22°C	46.1 \pm 14.4
	27°C	16.3 \pm 13.3

Table 23: Register of mean \pm s.d. values of the mean number of seeds per siliques in the humidity experiment of *bark1* and *bark2* T-DNA insertion lines.

line	humidity	mean number of seeds per silique \pm s.d.
<i>bark1-1</i>	50 %	36.6 \pm 18.1
	60 %	28.0 \pm 19.4
	90 %	12.6 \pm 14.6
seg. WT	50 %	51.8 \pm 4.7
	60 %	46.5 \pm 10.7
	90 %	33.0 \pm 19.7
<i>bark2-1</i>	50 %	41.2 \pm 10.3
	60 %	39.7 \pm 14.7
	90 %	33.0 \pm 19.4
seg. WT	50 %	52.3 \pm 6.6
	60 %	48.2 \pm 11.4
	90 %	32.7 \pm 7.8

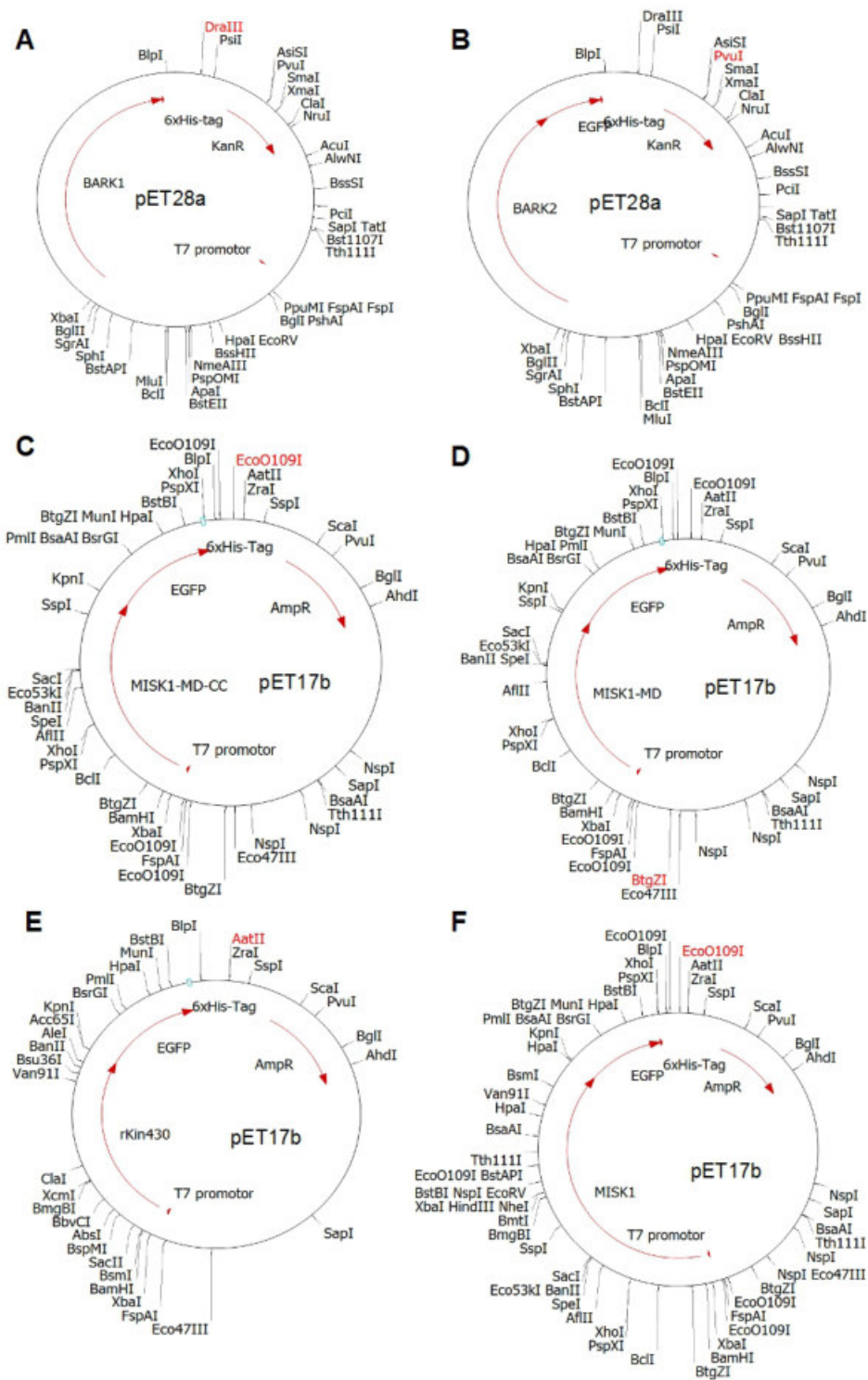


Figure 72: Expression vectors of the constructs pET28a-*AtBARK1*(aa1-1025)-6xHis (A), pET28a-*AtBARK2*(aa163-1140)-EGFP-6xHis (B), pET17b-*AtMISK1*(aa3-462)-EGFP-6xHis (C), pET17b-*AtMISK1*(aa3-415)-EGFP-6xHis (D), pET17b-rKin430-EGFP-6xHis (E), pET17b-*AtMISK1*-FL-EGFP-6xHis (F).

Sequence *A/BARK1(aa1-1025)-6xHis*

ATGGGCAGCAGCAATCCTATGCGTGATCAACCGGGCAGCCCTTATGGAGATTCAACTCCTCGTAGT
 CCGTTTTCTCCCTTTCTCCATTATCTGTAGATGATAGGCATAGAAATCATGCAGATACAAAACTC
 CTCGTAGTCCTTTCTCTCCATTTTCTCCATTATCCGGAGATGAAAGGCCAAAAAGTCTGGCAGAGTC
 CAAATTCAGCAAGCCCTTGCCAGCTCTGGCCAATTAGATCCATTATCTCCTGGATCAATGCATCAT
 GGAGGACACAAGTTTCATGAGGTTTTCCAAATGAAACAGGGGCGTTATGATCTTCAAGCTTCAAAG
 ATTTCTGAAATGATGAAATCAAGTAGCTTAGATAATGCTCCTACGCAGTCATTGCTAAGCGTCTTG
 AATGGAATTCTAGATGAAAGTATCGAAAGAAAGAATGGTGAAATCCCTCAGCGTGTGGCATGCCT
 GTTAAGAAAAGTCGTGCAGGAGATTGAGCGGCGTATATCAACTCAAGCTGAACATCTAAGAACGC
 AAAACAATATTTTCAAACTCGCGAGGAAAAATACCAGTCAAGGATCAATGTCCTTGAAGCCTTAG
 CATCAGGAACTGGTGTAGAACACGAGATTGCAACACAACAGCTTAGACAGATAGAGACAGAAAAG
 TCAATGTGGGAGGAAAAGAAGAAACACGAAGAGGAAGATATGGTTAAGCTAATGAAACAAAATG
 ATCAGCACAACCTCGAAATTTCTGCGTGAAGCAAGAACTGGAGACAACTAAAAGAAAATATGAA
 CAACAATACTCGCAATTTGAAAGCCAAACAAGACAGAGAAGTCAAAGTGGGAAGAACAGAAGA
 AAAATGAAGAGGAGGATATGGACAAGCTATTGAAAGAAAATGATCAGTTCAACCTTCAGATTTCT
 GCGTTAAGGCAAGAGCTGGAGACAACAAGAAAAGCGTATGAACAGCAATGCTCGCAAATGGAAA
 GCCAAACAATGGTTCGCTACAACAGGACTTGAGAGCAGGCTCAAGGAACTTGAACAAGAGGGAAA
 AGTGGTAAACACTGCAAAAAATGCCCTTGAGGAAAAGGTTAAAGAGCTTGAACAAATGGGAAAAG
 AAGCACATTCTGCTAAAAATGCTCTTGAGGAAAAGATTAACAGCTTCAACAAATGGAAAAGAA
 ACAAAACTGCTAATACAAGCCTTGAAGGAAAGATCCAAGAGCTTGAAACAACTCGTAATGTG
 GAAGACTAAAGTCAGAGAAATGGAGAAAAAGTCTGAGTCCAACCACAAAGATGGAGTCAGAAA
 GAACTTTCCTATAAAAGCTTTATTGATAACCAGTCTCAGGCACTACTGGAGTTGAGGTCCTATTCAA
 GATCCATCAAGCAAGAAATACTGAAGGTACAAGAGAACTATACAGACCAGTTCAGCCAACTAGGA
 AAGAAACTGATTGAACTTAGCAATGCTGCTGAAAACATACACGCTGTACTAACTGAAAACCGGAA
 GCTTTTCAACGAGCTTCAGGAGCTAAAAGGAAACATCAGAGTGTTTTGCCGGGTGAGGCCTTTCCT
 TCCTGCACAGGGTGCAGCAAACACAGTGGTTCGAGTATGTCGGTGAAGATGGAGAATTAGTAGTTA
 CCAATCCAAGTACCCGGGAAAAGACGGTCTTCGCCAGTTAAGTTCAACAAGGTGTATAGTCCAA
 CTGCTTCACAAGCTGACGCTTTTTCAGACATAAGACCGCTGGTTAGGTCAGTACTTGATGGGTACA
 ATGTTTGTATATTTGCATATGGCCAGACAGGATCAGGGAAAACCTTATACAATGACTGGTCCAGATG
 GATCAAGTGAAGAAGACTGGGGAGTAAATTATCGCGCTCTCAATGATCTTTTTAAAATCTCTCAGT
 CCAGAAAGGGAAACATATCGTATGAAGTCGGGGTGCAAATGGTGGAGATATATAATGAACAAGTG
 CTCGATCTGCTGTCTGATGACAATTCTAAAAGAAAACACTAGGGATCCTTTCTACAACCTCAACAA
 AATGGCCTGGCTGTGCCTGACGCAAGCATGTATCCTGTGACATCAACTTCAGATGTGATTACATTG
 ATGGACATTGGACTACAGAATCGAGCCGTTGGTTCTACTGCCTTGAATGAAAGAAGTAGTCGTTCA
 CATAGCATTGTCAGTTCACGTTTCGCGTAAAGATTTAAAGACCGGTTCCGTGCTATACGGTAAT
 CTTCAATTTGGTGGATCTGGCAGGAAGTGAGAGAGTAGATCGCTCTGAAGTTACAGGAGACAGACT
 AAGAGAAGCACAACATATAACAAGTCGCTCTCATCTCTTGAGATGTGATATTCTCTCTCGCTTC
 AAAGAGTTCTCATGTACCATACAGAAACAGCAAGCTAACACAGCTTCTCCAAACCTCTCTTGAGG
 ACGAGCAAAGACACTAATGTTTGTGCAACTCAACCCTGACGCTACTTCATACTCAGAGTCAATGAG
 TACCTTGAATTTGCAGAGCGTGTCTCTGGAGTCGAACCTTGGTGCTGCAAAGACAAGTAAAGAAGG
 TAAAGATGTTTCGAGACTTGATGGAACAGTTAGCGTCCCTTAAGGACACCATAGCGAGAAAAGACG
 AAGAGATAGAGAGACTTCAGCATCAGCCTCAGAGACTTCAGAAAATCAATGATGAGAAGAAAAAGC
 ATAGGACATACAGATGACATAAACTCAGATACAGGAGAATATTCATCACAATCAAGATACTCTGTT
 ACTGACGGCGAAAGTTTAGCATCCTCTGCCGAGGCAGAGTACGACGAGAGACTAAGCGAGATTAC
 GTCTGATGCTGCATCTATGGGAACACAAGGATCCATTGATGTTACCAAAGACCACCCAGAATTTTC
 AGACAGAGCTAAGTCGGTACTGCAAATCATCTACGAGTGTAACACGGCCACTCGATAAACTTC
 GGAAAGTAGCTACAAGAACAACATCGACCGTTGCTAAGGTCACGGGCTTGACATCATCAAGTAAA
 GGCTTAGCGTCATCAAGCATTAAAGAAGACGGGAAGTACATCAAGTTTGGCAAAGTCTTCAAAACG
 GTGGGCGACCACCACCACCACCTGA

motor domain, F-BAR domain, coiled-coil domain, EGFP, 6xHis-tag, CRISPR guided RNA

Sequence *A/BARK2(aa162-1140)-EGFP-6xHis*

ATGGGCAGCAGCAATTCTCTCACTGATCAATCGGCAGCTCTCATGGAGGTTCAACTCCCCGTAGTC
 CCTTCTCTCCATCATCTCCACGTGAAAGGCATAATAAAGGTCTGGCGGATTCCAGATTTCAACGTCC
 CCTGCCAATTCTTCAGCTCTAGATCCATCATCCCCTGGATCAATGCTCCATGGAGGACACAAGTCC
 CACGAGGCTTTCCAAATGAAACAGGGGCGATTTGATCTCCAAGCCGCAAAGATTTCAGAAGTATG
 AAATCAAACAATTTAGATAATGCTCCCACACAGTCACTTCTAAGTATCGTTAATGGAATTTCTGAT
 GAAACTATTGAGAGAAAGAATGGTGAACCTCCTCAGCGTGTAGCATGTCTGCTGAGAAAAGTCGT
 GCAGGAAATCGAGCGACGAATTTCAACTCAATCTGAACATCTAAGAACGCAAAAACAGTGTGTTTA
 AAGTCGTGAGGAGAAGTACCAGTCAAGGATCAAAGTTCTTGAAACCTTAGCTTCAGGAACTAGT
 GAAGAAAATGAGATTGCTACAAGACAACCTTCGACGGATAAAGACAGAAAAGTCCAAGCTGGAAG
 AAAAGAAGAAAGACAAAGAGGAGGATATGGTTGGGATAGAGAAAAGAAAATGGTCATTATAATCT
 TGAAATTTCTACTCTAAGGCGAGAAGTGGAGACAACCAAGAAAGCATATGAACAACAATGCTTAC
 AAATGGAAAAGCAAAAACAAAAGGCGCTACAGCTGGTATCGAGGACAGGGTTAAGGAGCTTGAACA
 AATGAGAAAAGGATGCAAGCGTTGCAAGAAAAGCCCTTGAGGAAAGGGTTAGGGAGCTTGA AAAAG
 ATGGGAAAAGAAGCAGATGCTGTTAAAATGAATCTTGAGGAAAAGGTGAAGGAGCTTCAAAAATA
 TAAAGATGAGACGATAACTGTCACTACAAGCATTGAAGGTAAAAATCGAGAGCTTGAACAATTTA
 AACAGGAGACAATGACCGTCACTACAAGCCTTGAAGCTCAAAACCGAGAGCTTGAACAAGCTATA
 AAAGAGACAATGACTGTTAATACAAGCCTTGAAGCTAAAAACCGAGAGCTTGAACAATCTAAAAA
 AGAGACAATGACTGTTAATACAAGCCTTAAAGCGAAAAACCGAGAGCTTGAACAAAATCTCGTCC
 ACTGGAAGAGTAAAGCCAAAGAAATGGAAGAAAAATCAGAGTTAAAGAATCGAAGTTGGAGTCA
 GAAAGAACTTTCTATAGAAGCTTTATCAGTTTCCAGTGCCAGGCGCTACAAGAGTTGAGGTTCTA
 TTCTAAGTCTATCAAACAAGAAATACTAAAAGTTCAAGATAAGTATACAGTAGAGTTTAGTCAATT
 AGGGAGGAAATTGCTTGAACCTGGAGATGCTGCCGCAAACCTATCACGAAGTCTAACTGAAAACC
 AAAAGCTCTTCAATGAACCTCAGGAGCTTAAAGGAAACATTAGAGTGTATTGTTCGAGTGAGGCCTT
 TCTTGCGTGGGCAAGGTGCATCAAAAACCTGTGGTAGAACACATTGGTGATCATGGGGAGTTGGTAG
 TTCTCAATCCAACAAAACCTGGCAAGGATGCTCATCGAAAATTTAGGTTCAATAAGGTCTACAGTC
 CTGCCTCTACTCAAGCTGAGGTATTTTCAGATATAAAAACCTCTTATTCGATCAGTTCTTGACGGGTA
 CAATGTATGTATCTTGCATATGGTCAGACAGGATCAGGGAAAACTTACACAATGACTGGTCCAGA
 TGGAGCAAGCGAAGAAGAGTGGGGAGTAAACTATCGTGCTCTCAATGACCTCTTCAGAATCTCTCA
 ATCCCGTAAAAGCAACATAGCGTATGAAGTTGGGGTGCAGATGGTGGAGATATACAATGAACAAG
 TGCGCGATTTACTCTCTGGTGACAGTTCTCAAAGAAACTAGGGATTCTCTCTACAACCTCAACAGA
 ACGGTCTTGCTGTACCTGATGCAAGCATGTATCCTGTGACATCCACCTCGGATGTTCTTGAATTAAT
 GAGCATTGGGCTACAAAACCGAGTTGTTAGCTCCACTGCCTTGAACGAAAGAAGTAGCCGCTCTCA
 CAGCATTGTCAGTTCATGTTCTGGCAAGGACTTGAAGACTGGTTCTGCGCTGTATGGAAATCT
 ACATTTGGTAGATCTAGCAGGTAGTGAGAGAGTTGATCGCTCGGAAGTTACAGGAGACAGACTTA
 AAGAAGCACACATATAAACAAGTCACTCTCAGCTCTAGGAGATGTGATATTCTCTCTTGCTTCAA
 AAAGTTCTCATGTACCATACAGGAACAGCAAACCTCACTCAGCTTCTCCAAAGCTCTTAGGTGGTC
 GAGCAAAGACACTAATGTTTGTCAACTGAATCCTGATATTACTTCATATTCAGAGTCAATGAGTA
 CTTTGAAATTCGCAGAGCGTGTCTCTGGAGTTGAGTTAGGAGCTGCTAAGAGCAGCAAAGATGGTA
 GAGACGTTAGAGAATTAATGGAGCAGTTAGGGTCCCTTAAAGACACAATAGCGAGAAAAGACGAT
 GAGATAGAGCGGCTTCATTTGCTTAAAGGACATAAATTACCCACAGAGACTGCAGAAAAGAGCTT
 AGGACAATCCGATGACTTTAACTCAGAAGCGGGAGATTTCGCAGTTGTCTATAGAAGATGACTCAA
 GATTCCAACACGATTATACCAGACAGTACGACACTCTGTCACGGACGGGGAGGCCCTTAGCTTCTT
 CCACTGATGCGGAGTATGATGATGAAACAGAAGGATCCACTGATGCTCCTTGTGCAGCAGAAGGG
 AGAAAACCTTTAAAGATTTAGACAAAACCTAAACCGGTGACTCCAAGGAGTAATACGACAACATC
 ACGACCACTTGATAAACTCAAGCAAGTCACTATGAGGACGACAAACATTGCAAAGGCTACGTCAG
 CCTTGTGTACCCGAGTTCTCAAGGCATGAAGAAGACGGGAAGTGCTTCTAATTTTCTAAAGTCAC
 CGAAAGATTCGAAACGTTGGTCTAGTAAAGGAGAAGAAGCTTTTCACTGGAGTTGTCCTCAATTCTTG
 TTGAATTAGATGGTGTATGTTAATGGGCACAAATTTTCTGTCAGTGGAGAGGGTGAAGGTGATGCAA
 CATAAGGAAAACCTTACCCTTAAATTTATTTGCACTACTGGAAAACCTACCTGTTCCATGGCCAACACT
 TGTCACTACTTTAACTTATGGTGTTCATGCTTTTCAAGATACCCAGATCATATGAAACGGCATGAC
 TTTTTCAAGAGTGCCATGCCGAAGGTTATGTACAGGAAAGAACTATATTTTTCAAGATGACGGG
 AACTACAAGACACGTGCTGAAGTCAAGTTTGAAGGTGATACCCTTGTTAATAGAATCGAGTTAAAA
 GGTATTGATTTTAAAGAAGATGGAAACATTCTTGACACAAATTGGAATACAACATAACTCACAC
 AATGTATACATCATGGCAGACAAAACAAAAGAATGGAATCAAAGTTAACTTCAAAATTAGACACAA

CATTGAAGATGGAAGCGTTCAACTAGCAGACCATTATCAACAAAATACTCCAATTGGCGATGGCCC
TGTCTTTTACCAGACAACCATTACCTGTCCACACAATCTGCCCTTTCGAAAGATCCCAACGAAAA
GAGAGACCACATGGTCCTTCTTGAGTTTGTAAACAGCTGCTGGGATTACACATGGCATGGATGAACT
ATACAAAATCACCATCATCACCATTAA

motor domain, F-BAR domain, coiled-coil domain, EGFP, 6xHis-tag

Sequence rKin430-EGFP-6xHis

ATGGCGGATCCAGCCGAATGCAGCATCAAAGTGATGTGCCGGTCCGGCCCCCTCAACGAAGCTGA
GATCCTCCGCGGGGACAAATTCATCCCCAAATCAAAGGCGAGGAGACGGTGGTGATCGGGCAAG
GGAAGCCGTATGTCTTTGACCGAGTTCTGCCGCCAACACAACCCAGGAGCAGGTCTACAATGCCT
GTGCGAAGCAGATTGTCAAAGATGTCCTCGAGGGTTACAATGGGACAATTTTTGCATACGGGCAGA
CTTCATCAGGAAAACTCATACCATGGAGGGGAAGCTGCACGATCCTCAGCTTATGGGTATCATA
CCAGGATCGCACACGATATTTTCGATCACATCTATTCCATGGATGAGAAGTTGGAGTTTCATATCA
AGGTTTCCTATTTTGGAGATCTACTTGGACAAAATAAGGGACTTGCTTGACGTGTCCAAGACCACT
TGGCTGTTTCATGAAGACAAAAACAGAGTCCCCTATGTAAAGGGGTGCACCGAGAGGTTTGTGTCA
AGCCCGGAGGAGGTCATGGATGTGATCGATGAGGGCAAAGCAAACCGACATGTGGCTGTGACAAA
CATGAACGAA

CACAGCTCCAGGAGTCACAGTATCTTCCTGATTAACATTAACAAGAGAATGTGGAGACTGAAAA
AAAACCTCAGCGGGAAGCTGTATTTGGTTGATTTGGCTGGGAGTGAAAAGGTCAGCAAAACTGGTG
CCGAGGGAGCTGTTCTTGATGAAGCTAAAAATATCAACAAGTCTTTGTCTGCTCTTGAAATGTGA
TCTCTGCCTTGGCAGAAGGGACAAAAACACATGTGCCATACCGGGACAGCAAGATGACTCGGATT
CTCCAGGACTCTCTGGGTGGGAAGTGCAGGACCACCATTTGTCATTTGCTGTTCTCCTCAGTCTTCA
ATGAGGCTGAGACCAAGTCCACGCTGATGTTTGGACAGAGAGCAAAGACCATCAAGAATACAGTC
TCTGTGAACTTGGAACTAACAGCAGAAGAATGGAAGAAGAAATATGAAAAAGAGAAAGAGAAGA
ATAAGGCCCTGAAGAGTGTCCATCCAGCATCTGGAGGTGGAGCTGAACAGGTGGAGGAACGGGGAA
GCTGTGCCTGAGGATGAACAGATCAGTGCCAAGGACCAGAAGAACCTGGAGCCCTGCGACAACAC
ACCCATCATAGACAACATCACACCTGTGGTTGACGGCATCTCTGCTGAGAAAGAGAAGTATGACG
AGGAAATCACCAGTCTGTACCGACAGCTGGATGACAAGGGTACCATGAGTAAAGGAGAAGAAGT
TTCCTGAGGTTGTCCCAATCTTGTGTTGAATTAGATGGTGATGTTAATGGGCACAAAATTTCTGTCA
GTGGAGAGGGTGAAGGTGATGCAACATACGGAAAACCTTACCCTTAAATTTATTTGCACTACTGGAA
AACTACCTGTTCCATGGCCAACACTTGTCACTACTTTAACTTATGGTGTTCAATGCTTTTCAAGATA
CCCAGATCATATGAAACGGCATGACTTTTTCAAGAGTGCCATGCCGAAGGTTATGTACAGGAAAG
AACTATATTTTTCAAAGATGACGGGAACTACAAGACACGTGCTGAAGTCAAGTTTGAAGGTGATAC
CCTTGTTAATAGAATCGAGTTAAAAGGTATTGATTTTAAAGAAGATGGAAACATTCTTGGACACAA
ATTGGAATACAACATAACTCACACAATGTATACATCATGGCAGACAAAACAAAAGAATGGAATCA
AAGTTAACTTCAAATTAGACACAACATTGAAGATGGAAGCGTTCAACTAGCAGACCATTATCAAC
AAAATACTCCAATTGGCGATGGCCCTGTCCTTTTACCAGACAACCATTACCTGTCCACACAATCTGC
CCTTTCGAAAGATCCCAACGAAAAGAGAGACCACATGGTCCTTCTTGAGTTTGTAAACAGCTGCTGG
GATTACACATGGCATGGATGAACTATACAAAATCACCATCATCACCATTAA

EGFP, 6xHis-tag

Sequence *Af*MISK1-FL-EGFP-6xHis

ATGGCGGATCCAACAAGATCGAAACCGGTTTCGGAATCTACCCGAGACAATCCATTCTTTGCTCGGT
 TTGAAATCTCATATGACTTCTGATTGGGTAAATCTGTATGCAACATCGCCAAGAATACTTCTTCAA
 CGTCAAAGAAAGAAGAAGACGACTTTGTTTCTGTGATTACAGAGCATTAGAGATCAGCTCTCTG
 CACTAACTGTTCAAGTCAACGATCAGAACAACCTGAGAAGACAAATTCTTAATGAGTTCTTGGACC
 TTAAGGGAAACATTCGTGTGTTTTGTGCGAGTCAAACCCCTGGGAGCCACCGAAAAAGTTGAGACCAC
 CGGTTGCTTCGGATACAAGAAATGTGATCATCAAGTTATCAGAAACCAAGAGAAAAACCTACAAC
 TTCGACAGAGTTTTCCAACCTGATTCATCCCAAGATGATGTTTTCTTAGAGATCGAACCCAGTAATCA
 AGTCAGTTATCGATGGCTACAACGCTTGCATTTTCGCATACGGGCAAACCGGTACTGGAAAAACTT
 ATACAATGGAGGGTCTCCGAACCTCCAGGTATCGTTCCCTCGAGCGATCAAGGGATTGTTCAAAC
 AAGTCGAGGAAAGTAATCATATGTTTACAATCCACTTTAGTATGCTTGAGATTTACATGGGAAATC
 TTAAGACTTGCTTCTTTCTGAAGCAACTAAACCCATTTCTCCAATACCTCCAAGTCTTTCTATCAC
 ACAGACCCAAATGGAGAGATAGATATTGAGAACTTGGTGAACCTTAAAGTGGATGACTTTAATGA
 AATCTTAAGGTTATACAAAGTAGGTTGTCGTAGCAGAGCAACTGCCTCCACTAACTCTAACTCTGT
 TTCCAGCAGATCACACTGTATGATCCGTGTATCGGTCACTAGTCTTGGAGCTCCTGAGAGACGGCG
 TGAACAAACAAGATTTGGCTAGTGGATCTTGGAGGAAGCGAGCGCGTGTGAAAACAAGAGCCA
 CTGGTCGGCGTTTTGATGAAGGCAAAGCCATTAATCTCTCTTTATCTGCTCTTGGAGATGTCATCAA
 CTCTCTCAACGCAAGAACTCTCACATTCCTTACAGGAACAGCAAGCTCACACAGGTTCTAAAAGA
 CTCTCTCGGGCAAGACTCAAAAACGTTGATGCTTGTTCATATCAGCCCTAAAGAGGATGATCTATG
 TGAACCATATGTTCTTTAACTTTGCAACGAGGGCAAAGAATATTCATTTAGGGCAGGACGAATC
 AACGGAAGAACAAGCGAAAAAGGAGGCTGTGATGATGAATCTGCAGAAGATGATGGAAAAGATT
 GAACAAGAGCGTGAGATGTCGTTAAGAAAGATGAGAAATCTAAACGAGACGTTGGAGAAACTCAC
TGGTAAGCCCTCATGTTATTGAAGAAGAAGAAAAGGATGTGGTTAGAGAAGTGATTCATGTGACTC
 CAAAGAAACCAAGAAACAAATCAAGACGTGCTTCAGATGTTTTCTAGCTTCATGAGACCAACAG
 CTAGCAGCAACAGAAGATTATCAGGAGCAGATTTTAGCGTAACCCCTAATTCTTCAAGCTTCAAGT
 CTAGAAGGAACTCAATGATATCTGTCCGAGCTGAATCTGCGTGTCTTCCGGTGAAGAAGAAGAAG
 AACAGATTTGATTCTGCATGTGACTCATCAGACAGGAGCGTTTCGAAATCGACTAGCATTATGCGT
 CAAAATACAGCAGATGATGCAACGGTGTATAGTCAGGACATATCTGAATGTGACATTAAGTTGGTA
 GTGTCTGAACACAAGCCAAAACCGCTGCAGATGGGGCCTGGTTCTGCGACAAAGTCCCGCTCCAAC
 ATCAGTAACTTCGAGAAAGATGTGATGCAGAAAATAGGTGGAACAGAGTTTTCAAGGATTAACAG
 TTGGCTTCGTTGCAATCTGAAAACAGGAGTTACGTGCTTGACAAGACTCAACTTCCTGCGACTCA
 TTTCTAGAAAACCTAAACAGATCGTTGGAGAAGTCACCAACACAGAGTTTTACAACGGAGAAGA
 TCACTGGAAATGAACTGGAAGGTATAGAAGAGACTAAAACAAATGAGACAGTGGTTAACCCCTACA
 CTGATGCTTAAAAAACTGTTTGAAGCTGCAATGTCTCTGTTCTGCTGAAGAAGAGGATCAGATTTTGT
 CCAGATTCCTAATTCCTGGCTATGAGGATGATGATGAGTCTCGTTATCCTCCATTTTAGAAAACGAT
 GGATTTAGCCAGCACATAGACAATGAATGGTTTGGAGTCAATAATTACAGTGCGGATTGGGAGCG
 AGATTCACCAGCCACGATCCCGTTGTTAGAATGCGAACCGGATCTCAAACAGCTGTTACCGGAATT
 GGGTTTGGATCGATCACTTAAACCAAGAGGTTTGGCGGTGCGGAGGGTGCAGCTCCACCATTGCT
 TAGAGCACAAGAAACCTTGGGAGAAAGAGGAAAAGGTCCAACGTTTCATGCAGAAACTTCAGGCTT
 TATGCTCCGTATTCTTCTGGGATTAGGGTTTATGGATGTGGGCTTGGTAATGACTTCTTCAACGG
 GTTAACAAAGGGT**ACC**ATGAGTAAAGGAGAAGA**ACTTTTCACTGGAGTTGTCCCAATTCTTGTG**
ATTAGATGGTGATGTTAATGGGCACAAATTTTCTGTGAGTGGAGAGGGTGAAGGTGATGCAACATA
CGGAAAACCTTACCCTTAAATTTATTTGCACTACTGGAAAACCTACCTGTTCCATGGCCAACACTTGT
ACTACTTTAACTTATGGTGTTCATGCTTTTCAAGATACCCAGATCATATGAAACGGCATGACTTTT
TCAAGAGTGCCATGCCGAAGGTTATGTACAGGAAAGAACTATATTTTTCAAAGATGACGGGA**ACT**
ACAAGACACGTGCTGAAGTCAAGTTTGAAGGTGATACCCTTGTTAATAGAATCGAGTTAAAAGGTA
TTGATTTTAAAGAAGATGGAACATTCTTGGACACAAATGGAATACAACTATAACTCACACA**ATG**
TATACATCATGGCAGACAAACAAAAGAAATGGAATCAAAGTTA**ACTTCAA**AA**ATTAGACACA**AC**ATT**
GAAGATGGAAGCGTTCAACTAGCAGACCATTATCAACAAAACTCA**ATTGGCGATGGCCCTGT**C****
CTTTTACCAGACAACCATTACCTGTCCACACAATCTGCCCTTTCGAAAGATCCCAACGAAAAGAGA
GACCACATGGTCTTCTTG**AGTTTGTAAACAGCTGCTGGGATTACACATGGCATGGATGAACTATAC**
AAACATCACCATCATCACCATTAA

motor domain, coiled-coil domain, EGFP, 6xHis-tag, KpnI restriction site, site for the generation of a second KpnI restriction site by site-directed mutagenesis

Sequence *Af*MISK1(aa3-462)-EGFP-6xHis

ATGGCGGTACCAACAAGATCGAAACCGGTTTCGGAATCTACCCGAGACAATCCATTCTTTGCTCGGT
TTGAAATCTCATATGACTTCTGATTGGGTAAATCTGTATGCAACATCGCCAAGAATACTTCTTCAA
CGTCAAAGAAAGAAGAAGACGACTTTGTTTCTGTGATTACAGAGCATTAGAGATCAGCTCTCTG
CACTAACTGTTCAAGTCAACGATCAGAACAACCTGAGAAGACAAATTCTTAATGAGTTCTTGGACC
TTAAAGGGAACATTCGTGTGTTTTGTGCGAGTCAAACCCCTGGGAGCCACCGAAAAAGTTGAGACCAC
CGGTTGCTTCGGATACAAGAAATGTGATCATCAAGTTATCAGAAAACCAAGAGAAAAACCTACAAC
TTCGACAGAGTTTTCCAACCTGATTCATCCCAAGATGATGTTTTCTTAGAGATCGAACCCAGTAATCA
AGTCAGTTATCGATGGCTACAACGCTTGCATTTTCGCATACGGGCAAACCGGTACTGGAAAAACTT
ATACAATGGAGGGTCTTCCGAACCTCCAGGTATCGTTCCCTCGAGCGATCAAGGGATTGTTCAAAC
AAGTCGAGGAAAGTAATCATATGTTTACAATCCACTTTAGTATGCTTGAGATTTACATGGGAAATC
TTAAAGACTTGCTTCTTTCTGAAGCAACTAAACCCATTTCTCCAATACCTCCAAGTCTTTCTATTCA
CACAGACCCAAATGGAGAGATAGATATTGAGAAGTGGTGAAACTTAAAGTGGATGACTTTAATG
AAATCTTAAGGTTATACAAAGTAGGTTGTGCTAGCAGAGCAACTGCCTCCACTAACTCTAACTCTG
TTCCAGCAGATCACACTGTATGATCCGTGTATCGGTCCTAGTCTTGGAGCTCCTGAGAGACGGC
GTGAAACAAACAAGATTTGGCTAGTGGATCTTGGAGGAAGCGAGCGCGTGTGAAAACAAGAGCC
ACTGGTCGGCGTTTTGATGAAGGCAAAGCCATTAATCTCTCTTTATCTGCTCTTGGAGATGTCATCA
ACTCTCTCAACGCAAGAACTCTCACATTCCTTACAGGAACAGCAAGCTCACACAGGTTCTAAAAG
ACTCTCTCGGGCAAGACTCAAAAACGTTGATGCTTGTTCATATCAGCCCTAAAGAGGATGATCTAT
GTGAAACCATATGTTCTTTAAACTTTGCAACGAGGGCAAAGAATATTCATTTAGGGCAGGACGAA
TCAACGGAAGAACAAGCGAAAAAGGAGGCTGTGATGATGAATCTGCAGAAGATGATGGAAAAGA
TTGAACAAGAGCGTGAGATGTCGTTAAGAAAGATGAGAAATCTAAACGAGACGTTGGAGAAACTC
ACTGGTACCATGAGTAAAGGAGAAGAACTTTTACTGGAGTTGTCCCAATTCTTGTTGAATTAGAT
GGTGATGTTAATGGGCACAAATTTTCTGTGAGTGGAGAGGGTGAAGGTGATGCAACATACGGAAA
ACTTACCCTTAAATTTATTTGCACTACTGGAAAACCTGTTCCATGGCCAACACTTGTCACTACT
TTAACTTATGGTGTTCATGCTTTTCAAGATACCCAGATCATATGAAACGGCATGACTTTTTCAAGA
GTGCCATGCCCAGGTTATGTACAGGAAAGAACTATATTTTTCAAAGATGACGGGAACTACAAG
ACACGTGCTGAAGTCAAGTTTGAAGGTGATACCCTTGTTAATAGAATCGAGTTAAAAGGTATTGAT
TTTAAAGAAGATGGAAACATTCTTGGACACAAATTGGAATACAACATAACTCACACAATGTATAC
ATCATGGCAGACAAACAAAAGAATGGAATCAAAGTAACTTCAAATTAGACACAACATTGAAGA
TGGAAGCGTTCAACTAGCAGACCATTATCAACAAAATACTCCAATTGGCGATGGCCCTGTCCTTTT
ACCAGACAACCATTACCTGTCCACACAATCTGCCCTTTCGAAAGATCCCAACGAAAAGAGAGACC
ACATGGTCCTTCTTGAGTTTGTAAACAGCTGCTGGGATTACACATGGCATGGATGAACTATACAAAC
ATCACCATCATCACCATTAA

motor domain, coiled-coil domain, EGFP, 6xHis-tag, KpnI restriction site, site for the generation of a second KpnI restriction site by site-directed mutagenesis

Sequence *Af*MISK1(aa3-415)-EGFP-6xHis

ATGGCGGATCCAACAAGATCGAAACCGGTTTCGGAATCTACCCGAGACAATCCATTCTTTGCTCGGT
 TTGAAATCTCATATGACTTCTGATTGGGTAAATCTGTATGCAACATCGCCAAGAATACTTCTTCAA
 CGTCAAAGAAAGAAGAAGACGACTTTGTTTCTGTGATTACAGAGCATTAGAGATCAGCTCTCTG
 CACTAACTGTTCAAGTCAACGATCAGAACAACCTGAGAAGACAAATTCTTAATGAGTTCTTGGACC
 TTAAAGGGAACATTCGTGTGTTTTGTGCGAGTCAAACCCCTGGGAGCCACCGAAAAAGTTGAGACCAC
 CGGTTGCTTCGGATACAAGAAATGTGATCATCAAGTTATCAGAAACCAAGAGAAAAACCTACAAC
 TTCGACAGAGTTTTCCAACCTGATTCATCCCAAGATGATGTTTTCTTAGAGATCGAACCCAGTAATCA
 AGTCAGTTATCGATGGCTACAACGCTTGCATTTTCGCATACGGGCAAACCGGTACTGGAAAAACTT
 ATACAATGGAGGGTCTTCCGAACCTCCAGGTATCGTTCCCTCGAGCGATCAAGGGATTGTTCAAAC
 AAGTCGAGGAAAGTAATCATATGTTTACAATCCACTTTAGTATGCTTGAGATTTACATGGGAAATC
 TTAAAGACTTGCTTCTTTCTGAAGCAACTAAACCCATTTCTCCAATACCTCCAAGTCTTTCTATTCA
 CACAGACCCAAATGGAGAGATAGATATTGAGAACTTGGTGAAACTTAAAGTGGATGACTTTAATG
 AAATCTTAAGGTTATACAAAGTAGGTTGTGCTAGCAGAGCAACTGCCTCCACTAACTCTAACTCTG
 TTTCCAGCAGATCACACTGTATGATCCGTGTATCGGTCCTAGTCTTGGAGCTCCTGAGAGACGGC
 GTGAAACAAACAAGATTTGGCTAGTGGATCTTGGAGGAAGCGAGCGCGTGTGAAAACAAGAGCC
 ACTGGTCGGCGTTTTGATGAAGGCAAAGCCATTAATCTCTCTTTATCTGCTCTTGGAGATGTCATCA
 ACTCTCTCAACGCAAGAACTCTCACATTCCTTACAGGAACAGCAAGCTCACACAGGTTCTAAAAG
 ACTCTCTCGGGCAAGACTCAAAAACGTTGATGCTTGTTCATATCAGCCCTAAAGAGGATGATCTAT
 GTGAAACCATATGTTCTTTAAACTTTGCAACGAGGGCAAAGAATATTCATTTAGGGGGTACCATGA
 GTAAAGGAGAAGAACTTTTCACTGGAGTTGTCCAATTCTTGTGGAATTAGATGGTGATGTTAATG
 GGCACAAATTTTCTGTGAGTGGAGAGGGTGAAGGTGATGCAACATACGGAAAACTTACCCTTAAAT
 TTATTTGCACTACTGGAAAACTACCTGTTCCATGGCCAACACTTGTCACTACTTAACTTATGGTGT
 TCAATGCTTTTCAAGATACCCAGATCATATGAAACGGCATGACTTTTTTCAAGAGTGCCATGCCCGA
 AGGTTATGTACAGGAAAGAAGTATATTTTTCAAAGATGACGGGAACTACAAGACACGTGCTGAAG
 TCAAGTTTGAAGGTGATACCCTTGTTAATAGAATCGAGTTAAAAGGTATTGATTTTAAAGAAGATG
 GAAACATTCTTGGACACAAATTGGAATACAACATAACTCACACAATGTATACATCATGGCAGACA
 AACAAAAGAATGGAATCAAAGTTAACTTCAAAATTAGACACAACATTGAAGATGGAAGCGTTCAA
 CTAGCAGACCATTATCAACAAAATACTCCAATTGGCGATGGCCCTGTCCTTTTACCAGACAACCAT
 TACCTGTCCACACAATCTGCCCTTCGAAAGATCCCAACGAAAAGAGAGACCACATGGTCCTTCTT
 GAGTTTGTAAACAGCTGCTGGGATTACACATGGCATGGATGAACTATACAAA**CATACCATCATCAC**
CATTAA

motor domain, coiled-coil domain, EGFP, 6xHis-tag, KpnI restriction site

The non-processive rice kinesin-14 OsKCH1 transports actin filaments along microtubules with two distinct velocities

Wilhelm J. Walter^{1,2*}, Isabel Machens¹, Fereshteh Rafieian² and Stefan Diez^{2,3*}

Microtubules and actin filaments function coordinately in many cellular processes^{1–3}. Although much of this coordination is mediated by proteins that statically bridge the two cytoskeletal networks^{4–6}, kinesin-14 motors with an actin binding calponin homology domain (KCHs) have been discovered as putatively dynamic crosslinkers in plants^{7,8}. OsKCH1, a KCH from rice, interacts with both microtubules and actin filaments *in vivo* and *in vitro*⁹. However, it has remained unclear whether this interaction is dynamic or if actin binding reduces or even abolishes the motor's motility on microtubules^{10,11}. Here, we directly show *in vitro* that OsKCH1 is a non-processive, minus-end-directed motor that transports actin filaments along microtubules. Interestingly, we observe two distinct transport velocities dependent on the relative orientation of the actin filaments with respect to the microtubules. In addition, torsional compliance measurements on individual molecules reveal low flexibility in OsKCH1. We suggest that the orientation-dependent transport velocities emerge from OsKCH1's low torsional compliance combined with an inherently oriented binding to the actin filament. Together, our results imply a central role of OsKCH1 in the polar orientation of actin filaments along microtubules, and thus a contribution to the organization of the cytoskeletal architecture.

The interaction of OsKCH1 with microtubules and actin filaments has been studied *in vitro* and *in vivo*. Co-sedimentation assays with truncated constructs proved that binding occurs via the motor and calponin homology (CH) domains respectively^{9,10}. Similar results have been obtained for the closely related cotton homologue GhKCH2^{12,13}. A monomeric CH domain of OsKCH1 showed no actin binding *in vitro*, indicating the need of dimerization for the CH domain's functionality⁹ as expected¹⁴. Similarly, OsKCH1^{9,10} and its homologues GhKCH2¹³ and NtKCH1¹¹ co-localize with both microtubules and actin filaments *in vivo*. It has been previously observed¹⁵ that OsKCH1 plays a major role in nuclear positioning and two models to explain the function of OsKCH1 within this process have been proposed: (1) in the 'pulling/pushing' model the forces generated to position the nucleus result from growing and shrinking microtubules anchored to the perinuclear actin network and the cortex respectively by static KCH motors; (2) in the 'sliding' model forces are generated by KCH motors anchored to the cortex. They actively pull microtubules that on the other side are anchored to the perinuclear actin network by static KCHs. The latter model implies two motor subpopulations — one active and one static. Interestingly, two distinct subpopulations of NtKCH have been found—a motile population on the cortical microtubules and a non-motile population at the

nuclear periphery bound to actin cables¹¹, and it was hypothesized that binding to actin might cripple the motor's activity. This is supported by a significantly decreased activity of OsKCH1 in ATPase assays in the presence of actin, even in the absence of its CH domain¹⁰. To dissect how actin binding affects the motility *in vitro*, experiments were proposed containing only purified KCH motors in the presence of microtubules and actin filaments^{16,17}.

To study the interaction of OsKCH1 with microtubules and actin filaments, we performed actin transport motility assays where motors could interact simultaneously with surface-immobilized microtubules and free actin filaments in the presence of ATP (Fig. 1a). We found that the previously described construct OsKCH1(aa1-744) (ref. 9, Supplementary Fig. S1) actively transported actin filaments along microtubules in a unidirectional manner (Fig. 1b–d and Supplementary Movie 1). Interestingly, we observed two populations of actin filaments being transported with distinct velocities $v_1 = 82 \pm 39 \text{ nm s}^{-1}$ and $v_2 = 11 \pm 7 \text{ nm s}^{-1}$ (mean \pm s.d., $N = 201$ total transport events, Fig. 1e,f) independent of the length of the transported filaments (Supplementary Fig. S2).

OsKCH1-mediated transport of actin filaments appeared to be highly robust and many of the transported actin filaments reached the microtubule ends ($N = 61$). There, most of the actin filaments ($N = 54$) immediately detached from their tracks. However, some actin filaments ($N = 7$) spontaneously flipped back on their track by 180°, thereby changing their relative orientation with respect to the microtubule (Supplementary Fig. S3). Three more flips that did not happen at the microtubule end were observed. After flipping, transport persisted (unlike observed for kinesin-14 Ncd (ref. 18) and kinesin-5 Eg5 (ref. 19) involved in directional microtubule–microtubule sliding) (Fig. 1g and Supplementary Movie 2). Interestingly, the change in relative orientation coincided with a distinct change in the transport velocity (Fig. 1h). This suggests that the two velocity populations result from the two different orientations an actin filament can have with respect to the microtubule.

To test whether actin acts as a regulator of the OsKCH1 transport velocity, we performed a microtubule 'gliding' motility assay²⁰ in the absence of actin. Therefore, we generated a recombinant OsKCH1 (aa292-744) construct with an amino-(N)-terminal His-tag derived from the OsKCH1(aa1-744) expression plasmid (Supplementary Fig. S1). Motors immobilized to the surface drove the motion of fluorescently labelled, polarity-marked microtubules in the presence of ATP (Fig. 2a). We determined a gliding velocity of about 90 nm s^{-1} (Fig. 2b) independent of the motor protein density (Fig. 2c). This velocity corresponds to the velocity of the faster population observed in our actin transport assay (see Fig. 1), whereas the slower population was not observed.

¹Molecular Plant Physiology, Biocentre Klein Flottbek, University of Hamburg, 22609 Hamburg, Germany. ²B CUBE – Center for Molecular Bioengineering, Technische Universität Dresden, 01307 Dresden, Germany. ³Max Planck Institute of Molecular Cell Biology and Genetics, 01307 Dresden, Germany.

*e-mail: wim.walter@uni-hamburg.de; diez@bcube-dresden.de

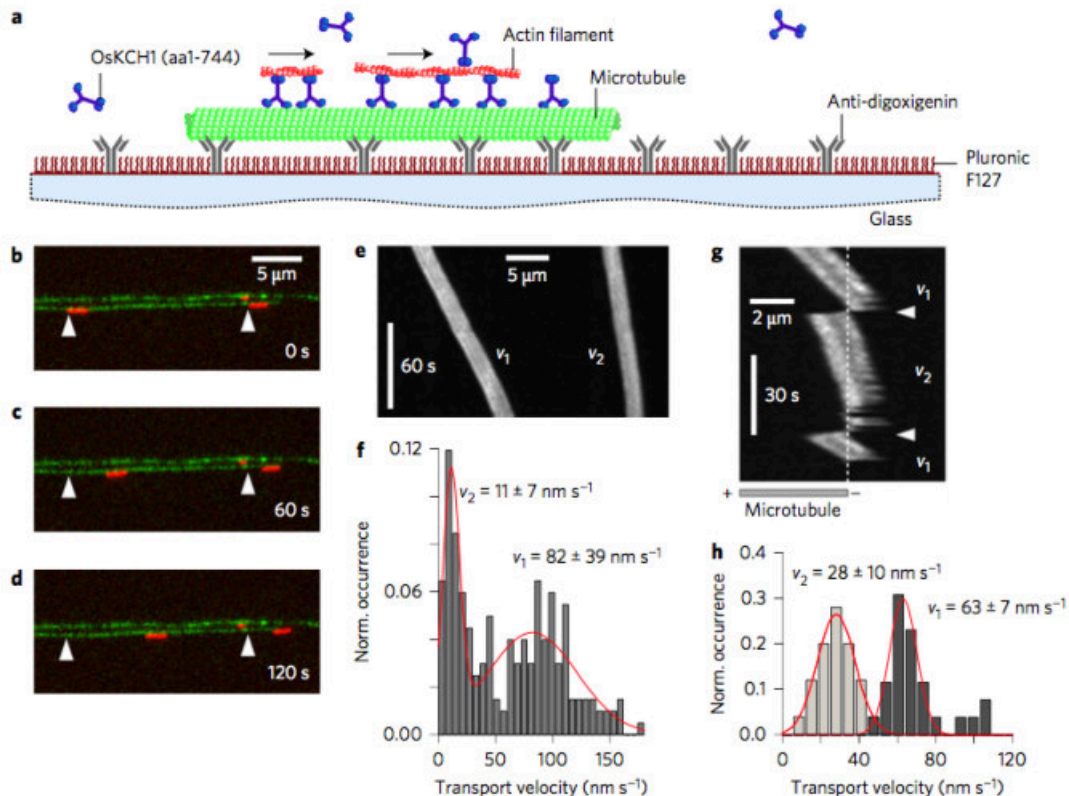


Figure 1 | OsKCH1 transports actin filaments along microtubules with two distinct velocities. **a**, Schematic representation of the transport motility assay using OsKCH1(aa1-744) (see Methods for details). **b–d**, Fluorescence micrographs of representative actin filaments (red) being transported by OsKCH1(aa1-744) along a the lower of the two microtubules (green) at different points in time. The starting positions of the transported actin filaments are marked by the white arrowheads. **e**, Kymographs of the two actin filaments for 201 transported actin filaments. Two distinct velocity populations are visible (v_1 and v_2). A double Gaussian fit of the histogram delivers the velocities $v_1 = 82 \pm 39 \text{ nm s}^{-1}$ and $v_2 = 11 \pm 7 \text{ nm s}^{-1}$ (mean \pm s.d.). **g**, Kymograph of a representative actin filament being transported to the end of a microtubule by OsKCH1(aa1-744). Each flipping event (indicated by a white arrowhead) coincides with a change in transport velocity (between v_1 and v_2). **h**, Histogram of the instantaneous frame-to-frame transport velocities deduced from the flipping actin filament in **g**. The two emerging velocity populations (v_1 and v_2) result from the changing orientation of the actin filament with respect to the microtubule. Gaussian fits of the histograms deliver the velocities $v_1 = 63 \pm 7 \text{ nm s}^{-1}$ and $v_2 = 28 \pm 10 \text{ nm s}^{-1}$ (mean \pm s.d.). The length of flipping actin filaments ($2.62 \pm 0.88 \mu\text{m}$, mean \pm s.d., $N = 10$) and the mean length of all transported actin filaments ($1.77 \pm 1.42 \mu\text{m}$, mean \pm s.d., $N = 201$) did not differ significantly.

Moreover, we confirmed that OsKCH1 is a minus-end-directed motor (Fig. 2d,e and Supplementary Movie 3) as predicted from the consensus neck linker motif for microtubule minus-end-directed kinesins²¹ found in the amino acid sequence.

To determine whether OsKCH1 is processive (that is, if it is capable of performing a significant number of consecutive steps per encounter with a microtubule), we generated an OsKCH1(aa292-744) construct with a N-terminal mGFP tag²² (Supplementary Fig. S1) and performed a single-molecule ‘stepping’ assay. The interaction of the motors with surface-bound microtubules was observed using total internal reflection fluorescence (TIRF) microscopy. We found that OsKCH1 is a non-processive motor that interacted only transiently with the microtubule (Supplementary Fig. S4 and Movie 4) as previously shown for other plant motors of the kinesin-14 family²³.

How can the transport velocity depend on the orientation of the cargo? If there is no significant, orientation-dependent friction between the transported actin filaments and the microtubules—which we assume to be unlikely as no interactions between actin filaments and microtubules are observed in the absence of OsKCH1—we speculated steric limitations in the motor geometry to be the reason. If the CH domain-mediated binding of OsKCH1 to actin filaments were stereo-specific and if OsKCH1 itself comprised a low torsional compliance, one could envision that the two possible orientations of the actin filament may generate two

distinct, non-isotropic orientations of the kinesin motor heads with respect to the microtubule. As OsKCH1 motility always occurs towards the microtubule minus end, one orientation may be more favourable for efficient transport than the other. To test this hypothesis, we investigated the torsional compliance of OsKCH1 by measuring the thermally driven rotational Brownian motion of short microtubules bound to single OsKCH1(aa4-744) molecules (Supplementary Figs S1, S5 and Movie 5 for functionality verification of this construct) sparsely attached to immobilized actin filaments in the presence of the non-hydrolysable ATP analogue AMPPNP (Fig. 3a). The rotation of the microtubules was monitored for 10 min. Indicative of single-molecule binding, the short microtubules rotated around a single centre point for the whole observation period (Fig. 3b and Supplementary Movie 6). The unchanged centre positions of the rotations for the whole measurement indicated a strong and static binding of the CH domain to the actin filaments. Most importantly, maximum projections of the rotation time lapses (representative example in Fig. 3c) show that the rotational freedom of the microtubules attached to actin-bound OsKCH1(aa4-744) was restricted to angles of $\theta = 40 \pm 15^\circ$ ($N = 13$ microtubules, mean \pm s.d.). This finding indicates low torsional compliance of OsKCH1. Control experiments, where OsKCH1(aa4-744) molecules were sparsely attached to the surface via anti-His antibodies, revealed a $>360^\circ$ rotational freedom of the microtubules (Fig. 3d–f and Supplementary Movie 7).

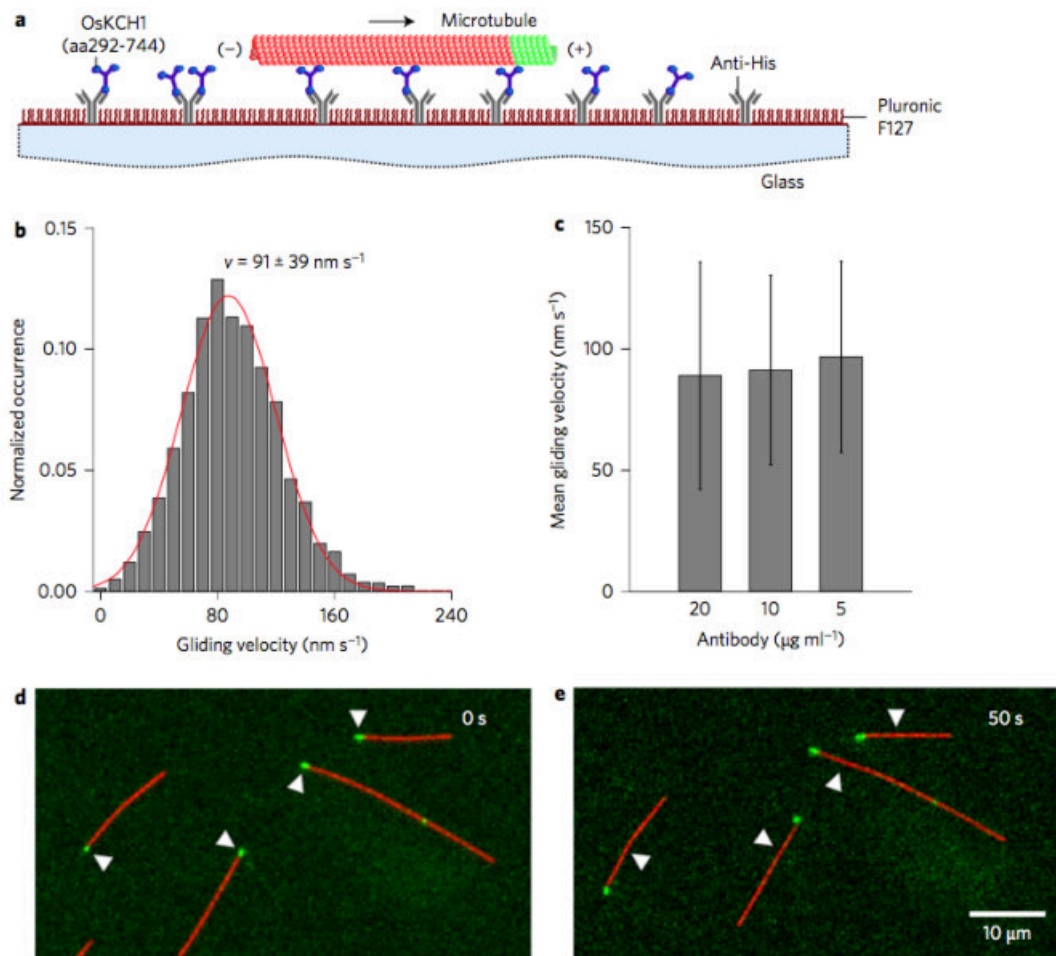


Figure 2 | OsKCH1 is a microtubule minus-end-directed motor. **a**, Schematic representation of the microtubule gliding motility assay using OsKCH1(aa292-744) (see Methods for details). **b**, Histogram of the instantaneous frame-to-frame gliding velocities for 130 gliding microtubules in experiments where an antibody concentration of $10 \mu\text{g ml}^{-1}$ was applied to coat the substrate surface with antibodies for further motor attachment. A Gaussian fit of the histogram delivers a velocity of $91 \pm 39 \text{ nm s}^{-1}$ (mean \pm s.d.). **c**, Histogram of the mean gliding velocity at different applied antibody concentrations. $v_{20 \text{ mg ml}^{-1}} = 88 \pm 46 \text{ nm s}^{-1}$ (mean \pm s.d., $N = 70$), $v_{10 \text{ mg ml}^{-1}} = 91 \pm 39 \text{ nm s}^{-1}$ (mean \pm s.d., $N = 130$), $v_{5 \text{ mg ml}^{-1}} = 96 \pm 39 \text{ nm s}^{-1}$ (mean \pm s.d., $N = 54$). **d,e**, Fluorescence micrographs of polarity-marked microtubules gliding on the OsKCH1(aa292-744)-coated surface at different points in time. The leading microtubule plus ends (green, starting positions marked by the white arrowheads) are indicative of a minus-end-directed motor. This was the case for all 33 observed gliding microtubules with one clearly labelled plus end.

We showed that OsKCH1 is a non-processive, microtubule minus-end-directed motor that actively transports actin filaments along microtubules. This finding strongly supports the hypothesis that OsKCH1 plays an active 'sliding' role rather than a passive 'anchoring' role in the positioning of the nucleus. We found two distinct transport velocities that depend on the polarity of the transported actin filament in respect to the microtubule. Interestingly, the velocity of the fast population largely matches the velocities observed in a gliding motility assay in the absence of actin. Thus, we can rule out that actin is fundamentally crippling the motility of OsKCH1. This observation contradicts previous hypotheses derived from *in vivo* observations^{11,16} and ATPase activity measurements¹⁰ with tobacco and cotton homologues of OsKCH1.

We found that the binding of OsKCH1 to actin filaments is stable for several minutes. Despite the dynamic nature of actin filaments²⁴, motors bound to relatively stable actin cables are likely to appear non-motile within the short timeframe of recent *in vivo* measurements¹¹. However, some of the differences between the study by Klotz *et al.*¹¹ and our observations might result from differences between the homologues in rice and tobacco or the conditions in the *in vitro* assays, including truncation of the motor and the lack of regulation. The reported reduction of *in vitro* ATPase activity

upon addition of actin filaments¹⁰ may be explained by the high affinity of the CH domain to actin filaments. As the motor gets sequestered from the solution, the probability of interactions with microtubules decreases, which causes a lower observed ATPase rate. Moreover, measurements on the actin-dependent ATPase rate of KCHs lacking the CH domain might potentially have been complicated by the sensitivity of the assays with respect to the buffer conditions, including salt concentration and pH.

We propose that orientation-dependent transport velocities emerge from the steric limitations that result from OsKCH1's low torsional compliance in combination with an inherent binding orientation to the actin filament (Fig. 4). Those steric limitations might impair the binding rate of the motor domain to the microtubule, resulting in a slower overall velocity. In conjunction with future structural work on OsKCH1 and its interaction geometry with microtubules and actin filaments, it will be of interest to relate the fast and slow velocity modes to the relative orientation of the filaments. Interestingly, the velocity regulation of OsKCH1 as a function of actin polarity is reminiscent of the regulation of tetrameric kinesin-5 motors that can also sense the relative orientation of the two microtubules they crosslink, supposedly by an allosteric mechanism that involves a twist in the stalk²⁵. Similarly, *in vitro*

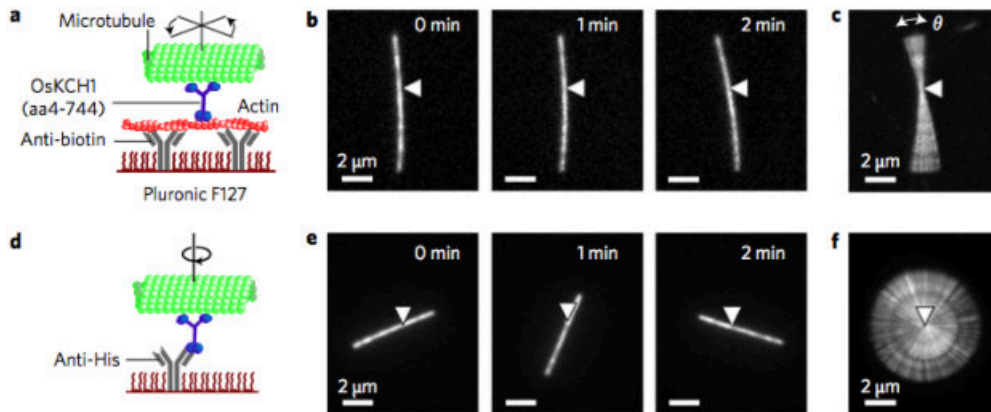


Figure 3 | OsKCH1 has a low torsional compliance when bound to an actin filament. **a**, Schematic representation of the rotation assay where single OsKCH1(aa4-744) molecules were immobilized on surface-bound actin filaments (see Methods for details). **b**, Fluorescence micrographs of a representative microtubule rotating on a single OsKCH1(aa4-744) molecule bound to actin at different points in time. The white arrowhead marks the stationary centre position of the rotation. **c**, Maximum projection over 10 min (200 frames) of the example in **b**. The rotational motion of the microtubules was restricted to $\theta = 40 \pm 15^\circ$ (mean \pm s.d., $N = 13$ microtubules). **d-f**, Schematic representation and data as in (**a-c**) for the case where single OsKCH1 molecules were immobilized to the surface via anti-His antibodies. Here, the rotational freedom of the microtubule was $>360^\circ$ for 15 out of 19 observed microtubules.

experiments with actin filaments transported along surface-bound muscle myosin filaments showed a higher velocity when movement was directed towards the centre of the myosin filament, indicating a preferred binding orientation of a presumably stiff motor²⁶. This mechanism is very distinct from motors with a highly flexible tail domain, such as kinesin-1, that show no dependence on the orientation of the cargo²⁷⁻²⁹. However, it has been shown that truncation of kinesin-1 leading to decreased torsional compliance resulted in reduced velocities in gliding motility assays. The reason for the high velocity we measured in our gliding motility assay is most likely to be the $>360^\circ$ rotational freedom we observed for

antibody-bound motors, as could be expected from the high intrinsic rotational freedom of immunoglobulin G molecules³⁰.

The structural basis for OsKCH1's low torsional compliance and the inherent binding orientation to actin filaments might lie in the presence of a second predicted coiled-coil region carboxy (C)-terminal of the motor domain. This coiled-coil could either dimerize or fold back onto the coiled-coil N-terminal of the motor domain to form a tetramer. In particular, the latter might significantly decrease the compliance³¹. Moreover, this second dimerization domain is likely to break any possible twofold rotational symmetry of the dimeric motor protein, explaining both the presence of a preferred binding orientation of the CH domains to the translationally symmetric actin filament and a preferred orientation of the kinesin motor domains when interacting with the translationally symmetric microtubule track.

As the polarity of the actin filament directly determines the motor's velocity, we agree with the statement that filamentous actin is an important regulator of KCH activity^{11,16}. Furthermore, we propose that OsKCH1's preference for one actin orientation may lead to a disequilibrium in the polar distribution of actin filaments in the region of the microtubule minus ends. This kind of sorting effect may contribute to define the general orientation of the cytoskeleton.

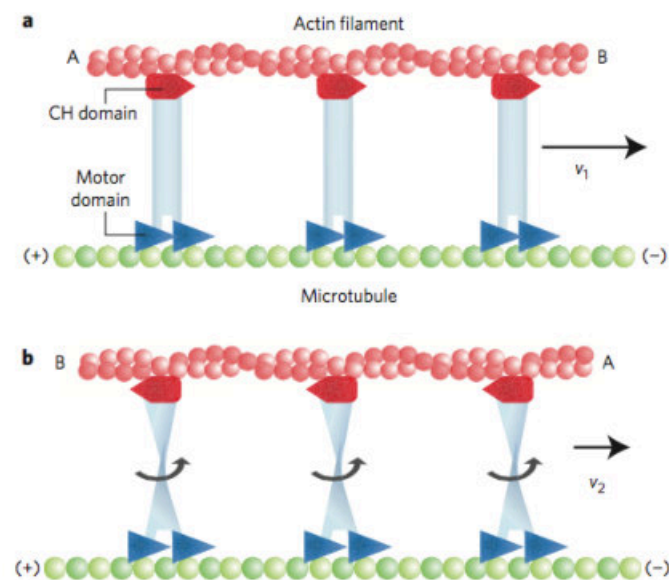


Figure 4 | Proposed model for the mechanism underlying OsKCH1's two transport velocities. **a**, OsKCH1 binds to actin filaments (polarity denoted by the letters A and B at the filament ends) with an inherent orientation. When the actin filament is aligned in its favourable orientation with respect to the microtubule, the transport velocity is not impacted. **b**, When the orientation of the actin filament is opposite from the orientation in **a**, OsKCH1 molecules need to twist to bind to the microtubule. The low torsional compliance of the motor then leads to an impaired binding to the microtubule, resulting in a decreased transport velocity.

Methods

Proteins. All OsKCH1 constructs used in this study (Supplementary Fig. S1) derived from an expression plasmid for OsKCH1(aa1-744) kindly provided by Peter Nick (Karlsruher Institut für Technologie) using standard polymerase chain reaction and cloning techniques. After expression in *Escherichia coli* BL21(DE3)-pRARE (Millipore), His-tagged motors were purified from cell lysate using a metal affinity column (GE Healthcare), snap-frozen in liquid nitrogen, and stored at -80°C . Microtubules were polymerized as described before^{32,33}. Actin filaments were polymerized from 3 μM rabbit skeletal muscle actin in 10 mM 4-(2-hydroxyethyl)-1-piperazineethanesulfonic acid/NaOH pH 7.0, 100 mM KCl, 2 mM ATP and 5 μM rhodamine phalloidin (life technologies) for 60 min at 4°C .

In vitro assays. Gliding assays and single-molecule stepping assays were performed as described before³². In the transport motility assay, microtubules co-labelled with digoxigenin and Cy5 were immobilized to the glass surface via digoxigenin antibodies (Roche). After blocking with 1% Pluronic F127 OsKCH1(aa1-744) motors were added to the microtubules in the absence of ATP. Subsequently, actin filaments in imaging solution were allowed to bind to the motors, and transport was monitored in presence of 2 mM ATP. For the rotation assays OsKCH1(4-744) molecules were sparsely attached to the surface via penta-His antibodies (Qiagen) or actin filaments immobilized to the surface via rhodamine antibodies (abcam). Thermally driven rotation of microtubules bound to single motors was observed in the presence of the non-hydrolysable ATP analogue AMPPNP.

Imaging and data analysis. Fluorescently labelled microtubules and actin filaments were visualized using epi-illumination on an inverted fluorescence microscope (Axiovert 200M, Zeiss or Ti-E, Nikon). Single OsKCH1 molecules were observed using TIRF illumination. Positions of microtubules and actin filaments were obtained using FIESTA tracking software as described before³⁴. Mean velocities were determined by fitting Gaussian functions to the velocity histograms using MatLab (Mathworks).

Received 5 February 2015; accepted 2 July 2015;
published 3 August 2015

References

- Collings, D. A. *Plant Microtubules* Vol. 11 (ed. Nick, P.) (Plant Cell Monographs, Springer, 2008).
- Wasteneys, G. O. & Galway, M. E. Remodeling the cytoskeleton for growth and form: an overview with some new views. *Annu. Rev. Plant Biol.* **54**, 691–722 (2003).
- Petrasek, J. & Schwarzerova, K. Actin and microtubule cytoskeleton interactions. *Curr. Opin. Plant Biol.* **12**, 728–734 (2009).
- Deeks, M. J. *et al.* The plant formin AtFH4 interacts with both actin and microtubules, and contains a newly identified microtubule-binding domain. *J. Cell Sci.* **123**, 1209–1215 (2010).
- Sun, D., Leung, C. L. & Liem, R. K. Characterization of the microtubule binding domain of microtubule actin crosslinking factor (MACF): identification of a novel group of microtubule associated proteins. *J. Cell Sci.* **114**, 161–172 (2001).
- Rothenberg, M. E., Rogers, S. L., Vale, R. D., Jan, L. Y. & Jan, Y. N. *Drosophila* pod-1 crosslinks both actin and microtubules and controls the targeting of axons. *Neuron* **39**, 779–791 (2003).
- Reddy, A. S. & Day, I. S. Kinesins in the *Arabidopsis* genome: a comparative analysis among eukaryotes. *BMC Genomics* **2**, 2 (2001).
- Richardson, D. N., Simmons, M. P. & Reddy, A. S. Comprehensive comparative analysis of kinesins in photosynthetic eukaryotes. *BMC Genomics* **7**, 18 (2006).
- Frey, N., Klotz, J. & Nick, P. Dynamic bridges—a calponin-domain kinesin from rice links actin filaments and microtubules in both cycling and non-cycling cells. *Plant Cell Physiol.* **50**, 1493–1506 (2009).
- Umez, N., Umeki, N., Mitsui, T., Kondo, K. & Maruta, S. Characterization of a novel rice kinesin O12 with a calponin homology domain. *J. Biochem.* **149**, 91–101 (2011).
- Klotz, J. & Nick, P. A novel actin-microtubule cross-linking kinesin, NtKCH, functions in cell expansion and division. *New Phytol.* **193**, 576–589 (2012).
- Xu, T., Sun, X., Jiang, S., Ren, D. & Liu, G. Cotton GhKCH2, a plant-specific kinesin, is low-affinitive and nucleotide-independent as binding to microtubule. *J. Biochem. Mol. Biol.* **40**, 723–730 (2007).
- Xu, T. *et al.* A cotton kinesin GhKCH2 interacts with both microtubules and microfilaments. *Biochem. J.* **421**, 171–180 (2009).
- Gimona, M. & Mital, R. The single CH domain of calponin is neither sufficient nor necessary for F-actin binding. *J. Cell Sci.* **111**(Pt 13), 1813–1821 (1998).
- Frey, N., Klotz, J. & Nick, P. A kinesin with calponin-homology domain is involved in premitotic nuclear migration. *J. Exp. Bot.* **61**, 3423–3437 (2010).
- Dixit, R. Putting a bifunctional motor to work: insights into the role of plant KCH kinesins. *New Phytol.* **193**, 543–545 (2012).
- Schneider, R. & Persson, S. Connecting two arrays: the emerging role of actin-microtubule cross-linking motor proteins. *Front. Plant Sci.* **6**, 415 (2015).
- Fink, G. *et al.* The mitotic kinesin-14 Ncd drives directional microtubule-microtubule sliding. *Nature Cell Biol.* **11**, 717–723 (2009).
- Kapitein, L. C. *et al.* The bipolar mitotic kinesin Eg5 moves on both microtubules that it crosslinks. *Nature* **435**, 114–118 (2005).
- Nitzsche, B. *et al.* Studying kinesin motors by optical 3D-nanometry in gliding motility assays. *Methods Cell Biol.* **95**, 247–271 (2010).
- Endow, S. A. Determinants of molecular motor directionality. *Nature Cell Biol.* **1**, E163–E167 (1999).
- Kobayashi, T. *et al.* Engineering a novel multifunctional green fluorescent protein tag for a wide variety of protein research. *PLoS ONE* **3**, e3822 (2008).
- Jonsson, E., Yamada, M., Vale, R. D. & Goshima, G. Clustering of a kinesin-14 motor enables processive retrograde microtubule-based transport in plants. *Nature Plants* **1**, 15087 (2015).
- Staiger, C. J. *et al.* Actin filament dynamics are dominated by rapid growth and severing activity in the *Arabidopsis* cortical array. *J. Cell Biol.* **184**, 269–280 (2009).
- Gerson-Gurwitz, A. *et al.* Directionality of individual kinesin-5 Cin8 motors is modulated by loop 8, ionic strength and microtubule geometry. *EMBO J.* **30**, 4942–4954 (2011).
- Sellers, J. R. & Kachar, B. Polarity and velocity of sliding filaments: control of direction by actin and of speed by myosin. *Science* **249**, 406–408 (1990).
- Hunt, A. J. & Howard, J. Kinesin swivels to permit microtubule movement in any direction. *Proc. Natl Acad. Sci. USA* **90**, 11653–11657 (1993).
- Gutierrez-Medina, B., Fehr, A. N. & Block, S. M. Direct measurements of kinesin torsional properties reveal flexible domains and occasional stalk reversals during stepping. *Proc. Natl Acad. Sci. USA* **106**, 17007–17012 (2009).
- Reuther, C., Hajdo, L., Tucker, R., Kasprzak, A. A. & Diez, S. Biotemplated nanopatterning of planar surfaces with molecular motors. *Nano Lett.* **6**, 2177–2183 (2006).
- Nezlin, R. S., Zagayansky, Y. A. & Tumerman, L. A. Strong evidence for the freedom of rotation of immunoglobulin G subunits. *J. Mol. Biol.* **50**, 569–572 (1970).
- Lupas, A. N. & Gruber, M. The structure of alpha-helical coiled coils. *Adv. Protein Chem.* **70**, 37–78 (2005).
- Walter, W. J., Beranek, V., Fischermeier, E. & Diez, S. Tubulin acetylation alone does not affect kinesin-1 velocity and run length in vitro. *PLoS ONE* **7**, e42218 (2012).
- Walter, W. J., Koonce, M. P., Brenner, B. & Steffen, W. Two independent switches regulate cytoplasmic dynein's processivity and directionality. *Proc. Natl Acad. Sci. USA* **109**, 5289–5293 (2012).
- Ruhnow, F., Zwicker, D. & Diez, S. Tracking single particles and elongated filaments with nanometer precision. *Biophys. J.* **100**, 2820–2828 (2011).

Acknowledgements

We thank C. Thodt, C. Bräuer and J. Sandberg-Meinhardt for technical assistance, P. Nick (KIT) for providing the OsKCH(aa1-744) expression plasmid and T. Scholz (Hannover Medical School) for providing rabbit muscle actin. W.J.W. and S.D. acknowledge support from the European Research Council (ERC starting grant 242933 to S.D.) and the Deutsche Forschungsgemeinschaft (Heisenberg programme grant DI 1226/4 and research unit SFG 877 grant DI 1226/5).

Author contributions

W.J.W. and S.D. initiated research, designed experiments and wrote the manuscript. W.J.W. created reagents. W.J.W., I.M. and F.R. performed experiments and analysed data. All authors read the manuscript.

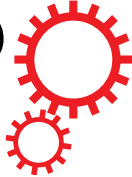
Additional information

Supplementary information is available [online](http://www.nature.com/online). Reprints and permissions information is available [online](http://www.nature.com/reprints) at www.nature.com/reprints. Correspondence and requests for materials should be addressed to W.J.W. and S.D.

Competing interests

The authors declare no competing financial interests.

SCIENTIFIC REPORTS



OPEN

A rice class-XIV kinesin enters the nucleus in response to cold

Xiaolu Xu¹, Wilhelm J. Walter², Qiong Liu¹, Isabel Machens² & Peter Nick¹

Higher plants possess a large number of kinesins, but lack the minus-end directed dynein motors. However, the kinesin class XIV has strongly expanded, and minus-end directed motors from this class may have taken over functions of cytoplasmic dyneins. In this study, we address the functional aspects of a novel rice homologue of the *Arabidopsis* class-XIV kinesins ATK1 and ATK5. Since a loss-of-function rice mutant of this kinesin is not viable, the function was studied in tobacco BY-2 as heterologous system. OsDLK-GFP stably expressed in BY-2 cells decorates cortical microtubules, but also can shift into the nucleus of interphase cells. Because of this peculiar localisation, we coined the name Dual Localisation Kinesin (DLK). The nuclear import of this protein is strongly and reversibly promoted in response to cold. During mitosis, OsDLK is repartitioned between spindle and phragmoplast. Motility assays *in vitro* using show that OsDLK can convey mutual sliding of microtubules and moves at a velocity comparable to other class-XIV kinesins. When tobacco cells overexpressing OsDLK are synchronised, they exhibit a delayed entry into metaphase, while the later phases of mitosis are accelerated. The data are discussed in relation to additional functions of this kinesin type, beyond their transport along microtubules.

Plant cells show a distinct directionality (cell axis, cell polarity), which is guiding morphogenesis up to the organismic level. Both, microtubules and actin filaments, are endowed with an innate directionality as well, which is translated by molecular motors into a directionality of dynamic processes. One of the most striking peculiarities of plant directionality is the absence of microtubule minus end-directed cytoplasmic dynein motors in most Gymnosperms, and in all Angiosperms¹. However, the minus end-directed kinesins^{2,3}, generally referred to as class-XIV kinesins, have proliferated conspicuously, which is probably linked with the loss of flagella-driven motility that was progressively confined to the motile sperm cells (in Bryophytes, Pteridophytes, and early Gymnosperms), and, eventually, became dispensable by the development of a pollen tube. An interesting missing link is found in primitive gymnosperms, such as *Ginkgo* or *Cycas*, where the pollen tube bursts open only 50 µm before reaching the egg cell, releasing the flagellate spermatozoid⁴. The loss of flagellae was accompanied by a loss of centrioles as major microtubule-organizing centres, preceded by a progressive increase of acentriolar nucleation during mitosis. Instead, a novel microtubular structure, the phragmoplast, emerged in several lineages of the Green Algae and adopted the spatial organisation of the new cell plate (recently reviewed in⁵).

Since the functionality of the division spindle requires microtubular transport in both directions, the functions conveyed by dyneins in animal cells must be taken over by minus-end directed kinesins in plants. In fact, the class-XIV kinesins ATK1 (KatA) and ATK5 have been shown to bundle microtubules in the spindle mid-zone to generate inward forces to shorten the spindle length and focus spindle poles by gathering parallel microtubules towards the poles^{6,7}. Of special interest are kinesin motors linked with phragmoplast and preprophase band, because these motors should reflect the cellular specificities of plant cell division. Indeed, the organisation of the phragmoplast seems to be linked with specific motors, such as the plant specific myosin motor myosin VIII⁸, the class-XII kinesins AtKinesins 12A, B⁹, the calcium-binding class-XIV kinesin KCBP¹⁰, and the class-XIV kinesin KCH¹¹. Interestingly, some kinesins seem to be shared between phragmoplast and PPB. For instance, POK1 not only participates in the spatial control of cytokinesis¹², but also, in concert with other proteins, tethers components required for later phragmoplast insertion at the site of the PPB¹³.

Similar to the phragmoplast, cortical microtubules (cMTs), the exclusive microtubule array in non-cycling plant cells, participate in the organisation of the cell wall¹⁴. Actually, it is this function, which led to the discovery of microtubules by Ledbetter and Porter¹⁵, and from the early days was proposed to be linked with transport along

¹Molecular Cell Biology, Botanical Institute, Karlsruhe Institute of Technology (KIT), Fritz-Haber-Weg 4, 76131, Karlsruhe, Germany. ²Molecular Plant Physiology, Biocentre Klein Flottbek, University of Hamburg, 22609, Hamburg, Germany. Correspondence and requests for materials should be addressed to X.X. (email: xiaolu.xu@student.kit.edu)

microtubules¹⁶. A class-IV kinesin, the KIF4 family member FRA1, is discussed as candidate for microtubular control of cellulose microfibril texture¹⁷. Interestingly, several kinesins are shared between phragmoplast and cortical array, including several class-XIV kinesins, such as ATK5⁷, or KCH¹¹. This shared localisation might indicate that the machinery used to organise the new cell plate in dividing cells later has been recruited to organise also the cell wall in expanding cells. However, one should keep in mind that colocalisation with cortical microtubules does not necessarily mean that the respective kinesin is functional in organisation of cortical microtubules. For instance, although ATK5 accumulates at the plus ends of growing cMTs, the *atk5* mutant shows a normal organisation of cMT⁷.

Similar to the situation in animals, kinesins have progressively invaded other topological cellular functions in addition to mitotic chromosomal transport, such as the positioning of organelles, including premitotic nuclear migration¹⁸, transport of Golgi vesicles¹⁹, of mitochondria²⁰, or light-induced chloroplast movement²¹.

A new and emerging topic is the link of such topological functions with signalling. The classical example is the kinesin-driven transport of synaptic vesicles in the axon - here, a directional transport function is used to sustain signalling. Likewise, non-translated mRNA for the transcription factor *oskar* driving gene expression required for abdominal development is located at the posterior pole of the *Drosophila* oocyte by virtue of a kinesin motor²². Signal-triggered, kinesin-dependent transport of a regulatory molecule can also be used to trigger specific responses in gene expression. For instance, in *Drosophila*, nuclear import of the CUBITUS INTERRUPTUS protein depends on the kinesin Costal2/Kif7, and regulates the hedgehog signalling pathway²³. The surprising finding that the kinesin OsBC12/GDD1 not only binds to cortical microtubules, but can enter the nucleus and activate there a specific step of gibberellin biosynthesis, suggests that kinesin-dependent signalling is also a topic in the plant field²⁴.

While in the dicot model *Arabidopsis* the closely related class-XIV kinesins ATK1 and ATK5 seem to localise both to the phragmoplast, the monocot model rice harbours only one homologue of these kinesins, leading to the question, whether this homologue (SwissProt accession number B8B6J5, GN = Os07g0105700) might represent a minimal system to fulfil the functions conveyed by ATK1 and ATK5. In this study, we characterized the molecular and cellular functions of this rice kinesin. However, the rice insertion mutant of OsDLK not only showed delayed seed germination, but even died in the early stage of seedling development. Thus, the function seemed to be essential, and we, therefore, used the approach to express this kinesin in tobacco BY-2 cells as heterologous system to address localisation and cellular functions. Using the recombinantly expressed full-length OsDLK, we showed by *in-vitro* sliding that it is a minus-end directed microtubule motor. A fusion with GFP decorates cortical microtubules, spindle, and phragmoplast. When the cell cycle was synchronised, the progression into metaphase was delayed in these overexpressor cells. Surprisingly, this protein was found to occur in two populations during interphase - one subpopulation was associated with cortical microtubules as observed in other class-XIV kinesins, the other population was localised inside the nucleus. This dual localisation was also confirmed by transient expression in other systems (*Arabidopsis* protoplasts, leaves of *Nicotiana benthamiana*, leaf sheath of rice). This partitioning of the protein to the nucleus could be induced by a chilling treatment and was reversible, when cells were returned to room temperature. Likewise, inhibition of nuclear export by Leptomycin B partitioned the protein to the nucleus. Since this kinesin was able to shuttle between two subcellular locations in a specific manner, we named this particular kinesin OsDLK for Dual Localisation Kinesin.

Results

Isolation and sequence analysis of OsDLK. A putatively full-length cDNA for rice DLK (Dual Located Kinesin) was isolated by RT-PCR. The obtained amino-acid sequence coding for the OsDLK protein is identical to the sequence published for the rice reference genome (UniProtKB/Swiss-Prot accession no. B8B6J5). The putative kinesin is predicted to harbour a highly conserved kinesin motor domain (aa 404–764) at the C-terminal region, including an ATP-binding consensus (aa 498–506), a putative microtubule binding site (aa 700–706)²⁵ (Fig. 1a), and a coiled-coil stalk (aa 109–422) for protein dimerization²⁶. A 14-amino-acid neck-linker region (aa 405–418) directly upstream of the catalytic core comprises the consensus neck motif found among kinesins that move towards the minus end of microtubules²⁷. Specifically, this region contains two critical amino acids known to be crucial for kinesin minus-end directed movement (Supplementary Fig. S1). Thus, OsDLK displays all sequence motives indicative of a microtubule minus end-directed motor. Interestingly, three putative Nuclear Localization Signal are predicted by algorithms such as the http://nls-mapper.iab.keio.ac.jp/cgi-bin/NLS_Mapper. While one motif of 11 amino acids length (aa 401–411) overlaps with the neck-linker domain, there are two additional putative bi-partite sites with long linkers at positions 64–93 and 207–237.

OsDLK shows clear homology with other kinesin-14 sequences known from other organisms (Supplementary Fig. S1). For instance, the N-terminus of the *Arabidopsis* kinesins ATK1 and ATK5 (with mutual amino-acid identities of 75.5%), exhibit 38.2% and 40.6% amino-acid similarity to OsDLK, respectively. In the motor domains, both ATK1 and ATK5^{7,28} showed around 75% amino-acid identity to OsDLK. Both ATK1 and ATK5 are C-terminally localized kinesins with a coiled-coil stalk in the middle of the protein. A phylogenetic tree (Fig. 1b) placed OsDLK (marked by an asterisk) clearly into the C-terminally class-XIV kinesins with a close relationship to ATK5 and ATK1.

In-silico data on expression patterns obtained from the *Genevestigator* microarray database^{29,30} indicate an overall high expression in all tested tissues of rice as well as through all developmental stages (Supplementary Fig. S2).

Dual localisation of OsDLK during interphase. In order to gain insight into the unknown functions of OsDLK during the cell cycle, two constructs (OsDLK-GFP and OsDLK-RFP) were generated for stable and transient expression in tobacco BY-2 cells, respectively, whereby a full-length OsDLK cDNA (2295 bp) was fused upstream of the green fluorescent protein (GFP) or red fluorescent protein (RFP).

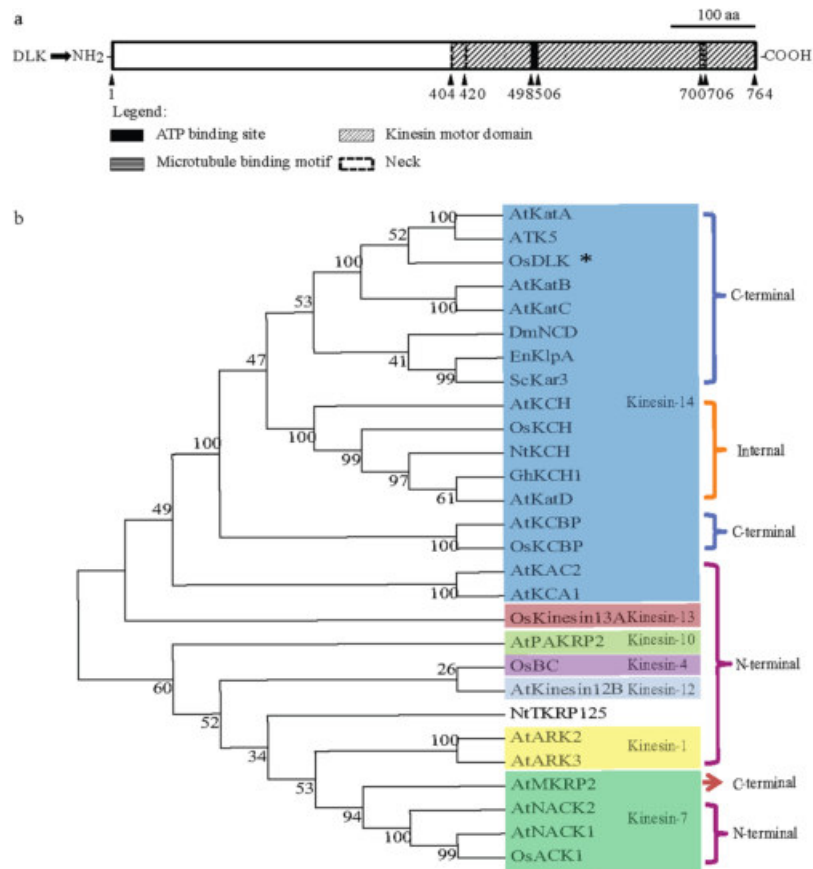


Figure 1. Sequence analysis of OsDLK from *Oryza sativa* L. *ssp. japonica*. **(a)** Predicted domains in the full-length protein (upper row). A putative kinesin motor domain is found in the C-terminal region and includes a conserved neck region, and ATP, as well as microtubule-binding sites. **(b)** Phylogenetic relationship of OsDLK (marked by an asterisk) with other members of the kinesin-14 family and selected members from other several kinesin subgroups from different animal and plants.

When the subcellular localisation of OsDLK-GFP was followed through the cell cycle (Fig. 2), the fluorescent signal was seen to undergo a dynamic reorganisation: During prophase, the signal in the cell cortex disappeared completely, and the intranuclear signal appeared agglomerated (Fig. 2a–d) and was later replaced by a mesh-like structure wrapping the nucleus (Fig. 2e–h). During early metaphase, OsDLK-GFP was found in form of (relatively scarce) beads on a string distally from the metaphase plate, along with agglomerations in the metaphase plate, mostly proximally of the chromosomes (Fig. 2i–l). During late metaphase (Fig. 2m–p), the signal distal to the metaphase plate had increased into clear and continuous fibres, whereas the signal in the metaphase equator had almost vanished. When anaphase was completed, OsDLK-GFP returned to the equatorial region (Fig. 2q–t) localising to give rise to the phragmoplast, i.e. to the microtubular array which deposits cell plate material as it expands outward, and therefore, similar to the cortical microtubules that form later, associates with the cell wall. While OsDLK-GFP was found in all arrays of microtubules, it was not seen to label all microtubules of these arrays, but was concentrated at specific flanks of the structure, for instance in the late anaphase spindle (Fig. 3).

During interphase, surprisingly, OsDLK-GFP was localised in two populations: On the one hand, OsDLK-GFP was continuously decorating cortical microtubules (Figs 2u–w, 4a–c). Simultaneously, intensive fluorescent signals were found inside the nucleus (Figs 2u–w, 4d–f). The dual localisation of OsDLK in cell cortex and nucleus was therefore validated in additional systems: the epidermal cells of the rice leaf sheath as homologous system (Fig. 5a), and two further experimental models, *Arabidopsis thaliana* mesophyll protoplasts, and pavement cells of *Nicotiana benthamiana* leaves as additional heterologous systems (Fig. 5b,c).

To get more insight into these complex migrations of OsDLK-GFP during the later phase of mitosis, detailed time-lapse series were recorded (Fig. 3, Supplementary Movie S1). These series show how OsDLK-GFP at the final stage of metaphase is organised in rod-like structures at the proximal edge of the metaphase plate that are aligned poleward. Then, within 3 min, the signal moves towards the spindle poles and contracts in two helmet-like clusters just beneath a terminal, smaller cluster. Subsequently, the entire structure shortens rapidly, such that 5 min later the two helmets have reached the equator again lining from two sides a dark zone that probably corresponds to the newly emerging cell plate. During this contraction process, the first strongly aggregated bundles in the helmet detach into finer fibres that probably represent the microtubules of the phragmoplast. During expansion of this *bona-fide* phragmoplast, OsDLK-GFP remains over the next 15 min at the site, where phragmoplast microtubules are presumed to be. That OsDLK-GFP is indeed decorating phragmoplast microtubules, can be

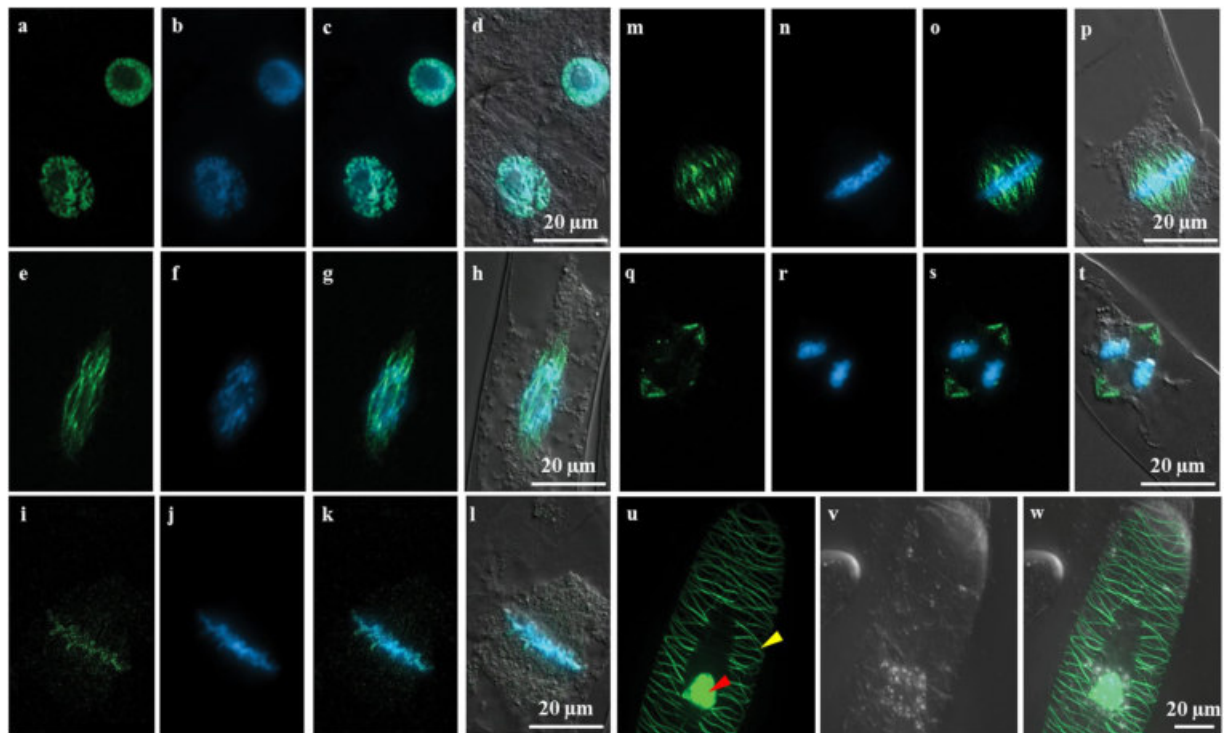


Figure 2. Subcellular localisation of OsDLK-GFP upon heterologous expression tobacco (*Nicotiana tabacum*) BY-2 cells. (a–t) Cells in subsequent stages of mitosis upon dual visualisation of full-length OsDLK (GFP signal) and DNA (Hoechst 33258). (a–d) preprophase. (e–h) prophase. (i–l) metaphase. (m–p) Transition metaphase to anaphase. (q–t) Transition anaphase to telophase. The GFP signal indicative of OsDLK is shown in a, e, i, m and q; the Hoechst 33258 signal indicative of DNA is shown in b, f, j, n and r; both GFP and Hoechst signal channels are merged in c, g, k, o and s; d, h, l p and t show the merge of all the channels. (u–w) Dual localisation of full-length OsDLK in fusion with GFP during interphase. GFP signal (u), differential interference contrast (DIC) (v) and merged images (w). Signals of OsDLK-GFP in nucleus and cortex are shown with red and yellow arrows, respectively. Scale bars: 20 µm.

shown by visualising microtubules by immunofluorescence (Fig. 4k–n). Afterwards, the signal starts to appear at the nuclear envelopes of the newly formed daughter nuclei, and first concentrates at the trailing edge of the nuclei (that move apart from the cell plate). Eventually, when the daughter nuclei have reached their position in the symmetry planes of the newly formed cells, this gradient is progressively levelled out.

To test, whether OsDLK was really associated with microtubules, we used two approaches - transient co-transformation of OsDLK-RFP and the microtubule marker TuB6-GFP, as well as immune-labelling of microtubules in cells expressing OsDLK-GFP. We found that OsDLK-RFP decorated the GFP-labelled cortical microtubules (Fig. 4a–c), whereas the nucleus of the same cells harboured the RFP signal indicative of OsDLK, but no microtubular signal (Fig. 4d–f). This uncoupling of the two signals in the nucleus could also be confirmed using TRITC-based immunostaining of microtubules (Fig. 4g–j). Conversely, immune-labelling of the phragmoplast (Fig. 4k–n) showed a tight colocalisation of OsDLK-GFP and microtubules, whereas the interior of the newly formed daughter nuclei was not labelled. Thus, OsDLK-GFP co-localised with the wall associated arrays of microtubules (cortical microtubules, phragmoplast). However, during interphase, it can occur in a second form that resides inside the nucleus and seems to be dissociated from microtubules. The fact that the intranuclear signal depends on the cell cycle (present in interphase, absent in telophase) argues against a scenario, where GFP or RFP are cleaved from DLK fusions, also because a cleaved label should distribute equally through cytoplasmic strands, which is not seen.

The kymograph data revealed that OsDLK-GFP is a dynamic motor, moving with an average *in-vivo* speed of $16.28 \pm 1.05 \mu\text{m}\cdot\text{min}^{-1}$ on cMTs (Fig. 6a–c, Supplementary Movie S2). This speed exceeds that of NtKCH, a different member of the class-XIV kinesins (Table 1). However, there exist members of other kinesin families (such as RnKHC, a class-I kinesin) that are much faster.

Overexpression of OsDLK-GFP prolongs mitosis. To get insight into the cellular function of OsDLK-GFP, mitotic index and cell expansion were followed in comparison with the non-transformed BY-2 cell line. The mitotic index of the expressor was significantly higher during the 4 days after subcultivation, especially at the second and third day (Fig. 7a). Since the doubling time of the transgenic cell line was determined to be similar to WT (Supplementary Fig. S3a), the increase in mitotic index was not caused by a higher frequency of cells entering mitosis, but by a longer passage through the mitotic phase.

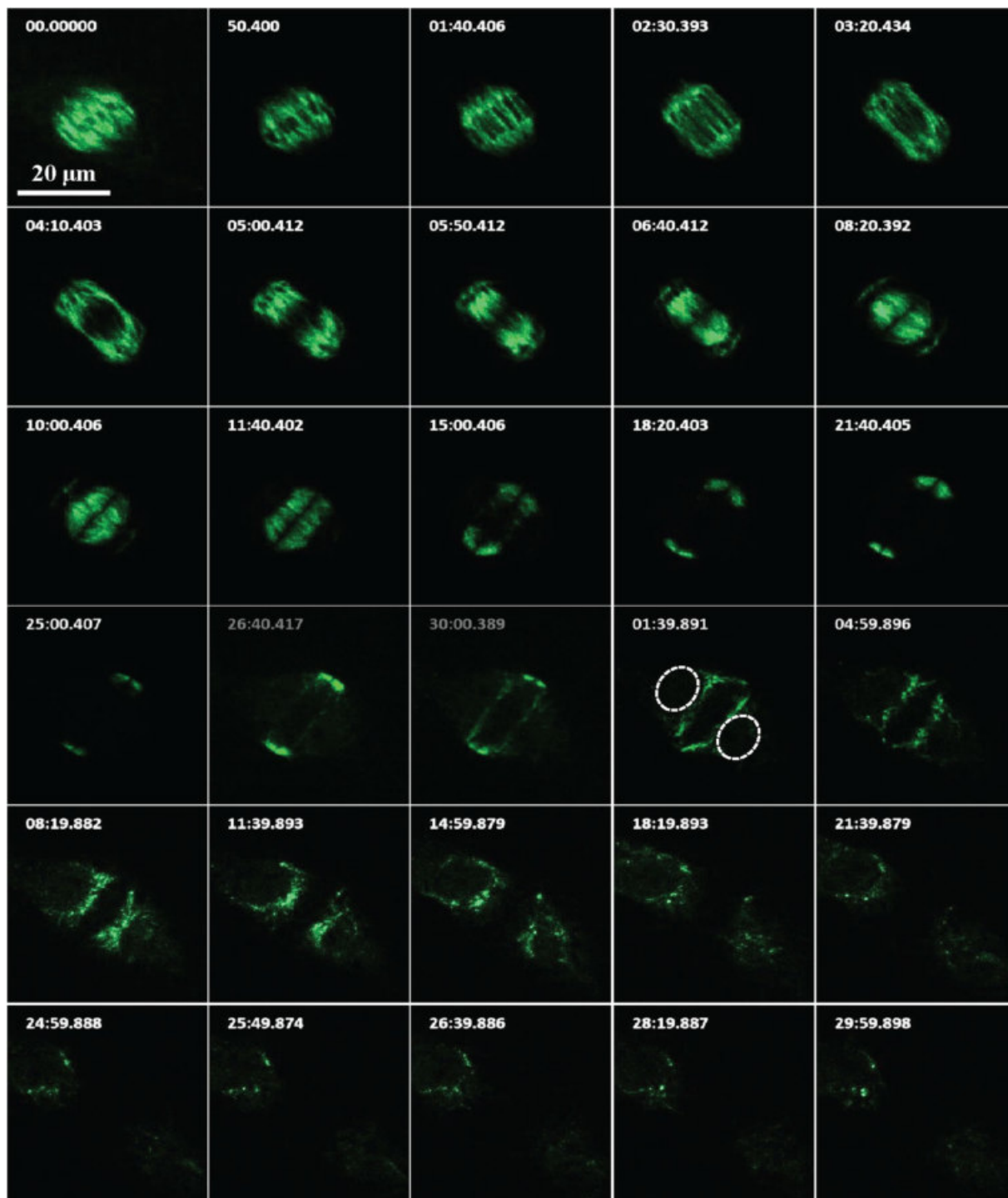


Figure 3. Time-lapse series of OsDLK-GFP localisation during the later phases mitosis and during cytokinesis (see also Supplementary Movie S1), time unit: s. The nucleus is marked with white dotted line. Scale bars: 20 µm.

However, during the cell expansion (during 4 day to 7 day cultivation), the packed cell volume (PCV) of the OsDLK-GFP overexpressor was significantly increased compared to the WT cell line (Fig. 7b), which compensated the decrease during the first 3 days of cultivation. So that the PCV exhibited no difference after 6 days of cultivation. In order to determine whether this compensation was due to cell expansion or cell proliferation, cell length and width were determined. The cells of OsDLK-GFP overexpressor were more elongated than the WT cells, while the increment of cell width was reduced. Thus, overexpression of OsDLK-GFP slowed mitotic activity during the proliferation phase of the culture while delaying cell elongation. This, along with a more pronounced elongation during the expansion phase of the culture resulted in a similar final packed cell volume.

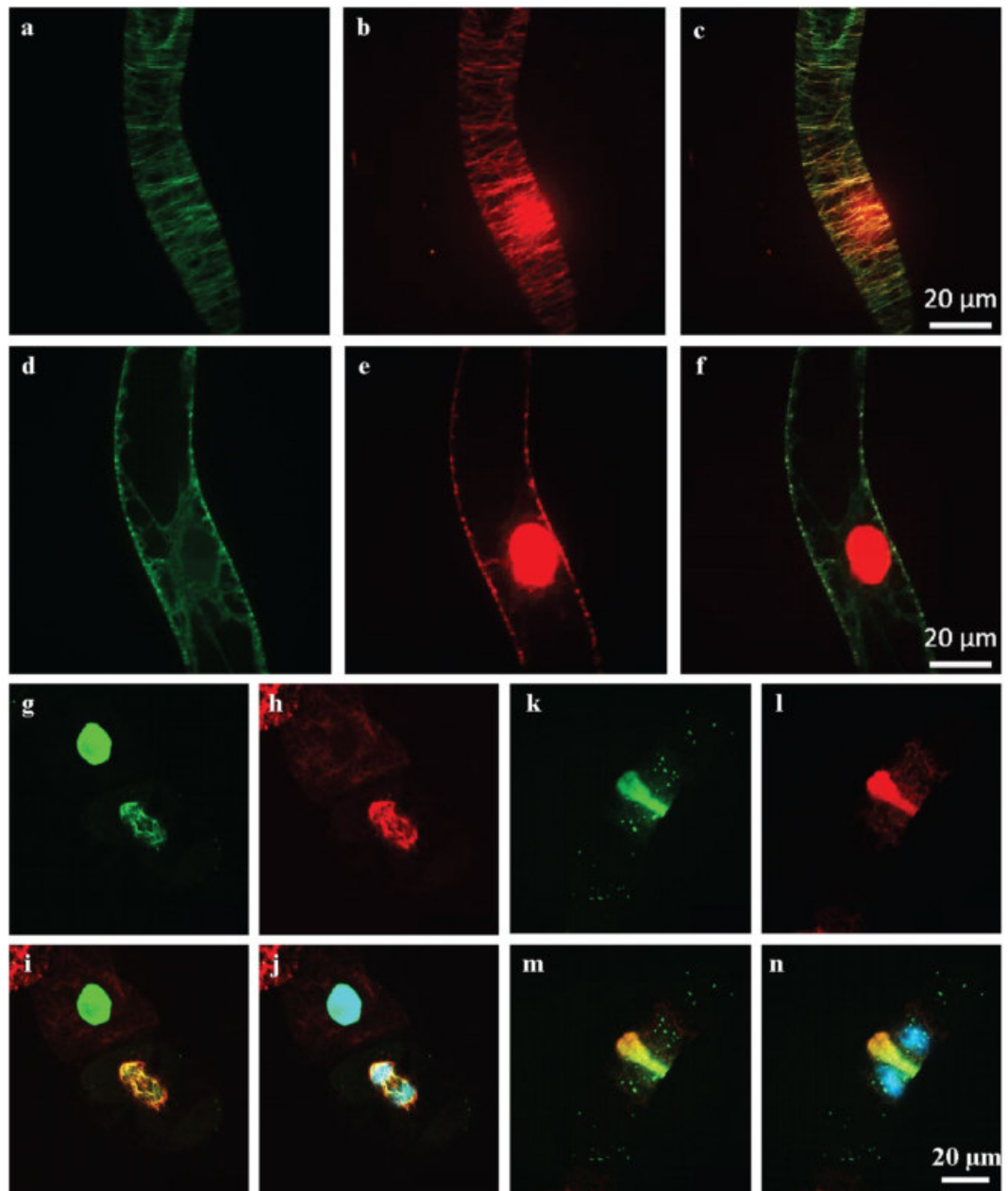


Figure 4. Co-localisation of OsDLK fusions with fluorescent proteins and microtubules upon heterologous expression in tobacco BY-2 cells. (a–f) Cortical and central confocal section of a cell transiently transform with OsDLK-RFP and GFP-pCambiaTuB6 showing the colocalisation of OsDLK (b) with cMTs (a) in periphery, and the intranuclear localisation of OsDLK-RFP (e) while GFP-Tub6 (d) localized in radial MTs tethering the nucleus. Merged signals are shown in c and f. (g–n) Triple staining of OsDLK-GFP, microtubules visualised by immunofluorescence with rhodamine, and DNA visualised by Hoechst 33258 of representative cells in late anaphase (g–j) and telophase (k–n). The OsDLK-GFP signal is shown in g and k, the microtubule signal in h and l, the merge of these signals in i and m, the merge of all three signals in j and n. Scale bars: 20 μm .

Overexpression of OsDLK-GFP delays the transition into metaphase. The fact that the OsDLK-GFP overexpressor exhibited a higher mitotic index, but a similar length of the cell cycle indicates that the lines differ with respect to the duration of mitosis. We, therefore, monitored the temporal progression through mitosis in synchronized BY-2 cells. Cells were treated first with the ribonucleotide reductase inhibitor hydroxyurea (which arrests the cells in S-phase) and then with the reversible anti-microtubular inhibitor propyzamide (which arrests the cells in prophase). Following the treatment with hydroxyurea, the mitotic index was 0%, indicative of full suppression of cell cycle progression into the M-phase. Upon release from propyzamide, the non-transformed cell line had a more efficient synchronisation with a higher MI (70%) while it was lower (60%) in the OsDLK-GFP overexpressor line (Supplementary Fig. S4a,b).

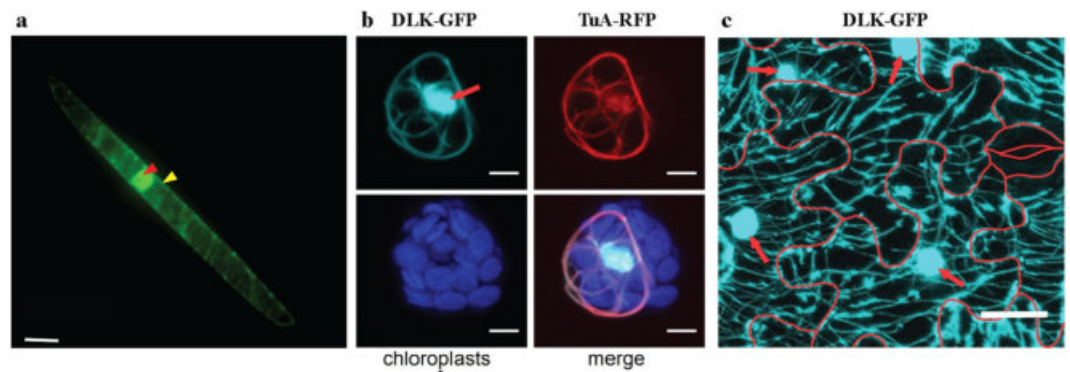


Figure 5. Dual localisation of full-length OsDLK-GFP in different plant models. **(a)** Dual localisation of full-length OsDLK-GFP in interphase cells of the rice leaf sheath. Nuclear and cortical OsDLK-GFP signals are indicated by red and yellow arrows, respectively. Scale bar: 20 μm . **(b)** Co-localisation of OsDLK-GFP and microtubules in *Arabidopsis thaliana* protoplasts. Representative maximum intensity projections of fluorescent image stacks showing transient expression of OsDLK-GFP (cyan), stable expression of the microtubule marker TuA-RFP (red), and chloroplast autofluorescence (blue) in an *Arabidopsis thaliana* mesophyll protoplast. Scale bar: 5 μm . **(c)** Representative maximum intensity projection of fluorescent image stacks showing transient expression of OsDLK-GFP (cyan) in *Nicotiana benthamiana* leaf pavement cells. Red arrows show the OsDLK-GFP localisation in the nuclei. Cell borders are indicated by red lines generated from bright field images taken at the same field of view. Scale bar: 25 μm .

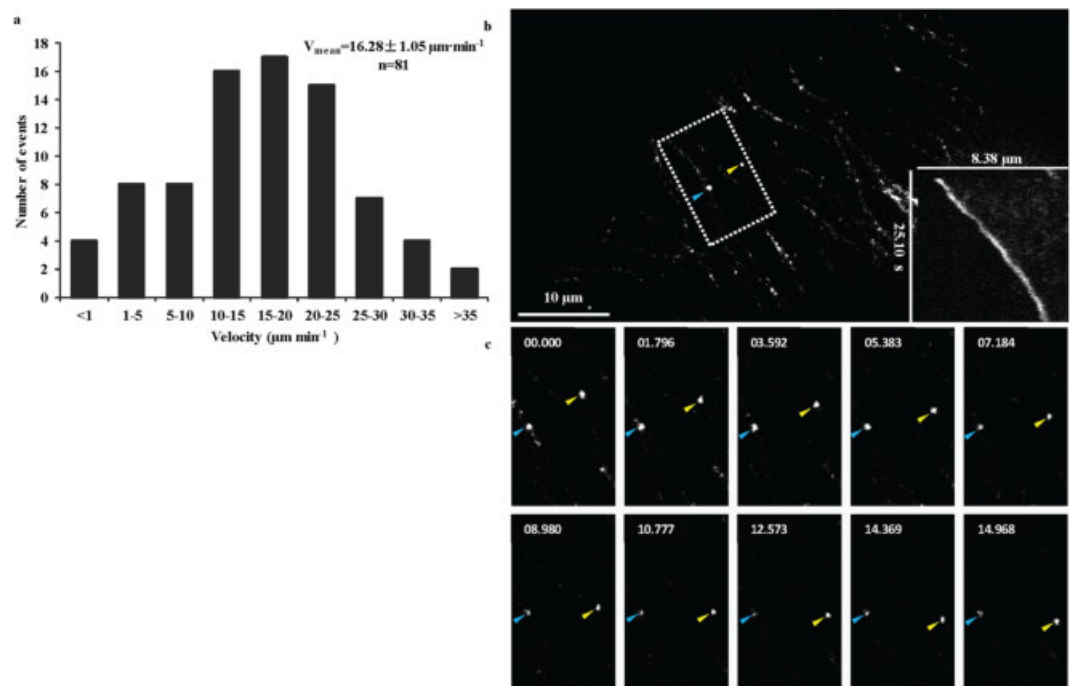


Figure 6. Time-lapse studies on the dynamic behaviour of different OsDLK subpopulations in stably transformed OsDLK-GFP BY-2 cells. **(a)** Velocity distribution of OsDLK-GFP moving on cortical microtubules (cMTs) with an average velocity $16.28 \pm 1.05 \mu\text{m}\cdot\text{min}^{-1}$ ($x \pm \text{SE}$; $n = 81$). **(b)** Representative kymograph experiment showing kinesin movement in an interphase BY-2 cell. The kymograph shown in the bottom right corner represents the OsDLK-GFP signal marked by a yellow arrowhead. The left bar indicates the time, and the top bar indicates the distance. **(c)** Time-lapse series showing in detail the dynamic behaviour of the OsDLK-GFP highlighted with blue and yellow arrowhead (see Supplementary Movie S2). Time unit: s, Scale bars: 10 μm .

The frequency of the individual mitotic phases was followed over time (Supplementary Fig. S4c,d). Whereas the metaphase peak in the OsDLK-GFP line was seen 90 min after removal of propyzamide, which was half an hour later than in the WT (Fig. 7c), the telophase peak of OsDLK-GFP cells occurred 30 min earlier (Fig. 7d). These time courses report that, in the OsDLK-GFP overexpressor, the mitotic phases preceding metaphase are

Kinesin	Velocity ($\mu\text{m}\cdot\text{min}^{-1}$)	(Predicted) Directionality	Position	Reference
OsDLK	16.28 \pm 1.1	–	<i>In vivo</i>	<i>This research</i>
	5.2 \pm 1.1	–	<i>In vitro</i>	
DmNCD	8–12	–	<i>In vitro</i>	64
AtKatA	9.6 \pm 5.2	–	<i>In vitro</i>	28
OsKCH1	5.4 \pm 2.3	–	<i>In vitro</i>	65
NtKCH	3.26 \pm 0.1	–	<i>In vivo</i>	11
ATK5	6.30 \pm 1.4	–	<i>In vitro</i>	7
ScKar3	1.30 \pm 0.1	–	<i>In vitro</i>	66
AtKCBP	10.0 \pm 0.4	–	<i>In vitro</i>	67
RnKHC	46.8 \pm 6.6	+	<i>In vivo</i>	68
RnKin430	52.4 \pm 1.5	+	<i>In vitro</i>	69
DmKHC	45.6 \pm 6.0	+	<i>In vitro</i>	70

Table 1. Velocity of OsDLK-GFP compared to velocities of other kinesins from plant and animal species and the conventional KHC from *Drosophila melanogaster* and *Rattus norvegicus*.

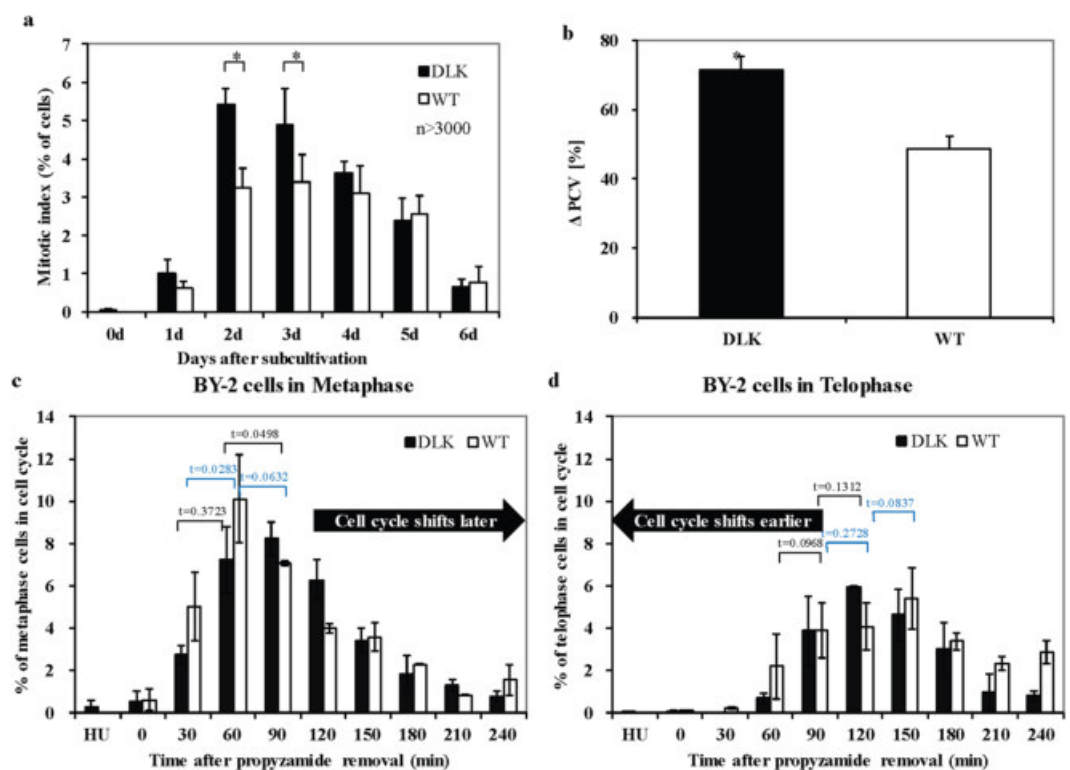


Figure 7. Phenotype detection of OsDLK-GFP overexpressor. (a) Stimulation of mitotic index in OsDLK-GFP BY2 compared to non-transformed BY-2 WT. More than a total of 3000 cells per time point and sample were collected cumulatively from three independent experimental series. Asterisk (*) indicate significant differences between the cell lines at $P < 0.05$ as evaluated by a t test for unpaired data. Error bars represent the standard error of triplicate measurements. (b) Increased packed cell volume in the OsDLK-GFP overexpressor compared to the non-transformed BY-2 WT during 4 to 6 days after subcultivation. *Significant difference between the cell lines at $P < 0.05$ as evaluated by a t test for unpaired data. Error bars represent the standard error of triplicate measurements. (c,d) OsDLK-GFP cells (black bars) progress through mitosis with a different temporal pattern compared to the non-transformed wildtype (white bars). (c) Frequency of metaphase cells over the time after release from propyzamide. (d) Frequency of telophase cells over the time after release from propyzamide. Error bars represent the standard error of biological triplicates comprising a population of 3000 cells per data point.

prolonged, whereas the mitotic phases following metaphase are accelerated. These results are supported by time courses of nuclear positioning recorded over the cultivation cycle (Supplementary Fig. S5). Here, the initial pre-mitotic migration of the nucleus from the lateral wall to the cell centre was delayed in the OsDLK overexpressor.

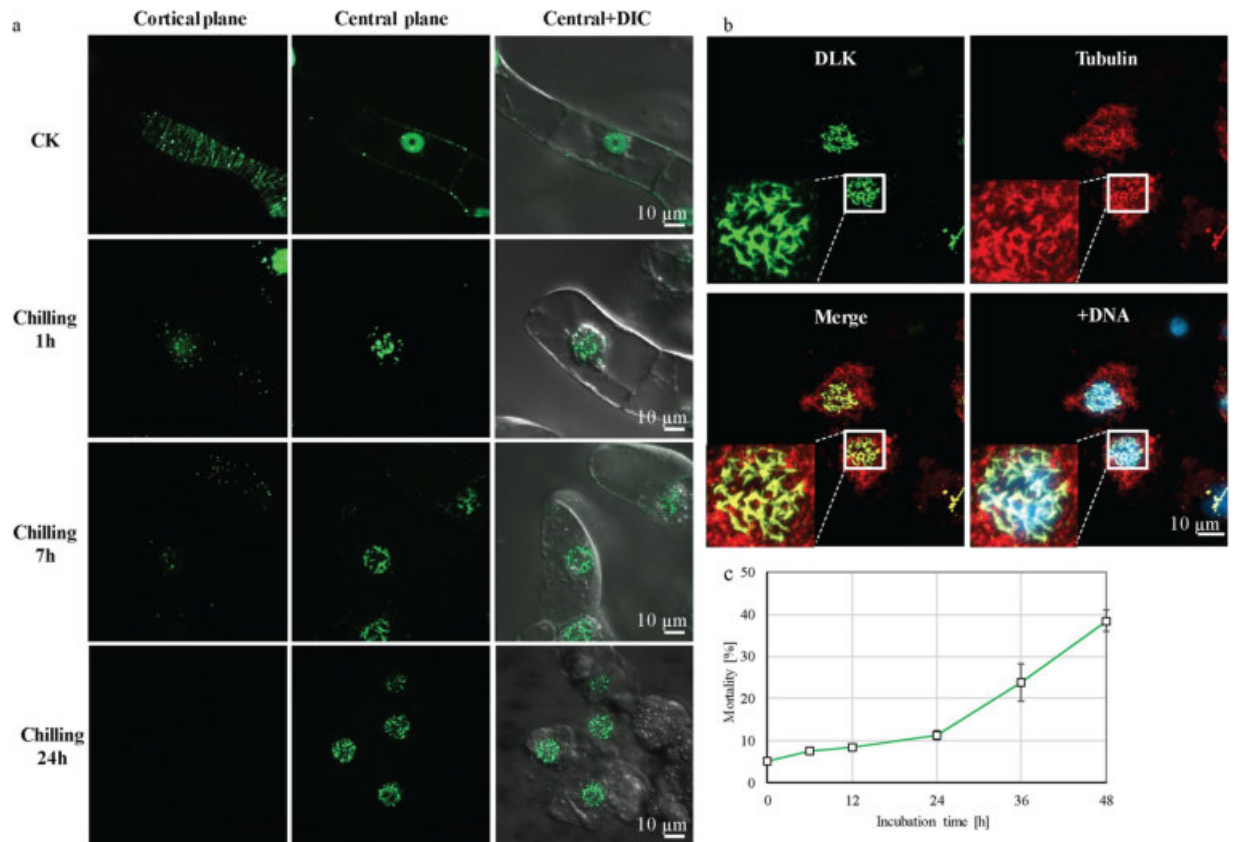


Figure 8. OsDLK-GFP enters the nucleus in response to cold stress. (a) Progressive nuclear import of OsDLK-GFP with increasing time of cold treatment. Confocal sections collected from the cortical and nuclear planes are shown either for the GFP signal alone or merged with the differential interference contrast image to show the topology. CK represent cells cultivated at 25 °C serving as negative control. (b) Representative cells challenged by cold for 7 hours and triple stained for microtubules (immunofluorescence using a TRITC conjugated antibody), OsDLK-GFP, a merge of both signals, and DNA visualised by Höchst 33258. The white square has been magnified to show details of colocalisation (arrow). Scale bars: 10 μ m. (c) Time course of non-transformed BY-2 cells mortality after treatment with ice water.

Nuclear import of OsDLK-GFP in response to cold stress. To determine, whether the two interphase population of OsDLK-GFP (at cMTs and inside the nucleus) can be interconverted, the OsDLK-GFP cells were followed during their response to cold stress, since cold treatment can induce a nuclear import of tobacco tubulin³¹. With progressive time of cold treatment, the GFP signal indicative of OsDLK disintegrated into punctate residual signals in the cell cortex; simultaneously the signal accumulated inside the nucleus, as well in a punctate manner (Fig. 8a). This response was rapid and already clearly manifest after 1 h of cold treatment. With progressive cold treatment, the intranuclear signal organised in rods and filaments, evident from 7 hours after the onset of the treatment. After 24 hours, the cortical signal had vanished completely, whereas the filamentous organisation of the intranuclear signal was fully developed. To get insight into the nature of these filaments, immunostaining of microtubules was carried out in the background of OsDLK-GFP cells following cold treatment for 7 hours (Fig. 8b). Tubulin was seen in and around the nucleus in form of punctate or sometimes rod-shaped structures, whereas the cortical microtubules were not detectable. The signal for OsDLK-GFP was exclusively observed inside the nucleus. Here, the filamentous or rod-shaped structures visualised by OsDLK-GFP tightly overlapped with the tubulin signal and also with the chromatin (Fig. 8b, insets, white frame), whereas in the cytoplasm around the nucleus (delineated by the absence of DNA), the tubulin signal was not accompanied by OsDLK-GFP signal. The viability of non-transformed BY-2 cells in ice water was followed by the Evans Blue dye exclusion assay (Fig. 8c). In the time range till 24 h, the mortality is only around 10%. Only for longer treatments mortality increases significantly. Thus, during the time intervals used for cold treatments inducing nuclear localisation of DLK cells are almost fully viable. To test, whether the nuclear import of OsDLK-GFP was reversible, we conducted a recovery experiment, where cells were subjected to cold treatment for 7 h to induce complete dismantling of the cortical signal. Then, the cells were returned to 25 °C for recovery. During recovery, the rod-like structures in the nucleus disassembled, such that the signal was spread more or less evenly over the entire karyoplasm (Supplementary Fig. S6). At the same time, punctate signals appeared in the cytoplasm around the nucleus that were aligned in transverse orientation like beads on a string. Thus, the nuclear import and the intranuclear filamentous organisation of OsDLK-GFP were reversible.

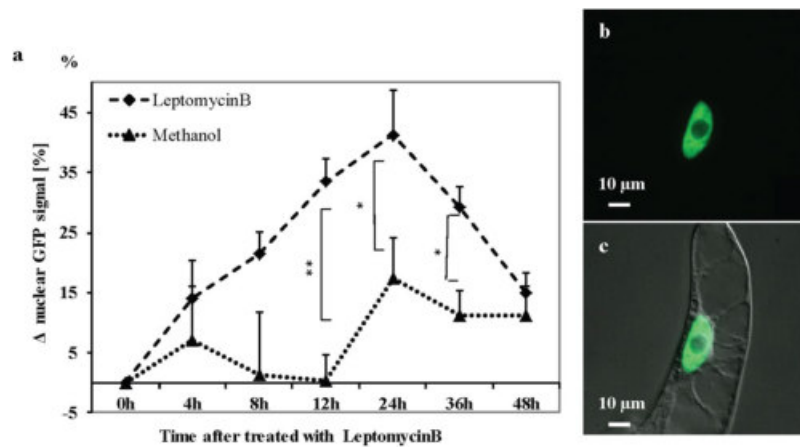


Figure 9. Effect of Leptomycin B, a specific inhibitor of nuclear export on localisation of OsDLK-GFP. **(a)** Time course of intranuclear signal increment in response to 200 nM LeptomycinB compared to the solvent control (the same volume of 70% methanol, corresponding to a final concentration of 1.37% MetOH in the assay as control). At least a total of 20 cells per time point and sample were collected in each experimental series. The results were tested for significance using Student's t-test at 95% and 99% confidence level, labeled with asterisks. Error bars represent the standard error of triplicate measurements. **(b,c)** Representative image of an OsDLK-GFP cell after 3 days of treatment with 200 nM Leptomycin B. GFP signal shown in **(b)**, overlay with differential interference contrast shown in **(c)**. Scale bars: 10 μ m.

Leptomycin B causes accumulation of OsDLK-GFP in the nucleus. To get insight into the mechanism responsible for the cold-induced accumulation of OsDLK-GFP in the nucleus, we treated OsDLK-GFP cells with Leptomycin B (a specific inhibitor of nuclear export³²), but in the absence of cold stress, i.e., at 25 °C. We quantified the proportion of GFP signal located inside the nucleus and followed this parameter over time of Leptomycin B treatment (Fig. 9a). In the OsDLK-GFP cells, the proportion of intranuclear GFP increased by around 40% of the initial value over 24 hours after onset of the treatment, and then dropped back to an intermediate level during the following day. The solvent control did not show this sharp increase, although it should be noted that values increased as well, however only by 15% at 24 h and then levelled off at below 10% for longer incubation. This increase of the intranuclear signal was linked with the loss of the cortical signal (Fig. 9b,c). These results indicate that the intranuclear OsDLK-GFP signal results from a dynamic equilibrium established by import and export. This cycling takes place also at normal temperature. On the assumption of around 50% of the signal being located in the nucleus under steady-state conditions (Fig. 9a), and the increase of the intranuclear signal to around 75% within 24 h of Leptomycin B treatment, it can be estimated that, at 25 °C, roughly half of the intranuclear population is turned over within one day. Compared to the accumulation of signal observed under cold stress, the entry of DLK under room temperature must be much slower (almost by one order of magnitude).

OsDLK is capable of MT sliding *in vitro*. In order to study the interaction of OsDLK with microtubules, we performed microtubule sliding assays, where motors could interact simultaneously with surface-immobilized and free microtubules in the presence of ATP (Fig. 10a). We found that OsDLK actively transports microtubules along each other in a unidirectional manner *in vitro* (Fig. 10b) with a velocity of $v = 5.2 \pm 1.1 \mu\text{m}\cdot\text{min}^{-1}$ (mean \pm SD, $N = 155$, Fig. 10c), which is comparable to the other members of the class-XIV family (Table 1).

Discussion

The current work deals with the functional characterisation of a class-XIV kinesin from rice, which is homologous to the *Arabidopsis* kinesins ATK1 and ATK5. While this rice homologue shares several molecular and cellular features with its *Arabidopsis* counterparts, moves towards the minus end of microtubules in a dynamic fashion, and shows a similar dynamic relocalisation during mitosis, it shows a specific difference during interphase: A part of this rice kinesin decorates cortical microtubules, while the other part is found in the nucleus. In response to cold treatment (eliminating cortical microtubules), the intranuclear population increased and formed rod-shaped and reticulate structures. Likewise, inhibition of nuclear export by Leptomycin B increased the abundance of intranuclear kinesin, such that the name Dual Localisation Kinesin (DLK) was coined for this protein.

Based on sequence homologies in their motor domains, kinesins are classified into 14 sub-families³³. In land plants, the class-XIV kinesins have strongly expanded, and many of them differ greatly in structure and function from their animal counterparts. In this study, we investigate a rice homologue, of two similar *Arabidopsis* class-XIV kinesins, ATK1 and ATK5^{6,7} with overlapping, but not identical function. This rice homologue, designated as OsDLK (for Dual Localisation Kinesin) shows typical structural features of class-XIV kinesins, such as a highly conserved motor domain at the C-terminus with an ATP binding motif, a long stalk region in the middle, and a tail at the N-terminus³⁴. The amino-acid signature in the neck region (Supplementary Fig. S1) predicts that OsDLK is moving towards microtubular minus-ends. The motor velocity *in vitro* is comparable to other class-XIV kinesins (around 5 $\mu\text{m}\cdot\text{min}^{-1}$, Fig. 10), while the motility along cortical MTs *in vivo* is considerably higher (16 $\mu\text{m}\cdot\text{min}^{-1}$, Table 1), excelling the velocity of its *Arabidopsis* counterpart ATK5 almost threefold⁷. Whether this high

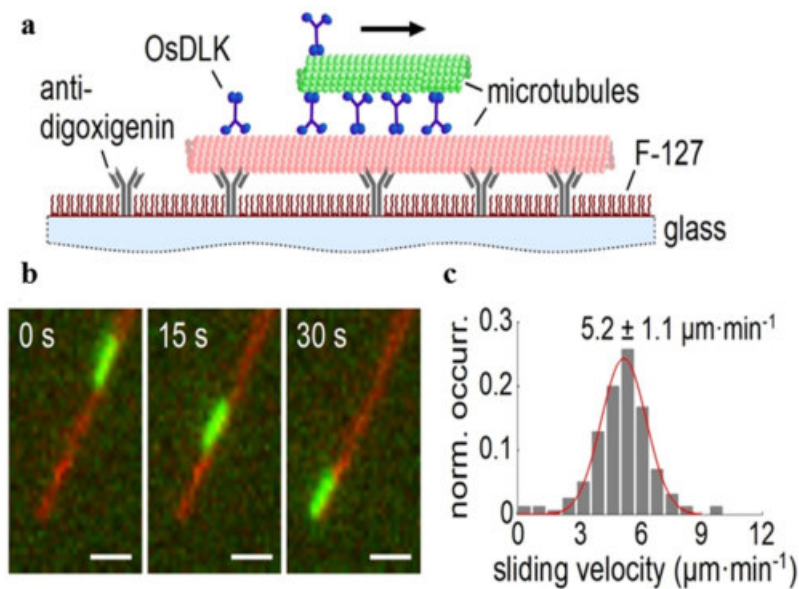


Figure 10. OsDLK is a microtubule minus-end-directed motor along microtubules. **(a)** Schematic representation of the microtubule sliding assay using recombinant OsDLK (see Methods for details). **(b)** Fluorescence micrographs of a cargo microtubule (green) being transported by OsDLK along a surface-bound template microtubule (red) at different points in time. Scale bar = 1 μm . **(c)** Histogram of the point-to-point sliding velocities. A Gaussian fit of the histogram delivers the sliding velocity $v = 5.2 \pm 1.1 \mu\text{m}\cdot\text{min}^{-1}$ (mean \pm SD, $N = 155$).

velocity *in vivo* is caused by motor clusters, or by cotransport with growing or shrinking MT ends, remains to be elucidated, for instance by means of single-molecule tracking *in vitro*. However, except this elevated velocity (which is not unusual if compared with other kinesins), the molecular features of OsDLK are that of a mostly non-conspicuous member of the class-XIV kinesin family.

As the rice mutant was not viable beyond early seedling development (Supplementary Fig. S7), OsDLK was assumed to convey essential functions, such as the cell cycle. Thus, the function was addressed in tobacco BY-2, as classical model, where the cell can be synchronized efficiently. To avoid that individual insertion events bias the readout, and to overcome potential impact from somatoclonal variation which is always an issue in cell culture systems, we pooled the different calli during transformation. Thus, any significant phenotype averages over a population of different clones, where the transgene has been inserted in different sites. As fundamental process in plant development, cell division is a major target for kinesins. For instance, in *Arabidopsis*, more than one third of kinesins have been found to participate in mitosis³⁵. In a synchronized cell culture of *Arabidopsis*, 7 class XIV- kinesins were upregulated during re-entry into the cell cycle³⁶, suggesting a core role in mitosis. Consistent with this, transgenic BY-2 cells overexpressing OsDLK showed characteristic alterations of proliferation with a higher frequency seen in mitosis (Fig. 7a,b). At the same time, the doubling time of the culture was not altered (Supplementary Fig. S3a), indicative of a prolonged progression through mitosis. In fact, synchronisation experiments showed that the OsDLK line required more time to pass metaphase, while telophase was passed more rapidly (Fig. 7c,d). During the subsequent expansion phase of the culture, The transgenic cells passed more rapidly from proliferation to expansion, as indicated by accelerated nuclear migration from the cell centre towards the periphery after proliferation had ceased (Supplementary Fig. S5), accompanied by a (slight) promotion of cell elongation (Fig. S3b,c). Interestingly, the pattern differs from that seen for overexpression of a different class-XIV kinesin, OsKCH. Here, the exactly opposite pattern had been observed, where the overexpressors show stimulated cell elongation but delayed mitosis during the first 3 days after subcultivation¹⁸. Thus, different members of this kinesin class seem to convey different and specific functions.

When we followed the dynamic redistribution of OsDLK, we observed a pattern that is known from other class-XIV kinesins: In yeast and human cells, class-XIV kinesins (antagonised by class-V kinesins) can regulate microtubule nucleation through the γ -TuRC complex and are conserved elements during formation and function of the spindle apparatus³⁷. Typically, class-XIV kinesins bind to the midzone of spindle, thus contributing to the straightening of the spindle axis and the shortening of the spindle. Consistently with this rule, OsDLK accumulated in the metaphase plate and then redistributed into clear fibres distal to the metaphase (Fig. 2i-p). A second feature of class-XIV kinesins is the bundling of parallel MTs to focus the spindle poles. Conversely, OsDLK accumulated at the minus ends of parallel MTs at the spindle pole during anaphase (Supplementary Movie S1), as shown for *ncd*³⁸. Overall, the localisation pattern of OsDLK resembles that of its *Arabidopsis* homologues, ATK1 and ATK5, both of which are observed at spindle poles and midzone^{6,7}. This indicates that ATK1/ATK5 and OsDLK may have similar functions in mitosis. Whether OsDLK contributes to microtubule bundling during organisation of the PPB, as had been shown for KCBP^{39,40}, remains to be elucidated. The fact that binding

of OsDLK to the PPB was not observed during this study, along with the fact that overexpression of OsDLK in BY-2 cells did not lead to abnormal spindles, would be more consistent with a function of OsDLK that differs from that of KCBP.

While the mitotic localisation of OsDLK was consistent with the findings on its *Arabidopsis* homologues ATK1 and ATK5, its subcellular localisation during interphase was unexpected. During interphase, OsDLK was found in two populations, one associated with cortical microtubules, the other inside the nucleus. Moreover, this localisation was dynamic and regulated in response to cold (in a reversible manner). Thus, this kinesin was re-partitioned from the cortical cytoplasm into the nucleus, and even in the absence of cold the intranuclear population of DLK was constantly cycled between cytoplasm and nucleoplasm, because inhibition of export by Leptomycin B leads to a nuclear accumulation, however, at a much slower rate (almost by one order of magnitude). Thus, the rapid accumulation under cold stress is more likely to be caused by a stimulation of import, rather than a block of export.

The association of OsDLK with cortical microtubules (Fig. 4a–c) is not unexpected for a plant kinesin. Some kinesins move cargoes linked with cellulose synthesis⁴¹, and also others that are not known to interact with cellulose synthases, nevertheless decorate cMTs. These include the class-XIV kinesins KCH and ATK5^{7,11}. OsDLK moves along cMTs at high speed (Supplementary Movie S2), which might be linked with a function in cell growth.

Unexpected for a kinesin, OsDLK not only decorates cMTs, but simultaneously appears in the nucleus (Fig. 4d–j). This dual localisation was validated in three additional experimental systems using transient transformation: the leaf sheath of rice itself, protoplasts of *Arabidopsis*, and leaves of *Nicotiana benthamiana* (Fig. 5). In all four cases, the fluorescent signal was seen in the nucleus, although interphase microtubules are strictly excluded from the karyoplasm by the interphasic nuclear envelope^{31,42}. However, this canonical strict exclusion of cytoskeletal proteins from the nucleus is progressively challenged by observations that kinesins can be found in the nucleus. For instance, certain animal KIF4s contain a NLS and are in fact found in the nucleus⁴³ while AtFRA1 localizes only in cytoplasm¹⁷. Interestingly, a rice homologue of the exclusively cytoplasmic kinesin OsBC12 shown to localize in both cytoplasm and nucleus was found to be linked with a function as transcriptional regulator for a specific step in gibberellic acid (GA) biosynthesis⁴⁴. When we probed this intranuclear population of OsDLK in more detail, we observed that cold-induced disassembly of cMTs was followed by a progressive accumulation of OsDLK that was organised in a reticular structure closely associated with chromatin and also tubulin (Fig. 8). This nuclear transport was reversible since cortical OsDLK recovered after cells were returned to room temperature. This behaviour parallels the cold-induced accumulation of tubulin in the nucleus observed in those cells³¹. However, even under normal temperature, there seems to be considerable recycling between the intranuclear and the cortical population of OsDLK, since treatment with the specific nuclear-export inhibitor Leptomycin B caused a progressive accumulation of the fluorescent signal in the nuclei of transgenic BY-2 cells (Fig. 9a), while the cortical signal was depleted (Fig. 9b–c).

Conclusion and Perspectives. A rice member of the class-XIV kinesin family, OsDLK, has been found to cycle during interphase between the cortical MTs and the nucleus, and accumulates in the nucleus in response to cold. The same protein also conveys some functions during mitosis. These functions seem to overlap with those of the previously published homologues in *Arabidopsis* (ATK1 and ATK5). To get more insight into this mitotic function, a double visualisation with microtubules *in vivo* would be desirable, but this will require stable double transformation and selection of clones with balanced expression. The fact that nuclear transport of OsDLK occurs also under room temperature, but is promoted by cold stress, indicates that this kinesin plays a specific function in the nucleus. This function, at the current stage, is completely enigmatic. Preliminary data from rice insertion mutants indicate that OsDLK is essential for early development. This is supported by the observation that the steady-state levels of OsDLK transcripts are upregulated during coleoptile elongation. We have currently found that OsDLK can bind to DNA in a specific manner, however, whether it can exert transcriptional regulation similar to rice fra1 homologue is not clear. In other words: there is still a lot to be discovered, even for homologues of well-studied members of the kinesin superfamily.

Materials and Methods

Isolation and cloning of OsDLK. Rice (*Oryza sativa* L. *japonica* cultivar *Nipponbare*) seedlings were grown in darkness at 25 °C for 4 days and coleoptiles excised and shockfrozen in liquid nitrogen in aliquots of 100 mg, followed by grinding in a TissueLyser (Qiagen/Retsch Hilden, Germany). Total RNA was extracted with the innuPREP Plant RNA kit (Analytik, Jena, Germany), including on-column digest of genomic DNA with RNase-free DNase I (Qiagen) according to the manufacturer instructions. After quality check by electrophoresis on 1% [w/v] agarose gels, 1 µg RNA was used for cDNA synthesis with the M-Mulv cDNA Synthesis Kit (NEB). Plasmids for plant transformation were constructed via GATEWAY® cloning as described in Klotz and Nick¹¹. The full-length coding sequence of OsDLK was amplified from the cDNA template with a pair of primers containing attB-sites. To get the full-length OsDLK the forward primer: 5'-GGGGACAAGTTTGTACAAAAAAGCAGGCTTCATGTCCACGCGGCCACTCGCC-3', and the reverse primer: 5'-GGGGACCACTTTGTACAAGAAAGCTGGGTCTCCTTGCGCCAAGCTACGCACT-3' were used.

Sequence analysis of OsDLK. The sequence motives and domains of OsDLK from *Oryza sativa* L. *japonica* were analysed by Prosite (<http://prosite.expasy.org/cgi-bin/prosite>) and SMART (<http://smart.embl-heidelberg.de/smart>). The neck region was predicted^{27,45,46}. The software COILS (http://www.ch.embnet.org/software/COILS_form.html) was used²⁶ to test the coiled coil regions. Candidate kinesins from different kinesin subfamilies of plants, animals and fungi, such as *Arabidopsis thaliana*, *Oryza sativa*, *Nicotiana tabacum*, *Gossypium hirsutum*, *Emericella nidulans*, *Drosophila melanogaster*, and *Saccharomyces cerevisiae* were aligned and then inferred into a phylogenetic tree by in MEGA5 (<http://www.megasoftware.net/>)⁴⁷.

Accession numbers in UniProtKB/Swiss-Prot (<http://www.uniprot.org>) for the protein sequences used in the phylogenetic analysis can be accessed as follows: OsDLK(B8B6J5), DmNCD(P20480), EnKlpA(P28739), GhKCH1(Q5MNW6), NtTKRP125(O23826), NtKCH(F8UN41), ScKar3(P17119), OsACK1(Q9AWM8), OsKinesin13A(Q0DKM5), OsBC2(Q6YUL8), OsKCH(Q0IMS9), ATK5(F4JGP4), AtARK2(Q9LPC6), AtNACK1(Q8S905), AtARK3(Q9FZ06), AtKatA(Q07970), AtKinesin12B(F4J464), AtNACK2(Q8LNZ2), AtKCH(Q8W1Y3), AtKatB(P46864), AtPAKRP2(Q8VWI7), AtMKRP2(Q8W5R5), AtKCA1(Q9LX99), AtKatD(O81635), AtKatC(P46875), AtKAC2(Q9FKP4), AtKCBP(Q9FHN8).

Plasmid construction. Using the GATEWAY[®]-Cloning technology (Invitrogen Corporation, Paisley, UK), the amplified PCR products of OsDLK were first recombined into the entry plasmid pDONR/Zeo (Invitrogen), and then cloned into the binary plasmid pK7FWG2 and pH7WGF2⁴⁸ for stable and transient transformation, respectively. In these constructs, OsDLK was placed under control of the constitutive CaMV-35S promoter, and GFP was located C-terminally. Correct and complete insertion was verified by DNA sequencing (GATC Biotech, Cologne, Germany). Microtubules were visualised with the construct GFP-pCambiaTuB6⁴⁹, in which GFP was fused to *Arabidopsis* β -Tubulin 6. The OsDLK bacterial expression construct was amplified using the primers 5'-CACAGCAGCGCCTGGTGCCGACTCGCCCCGGGATGCTCCACCAGAAG and 5'-CTTTCGGGCTTTGTTAGCAGCCGGATCTCATCCTTGCGCCAAGCTACGCACTTGGG and inserted into the pET28a bacterial expression vector (Novagen) via overlap extension cloning⁵⁰.

Transformations and cell culture. pK7FWG2-OsDLK was transformed into BY-2 (*Nicotiana tabacum* L. cv. *Bright Yellow 2*) cells via the *Agrobacterium* strain LBA4404 (Invitrogen) for establishment of stable overexpression cell line based on standard protocol⁵¹ with minor modifications described by Klotz and Nick¹¹. Cell suspension cultures were then maintained in liquid Murashige and Skoog (MS) medium and subcultured weekly⁵². For transient transformation⁵³, pH7RWG2-OsDLK and GFP-pCambiaTuB6 were co-transformed into LBA4404, subsequently grown on solid Paul's medium for 3 days, and then examined microscopically without preceding selection.

Transient protein expression in mesophyll protoplast of *Arabidopsis thaliana* was performed as described in by Tong *et al.*⁵⁴. Protoplasts were incubated for 24 hours at room temperature in the dark. Also transient protein expression in *Nicotiana benthamiana* leaves was carried out according Tong *et al.*⁵⁴ via *Agrobacterium tumefaciens* C58C1 strains⁵⁵ harbouring the pK7FWG2-OsDLK construct or a construct for the tobamovirus RNA silencing suppressor p19⁵⁶. Rice (*Oryza sativa* L. *japonica* cultivar *Nihonmasari*) seedlings were grown in phytoagar at 25 °C for 10 days⁵⁷. pK7FWG2-OsDLK DNA was transformed into the second leaf blades following the protocol by Holweg *et al.*⁵³. The transformed rice blades were incubated in the dark at 25 °C for 24 h before examination by microscopy.

In vivo microscopy and image analysis. Cellular details of individual cells or cells population were examined under an AxioObserver Z1 microscope (Zeiss, Jena, Germany) equipped with a cooled digital CCD camera (AxioCam MRm) and a spinning-disc device (YOKOGAWA CSU-X1 5000) or an ApoTome microscope slider for optical sectioning. GFP fluorescence and RFP/TRITC fluorescence signals were observed through the 488 nm and 561 nm emission line of an Ar-Kr laser (Zeiss), DNA labelling by Hoechst 33258 was recorded using the filter set 49 DAPI¹¹. To detect fluorescence of DLK-GFP in living *N. benthamiana* leaf cells and *A. thaliana* protoplasts, confocal laser scanning microscopy was applied by using the Leica TCS SP8 Confocal Platform (Leica Microsystems, Wetzlar, Germany). The detection windows ranged from 496 to 511 nm (GFP), 569 to 591 nm (RFP), as well as 690 to 708 nm for the detection of chlorophyll autofluorescence. Acquired images were operated via the Zen 2012 (Blue edition) software platform, AxioVision (Rel. 4.8.2) software and ImageJ (NIH, Bethesda, USA).

Determination of packed cell volume. To quantify culture growth, packed cell volume (PCV) was measured at days 4 (after the proliferation phase) and 6 (at the end of expansion phase) after subcultivation⁵⁸. The cell suspension was poured into a 15-mL Falcon tube and kept vertically at 4 °C for 48 hours, till most cells had settled to the bottom. The PCV could then be read directly from the scale of the 15-mL Falcon tube.

Determination of mitotic index. Tobacco BY-2 cell cycle progress was monitored by mitotic indices (MI), defined as the relative frequency of dividing cells. BY-2 cells were fixed by Carnoy fixative and Hoechst 33258 (Sigma, Taufkirchen, Germany) at a final concentration of 1 $\mu\text{g}\cdot\text{mL}^{-1}$, and samples were immediately investigated with microscope.

Cell cycle synchronization. Cells were synchronized according to a protocol modified from Samuels *et al.*⁵⁹ by using hydroxyurea instead of aphidicolin⁶⁰. 7-d-old BY-2 cells were subcultured in MS medium complemented with 4 mM hydroxyurea (HU, Sigma) for 24 h. After 24 hours, HU was washed out by a Nalgene filter holder (Thermo Scientific, Langensfeld, Germany) in combination with a Nylon mesh with pores of diameter of 70 μm (Mehlsieb, Franz Eckert, Waldkirch, Germany). Then the cells were resuspended in fresh MS medium for cultivation, returned into flask and shaken for a further 3 h. 6 μM Propyzamide (Sigma) was added into the culture and the suspension was shaken for another 6 h. Subsequently, propyzamide was removed. After washing, cells were resuspended again in fresh MS medium and cultured on a shaker, while MI was monitored every 30 min over 4 hours.

Immunostaining of microtubules. Microtubules were visualized by indirect immunofluorescence as described in Nick *et al.*⁶¹ with mouse monoclonal antibodies against α -tubulin, DM1A (Sigma) and a polyclonal secondary TRITC-conjugated anti-mouse IgG antibody (Sigma). In some cases, the DNA was also stained with Hoechst 33258.

Cold treatment and cell mortality. Suspensions of 3-day-old BY-2 cells overexpressing OsDLK-GFP in Erlenmeyer flasks were placed in a bath of ice water to maintain a temperature of 0 °C and shaken on an orbital shaker at 100 rpm in darkness for 24 h. Samples of cells were collected at specified time points during the cold treatment for cytological observation and immunostaining. Cell mortality was quantified using Evans Blue assay⁶². After remove the dye by washing 3 times in water, cells were viewed under AxioImager Z.1 microscope (Zeiss). Data represent means and standard deviations from three biological replicates with 500 individual cells scored for each value.

Leptomycin B treatment. To measure the accumulation of OsDLK in nuclei, OsDLK-GFP BY-2 cells in their exponential phase of growth (3 days after inoculation) were treated with 200 nM Leptomycin B (Sigma), an inhibitor of nuclear export. The cells were incubated for a further 48 h under standard conditions, and z-stacks of GFP signal were recorded (AxioImager Z.1). For the quantification, geometrical projections (maximum intensity algorithm) were quantified using Image J. Intensity profiles along a very broad probing line (in the thickness of roughly the nucleus) were collected across the entire cross section of the cell and then a second time along the same plane, but just covering the nucleus. The two integral over these two profiles were used to calculate the percentage of signal located inside the nucleus. Control treatments were performed by treating the cells with the corresponding volume of solvent [70% methanol].

Protein expression and purification. C-terminally hexa-histidine-tagged OsDLK(aa 1–764) was expressed in *Escherichia coli* BL21(DE3)-pRARE (Millipore) grown in LB medium and induced with 0.2 mM IPTG for 3 h at 37 °C. Harvested cells were resuspended in buffer A (pH 7.4, 274 mM NaCl, 5.4 mM KCl, 16.2 mM Na₂HPO₄, 3.52 mM KH₂PO₄, 2 mM MgCl₂, 1 mM ATP, 1 mM dithiothreitol, and EDTA-free protease inhibitors (Roche)) and lysed using a high pressure homogenizer. The crude lysate was centrifuged at 17,400 g at 4 °C and loaded onto a 5 mL HiTrap NiNTA column (GE Healthcare). The column was washed with 50 mL buffer A containing 30 mM imidazole. Proteins were eluted in buffer A containing 500 mM imidazole, pH 8.0. Proteins were snap-frozen in liquid nitrogen and stored at –80 °C.

Motility assays *in vitro*. Microtubules were polymerized as described before using DyLight594-labeled or a mixture of Cy5-labeled and digoxigenin-labeled (1:5) tubulin. For the microtubule sliding motility assay, microtubules co-labeled with digoxigenin and Cy5 were immobilized to the glass surface via digoxigenin antibodies (Roche). After blocking with 1% Pluronic F127, OsDLK motors were added to the microtubules in absence of ATP. Subsequently, microtubules labeled with DyLight594 in imaging solution were allowed to bind to the motors and transport was monitored in presence of 2 mM ATP. Fluorescently labeled microtubules were visualized using epi-illumination on an inverted fluorescence microscope (Ti-E, Nikon) equipped with an EMCCD camera (iXon Ultra, Andor). Positions of microtubules were obtained using FIESTA tracking software as described before⁶³. The mean velocity was determined by fitting the velocity histograms to Gaussian functions using MatLab (Mathworks).

Data availability. The datasets generated during and/or analysed in the current study are available from the corresponding author on reasonable request.

References

- Wickstead, B. & Gull, K. Dyneins across eukaryotes: a comparative genomic analysis. *Traffic* **8**, 1708–1721 (2007).
- Jonsson, E., Yamada, M., Vale, R. D. & Goshima, G. Clustering of a kinesin-14 motor enables processive retrograde microtubule-based transport in plants. *Nature Plants* **1**, 15087 (2015).
- Yamada, M., Tanaka-Takiguchi, Y., Hayashi, M., Nishina, M. & Goshima, G. Multiple kinesin-14 family members drive microtubule minus end-directed transport in plant cells. *The Journal of Cell Biology* **216**, 1705–1714 (2017).
- Fujii, K. On the morphology of the spermatozoid of *Ginkgo biloba*. *Bot. Mag. Tokyo* **13**, 260–266 (1899).
- Buschmann, H. & Zachgo, S. The evolution of cell division: From streptophyte algae to land plants. *Trends in Plant Science* **21**, 872–883 (2016).
- Liu, B., Cyr, R. J. & Palevitz, B. A. A kinesin-like protein, KatAp, in the cells of arabidopsis and other plants. *The Plant Cell* **8**, 119–132 (1996).
- Ambrose, J. C., Li, W. X., Marcus, A., Ma, H. & Cyr, R. A minus-end directed kinesin with plus-end tracking protein activity is involved in spindle morphogenesis. *Molecular Biology of the Cell* **16**, 1584–1592 (2005).
- Wu, S.-Z. & Bezanilla, M. Myosin VIII associates with microtubule ends and together with actin plays a role in guiding plant cell division. *Elife* **3**, e03498 (2014).
- Lee, Y.-R. J., Li, Y. & Liu, B. Two *Arabidopsis* phragmoplast-associated kinesins play a critical role in cytokinesis during male gametogenesis. *The Plant Cell* **19**, 2595–2605 (2007).
- Buschmann, H. *et al.* *Arabidopsis* KCBP interacts with AIR9 but stays in the cortical division zone throughout mitosis via its MyTH4-FERM domain. *Journal of Cell Science* **128**, 2033–2046 (2015).
- Klotz, J. & Nick, P. A novel actin-microtubule cross-linking kinesin, NtKCH, functions in cell expansion and division. *New Phytologist* **193**, 576–589 (2012).
- Müller, S., Han, S. C. & Smith, L. G. Two kinesins are involved in the spatial control of cytokinesis in *Arabidopsis thaliana*. *Current Biology* **16**, 888–894 (2006).
- Zhu, C. M. & Dixit, R. Functions of the *Arabidopsis* kinesin superfamily of microtubule-based motor proteins. *Protoplasma* **249**, 887–899 (2012).
- Lloyd, C. & Chan, J. The parallel lives of microtubules and cellulose microfibrils. *Current Opinion in Plant Biology* **11**, 641–646 (2008).
- Ledbetter, M. C. & Porter, K. R. A “microtubule” in plant cell fine structure. *The Journal of Cell Biology* **19**, 239–250 (1963).
- Heath, I. B. A unified hypothesis for the role of membrane bound enzyme complexes and microtubules in plant cell wall synthesis. *Journal of Theoretical Biology* **48**, 445–449 (1974).
- Zhong, R. Q., Burk, D. H., Morrison, W. H. & Ye, Z. H. A kinesin-like protein is essential for oriented deposition of cellulose microfibrils and cell wall strength. *The Plant Cell* **14**, 3101–3117 (2002).

18. Frey, N., Klotz, J. & Nick, P. A kinesin with calponin-homology domain is involved in premitotic nuclear migration. *Journal of Experimental Botany* **61**, 3423–3437 (2010).
19. Liu, G. Q., Cai, G., Casino, C. D., Tiezzi, A. & Cresti, M. Kinesin-related polypeptide is associated with vesicles from *Corylus avellana* pollen. *Cytoskeleton* **29**, 155–166 (1994).
20. Ni, C. Z., Wang, H. Q., Tao, X. U., Zhe, Q. U. & Liu, G. Q. AtKIP1, a kinesin-like protein, mainly localizes to mitochondria in *Arabidopsis thaliana*. *Cell Research* **15**, 725–733 (2005).
21. Suetsugu, N. *et al.* Two kinesin-like proteins mediate actin-based chloroplast movement in *Arabidopsis thaliana*. *Proceedings of the National Academy of Sciences of the United States of America* **107**, 8860–8865 (2010).
22. Clark, I., Giniger, E., Ruohola-Baker, H., Jan, L. Y. & Jan, Y. N. Transient posterior localization of a kinesin fusion protein reflects anteroposterior polarity of the *Drosophila oocyte*. *Current Biology* **4**, 289–300 (1994).
23. Cheung, H. O.-L. *et al.* The kinesin protein Kif7 is a critical regulator of Gli transcription factors in mammalian hedgehog signaling. *Science Signaling* **2**, ra29–ra29 (2009).
24. Li, J. *et al.* Mutation of rice BC12/GDD1, which encodes a kinesin-like protein that binds to a GA biosynthesis gene promoter, leads to dwarfism with impaired cell elongation. *The Plant Cell* **23**, 628–640 (2011).
25. Yang, J. T., Laymon, R. A. & Goldstein, L. S. B. A three-domain structure of kinesin heavy chain revealed by DNA sequence and microtubule binding analyses. *Cell* **56**, 879–889 (1989).
26. Lupas, A., Van Dyke, M. & Stock, J. Predicting coiled-coils from protein sequences. *Science* **252**, 1162–1164 (1991).
27. Endow, S. A. Determinants of molecular motor directionality. *Nature Cell Biology* **1**, E163–E167 (1999).
28. Marcus, A. I., Ambrose, J. C., Bickley, L., Hancock, W. O. & Cyr, R. J. *Arabidopsis thaliana* protein, ATK1, is a minus-end directed kinesin that exhibits non-processive movement. *Cytoskeleton* **52**, 144–150 (2002).
29. Zimmermann, P., Hirsch-Hoffmann, M., Hennig, L. & Gruissem, W. GENEVESTIGATOR. *Arabidopsis* microarray database and analysis toolbox. *Plant Physiology* **136**, 2621–2632 (2004).
30. Hruz, T. *et al.* Genevestigator v3: a reference expression database for the meta-analysis of transcriptomes. *Advances in Bioinformatics* **2008**, 420747 (2008).
31. Schwarzerová, K. *et al.* Intranuclear accumulation of plant tubulin in response to low temperature. *Protoplasma* **227**, 185–196 (2006).
32. Kudo, N. *et al.* Leptomycin B inhibition of signal-mediated nuclear export by direct binding to CRM1. *Experimental Cell Research* **242**, 540–547 (1998).
33. Richardson, D. N., Simmons, M. P. & Reddy, A. S. N. Comprehensive comparative analysis of kinesins in photosynthetic eukaryotes. *BMC Genomics* **7**, 18 (2006).
34. Mazumdar, M. & Misteli, T. Chromokinesins: multitasking players in mitosis. *Trends in Cell Biology* **15**, 349–355 (2005).
35. Vanstraelen, M., Inzé, D. & Geelen, D. Mitosis-specific kinesins in *Arabidopsis*. *Trends in Plant Science* **11**, 167–175 (2006).
36. Menges, M., Hennig, L., Gruissem, W. & Murray, J. A. H. Genome-wide gene expression in an *Arabidopsis* cell suspension. *Plant Molecular Biology* **53**, 423–442 (2003).
37. Vale, R. D. The molecular motor toolbox for intracellular transport. *Cell* **112**, 467–480 (2003).
38. Fink, G. *et al.* The mitotic kinesin-14 Ncd drives directional microtubule-microtubule sliding. *Nature Cell Biology* **11**, 717–723 (2009).
39. Bowser, J. & Reddy, A. S. N. Localization of a kinesin-like calmodulin-binding protein in dividing cells of *Arabidopsis* and tobacco. *The Plant Journal* **12**, 1429–1437 (1997).
40. Marcus, A. I., Li, W. X., Ma, H. & Cyr, R. J. A kinesin mutant with an atypical bipolar spindle undergoes normal mitosis. *Molecular Biology of the Cell* **14**, 1717–1726 (2003).
41. Cai, G. & Cresti, M. Are kinesins required for organelle trafficking in plant cells? *Frontiers in Plant Science* **3**, 170 (2012).
42. Hasezawa, S. & Kumagai, F. Dynamic changes and the role of the cytoskeleton during the cell cycle in higher plant cells. *International Review of Cytology* **214**, 161–191 (2002).
43. Wang, S.-Z. & Adler, R. Chromokinesin: a DNA-binding, kinesin-like nuclear protein. *The Journal of Cell Biology* **128**, 761–768 (1995).
44. Zhang, M. *et al.* Brittle Culm 12, a dual-targeting kinesin-4 protein, controls cell cycle progression and wall properties in rice. *The Plant Journal* **63**, 312–328 (2010).
45. Amos, L. A. & Hirose, K. The structure of microtubule-motor complexes. *Current Opinion in Cell Biology* **9**, 4–11 (1997).
46. Sablin, E. P. *et al.* Direction determination in the minus-end-directed kinesin motor ncd. *Nature* **395**, 813–816 (1998).
47. Tamura, K. *et al.* MEGA5: molecular evolutionary genetics analysis using maximum likelihood, evolutionary distance, and maximum parsimony methods. *Molecular Biology and Evolution* **28**, 2731–2739 (2011).
48. Karimi, M., Inzé, D. & Depicker, A. GATEWAY™ vectors for *Agrobacterium*-mediated plant transformation. *Trends in Plant Science* **7**, 193–195 (2002).
49. Nakamura, M., Naoi, K., Shoji, T. & Hashimoto, T. Low concentrations of propyzamide and oryzalin alter microtubule dynamics in *Arabidopsis* epidermal cells. *Plant and Cell Physiology* **45**, 1330–1334 (2004).
50. Bryksin, A. & Matsumura, I. Overlap extension PCRcloning. *Synthetic Biology*, 31–42 (2013).
51. Buschmann, H., Green, P., Sambade, A., Doonan, J. H. & Lloyd, C. W. Cytoskeletal dynamics in interphase, mitosis and cytokinesis analysed through *Agrobacterium*-mediated transient transformation of tobacco BY-2 cells. *New Phytologist* **190**, 258–267 (2011).
52. Nagata, T., Nemoto, Y. & Hasezawa, S. Tobacco BY-2 cell line as the “HeLa” cell in the cell biology of higher plants. *International Review of Cytology* **132**, 1–30 (1992).
53. Holweg, C., Süßlin, C. & Nick, P. Capturing *in vivo* dynamics of the actin cytoskeleton stimulated by auxin or light. *Plant and Cell Physiology* **45**, 855–863 (2004).
54. Tong, M. *et al.* E3 ligase SAUL1 serves as a positive regulator of PAMP-triggered immunity and its homeostasis is monitored by immune receptor SOC3. *New Phytologist* **215**, 1516–1532 (2017).
55. Deblaere, R. *et al.* Efficient octopine Ti plasmid-derived vectors for *Agrobacterium*-mediated gene transfer to plants. *Nucleic Acids Research* **13**, 4777–4788 (1985).
56. Silhavy, D. *et al.* A viral protein suppresses RNA silencing and binds silencing-generated, 21- to 25-nucleotide double-stranded RNAs. *The EMBO Journal* **21**, 3070–3080 (2002).
57. Brendel, R. *et al.* Effects of light and wounding on jasmonates in rice phyAphyC mutants. *Plants* **3**, 143–159 (2014).
58. Jovanović, A. M., Durst, S. & Nick, P. Plant cell division is specifically affected by nitrotyrosine. *Journal of Experimental Botany* **61**, 901–909 (2010).
59. Samuels, A. L., Meehl, J., Lipe, M. & Staehelin, L. A. Optimizing conditions for tobacco BY-2 cell cycle synchronization. *Protoplasma* **202**, 232–236 (1998).
60. Kuthanova, A., Fischer, L., Nick, P. & Opatrný, Z. Cell cycle phase-specific death response of tobacco BY-2 cell line to cadmium treatment. *Plant, Cell & Environment* **31**, 1634–1643 (2008).
61. Nick, P., Heuing, A. & Ehmann, B. Plant chaperonins: a role in microtubule-dependent wall formation? *Protoplasma* **211**, 234–244 (2000).
62. Chang, X. L., Riemann, M., Liu, Q. & Nick, P. Actin as deathly switch? How auxin can suppress cell-death related defence. *PLoS One* **10**, e0125498 (2015).

63. Ruhnnow, F., Zwicker, D. & Diez, S. Tracking single particles and elongated filaments with nanometer precision. *Biophysical Journal* **100**, 2820–2828 (2011).
64. Chandra, R., Salmon, E. D., Erickson, H. P., Lockhart, A. & Endow, S. A. Structural and functional domains of the *Drosophila* ncd microtubule motor protein. *Journal of Biological Chemistry* **268**, 9005–9013 (1993).
65. Walter, W. J., Machens, I., Rafeian, F. & Diez, S. The non-processive rice kinesin-14 OsKCH1 transports actin filaments along microtubules with two distinct velocities. *Nature Plants* **1**, 15111 (2015).
66. Endow, S. A. *et al.* Yeast Kar3 is a minus-end microtubule motor protein that destabilizes microtubules preferentially at the minus ends. *The EMBO Journal* **13**, 2708 (1994).
67. Song, H., Golovkin, M., Reddy, A. S. N. & Endow, S. A. *In vitro* motility of AtKCBP, a calmodulin-binding kinesin protein of *Arabidopsis*. *Proceedings of the National Academy of Sciences of the United States of America* **94**, 322–327 (1997).
68. Cai, D., Verhey, K. J. & Meyhöfer, E. Tracking single kinesin molecules in the cytoplasm of mammalian cells. *Biophysical Journal* **92**, 4137–4144 (2007).
69. Walter, W. J., Beránek, V., Fischermeier, E. & Diez, S. Tubulin acetylation alone does not affect kinesin-1 velocity and run length *in vitro*. *PLoS One* **7**, e42218 (2012).
70. Hancock, W. O. & Howard, J. Processivity of the motor protein kinesin requires two heads. *The Journal of Cell Biology* **140**, 1395–1405 (1998).

Acknowledgements

We thank Dr. Jan Maisch for the pDONR/Zeo-FABD2 plasmid and pCambia-TuB6 plasmid. We thank Tobias Strauß for his help in confocal microscopy of *Arabidopsis thaliana* protoplasts and *Nicotiana benthamiana* leaf cells. This work was financially supported by China Scholarship Council (CSC) to Xiaolu Xu and German Research Foundation (DFG, Ni 324-19/1). We acknowledge support by Deutsche Forschungsgemeinschaft and open access publishing fund of Karlsruhe Institute of Technology.

Author Contributions

X.X., W.W. and P.N. designed the research. X.X., M.I. performed the experiments. X.X., Q.L., W.W. and P.N. analysed data. X.X., W.W. and P.N. wrote the manuscript.

Additional Information

Supplementary information accompanies this paper at <https://doi.org/10.1038/s41598-018-21816-w>.

Competing Interests: The authors declare no competing interests.

Publisher's note: Springer Nature remains neutral with regard to jurisdictional claims in published maps and institutional affiliations.



Open Access This article is licensed under a Creative Commons Attribution 4.0 International License, which permits use, sharing, adaptation, distribution and reproduction in any medium or format, as long as you give appropriate credit to the original author(s) and the source, provide a link to the Creative Commons license, and indicate if changes were made. The images or other third party material in this article are included in the article's Creative Commons license, unless indicated otherwise in a credit line to the material. If material is not included in the article's Creative Commons license and your intended use is not permitted by statutory regulation or exceeds the permitted use, you will need to obtain permission directly from the copyright holder. To view a copy of this license, visit <http://creativecommons.org/licenses/by/4.0/>.

© The Author(s) 2018

List of publications

Kruger, J.P., Machens, I., Lahner, M., Endres, M., Kaps, C., Initial boost release of transforming growth factor-beta3 and chondrogenesis by freeze-dried bioactive polymer scaffolds. *Ann Biomed Eng*, 2014. 42(12): p. 2562-76.

Walter, W.J., Machens, I., Refieian, F., Diez, S., The non-processive rice kinesin-14 OsKCH1 transports actin filaments along microtubules with two distinct velocities. *Nature Plants*, 2015. 1(2015.111): p. 2015.111.

Xu, X., Walter, W.J., Liu, Q., Machens, I., Nick, P., al., A rice class-XIV kinesin enters the nucleus in response to cold. *Sci Rep*, 2018. 8(1): p. 3588.

Acknowledgements

Zuerst möchte ich mich bei Prof. Dr. Wim Walter für die Bereitstellung meines Promotionsthemas und die Begutachtung meiner Arbeit bedanken. Mit den zahlreichen fachlichen Diskussionen und deinem niemals versiegenden Optimismus hast du mich während meiner Promotion sehr unterstützt und meinen 'Realismus' ausgeglichen. Danke, dass ich an deinen spannenden Projekten und spontanen Einfällen mitarbeiten durfte.

Prof. Dr. Sigrun Reumann danke ich für die zweite Begutachtung dieser Arbeit.

Zudem bedanke ich mich bei der gesamten Abteilung der Molekularen Pflanzenphysiologie, allen Mitarbeitern, Doktoranden und Studenten, die für die angenehme und hilfsbereite Arbeitsatmosphäre in der Gruppe sorgen. Danke für die schöne, produktive Zusammenarbeit, sowie eure Zeit und eure Anregungen immer dann, wenn ich Hilfe gebraucht habe.

Ein besonderer Dank gilt Melanie Schulz, Pierre Endries und Julia Sandberg, die mir im Labor vor allem gegen Ende meiner Promotion eine große Hilfe waren.

Auch Frida Mandik, Zeynep Aydin, Janna Varady und Mirella Skiba möchte ich nicht vergessen. Ihr habt mich während eurer Abschlussarbeiten bzw. Praxissemester in meinen Projekten sehr unterstützt.

Bei Elke Woelken möchte ich mich für die Hilfe beim Einbetten, Präparieren und Dokumentieren der Dünnschnitte bedanken.

Dr. Friedrich Schwarz danke ich für die Bereitstellung einiger MATLAB Programme, die ich zur Auswertung meiner Daten nutzen konnte.

Saskia Schattner, Jan Knop und Tobias Strauß, ihr hattet immer ein offenes Ohr für mich und an schlechten Tagen auch immer einen guten Rat oder zumindest aufmunternde Worte.

Ihr Lieben, es war mir eine Freude mit euch zu arbeiten.

Zuletzt möchte ich mich noch bei meiner Familien bedanken. Bei meinen lieben Eltern, die durch ihre Unterstützung und die Finanzierung meines Studiums diese Arbeit erst ermöglicht haben. Und natürlich bei Alexander Schumacher. Du warst während der gesamten Zeit immer für mich da und hast meine Höhen und Tiefen ertragen müssen. Gott sei Dank hast du immer den richtigen Spruch auf Lager, um mich in jeder Situation zum Lächeln zu bringen.

Isabel Machens
Roggenkamp 6
22305 Hamburg

Berlin, den 23.03.2018

Erklärung

Sehr geehrte Damen und Herren,

hiermit bestätige ich Richard Forsythe, geboren am 24.01.1984 in Pembury, Großbritannien, dass die Dissertation von Isabel Machens in einem korrekten Englisch verfasst wurde.

Mit freundlichen Grüßen



Richard Forsythe

Affidavit

Hiermit erkläre ich an Eides statt, dass ich die vorliegende Dissertationsschrift selbst verfasst und keine anderen als die angegebenen Quellen und Hilfsmittel benutzt habe.

Hamburg, den